CPPM-T-2019-06

AIX-MARSEILLE UNIVERSITÉ

Ecole Doctorale 352 : Physique et Sciences de la Matière

Faculté Des Sciences de Luminy

Centre de Physique des Particules de Marseille

Thèse présentée pour obtenir le grade universitaire de docteur

Discipline : Physique et Sciences de la Matière
Spécialité : Physiques des Particules et Astroparticules

Nihal BRAHIMI

Search for the Higgs boson in the $t\bar{t}H(H \to b\bar{b})$ channel and measurement of the production cross-section of $t\bar{t}b\bar{b}$ with the ATLAS detector at the LHC

CERN-THESIS-2019-236
31/10/2019

Soutenue le 31/10/2019 devant le jury :

Aurelio JUSTE	Université Autonome de Barcelone, Espagne	Rapporteur
Jessica LEVEQUE	LAPP Annecy, France	Rapporteur
Andrea COCCARO	Université de Gênes, Italie	Examinateur
Cristinel DIACONU	CPPM, Marseille, France	Examinateur
Chafik BENCHOUK	USTHB, Alger, Algérie	Examinateur
Laurent VACAVANT	CPPM, Marseille, France	Directeur de thèse
Georges AAD	CPPM, Marseille, France	Co-directeur de thèse

Acknowledgments

This work would not have seen the light of the day if it weren't for all of those who accompanied me, both professionally and personally, the whole time leading up to writing these lines. The following statements are my modest attempt to acknowledge their support.

To my supervisors, Laurent Vacavant and Georges Aad, I am deeply grateful for granting me the opportunity to work on this thesis topic. It is thanks to your impressive knowledge, endless support, dedication and confidence in my abilities that I was capable to accomplish the research work documented in this manuscript. I would also like to stress how much I enjoyed your sense of humor which made it fun to work even when it got too overwhelming; I don't know many who laughed each time they got fired;-) I had a rewarding and enriching research experience under your supervision and I hope I get the chance one day to work with you again!

To the reviewers of this document, Aurelio Juste and Jessica Levêque, as well as the other jury members, Cristinel Diaconu, Andrea Coccaro and Chafik Benchouk, thank you for taking the time to read my work and listen to my defense. Thank you as well for the insightful comments which helped me widen my perspective and see my work in a new light.

To the ATLAS group of the CPPM, especially the $t\bar{t}H(H \to b\bar{b})$ analysis team, thank you for your valuable inputs and continuous feedback. It was a great honor and privilege working with such a fantastic group of people. I would also like to thank the rest of the CPPM staff (IT, HR, other research groups,..etc) who all collectively have created an atmosphere where it is an absolute joy to work.

To all my fellow PhD students, it was a tremendous pleasure sharing this journey with you. Special thanks go to those who have been with me since the P3TMA master year (Ziyu, Nghia, Grig and Cédric) in addition to my seniors (Rima and Anna) who as I am writing these lines have all become my fellow Doctors;-). Many thanks as well to my office-mate, Dawid "the martial artist", who has been so generous in demonstrating and transferring his skills even after long days of work!. Thank you all for the wonderful moments we spent together (birthdays, dinner parties, hikes including Luminy to Cassis! and 10K races!) and for the fruitful and heated discussions we had over the last four years which helped me look at the world from a different angle. I will always cherish these moments and look forward to our paths crossing again one day!

To my beloved family, especially my parents (Hayate and Lakhdar) and my baby sister Fadou (actually only two years younger), thank you so much for encouraging me to pursue my goals and supporting me unconditionally throughout all my endeavors even if they meant I had to spend a lot of time away from you and home. I could never thank you enough for your unlimited love and patience which got me through a lot of bumps in my road. Gazillion thanks to you for being there for me!

Last but not least, I would like to thank everyone who will (or had) read this document. Have a nice reading and good luck!

Abstract

Keywords: LHC, ATLAS, Higgs boson, $t\bar{t}H$, $H \to b\bar{b}$, $t\bar{t}$ + jets, $t\bar{t}b\bar{b}$, b-tagging, High Luminosity LHC.

Since the discovery of the Higgs boson at a mass around 125 GeV by both ATLAS and CMS collaborations in July 2012, it became crucial to measure its properties, such as its couplings to fermions, and unravel any deviations from the Standard Model (SM) predictions. The top quark Yukawa coupling is the strongest in the fermionic sector and one of the best probes to shed light on phenomena beyond the SM. The Higgs boson production in association with a pair of top quarks and its subsequent decay into a pair of bottom quarks, $t\bar{t}H(H \to b\bar{b})$, grants direct access to this coupling in addition to the bottom quark Yukawa coupling. Although the $t\bar{t}H$ production was recently established by both ATLAS and CMS combining several channels including $t\bar{t}H(H \to b\bar{b})$, the latter has never been observed directly. The complexity of the $t\bar{t}H(H \to b\bar{b})$ final state with a large number of b-jets, and the overwhelming background of the top pair production with additional jets ($t\bar{t}$ + jets), especially b-jets ($t\bar{t}b\bar{b}$), are the major challenges of this channel. Thus, b-jet identification referred to as b-tagging, and the control of the $t\bar{t}b\bar{b}$ background are key ingredients for this analysis. This thesis presents the search for $t\bar{t}H(H \to b\bar{b})$ performed with 36.1 fb^{-1}of LHC data collected by the ATLAS detector in 2015 and 2016. Novel techniques to improve the search sensitivity with full Run 2 data are also developed. Particularly, detailed studies are presented including a differential cross-section measurement of the main $t\bar{t}b\bar{b}$ background. The optimization of the b-tagging algorithms in view of the High Luminosity LHC upgrade, after the replacement of the ATLAS inner detector, is also presented.

Mots-clés: LHC, ATLAS, boson de Higgs, $t\bar{t}H$, $H \to b\bar{b}$, $t\bar{t}$ + jets, $t\bar{t}b\bar{b}$, b-tagging, LHC à haute luminosité.

Depuis la découverte du boson de Higgs de masse 125 GeV par les expériences ATLAS et CMS en juillet 2012, il est devenu crucial de mesurer ses propriétés, tel que son couplage aux fermions, pour établir sa nature et déceler toute déviation possible par rapport aux prédictions du Modèle Standard. Dans le secteur fermionique, le couplage Yukawa du quark top est le plus fort et ainsi joue un rôle majeur dans la découverte de nouvelle physique au delà du Modèle Standard. La production du boson de Higgs en association avec une paire de quark top et sa désintégration en deux quarks b, $t\bar{t}H(H \to b\bar{b})$, donne accès à ce couplage ainsi qu'à celui du quark b. Bien que la production $t\bar{t}H$ a été récemment établie par ATLAS et CMS en combinant plusieurs canaux dont $t\bar{t}H(H \to b\bar{b})$, ce dernier n'a jamais était observé directement. La complexité de l'état final de $t\bar{t}H(H \to b\bar{b})$ qui contient un grand nombre de b-jets, ainsi que la présence du bruit de fond dominant de la production de paire de quark top avec des jets supplémentaires ($t\bar{t}$ + jets), en particulier avec des b-jets ($t\bar{t}b\bar{b}$), sont les principaux défis de ce canal. Par conséquent, l'étiquetage des b-jets, appelé b-tagging, et le contrôle du bruit de fond $t\bar{t}b\bar{b}$ sont des ingrédients clés pour cette analyse. Cette thèse présente la recherche de $t\bar{t}H(H \to b\bar{b})$ avec 36.1 fb^{-1}de données LHC recueillies par le détecteur ATLAS en 2015 et 2016. Des techniques novatrices pour améliorer la sensibilité de l'analyse, exploitant les données complètes du Run 2, sont aussi développées. En particulier, des études détaillées sont présentées dont la mesure de la section efficace différentielle du bruit de fond $t\bar{t}b\bar{b}$. L'optimisation des algorithmes de b-tagging en vue du projet LHC à haute luminosité, après l'amélioration du trajectographe d'ATLAS, est également présentée.

Synthèse en français

Depuis l'Antiquité, l'humanité s'est interrogée sur les fondements de l'univers, posant des questions sur la matière, de quoi est-elle faite et qu'est-ce qui la tient ensemble. Certes, avec ces questions sont venues des réponses avec des degrés de complexité divers à travers les siècles. Ces réponses vont de la simple représentation de la nature en quatre éléments (air, eau, feu et terre), au tableau périodique des éléments chimiques et jusqu'au Modèle Standard (SM) de la physique des particules, qui résume notre compréhension moderne de l'univers et des lois qui le régissent. Le SM, présenté dans le chapitre 1, fournit un cadre théorique qui décrit les particules élémentaires et leurs interactions fondamentales, à l'exception de la gravité qui n'est pas encore couverte par ce modèle. Depuis l'introduction du SM dans les années 1960, la plupart de ses prédictions ont été vérifiées expérimentalement avec une précision impressionnante. En particulier, la découverte du boson de Higgs en 2012 par les collaborations ATLAS et CMS au Grand collisionneur de Hadrons (LHC) a été un triomphe remarquable du SM dans la mesure où il a établi le mécanisme responsable de l'attribution de masse aux particules élémentaires: mécanisme de Brout-Englert-Higgs. Dès lors, les expérimentateurs ont entrepris de mesurer les propriétés de la nouvelle particule (masse, couplage, largeur de désintégration, spin,..) avec la plus grande précision possible pour détecter tout écart par rapport aux prédictions du SM; une sélection de ces mesures sont présentées également dans le chapitre 1.

Le LHC, décrit au chapitre 2, est l'accélérateur de particules circulaire le plus sophistiqué jamais construit. Cette machine délivre des collisions proton-proton (pp) à une fréquence élevée et à haute énergie, constituant donc un environnement favorable pour l'étude expérimentale des particules élémentaires et de leurs interactions. Le détecteur ATLAS, également présenté dans le chapitre 2, est construit autour de l'un des quatre points de collision de l'anneau du LHC. Les travaux de recherche menés dans le cadre de cette thèse sont basés sur les données recueillies par ce détecteur durant le Run 2 du LHC (càd entre 2015 et 2018, le Run 1 étant entre 2010 et 2012) à une énergie au centre de masse de 13 TeV .

Pendant ma thèse, j'ai travaillé principalement sur deux sujets étroitement liés. Le premier concerne la recherche du boson de Higgs produit en association avec une paire de quarks tops et se désintégrant en deux quarks b, $t\bar{t}H(H \to b\bar{b})$, et le second correspond aux mesures des sections efficaces inclusives et différentielles de la production associée d'une paire de quarks tops avec des jets b, $t\bar{t}b\bar{b}$; ce dernier constitue le défi majeur de l'analyse $t\bar{t}H(H \to b\bar{b})$. Par ailleurs, dans le contexte du projet de qualification permettant de devenir auteur dans la collaboration ATLAS, j'ai caractérisé les performances d'identification des b-jets attendues pour le nouveau détecteur de traces d'ATLAS qui est en cours de développement et qui remplacera le détecteur actuel pour opérer dans la phase à haute luminosité du LHC. Mes contributions à chacun de ces projets, présentées en détail dans les chapitre 3, 4 et 5, sont résumées dans ce qui suit.

Etudes de b-tagging en vue de l'amélioration du détecteur de traces d'ATLAS pour HL-LHC

L'identification des b-jets (issus de la fragmentation des quarks b), aussi appelé b-tagging, est un ingrédient majeur dans le programme de recherche ciblé par l'expérience ATLAS, non seulement au LHC, mais également à la phase à haute luminosité du LHC (HL-LHC) dont le démarrage est prévu en 2026. Ce programme couvre, par exemple, le secteur de la physique des quarks tops, la mesure des couplages du boson de Higgs à des quarks lourds, la recherche de nouvelle physique au-delà du SM,..etc. C'est pourquoi plusieurs algorithmes de b-tagging, présentés dans le chapitre 3, ont été développés dans ATLAS. La performance de ces algorithmes repose fortement sur les informations fournies par le détecteur de traces actuel d'ATLAS (Inner Detector). Cependant, ce dernier sera remplacé par le Inner Tracker (ITk), pour opérer sous les conditions difficiles de la phase HL-LHC (empilement de $\langle\mu\rangle = 200$). La performance du nouveau détecteur en termes de b-tagging est l'une des références clés à considérer pour sa conception. À cette fin, les algorithmes de b-tagging doivent être adaptés pour exploiter optimalement les capacités de la géométrie de l'ITk: en effet, des algorithmes sous-optimaux pourraient masquer les avantages relatifs des différentes options considérées pour l'ITk. Les études que j'ai effectuées, pour adapter ces algorithmes à la géométrie de l'ITk, sont présentées en détail dans le chapitre 3.

Etiquetage des b-jets dans ATLAS

Les propriétés intrinsèques des b-hadrons (produits lors de l'hadronisation des quarks b) sont les ingrédients de base utilisées par les algorithmes de b-tagging pour distinguer les b-jets des jets d'autres saveurs (c-jets et light-jets issus des quarks c et des quarks légers (u,d,s), respectivement). La propriété la plus distinctive de ces hadrons est leur temps de vie relativement long, de l'ordre de 1.5 ps. Ainsi, un b-hadron de $p_T \sim 50$ GeV et une masse ~ 5 GeV aurait une distance de vol significative à travers le détecteur, $L_{xy} \sim 4$ mm dans la direction transversale, avant de se désintégrer. Ceci se traduit par deux signatures directement exploitables par les algorithmes de b-tagging. D'une part, la désintégration du b-hadron donne lieu à un vertex secondaire (SV) déplacé par rapport au vertex primaire (PV) où la collision des protons s'est produite. D'autre part, les traces de particules chargées issues de la désintégration des b-hadrons se caractérisent par de relativement larges paramètres d'impact. Le paramètre d'impact tranverse, d_0, est défini comme la distance d'approche de la trace au PV dans le plan transverse tandis que le paramètre d'impact longitudinal est défini comme $z_0 \sin\theta$ où z_0 est la coordonnée longitudinale de la trace au point d'approche au PV et θ son angle polaire. Ces signatures, indiquées dans la Figure 0.1 (gauche), peuvent être discernées par le détecteur ATLAS.

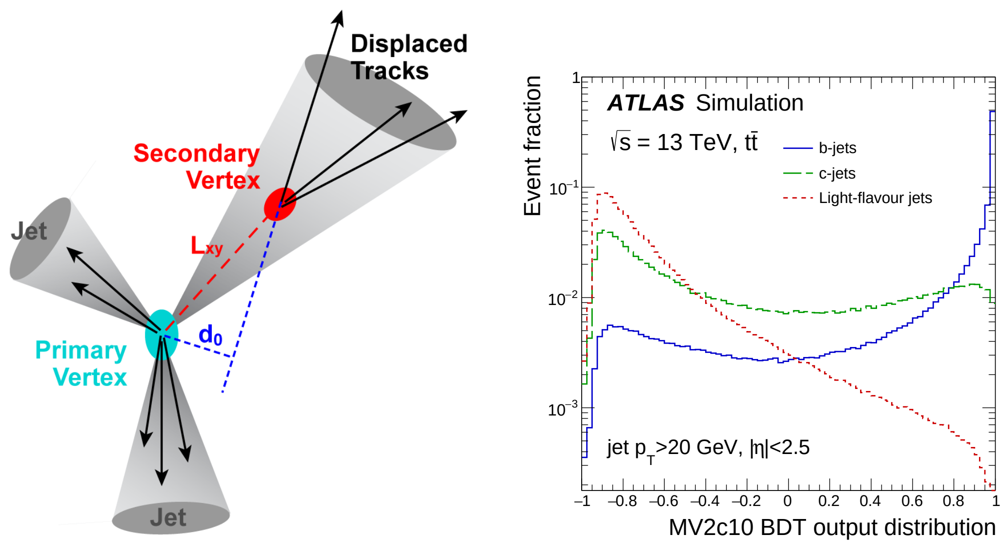

Figure 0.1.: (Gauche): Schéma illustrant les propriétés distinctives d'un b-jet notamment la présence d'un vertex secondaire à l'intérieur du jet et le large paramètre d'impact (d_0) des traces provenant du vertex déplacé. (Droite): Distribution du discriminant final de b-tagging, MV2, pour distinguer entre les b-jets et les jets d'autres saveurs (c- et light-jets).

Le discriminant final utilisé pour différencier les b-jets des c-jets et light-jets dans ATLAS est construit en deux étapes. La première consiste à définir des variables discriminantes, dites de bas-niveau, en exploitant directement les propriétés des b-hadrons présentées ci-dessus. Ainsi, deux classes d'algorithmes sont développées:

- **Les algorithmes basés sur les paramètres d'impact des traces**: tels que IP2D et IP3D
- **Les algorithmes basés sur la reconstruction de vertex de désintégrations secondaires**: tels que SV1.

Les informations obtenues à partir de ces algorithmes sont combinées, dans une seconde étape, par une méthode d'analyse multivariée basée sur un arbre de décision boosté (BDT). La distribution de sortie du BDT (voir Figure 0.1, droite), appelée MV2, est utilisé comme la variable discriminante finale, dite de haut-niveau, pour séparer entre les différentes saveurs de jets.

Amélioration du détecteur de traces d'ATLAS pour HL-LHC: Inner Tracker

Le détecteur de traces actuel d'ATLAS (ID) a été conçu pour 10 ans d'exploitation dans les conditions nominales de fonctionnement du LHC. Par conséquent, il ne sera pas en mesure de faire face aux conditions extrêmes de la phase HL-LHC avec un très fort empilement (jusqu'à 200) entraînant des doses de radiation intenses et des taux d'occupation importants. C'est pourquoi la collaboration ATLAS a décidé de remplacer complètement l'ID par un nouveau détecteur, ITk, afin de maintenir et éventuellement améliorer les performances trajectographiques d'ATLAS. Le détecteur ITk sera entièrement construit en silicium avec une plus haute granularité que celle de l'ID. Il comprend deux parties: un détecteur de micro-bandes externe couvrant jusqu'à $|\eta| = 2.7$ et un détecteur à pixels interne couvrant jusqu'à $|\eta| = 4$ (au lieu de $|\eta| = 2.5$ pour l'ID). Des schémas illustrant la géométrie de l'ITk sont montrés dans la Figure 0.2.

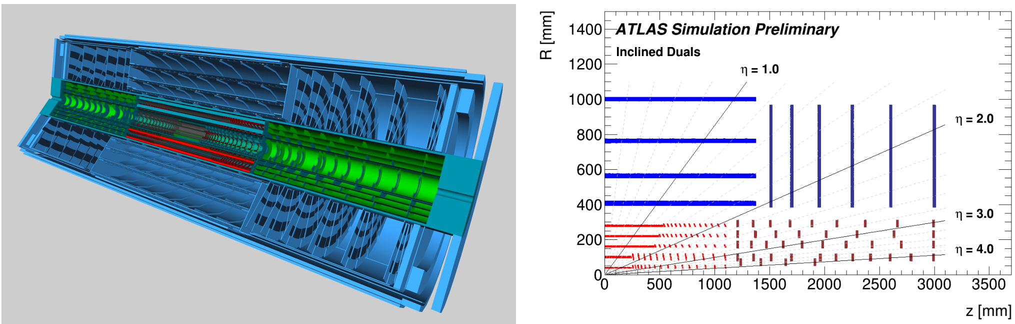

Figure 0.2.: (Gauche) vue 3D et (droite) diagramme schématique de la géométrie de l'ITk.

Optimisation des algorithmes de b-tagging pour l'ITk

Les algorithmes basés sur les paramètres d'impact des traces reposent sur un formalisme de "Log-Likelihood Ratio" qui exploite la catégorisation des traces avec des templates de références dédiés (PDFs), pour calculer le discriminant de b-tagging. Pour Run 2, cette catégorisation a été établie en se basant sur la géométrie de l'ID pour séparer les traces qui sont bien reconstruites et donc ont une meilleure résolution en paramètre d'impact de celles qui sont de moindre qualité. La première étape vers l'optimisation de cette classe d'algorithmes pour l'ITk consiste à redéfinir les catégories de traces de manière à refléter la géométrie du nouveau détecteur. Dans un premier temps, j'ai évalué les performances de b-tagging obtenues avec trois configurations préliminaires de catégories de traces définies pour l'ITk. Pour ce faire, j'ai développé un *Framework* permettant d'extraire des PDFs pour chacune de ces configurations que j'ai ensuite utilisés pour évaluer le discriminant de b-tagging dans chaque cas. En particulier, j'ai quantifié le gain en performances obtenu pour l'IP3D avec ces configurations par rapport à celui atteint avec les catégories du Run 2. Sur la base de ces comparaisons, j'ai proposé une nouvelle catégorisation de traces combinant les caractéristiques des configurations préliminaires afin de maximiser le gain de performance obtenu. L'utilisation de la configuration optimale améliore considérablement le rejet des light-jets par l'IP3D par rapport au cas où les catégories du Run 2 sont utilisées: en gardant 70% des b-jets, l'algorithme arrive à rejeter deux fois plus de light-jets avec les catégories ITk. Cette catégorisation de traces optimale est devenue la référence pour estimer les performances de b-tagging pour l'ITk. L'algorithme de MV2 a été entraîné en utilisant la nouvelle catégorisation et ses performances ont également été améliorées par rapport à la configuration du Run 2. En tenant compte de ces optimisations, j'ai caractérisé les performances de b-tagging de l'ITk et montré qu'elle surpasse celle de l'ID (voir Figure 0.3), et ce, malgré les conditions d'empilement plus difficiles de HL-LHC. Dans une dernière partie, j'ai testé la robustesse des algorithmes de b-tagging optimisés face à diverses configurations d'empilement dans HL-LHC et plusieurs scénarios de conditions dégradées du détecteur où la proportion des modules pixels non-fonctionnels varie entre 5 et 15%. J'ai montré qu'en utilisant de nouveaux templates adaptés aux conditions du détecteur, les performances de b-tagging sont quasi-complètement récupérées.

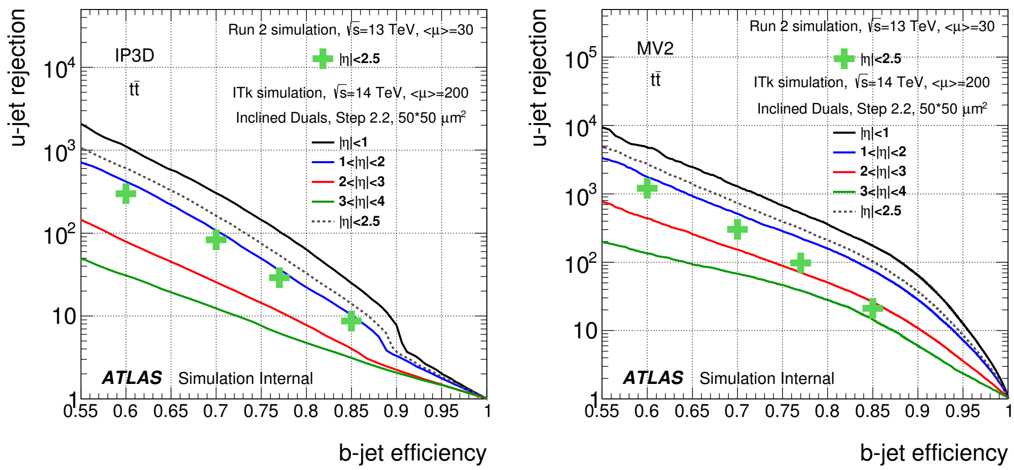

Figure 0.3.: Rejet de light-jets en fonction de l'efficacité de b-tagging pour (gauche) l'IP3D et (droite) MV2 attendues pour l'ITk. À titre de comparaison, les performances obtenues avec l'ID (configuration du Run 2) sont indiquées par des croix vertes.

Mesures de sections efficaces inclusives et différentielles de $t\bar{t}b\bar{b}$ avec ATLAS

La production d'une paire de quarks tops avec des b-jets, $t\bar{t}b\bar{b}$, suscite beaucoup d'intérêt non seulement dans le secteur de la physique des quarks tops où elle permet de tester les prédictions de la ChromoDynamique Quantique (QCD) mais aussi dans la recherche du boson de Higgs prédit par le Modèle Standard. En particulier, ce processus intervient comme le bruit de fond principal dans la recherche de la production $t\bar{t}H(H \to b\bar{b})$. Cette dernière donne un accès direct et unique aux couplages de Yukawa des quarks top et b. Les processus $t\bar{t}b\bar{b}$ et $t\bar{t}H(H \to b\bar{b})$ sont illustrés dans la Figure 0.4. La production de $t\bar{t}b\bar{b}$ est difficile à modéliser comme le reflètent les différents générateurs d'événements

Monte-Carlo (MC) qui présentent des variations importantes dans sa description. C'est pourquoi, les mesures de sections efficaces de $t\bar{t}b\bar{b}$ sont très attendues afin de contraindre les uncertitudes sur la modélisation de ce processus et d'ajuster les générateurs MC pour une meilleure description de $t\bar{t}b\bar{b}$.

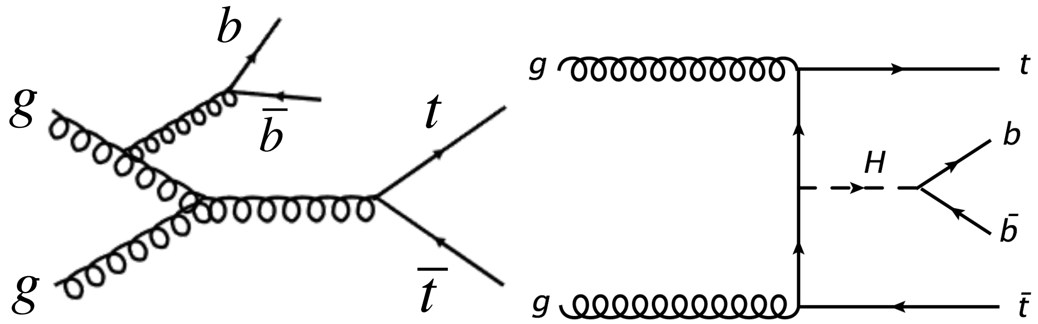

Figure 0.4.: Diagrammes de Feynman des processus (gauche) $t\bar{t}b\bar{b}$ et (droite) $t\bar{t}H(H \to b\bar{b})$.

Les mesures de sections efficaces inclusives et différentielles de $t\bar{t}b\bar{b}$ réalisées avec les données collectées par l'expérience ATLAS en 2015 et 2016, sont présentés dans le chapitre 4. Ces mesures sont effectuées dans les canaux un-lepton et deux-leptons exigeant un et deux leptons isolés, respectivement; les leptons sont issus de la désintégration des bosons W, eux-mêmes produits par les deux quarks tops. D'autres critères de sélection supplémentaires sont appliqués, dans chaque canal, conformément à la signature des événements $t\bar{t}b\bar{b}$ dans le détecteur: par exemple pour les mesures de sections efficaces différentielles dans le canal un-lepton, les événements ayant au moins 6 jets dont quatre au moins sont étiquetés b sont utilisés. Ma contribution à cette analyse est focalisée sur le canal un-lepton. En particulier, j'ai étudié dans ce canal la pureté de l'échantillon $t\bar{t}b\bar{b}$ obtenu après l'application des critères de sélection, et identifié les sources de bruit de fond à supprimer avant l'extraction des mesures de sections efficaces. Ces études ont montré que l'échantillon $t\bar{t}b\bar{b}$ est pur à $\sim 50\%$ uniquement et que la contamination provient des migrations de leptons et de jets (vers l'espace de phase ciblé par l'analyse) induites par la résolution du détecteur ainsi que l'inefficacité de l'algorithme de b-tagging causant des c- et des light-jets à être identifiés comme des b-jets.

Les Figures 0.5 et 0.6 montrent certains des résultats de mesures des sections efficaces inclusives et différentielles de $t\bar{t}b\bar{b}$, respectivement, publiés par la collaboration ATLAS en 2017. Bien que les sections efficaces inclusives prédites par les générateurs MC sont inférieures à celles mesurées, ces prédictions sont en accord avec les données si on tient compte des uncertitudes relativement larges associées aux mesures. Par ailleurs, les prédictions de distributions cinématiques utilisées dans cette analyse pour décrire les b-jets additionnels (voir Figure 0.6) ne présentent pas suffisamment de variations pour permettre aux données d'indiquer de façon concluante lequel des générateurs les reproduit le mieux. Ceci est dû au fait que les observables différentielles construites ne sont pas pures en b-jets additionnels mais plutôt comportent un mélange de ces jets avec les b-jets provenant des quarks tops.

Lors de cette thèse j'ai donc proposé une méthode pour augmenter la sensibilité des mesures de production de $t\bar{t}b\bar{b}$ dans les prochaines itérations de l'analyse, surtout pour les b-jets additionnels qui sont les plus difficiles à décrire par les modèles MC. Cette méthode consiste à identifier explicitement la provenance des b-jets en reconstruisant le système $t\bar{t}$ à l'aide d'un BDT. J'ai entrainé ce dernier sur des événements MC de $t\bar{t}b\bar{b}$ pour trouver la meilleure correspondance possible entre les jets reconstruits et les quarks produits par le système $t\bar{t}$; les jets qui n'ont pas été affecté au système $t\bar{t}$ par le BDT sont considérés comme étant additionnels. Le BDT ainsi entrainé est capable d'identifier correctement les jets additionnels avec une efficacité de 46%. Une meilleure performance du BDT peut être atteinte avec une optimisation dédiée.

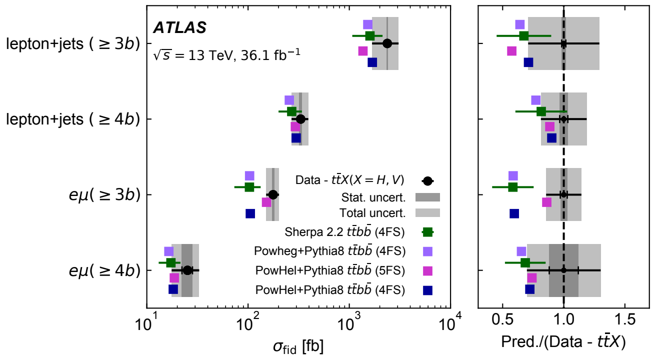

Figure 0.5.: Mesures de sections efficaces inclusives de production de $t\bar{t}b\bar{b}$ dans les canaux un-lepton et deux-leptons comparées aux prédictions MC.

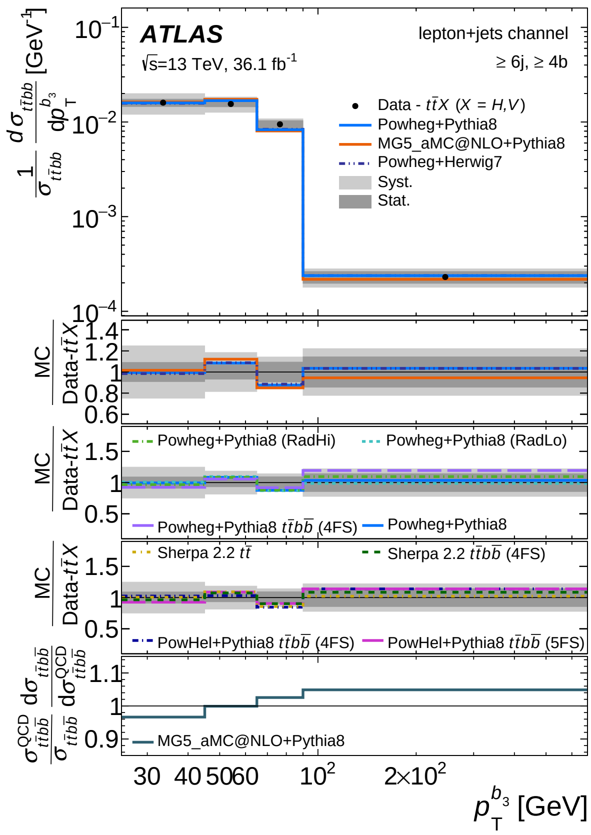

Figure 0.6.: Mesures de section efficace différentielle de production de $t\bar{t}b\bar{b}$ en fonction du moment transverse (p_T) du b-jet classé 3$^{\text{ème}}$ en p_T, comparées aux prédictions MC.

Recherche d'événements de production $t\bar{t}H(H \to b\bar{b})$

La découverte du boson de Higgs en juillet 2012 par les collaborations ATLAS et CMS au LHC a été un succès exceptionnel pour le Modèle Standard. Dès lors, l'objectif principal du LHC est devenu la mesure des propriétés de cette nouvelle particule, telles que ses couplages aux fermions, afin d'établir sa compatibilité avec les prédictions du SM. En particulier, le couplage Yukawa du quark top présente un intérêt spécial car il est le plus fort dans le SM et ainsi joue un rôle crucial dans sa stabilité aux hautes énergies: une déviation significative de ce couplage par rapport aux prédictions du SM indiquerait l'existence d'une nouvelle physique au-delà du SM. La production associée du boson de Higgs avec une paire de quarks tops, $t\bar{t}H$, donne un accès unique et direct au couplage Yukawa du quark top. Ce mode de production n'a néanmoins pas été établi avec les données du Run 1 du LHC et son observation est devenue donc l'un des objectifs les plus importants du Run 2 du LHC.

Le chapitre 5 de la thèse présente en détail la recherche d'événements $t\bar{t}H$ dans le cas où le boson de Higgs se désintègre en deux quarks b ($t\bar{t}H(H \to b\bar{b})$); le mode de désintégration $H \to b\bar{b}$ est le plus dominant dans le SM avec un rapport d'embranchement de 58%. Cette analyse est basée sur les données collectées par le détecteur ATLAS en 2015 et 2016 dont la luminosité intégrée correspondante est de 36.1 fb^{-1}. Le défi majeur pour l'analyse $t\bar{t}H(H \to b\bar{b})$ est le bruit de fond de production de $t\bar{t}$ avec des jets additionnels ($t\bar{t}$ + jets) et principalement quand ces jets sont de saveurs b ($t\bar{t}b\bar{b}$) (voir Figure 0.4). Plusieurs prédictions MC sont disponibles pour ce processus, cependant, elles présentent des différences d'ordre important surtout dans l'espace de phase visé par l'analyse. Ceci conduit à l'élaboration d'un modèle systématique complexe pour $t\bar{t}b\bar{b}$, afin de prendre en compte toutes les incertitudes possibles affectant sa description. À cet égard, j'ai mené des études détaillées comparant la modélisation de $t\bar{t}b\bar{b}$ entre les diverses prédictions MC, y compris celle utilisée pour estimer ce bruit de fond dans l'analyse, pour évaluer les différences entre elles et gagner en confiance dans le modèle systématique conçu pour ce processus. Les résultats de cette recherche ont révélé une force de signal μ, définie comme le rapport entre la section efficace mesurée pour $t\bar{t}H(H \to b\bar{b})$ et la section efficace prédite, de $0.84^{+0.64}_{-0.61}$ (voir Figure 0.7, gauche) correspondant à un excès de signal de significance de 1.4 σ (pour 1.6 σ attendu). Bien que le mode de production $t\bar{t}H(H \to b\bar{b})$ isolé ne soit pas encore établi à ce stade, la combinaison de ces résultats avec ceux d'autres canaux $t\bar{t}H$ utilisant jusqu'à 80 fb^{-1}de données de collisions a conduit à l'observation directe de la production $t\bar{t}H$ pour la première fois avec une significance de 5.8 σ (voir Figure 0.7, droite). La sensibilité de l'analyse $t\bar{t}H(H \to b\bar{b})$ est très limitée par les incertitudes systématiques qui sont dominées par l'incertitude sur la modélisation MC du bruit de fond $t\bar{t}b\bar{b}$ et l'incertitude statistique associée à la taille limitée des lots de simulations MC de la production associée de $t\bar{t}$ avec des jets de saveurs lourdes (b- et c-jets). La réduction de l'impact de ces sources d'incertitudes systématiques constitue l'objectif principal de l'analyse en cours visant à établir une évidence pour $t\bar{t}H(H \to b\bar{b})$ en utilisant les données complètes du Run 2 (139 fb^{-1}). Mes contributions à l'analyse en cours de $t\bar{t}H(H \to b\bar{b})$, présentées dans la $2^{\text{ème}}$ partie du chapitre 5, visent à réduire les erreurs systématiques mentionnées ci-dessus

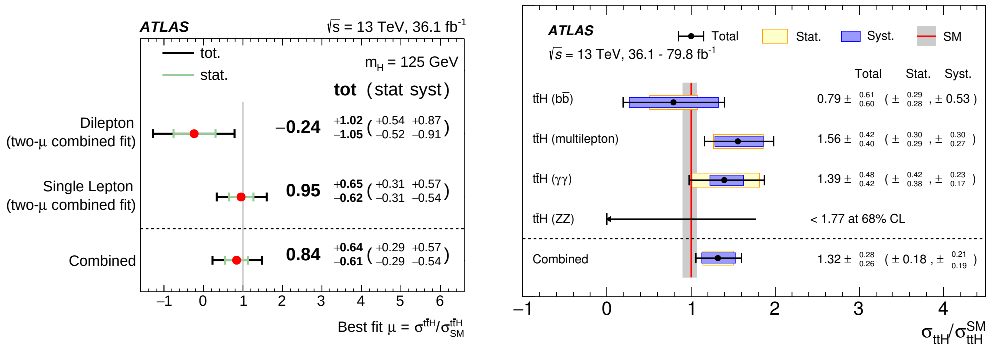

Figure 0.7.: Valeurs de μ pour (gauche) les canaux un-lepton et deux-leptons de $t\bar{t}H(H \rightarrow b\bar{b})$ ainsi que leur combinaison et (droite) les différents canaux $t\bar{t}H$ en plus de $t\bar{t}H(H \rightarrow b\bar{b})$, conduisant à la première observation directe de $t\bar{t}H$.

Pour mitiger l'impact des fluctuations statistiques induites par le nombre limité d'événements MC de $t\bar{t}$ produits avec des b-jets ou des c-jets, j'ai développé de nouveaux filtres de saveurs lourdes permettant d'augmenter la fraction générée de ces événements dans les lots de simulations. Ainsi, l'incorporation de ses filtres dans l'analyse en cours a permis de réduire significativement l'incertitude statistique sur le bruit de fond dans les régions d'analyse riches en signal (voir Figure 0.8).

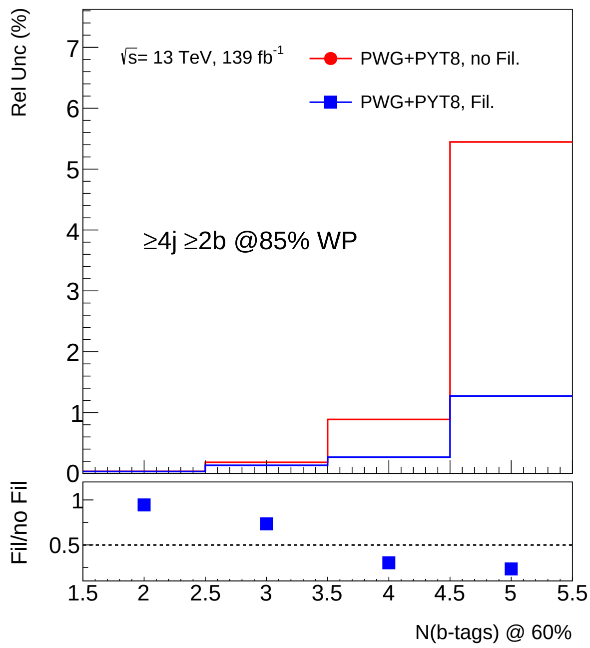

Figure 0.8.: Incertitude statistique relative en fonction du nombre de jets étiquetés b dans le lot MC de $t\bar{t}$ produit sans (rouge) et avec (bleu) les nouveaux filtres de saveurs lourdes.

D'autre part, j'ai exploré une méthode alternative pour estimer le bruit de fond $t\bar{t}b\bar{b}$ dans le but d'améliorer sa modélisation. Cette méthode, dite data-driven, consiste à corriger les distributions cinématiques de $t\bar{t}b\bar{b}$ à partir des données. Mes tests préliminaires sur la méthode data-driven ont révélé des résultats encourageants: la description du bruit de fond dans les régions de signal est améliorée présentant un meilleur accord avec les données et les différences entre générateurs, qui sont à l'origine des incertitudes systématiques associées, sont significativement réduites (voir Figure 0.9). Par contre, l'impact de cette méthode sur la sensibilité de l'analyse reste à quantifier. La méthode data-driven bien que prometteuse, plus d'études sont nécessaires afin de la valider et l'intégrer dans l'analyse. En particulier, le choix de l'observable à utiliser pour dériver les corrections aux données est l'un des défis de cette méthode. À cet effet, j'ai défini une nouvelle variable basée sur une analyse multivariée, dite "Reweighting BDT", pour dériver des corrections globales permettant d'améliorer la description de plusieurs distributions cinématiques à la fois.

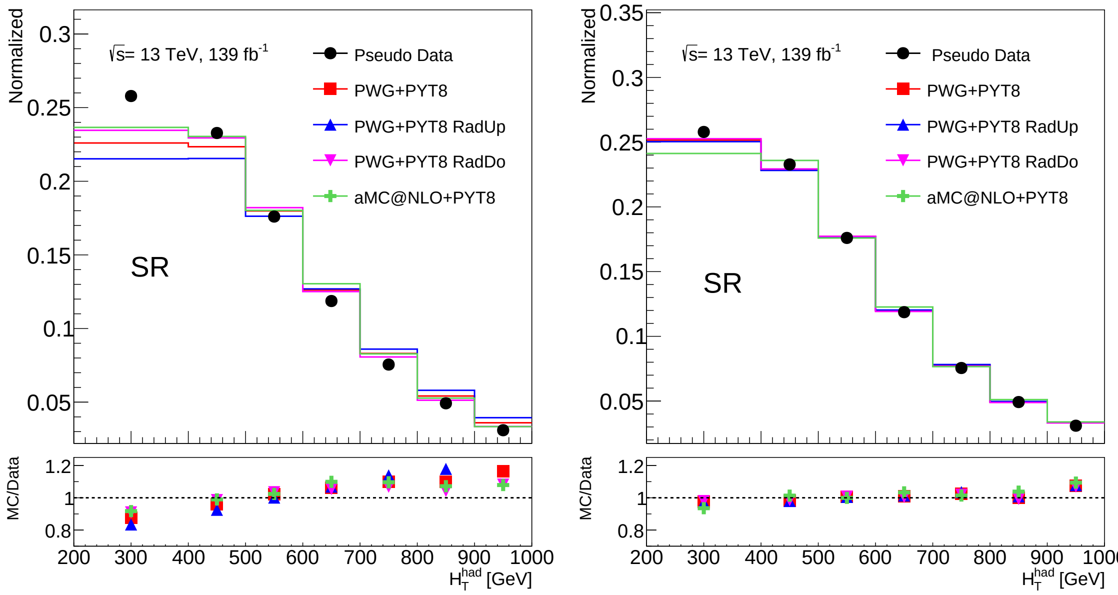

Figure 0.9.: Distribution normalisée de H_T^{had} (somme de p_T des jets) comparée entre des pseudo-données (prédiction MC de $t\bar{t}$) et des échantillons MC de $t\bar{t}$ (gauche) avant et (droite) après l'application des corrections de la méthode data-driven dans une région riche en signal (SR).

Les données complètes du Run 2 permettraient de mesurer la section efficace de production de $t\bar{t}H(H \to b\bar{b})$ avec une précision de $\sim 30\%$. En outre, elles offrent la possibilité de mesurer, avec une bonne précision, les sections efficaces différentielles de production du boson de Higgs en fonction de ses propriétés cinématiques. Ces mesures permettraient, par exemple dans le cas de $t\bar{t}H$, de tester la nature CP du couplage du boson de Higgs au quark top et de contraindre les prédictions des modèles de nouvelle physique au-delà du Modèle Standard. Le canal $t\bar{t}H(H \to b\bar{b})$ jouera un rôle clé dans ces mesures vu qu'il bénéficie d'un taux de production plus élevé que les autres canaux $t\bar{t}H$. C'est pourquoi j'ai mis en place le modèle d'analyse statistique permettant de mesurer, pour la première fois, le p_T du boson de Higgs dans le canal $t\bar{t}H(H \to b\bar{b})$. De plus, j'ai évalué la précision attendue pour ces mesures considérant différents scénarios pour le binning en p_T: la précision varie entre 50 et 80% pour $p_T < 150$ GeV et $p_T > 200$ GeV; ce niveau encourageant de sensibilité est atteint grâce à la bonne pureté de la méthode de reconstruction du boson de Higgs développée pour l'analyse $t\bar{t}H(H \to b\bar{b})$. Ces études ont permis, pour la première fois, l'accès à des informations sur le p_T du Higgs dans le mode de production $t\bar{t}H$.

Contents

List of Figures

List of Tables

Introduction

For as long as records have been kept, humankind have been wondering about the underpinnings of the universe asking questions about matter, what is it made of and what holds it together. Undoubtedly, with these questions came answers with varying degrees of complexity across the centuries. These answers range from the simple four elements depiction of nature (air, water, fire and earth) to the periodic table of chemical elements and all the way to the Standard Model, encapsulating our modern understanding of the universe and the laws that govern it. The Standard Model of Particle Physics provides a theoretical framework describing the elementary particles and their fundamental interactions, except for gravity which is not yet covered by this model. Ever since the Standard Model was introduced in the 1960s, most of its predictions have been experimentally verified with unprecedented precision. In particular, the discovery of the Higgs boson in 2012 by the ATLAS and CMS collaborations at the Large Hadron Collider (LHC) was an outstanding triumph of the Standard Model as it established the mechanism responsible for attributing mass to the elementary particles. Since then, experimentalists were set out to measure the properties of the newly found particle, such as its couplings to fermions, with the highest precision achievable to detect any deviations from the Standard Model predictions. Such deviations are clues for the existence of physics Beyond the Standard Model. The top quark Yukawa coupling to the Higgs boson is the strongest in the fermionic sector within the Standard Model and is regarded as one of the best probes to shed light on new physics phenomena. The associated production of the Higgs boson with a pair of top quarks ($t\bar{t}H$) is a particularly interesting process as it provides a unique access to this coupling at tree level and allows to measure it in a model independent way.

The main topic of this dissertation is the search for the $t\bar{t}H$ production mode where the Higgs boson subsequently decays into a pair of bottom quarks, $t\bar{t}H(H \to b\bar{b})$, using 36.1 fb^{-1}of proton-proton collision data at $\sqrt{s}$ = 13 TeV recorded by the ATLAS detector at the LHC during 2015 and 2016. A full overview of the analysis is given with more emphasis on the single lepton channel in which I was involved. The main challenge of this analysis is the overwhelming background of $t\bar{t}$ production with additional jets ($t\bar{t}$ + jets), especially when these originate from b-quarks ($t\bar{t}+\geq 1b$). This background is poorly modeled by the available Monte Carlo predictions which exhibit sizable differences namely in the phase space of interest for the $t\bar{t}H(H \to b\bar{b})$ analysis. The detailed studies that I performed to compare the modeling of the $t\bar{t}$+jets background among the different predictions, are presented. These are an essential input to gain confidence in the complex systematic model designed for this background in the analysis. The leading sources of systematic uncertainties limiting the sensitivity of this analysis were identified to be the large $t\bar{t}+\geq 1b$ modeling uncertainties and the statistical uncertainties on the simulated $t\bar{t}+\geq 1b$ and $t\bar{t}+\geq 1c$ ($t\bar{t}$ with additional c-jets) samples. In order to enhance the search sensitivity for the ongoing round of the analysis using the full Run 2 data, I developed methods to tackle these sources of uncertainties. The exploitation of the full Run 2 data allows access to differential cross section measurements as function of the produced Higgs boson properties. These measurements are of great interest as they enhance the sensitivity of this channel to new physics effects especially in the phase space where the Higgs boson is produced at high transverse momentum. In this respect, I developed the first analysis aiming to measure the Higgs boson transverse momentum in the $t\bar{t}H(H \to b\bar{b})$ channel.

To improve the modeling of the $t\bar{t}+\geq 1b$ process, it is crucial to provide measurements of its inclusive and differential production cross-section to be confronted with the available predictions. An overview of the analysis conducted to perform these measurements using the 36.1 fb^{-1}dataset collected by ATLAS is also presented in this document. For this analysis, I studied the definition of the fiducial phase space where measurements are unfolded to the particle level, in the single lepton channel. Additionally, I checked the modeling of multiple observables characterizing the b-jets from the $t\bar{t}$ system and additional b-jets to identify those which are the most interesting for the differential measurements. I also developed a method to reconstruct the $t\bar{t}$ system and isolate the additional b-jets produced with $t\bar{t}$. I showed that this method allows to build variables that greatly enhance the sensitivity to the mis-modeling of various generators in variables related to the additional $b\bar{b}$ system. This method will be used to improve the $t\bar{t}+\geq 1b$ differential cross section measurement in the next round of the analysis with the full Run 2 data.

The identification of b-jets, known as b-tagging, is a key ingredient in many physics analyses particularly the $t\bar{t}H(H \to b\bar{b})$ analysis, not only at the LHC but also at the foreseen HL-LHC. The b-tagging algorithms used in ATLAS rely heavily on the tracking information provided by the Inner Detector and were optimized based on its layout. However, at the end of Run 3, the Inner Detector will be decommissioned and replaced by the Inner Tracker to operate under the extreme conditions of High-Luminosity LHC. b-tagging is one of the key benchmarks to converge on the design of the Inner Tracker layout. My contribution to the optimization of the b-tagging algorithms to be in line with the new tracker geometry and to characterize its performance is also presented in this dissertation.

This thesis is laid out as follows. An overview of the Standard Model with a particular emphasis on the Higgs mechanism is given in Chapter 1; the Higgs boson properties measured so far at the LHC are also reviewed in this chapter. The experimental setup of the LHC collider and the ATLAS detector are described in Chapter 2. The optimization studies of the b-tagging algorithms for the Inner Tracker upgrade are presented in Chapter 3. Finally, Chapters 4 and 5 present the $t\bar{t}+\geq 1b$ production cross section measurements and the $t\bar{t}H(H \to b\bar{b})$ search using the ATLAS Run 2 dataset, respectively; my contributions to both analyses are highlighted in these chapters.

1. The Standard Model of Particle Physics

The *Standard Model* of particle physics (SM) is the theoretical framework that encompasses our current understanding of the realm of elementary particles and the laws that govern their interactions. A brief overview of the matter content as well as the fundamental forces described within the SM is given in Section 1.1 with further details about its electroweak and strong sectors summarized in sections 1.2 to 1.4; more emphasis is put on the Higgs mechanism through which elementary particles acquire their mass. This mechanism predicts the existence of a massive scalar particle, the Higgs boson, which was the last missing piece of the otherwise experimentally validated SM. The SM picture was then completed when the Higgs boson was discovered at the LHC in 2012. Details of this discovery as well as the knowledge gathered so far on the Higgs boson is presented in Section 1.5.

1.1. Brief overview of the Standard Model

The Standard Model of particle physics was introduced in the middle of the 1960s building on the work of S. Glashow [1], A. Salam [2] and S. Weinberg [3]. It offers the theoretical framework that encapsulates our best understanding of how the elementary particles and the fundamental interactions relate to each other. According to the SM, elementary particles occur in two types: fermions which are half-integer spin particles obeying the Fermi-Dirac statistics and bosons, particles of integer spin governed by the Bose-Einstein statistics. Fermions are the building blocks of matter and they are categorized into two groups: leptons and quarks with six members each. These are arranged in three families or generations following a mass hierarchy such that particle masses increase going from the first to the third. In what regards quarks, the first generation is formed of the up (u) and down (d) quarks, the second is made of the charm (c) and strange (s) quarks and the third is composed of of the top (t) and bottom (b) quarks. As for leptons, the three generations are made each of a charged lepton and an associated neutral lepton referred to as neutrino. The charged leptons are: the electron (e), the muon (μ) and the tau (τ), and the corresponding neutrinos are the electron-neutrino (ν_e), the muon-neutrino (ν_μ) and the tau-neutrino (ν_τ), respectively. The ordinary matter in the universe is made of the first generation fermions i.e the u and d quarks, which are the fundamental constituents of protons and neutrons, and electrons. The second and third generation particles can only be found in cosmic rays or produced in high energy experiments. The masses of the above particles as well as their electric charge are summarized in Table 1.1.

	Quarks			Leptons		
Generation	Flavor	Mass	Charge [e]	Flavor	Mass	Charge [e]
1	u	2.3 MeV	+2/3	e	0.511 MeV	-1
	d	4.8 MeV	−1/3	ν_e	<2 eV	0
2	c	1.28 GeV	+2/3	μ	105.7 MeV	-1
	s	95 MeV	-1/3	ν_μ	< 0.19 MeV	0
3	t	173.2 GeV	+2/3	τ	1776.8 MeV	-1
	b	4.18 GeV	-1/3	ν_τ	<18.2 MeV	0

Table 1.1.: The mass and electric charge of the quarks and leptons [4].

The SM fermions interact with each other through four fundamental forces: the strong, the electromagnetic, the weak and the gravitational force; the latter is the weakest among the four and is not yet accounted for in the SM. The first three interactions are determined by the quantum numbers characterizing the fermions which exchange gauge bosons that play the role of force carriers. Quarks have a unique feature referred to as the color charge which can be either red, green or blue. This property governs the quarks interaction within the strong sector, which is mediated by massless gluons (g) carrying themselves a color charge. Electrically charged particles are subjected to the electromagnetic force mediated by massless neutral photons (γ). Lastly, all SM fermions interact via the weak force which is mediated by massive vector bosons: two electrically charged $W^{\pm}$ bosons and one neutral Z boson. Table 1.2 summarizes the properties of the gauge bosons.

Boson	Interaction	Mass [GeV]	Charge [e]
g	Strong	0	0
γ	Electromagnetic	0	0
$W^{\pm}$	Weak	80.38	±1
Z		91.19	0

Table 1.2.: Gauge bosons properties in terms of the type of the interaction they mediate, mass and electric charge [4].

Furthermore, for each of the fermions and bosons presented above, an antiparticle which has the same mass but opposite quantum numbers exists; in particular, the Z and γ bosons are their own antiparticles.

The SM is a renormalizable and relativistic Quantum Field Theory (QFT) [5] whose fundamental objects, as its name suggests, are quantum fields which are defined at all points in space-time to represent matter and its interactions. It is built based on the Lagrangian formalism and relies heavily on the fundamental notion of symmetries. The SM Lagrangian ($\mathcal{L}_{SM}$) can be divided into two components: the quantum chromodynamics (QCD) Lagrangian ($\mathcal{L}_{QCD}$) describing the strong sector and the electroweak (EW) Lagrangian ($\mathcal{L}_{EW}$) describing the weak and electromagnetic interactions:

$$\mathcal{L}_{SM} = \mathcal{L}_{QCD} + \mathcal{L}_{EW} \tag{1.1}$$

The SM Lagrangian is required to be invariant under the following gauge symmetry group:

$$G_{SM} = SU(3)_C \otimes SU(2)_L \otimes U(1)_Y \tag{1.2}$$

where C stands for color, L refers to the left-handed fields components to which the $SU(2)_L$ symmetry exclusively applies and Y denotes the hypercharge defined by the Gell-Mann-Nishijima formula:

$$Q = I_3 + \frac{Y}{2} \tag{1.3}$$

where Q is the electric charge and I_3 is the third component of the weak isospin.

The first term featured in the gauge group, $SU(3)_C$, is a non-abelian[a] symmetry group encoding the underlying color symmetry of QCD. The second term $SU(2)_L \otimes U(1)_Y$ corresponds to the symmetry group of the electroweak interaction (see Section 1.2) where the weak isospin and hypercharge are the conserved quantities under the corresponding group transformations. The gauge invariance of the SM Lagrangian under this symmetry group requires the fermions as well as the W and Z mediators to be massless. This is in contradiction with the observed masses of fermions and the fact that the weak interaction has a short range, unlike the infinite-range electromagnetic interaction mediated by the massless photons. To reconcile the inconsistency between the theory and observations,

[a] A non-abelian symmetry group G is a group where the symmetry transformations are not commutative i.e $[a, b] \neq 0, a, b \in G$.

the Brout-Englert-Higgs (BEH) mechanism [6–8] was introduced to induce a spontaneous $SU(2)_L \otimes U(1)_Y$ symmetry breaking allowing to generate masses for the fermions and the weak gauge bosons. This mechanism predicts the existence of a scalar particle, the "Higgs" boson, whose mass is a free parameter of the theory. The BEH mechanism is described in more details in Section 1.3.

Although the SM proved to be a very successful theory with various experiments confirming its predictions to a high degree of precision, it is still incapable of answering some of the open questions in modern physics. For instance, the SM treats neutrinos as massless particles while the observation of neutrino oscillations conclusively demonstrated that these particles have a mass. Additionally, the gravitational interaction is still not describable within quantum field theory. These unsolved questions among others point to the fact that the SM is an incomplete theory which motivated the search for new phenomena beyond its reach.

1.2. The electroweak theory

The electroweak (EW) sector [9] of the SM combines into a single theoretical framework the Quantum Electrodynamics (QED) model [10–18] which describes the electromagnetic interactions taking place between the charged fermions and the photon, the corresponding vector boson mediator, and the theory of the weak interaction which is behind the weak decays of particles mediated by the W and Z bosons; the theory for weak interactions was not originally constructed as a gauge theory but rather as an extrapolation of QED by Fermi [19].

The EW Lagrangian comprises two terms: one corresponding to fermions and another to gauge bosons. Fermions are represented as Dirac spinor fields which can be decomposed into left-handed and right-handed components as follows:

$$\Psi_L = \frac{1}{2}(1-\gamma^5)\Psi \tag{1.4}$$

$$\Psi_R = \frac{1}{2}(1+\gamma^5)\Psi \tag{1.5}$$

where $\frac{1}{2}(1 \pm \gamma^5)$ are the chirality operators, $\gamma^5 = i\gamma^0\gamma^1\gamma^2\gamma^3$ such that γ^i with $i = 0, \ldots, 3$ are the Dirac matrices.

Only the left-handed projections of fermions participate in the charge current weak interactions (i.e those mediated by $W^\pm$) as motivated by the experimental observation of the violation of parity in weak interactions [20]. These projections can be grouped into weak isospin doublets ($I = \frac{1}{2}$) as follows:

$$\begin{pmatrix} u \\ d \end{pmatrix}_L \begin{pmatrix} \nu_e \\ e \end{pmatrix}_L \quad \begin{pmatrix} c \\ s \end{pmatrix}_L \begin{pmatrix} \nu_\mu \\ \mu \end{pmatrix}_L \quad \begin{pmatrix} t \\ b \end{pmatrix}_L \begin{pmatrix} \nu_\tau \\ \tau \end{pmatrix}_L \tag{1.6}$$

Since the right-handed components of fermions do not take part in the charge current interaction, they are considered as weak isospin singlets ($I = 0$):

$$u_R, d_R, e_R \quad c_R, s_R, \mu_R \quad t_R, b_R, \tau_R \tag{1.7}$$

Neutrinos (antineutrinos) are considered in the SM as massless particles and hence have only one chirality which is left-handed (right-handed).

The EW Lagrangian term describing fermions is given by:

$$\mathcal{L}_{\text{fermion}} = \sum_{\Psi=q,l} \overline{\Psi} i\gamma^\mu D_\mu \Psi \tag{1.8}$$

where q and l denote the quark and lepton fields respectively and D_μ, the covariant derivative defined as:

$$D_\mu = \partial_\mu - ig\vec{I}.\vec{W}_\mu - ig'\frac{Y}{2}B_\mu \tag{1.9}$$

g and g' are the coupling constants associated to the $SU(2)_L$ and $U(1)_Y$ symmetry groups, respectively. W_μ and B_μ represent the gauge fields of these groups which are described by the following Lagrangian term:

$$\mathcal{L}_{\text{gauge}} = -\frac{1}{4}F^i_{\mu\nu}F^{i\mu\nu} - \frac{1}{4}B_{\mu\nu}B^{\mu\nu} \tag{1.10}$$

where the field tensors $F^i_{\mu\nu}$ and $B_{\mu\nu}$ are defined as:

$$F^i_{\mu\nu} = \partial_\mu W^i_\nu - \partial_\nu W^i_\mu - g\epsilon_{ijk}W^j_\mu W^k_\nu$$
$$B_{\mu\nu} = \partial_\mu B_\nu - \partial_\nu B_\mu$$

where ϵ_{ijk} is the totally antisymmetric Levi-Civita tensor. The W^1_μ and W^2_μ mix to give the charged $W^\pm$ vector bosons whereas the rotation of W^3_μ and B_μ in the (I_3, Y) plane results in the neutral Z and photon vector bosons.

The EW Lagrangian, as constructed above, does not include any mass terms for the gauge bosons and fermions as they are prohibited by the Lagrangian invariance under the $SU(2)_L \otimes U(1)_Y$ group transformations. This does not reflect the experimental observations which confirm that these particles are massive. The spontaneous symmetry breaking of the $SU(2)_L \otimes U(1)_Y$ symmetry towards the $U(1)_{em}$[b] symmetry, via the BEH mechanism, allows to generate masses not only for the gauge bosons following their interaction with the Higgs field but also for fermions through what is known as the *Yukawa* interaction.

1.3. Symmetry breaking and the Higgs mechanism

The mechanism introduced by R. Brout, F. Englert and P. Higgs [6–8], also referred to as the "Higgs mechanism", was primarily included in the SM as a remedy for the theory of the EW interactions which until then did not accommodate massive weak interaction gauge fields. It relies on the concept of *Spontaneous Symmetry Breaking* which corresponds to situations where the ground state of a system does not share the symmetry, or in other words breaks the symmetry, of the physics laws that describe it; in the particular case of the Higgs mechanism, the $SU(2)_L \otimes U(1)_Y$ symmetry breaks down to $U(1)_{em}$.

The BEH mechanism starts off by introducing a complex scalar field, the"Higgs field", which has a hypercharge $Y = 1$ and an isospin doublet structure so that it can interact with gauge bosons and fermions as follows:

$$\phi = \begin{pmatrix} \phi^+ \\ \phi^0 \end{pmatrix} = \begin{pmatrix} \phi^+_1 + i\phi^+_2 \\ \phi^0_1 + i\phi^0_2 \end{pmatrix} \tag{1.11}$$

The Lagrangian of the Higgs field is given by:

$$\mathcal{L}_{\text{Higgs}} = (D_\mu\phi)^\dagger(D^\mu\phi) - V(\phi) \tag{1.12}$$

[b] $U(1)_{em}$ is the gauge group of electromagnetism.

which consists of a kinetic term where the covariant derivative is given by equation 1.9 and the Higgs field potential $V(\phi)$, defined as:

$$V(\phi) = \frac{1}{2}\mu^2\phi^\dagger\phi + \frac{1}{4}\lambda(\phi^\dagger\phi)^2 \tag{1.13}$$

Here the free parameters λ and μ^2 are real constants as required by unitarity. To have a stable vacuum i.e a finite minimal value of the potential, the condition $\lambda > 0$ is imposed; the Higgs field configuration at the minimum potential is referred to as the vacuum or ground state with its absolute value known as the vacuum expectation value (v.e.v). For the μ parameter, $\mu^2 < 0$ is required leading to a "Mexican hat" shape potential as illustrated in Figure 1.1.

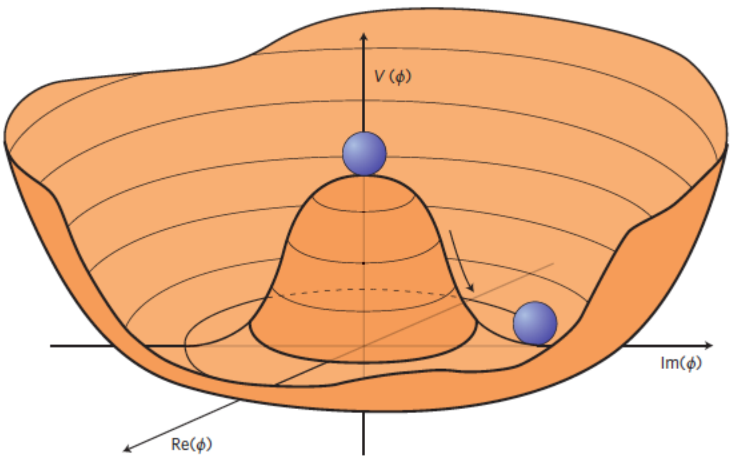

Figure 1.1.: The shape of the Higgs field potential $V(\phi)$ for a single complex field in the simplified case of the $U(1)$ rotational symmetry. There is an infinite number of ground state choices (circle on the bottom of the potential) such that nature picking one of them leads to spontaneously breaking the $U(1)$ symmetry.

The vacuum expectation value associated with this potential is:

$$\langle 0|\phi|0\rangle \equiv \phi_0 = \sqrt{\frac{-\mu^2}{\lambda}} = v \tag{1.14}$$

There is an infinity of physical ground states with the above expectation value however a particular vacuum state needs to be picked to apply the Feynman calculus. In particular, the ground state of the Higgs field is chosen to be:

$$\phi = \begin{pmatrix} 0 \\ v \end{pmatrix} \tag{1.15}$$

This state is not invariant under the $SU(2)_L$ and $U(1)_Y$ group symmetries, but it is under the action of the $U(1)_{em}$ group. As such, this specific choice breaks the symmetry of the Higgs Lagrangian.

To generate the physical states of the Higgs field, the latter is expanded about the minimum of its potential following a perturbative approach . A real field $H(x)$ attributed to a scalar boson, the Higgs boson, is added as a deviation from the vacuum state as follows:

$$\phi = \begin{pmatrix} 0 \\ v + H(x) \end{pmatrix} \tag{1.16}$$

Technically, a term $e^{i\frac{G^a(x)\sigma^a}{2v}}$ should be added above for a general perturbation in which $G^a(x)$ (with $a = 1, \ldots, 3$), corresponds to the Nambu-Goldstone bosons accounting for the broken continuous symmetry of $SU(2)_L$ [21] and σ^a are the Pauli matrices. However, an astute choice of the $SU(2)_L$ gauge leads to suppressing this term without any loss of generality. Then, the Higgs field Lagrangian in Equation 1.12 transforms into the following form after replacing the W^a_μ and B_μ by the weak gauge bosons ($W^\pm$ and Z):

$$\begin{aligned}\mathcal{L}_{\text{Higgs}} &= \frac{1}{2}\partial^\mu H \partial_\mu H \\ &+ \frac{1}{8}\left(\sqrt{g^2 + g'^2}\right)^2 v^2 Z^\mu Z_\mu + \frac{g^2 v^2}{4} W^{-\mu} W^+_\mu \\ &+ \left(\frac{2}{v}H + \frac{1}{v^2}H^2\right)\left(\frac{1}{8}\left(\sqrt{g^2 + g'^2}\right)^2 v^2 Z^\mu Z_\mu + \frac{g^2 v^2}{4} W^{-\mu} W^+_\mu\right) \\ &- \mu^2 \frac{(v+H)^2}{2} - \lambda \frac{(v+H)^4}{4}\end{aligned} \tag{1.17}$$

The second line of the equation above features the explicit mass terms (quadratic in the fields) of the weak gauge bosons:

$$m_W = \frac{gv}{2}, \quad m_Z = \frac{v}{2}\sqrt{g^2 + g'^2} \tag{1.18}$$

These masses are generated through the BEH mechanism or to express it in different terms invoking the Goldstone bosons: the originally massless gauge fields carry two degrees of freedom each (transverse polarizations); they acquire mass by grabbing a third longitudinal polarization through the absorption of the Goldstone bosons which then disappear from the theory [22]. The third line of the equation depicts the possible interactions between the Higgs boson and the weak gauge bosons whereas the fourth line reveals the mass term of the Higgs boson ($m_H = v\sqrt{2\lambda}$) in addition to its self-coupling. While the vacuum expectation value can be derived from the precise measurement of the Fermi coupling constant[c] and its dependence on the W boson mass ($v \simeq 246.2$ GeV), λ is a free parameter of the SM and consequently so is the Higgs boson mass.

The masses of fundamental fermions are generated using the same Higgs field ϕ by adding $SU(2)_L \otimes U(1)_Y$ invariant terms which correspond to *Yukawa* Lagrangian interactions as follows:

$$\mathcal{L}_{\text{Yukawa}} = -C_f \overline{\Psi_L} \phi \Psi_R + h.c \tag{1.19}$$

Following the same procedure as for the gauge bosons, the mass terms as well as those corresponding to the interaction with the Higgs boson can be built for the "weak-isospin-down-type" fermions (i.e d,s,b,e,μ,τ). This results in the Yukawa coupling constant associated with the f fermion C_f to be proportional to its mass: $C_f = \sqrt{2}\frac{m_f}{v}$.

On the other hand, the mass of the "weak-isospin-up-type" fermions (u,d,t) is included by repeating the same procedure as above but replacing the Higgs field doublet by $\phi' = i\sigma_2\phi$. The same results can then be derived such that the corresponding Yukawa Lagrangian is given by:

$$\mathcal{L}_{\text{Yukawa}} = -\frac{vC_f}{\sqrt{2}}\overline{\Psi_L}\Psi_R - \frac{C_f}{\sqrt{2}}\overline{\Psi_L}\Psi_R H + h.c \tag{1.20}$$

[c] The Fermi coupling constant G_F was introduced by Fermi in the first theory of the weak interaction, the 4-point interaction model, to describe the strength of the interaction.

where $C_f = \sqrt{2}\frac{m_f}{v}$. Consequently, the Higgs boson is more favorably produced in association with heavy particles and decays preferentially into the heaviest particles kinematically allowed.

Building on what was discussed above, the full expression of the EW Lagrangian then becomes:

$$\mathcal{L}_{\text{EW}} = \mathcal{L}_{\text{gauge}} + \mathcal{L}_{\text{fermion}} + \mathcal{L}_{\text{Higgs}} + \mathcal{L}_{\text{Yukawa}} \tag{1.21}$$

To recapitulate, the "Higgs mechanism" allowed to generate masses for the weak gauge bosons and fermions while keeping the photon massless and preserving invariance under the $SU(2)_L \otimes U(1)_Y$ symmetry.

1.4. Quantum chromodynamics

As previously mentioned, QCD is an non-abelian theory based on the $SU(3)_C$ gauge group describing strong interactions in which the color charge is conserved. The QCD Lagrangian is given by:

$$\mathcal{L}_{QCD} = \bar{q}i\gamma^{\mu}D_{\mu}q - \frac{1}{4}G^{a}_{\mu\nu}G^{a\mu\nu} \tag{1.22}$$

where q denotes the quark fields and D_μ is the covariant derivative given by:

$$D_\mu = \partial_\mu - ig_sT^aG^a_\mu \tag{1.23}$$

g_s is the strong coupling constant, T^a with $(a = 1, \ldots, 8)$ are the $SU(3)_C$ generators and G^a_μ are the gluon fields. The field strength tensor $G^a_{\mu\nu}$ is defined as:

$$G^a_{\mu\nu} = \partial_\mu G^a_\nu - \partial_\nu G^a_\mu - g_s f^{abc} G^b_\mu G^c_\nu \tag{1.24}$$

with f^{abc} being the structure constants of the $SU(3)_C$ group.

The non-abelian structure of QCD introduces self-interaction terms for gluons, which also carry a color charge, as depicted in the last term of the above equation. The self-interaction of gluons has important consequences on the energy dependence of the strong coupling constant. While QEœD interactions get stronger at short distances (high energy), the opposite effect is undergone for QCD such that the coupling constant becomes small and quarks behave as free particles. This phenomenon is known as the "asymptotic freedom" of QCD. On the other hand, at higher distances (lower energies), the coupling constant increases and gluons as well as quarks cannot exist as free particles but rather form color singlet bound states known as hadrons. This feature ensuring that quarks and gluons are trapped inside hadrons is referred to as "confinement".

1.5. Search for the Higgs boson at the LHC

Ever since the Higgs mechanism was postulated as a mean to generate masses for the elementary particles, an extensive amount of work was steered towards the search for the associated Higgs boson at several high energy colliders: Tevatron [23], LEP [24] and its successor the LHC (see Chapter 2). These efforts were rewarded when a new particle, compatible with the SM Higgs boson was observed at the LHC by both the ATLAS [25] and CMS [26] experiments as announced on the 4^{th} of July 2012. To definitely pin down the newly found particle as the long sought SM Higgs boson, the focus shifted towards measuring its properties in terms of its production and decay rates as well as its couplings to the elementary particles. This section goes over the Higgs boson discovery as well as the measurement of some of its properties at the LHC experiments.

1.5.1. Higgs boson production and decay modes

There are four main modes for the production of the SM Higgs boson in proton-proton (pp) collisions at the LHC as illustrated in Figure 1.2. They are listed in the following in decreasing order of the corresponding cross-section:

- **Gluon-gluon fusion (ggH)**: This is the leading production mode of the SM Higgs boson at the LHC given the overwhelming presence of gluons in pp collisions. It is mediated by a virtual quark loop to which the top quark contributes the most given its large Yukawa coupling.
- **Vector boson fusion (VBF)**: In this mode, two quarks from the colliding protons produce each a vector boson (either $W^{\pm}$ or Z), the fusion of which results in a Higgs boson. VBF gives direct access (no virtual loops involved) to the vector bosons coupling to the Higgs boson as does the channel where the latter decays via bosonic modes.
- **Associated production of the Higgs boson with a vector boson (VH)**, or Higgs Strahlung: In this mode, the Higgs boson is produced in association with a W or Z boson. These processes are beneficial for probing the $H \to b\bar{b}$ decay, allowing to profit from the leptonic decay signatures of the vector bosons to reduce the multi-jet background.
- **Associated production of the Higgs boson with one or two top quarks (tH/$t\bar{t}H$)**: These production modes are of great importance despite being the least dominant among the main four modes considered here. They are the only channels granting direct access to the top Yukawa coupling which is the strongest in the SM and has key implications on its stability at high energies. In these modes, the top Yukawa coupling takes place at the tree-level which allows to measure it in a model-independent way as opposed to the ggH mode, for instance, where the coupling occurs through a virtual loop which requires assumptions on its particle content to extract the coupling. The $t\bar{t}H$ mode where the Higgs boson is produced with a pair of top quarks has a higher cross-section compared to that where it is produced with a single top quark (tH). The latter, although more rare, is still interesting to probe as it is also sensitive to the sign of the top Yukawa coupling.

The dependence of the cross-sections of the main SM Higgs boson production modes on the center-of-mass energy in pp collisions, is shown in Figure 1.3. One can note that these cross-sections increase with the center-of-mass energy. Particularly, the $t\bar{t}H$ production cross-section was enhanced by a factor 4 in Run 2 of the LHC where the operating center-of-mass energy was 13 TeV compared to Run 1 in which pp collisions took place at 7 and 8 TeV ; Run 1 and 2 refer to the LHC data taking periods of 2011-2012 and 2015-2018, respectively.

The Higgs boson decays preferably to the heaviest particles kinematically accessible. Decays to photons and gluons, mediated by loops, are also possible. Figure 1.4 shows the branching ratios of the Higgs boson decay modes as a function of its mass. With a mass around 125 GeV, the Higgs boson decays mainly to a $b\bar{b}$ pair (58%). This thesis revolves mainly around the search for the Higgs boson produced via the $t\bar{t}H$ mode and decaying into a pair of bottom quarks (see Chapter 5).

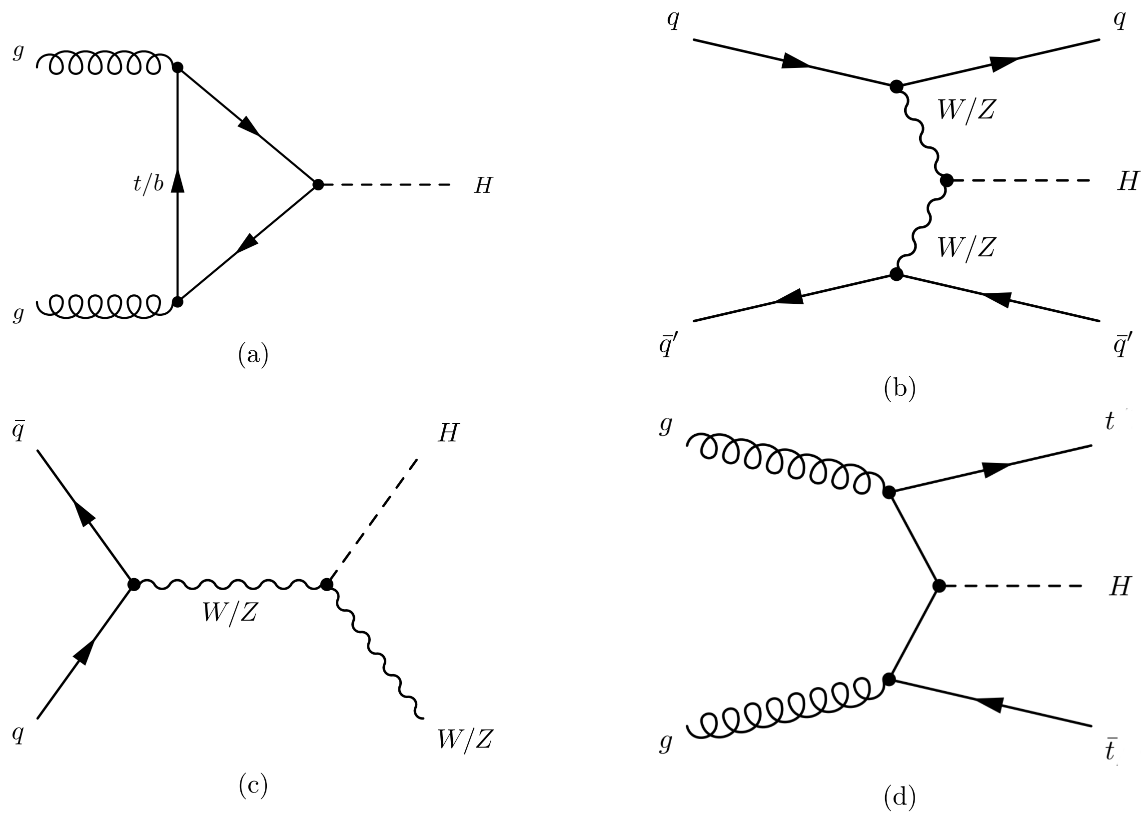

Figure 1.2.: Representative leading order Feynman diagrams of the four main production modes of the Higgs boson at the LHC [27]: (a) gluon-gluon fusion (ggH), (b): vector boson fusion (VBF), (c): associated production with a vector boson or Higgs strahlung (VH) and (d): associated production with a pair of top quarks ($t\bar{t}H$).

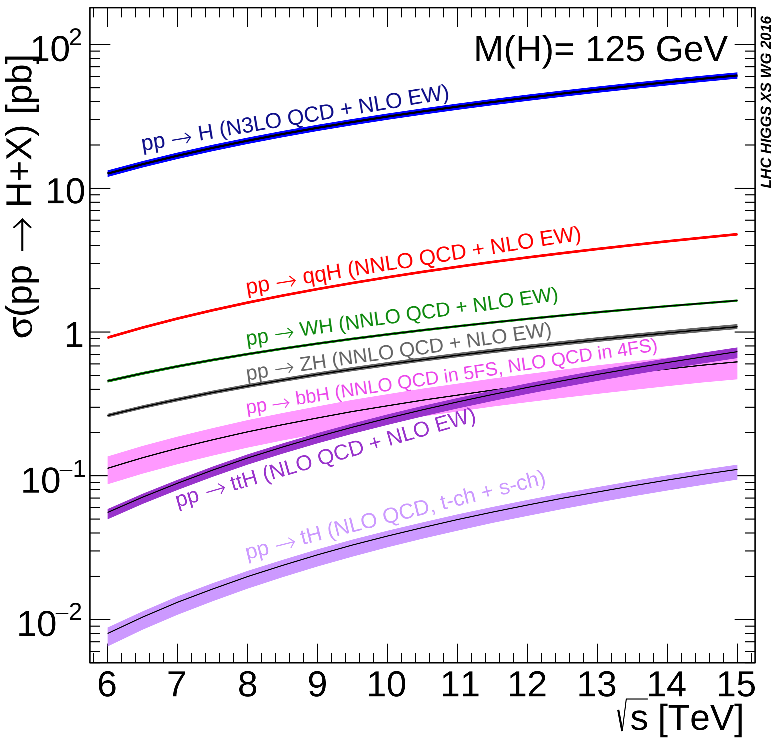

Figure 1.3.: The cross-section of the main production modes of the SM Higgs boson at the LHC, as a function of the pp collisions center-of-mass energy, for a Higgs boson mass of 125 GeV [28].

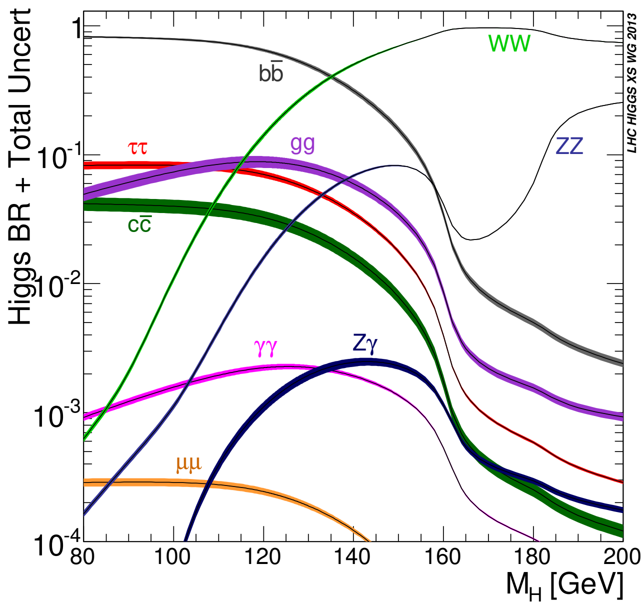

Figure 1.4.: The branching ratios of the various decay modes of the SM Higgs boson as a function of its mass [29].

1.5.2. The Higgs boson discovery at the LHC

On the 4^{th} of July 2012, the ATLAS and CMS collaborations announced the discovery of a new particle compatible with the SM Higgs boson [25, 26], thus reaching a major milestone in the physics program of the LHC. This discovery was made possible by exploiting the pp collision data delivered by the LHC in 2011 and 2012 at 7 and 8 TeV center-of-mass energies, respectively.

Particularly, the search for the Higgs boson was performed focussing on the topologies where it decays through bosonic modes as they offer better signal sensitivity compared to the fermionic final states. The most significant excesses were found in the high mass resolution channels i.e $H \to \gamma\gamma$ and $H \to ZZ^{(*)} \to 4\ell$ as illustrated in Figure 1.5 comparing the data recorded by ATLAS to the SM predictions. The bumps emerging at $\sim$ 125 GeV revealed the presence of a new particle consistent with the SM Higgs boson. The combined significance from these two channels gauging the discrimination with respect to the background hypothesis was found to be 5.9 σ, thus exceeding the discovery threshold of 5 σ. The corresponding significance achieved by CMS is 5.8 σ. The two independent observations of the same Higgs boson consolidate the discovery made by each of these two experiments.

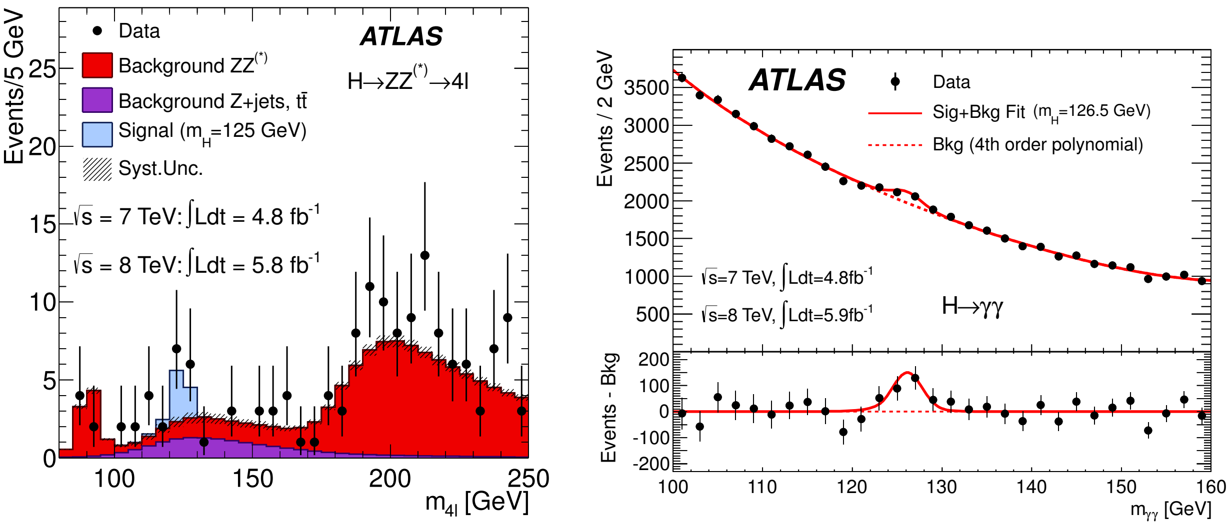

Figure 1.5.: The invariant mass distribution of the four leptons in the selected $H \to ZZ^{(*)} \to 4\ell$ candidate events (left) and of the diphoton system in the selected $H \to \gamma\gamma$ events (right), compared to the background expectation for the combination of the $\sqrt{s}$ = 7 TeV and $\sqrt{s}$ = 8 TeV datasets. A signal expectation for a SM Higgs boson with m_H = 125 GeV is also shown in the case of the $H \to ZZ^{(*)} \to 4\ell$ channel [25].

In addition to the observation of the Higgs boson in the golden decay channels (i.e discovery channels), its production in the ggH mode was also established by both ATLAS and CMS collaborations independently using Run 1 data. Moreover, a combination of the Run 1 analyses performed by ATLAS and CMS collaborations was carried out [30], allowing to improve our knowledge about the Higgs boson production and decay modes and leading to the observation of the VBF production and $H \to \tau\tau$ decay modes for the first time. The observation of the Higgs boson produced through the VH mode in addition to its decay via the $H \to b\bar{b}$ channel was made possible for both ATLAS [31] and CMS [32] by combining Run 1 data with that collected during Run 2 (from 2015 to 2017) at a center-of-mass energy of 13 TeV .

The $t\bar{t}H$ production mode was not yet discovered at the end of Run 1. The $t\bar{t}H$ signal strength, defined as the ratio of the observed rate to the SM prediction, was reported to be $2.3^{+0.7}_{-0.6}$ based on the ATLAS and CMS combined Run 1 measurement [30]. The corresponding observed significance with respect to the background only hypothesis is 4.4 σ while 2.0 σ was expected. Observing this production mode was among the priorities of the LHC Run 2 program, which was met by both ATLAS (see Chapter 5) and CMS [33].

At this stage, all four main production modes, the bosonic and the third generation fermionic decay modes of the Higgs boson are well established and found to be compatible with the SM predictions. This marks the beginning of the era of precision measurements for these processes at the LHC.

1.5.3. Properties of the Higgs boson

After the discovery of a new boson compatible with the predictions of the SM (See Section 1.3), the focus shifted towards measuring its properties with the best precision accessible. This is necessary in order to conclude on the identity of the discovered particle as the SM Higgs boson and exclude Beyond the Standard Model (BSM) scenarios which foresee particles with similar properties.

The precise measurement of the Higgs boson mass, which is a free parameter of the SM, is essential to evaluate the decay branching ratios and the cross-sections for the various production modes of the Higgs boson at the LHC. This measurement is typically performed in the $H \to \gamma\gamma$ and $H \to ZZ^{(*)} \to 4\ell$ channels which feature a high experimental resolution of the order of a few GeV. Combining these channels, ATLAS measured the Higgs boson mass to be 124.97 ± 0.24 GeV [34], using 36.1 fb^{-1}of pp collision data collected during Run 2 in addition to the Run 1 data. This measurement is in agreement with the combined ATLAS and CMS Run 1 measurement [35] as illustrated in Figure 1.6.

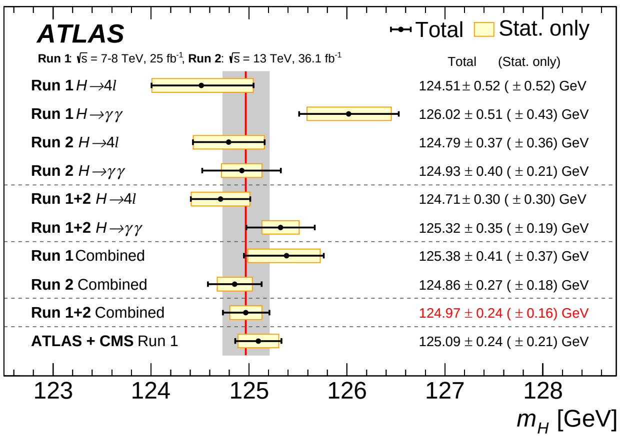

Figure 1.6.: Summary of the Higgs boson mass measurements from the individual and combined analyses, compared with the ATLAS and CMS combined Run 1 measurement. The statistical-only (horizontal yellow-shaded bands) and total (black error bars) uncertainties are indicated. The (red) vertical line and corresponding (grey) shaded column indicate the central value and the total uncertainty of the combined ATLAS Run 1+2 measurement, respectively [34].

With the Higgs boson mass being fixed by measurements, it is possible to calculate its production cross-sections and decay branching ratios from which the Higgs boson coupling strengths to the weak gauge bosons and fermions can be deduced. These are expressed in terms of coupling modifiers κ_i defined as the ratio of the measured coupling strength to the predicted one. The couplings measured by ATLAS [36] using Run 2 data, as a function of the particle mass, are shown in Figure 1.7 and found to be in agreement with their SM predictions; for these measurements, no BSM contributions are considered.

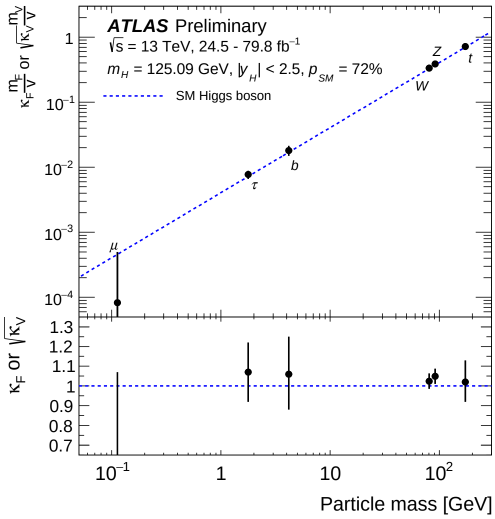

Figure 1.7.: Reduced coupling strength modifiers $\kappa_F m_F/v$ for fermions ($F = t, b, \tau, \mu$) and $\sqrt{\kappa_V} m_V/v$ for weak gauge bosons ($V = W, Z$) as a function of their mass. The SM prediction is also shown (dotted line) [36].

Furthermore, the spin and parity of the observed Higgs boson were closely examined in the $H \to \gamma\gamma$, $H \to ZZ^{(*)} \to 4\ell$ and $H \to WW^{(*)} \to \ell\nu\ell\nu$ channels [37, 38] and found to be consistent with the SM prediction of a scalar particle with positive parity ($J^P = 0^+$).

The measurement of the Higgs boson width Γ_H which corresponds to the total decay rate of the particle is of great interest as this parameter is sensitive to BSM effects. The expected width of the SM Higgs boson is $\Gamma_H^{\mathrm{SM}} \sim 4.1$ MeV [28] which is way below the direct measurement resolution of the order of a few GeV . This is why indirect measurements of Γ_H through off-shell Higgs boson production in $gg \to H \to ZZ$, for instance, are performed to constrain this parameter. The results of this measurement obtained by ATLAS using 36.1 fb^{-1}of Run 2 data yielded an observed (expected) upper limit on Γ_H of 14.4 (15.2) MeV at the 95% confidence level [39].

2. The ATLAS detector at the LHC and HL-LHC

The Large Hadron Collider (LHC) [40, 41], presented in Section 2.1, is the most sophisticated circular particle accelerator constructed to date. This machine delivers high energy proton-proton (pp) collisions at high rates and thus is a favorable environment for the experimental study of elementary particles and their interactions. The ATLAS detector, described in Section 2.2, is built around one of the four collision points in the LHC ring. The research work conducted in the framework of this thesis is based on data collected by this detector. An overview of the collision data simulation chain put in place for the ATLAS physics analyses, is given in Section 2.3, followed by a description of the procedures used for reconstructing the objects produced in these collisions, in Section 2.4. The foreseen High-Luminosity upgrade of the LHC ring together with that of the ATLAS detector are briefly discussed in Section 2.5.

2.1. The Large Hadron Collider

The LHC is the most powerful circular particle accelerator ever built. It consists of a 26.7 km ring, placed at a depth of $\sim$ 100 m underground at the Franco-Swiss border near Geneva. It is operated by the European Organization for Nuclear Research (CERN). The LHC was designed to collide charged particles (protons and heavy ions) at very high energies and at high rates. Nominally, two bunches of $\sim 10^{11}$ protons cross every 25 ns and collide at specific points where particle detectors are installed. This makes the LHC a prime facility for modern particle physics research, allowing not only to study various Standard Model (SM) processes but also offering a possibility to probe rare processes and new physics scenarios occurring at the high energy scale.

The LHC occupies the same tunnel that previously hosted the Large Electron Positron collider (LEP) until its physics program came to an end in early 2000, at which point the LHC ring construction began. The first data-taking with high energy pp collisions (7 then 8 TeV in the center-of-mass), referred to as *Run 1* started in 2010. From 2013 to 2015, the LHC ring and detectors underwent a series of upgrades to operate at higher center-of-mass energy and luminosity. The *Run 2* phase started in mid-2015 with the LHC delivering pp collisions at 13 TeV and spanned until the end of 2018. This thesis is based on data recorded during Run 2 until 2018.

2.1.1. proton-proton collider

The choice of pp collisions for the LHC follows directly from the design goals set for this accelerator i.e melding high energy and large amount of data to study physics at the TeV energy scale. Had electron collisions been chosen, as for LEP, the large energy loss due to synchrotron radiation -a phenomenon by which charged particles radiate energy when accelerated in a curved trajectory- would have been prohibitive at the targeted energies. Moreover, a proton-antiproton collider does not allow to reach the desired level of collision rate given the difficulty of producing antiprotons.

On the other hand, pp collisions bring about a set of challenges. Protons are not elementary particles thus the real interaction takes place between their constituents, either quarks (q) or gluons (g), generically referred to as partons. In particular, gg initiated processes are more favored at the LHC compared to their qg and $q\bar{q}$ counterparts as a result of the partons dynamics inside protons. Partons carry a fraction of the proton energy such that not all collisions happen at the same partonic center-of-mass energy $\sqrt{\hat{s}}$. While this allows to explore a large range of $\sqrt{\hat{s}}$, not knowing precisely the partonic initial energy can complicate precision measurements. Furthermore, the interactions between partons inside protons are not perturbative and so, cannot be described within perturbative QCD. The energy fraction carried by a parton is described by the Parton Distribution Function (PDF) for which input measurements from other experiments, affected by their own uncertainties, are required. Additionally, the remaining partons inside protons which are not involved in the collision of interest, may interact resulting in an underlying event. Such events are poorly described by the available models. Moreover, due to the large QCD coupling, quarks and gluons are overwhelmingly produced in pp collisions. Such processes end up being observed as *multi-jet* events which represent an important source of background for a wide range of physics analyses at the LHC and should be suppressed.

The cross-sections of various SM processes as a function of the pp center-of-mass energy are presented in Figure 2.1. The plots shown clearly illustrate the dominance of the multi-jet events production in pp collisions as mentioned above. The relatively large cross-section of the top-quark production modes makes of the LHC the first top quark factory, allowing to measure its properties with unprecedented precision. Moreover, the increased center-of-mass energy at the LHC compared to Tevatron for example, raises the Higgs boson production cross-section to a level where it is possible to measure it.

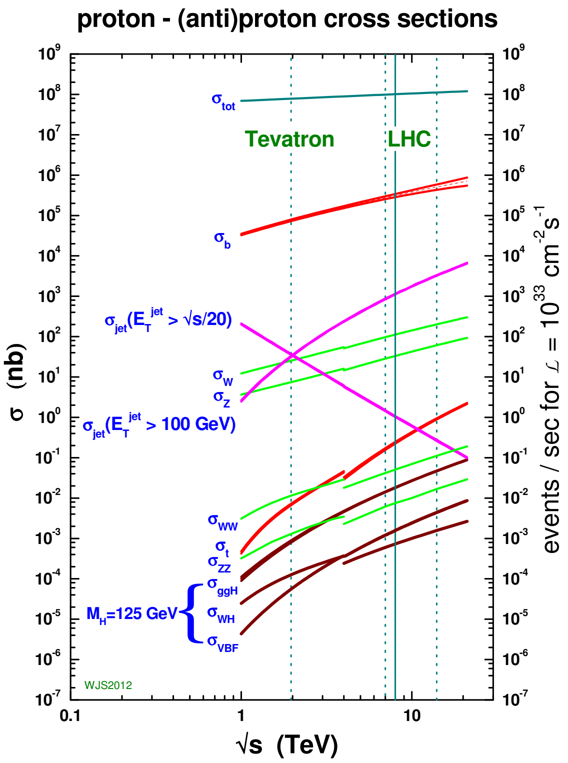

Figure 2.1.: Predicted cross-sections of various SM processes in proton-(anti) proton collisions as a function of the center-of-mass energy [42]. The discontinuity in some of the cross-sections at 4 TeV is due to the switch from proton-antiproton to proton-proton collisions at that energy.

Even though the LHC is mainly designed to provide pp collisions, it can also perform heavy ions collisions. When a large number of protons and neutrons collide at high energies (2.76 TeV per nucleon), a plasma of quarks and gluons is formed. This allows to study strongly interacting matter at extreme values of energy density and temperature which are similar conditions to those present just after the Big Bang.

2.1.2. The LHC setup

The protons used for collisions at the LHC are obtained by ionizing hydrogen gas using a strong electric field. These protons undergo consecutive accelerating stages before reaching the LHC which is the final element in the CERN accelerator chain depicted in Figure 2.2. As a first step, protons are injected into the Linear Accelerator 2 (LINAC 2) where they are accelerated up to an energy of 50 MeV (i.e $\sim \frac{1}{3}c$). After that, the proton beam goes through 3 successive circular accelerators: proton synchrotron BOOSTER, Proton Synchrotron (PS) and Super Proton Synchrotron (SPS), having its energy increased up to $\sim$ 1.4 GeV , 25 GeV and 450 GeV respectively. This phase lasts 4 mn and 20 s, after which the LHC ring is filled with two separate proton beams to be accelerated in opposite directions. After 20 mn, the proton beams at the LHC are stabilized and given their final shape while their energy is increased up to 6.5 TeV , the maximum energy reached up until the end of Run 2.

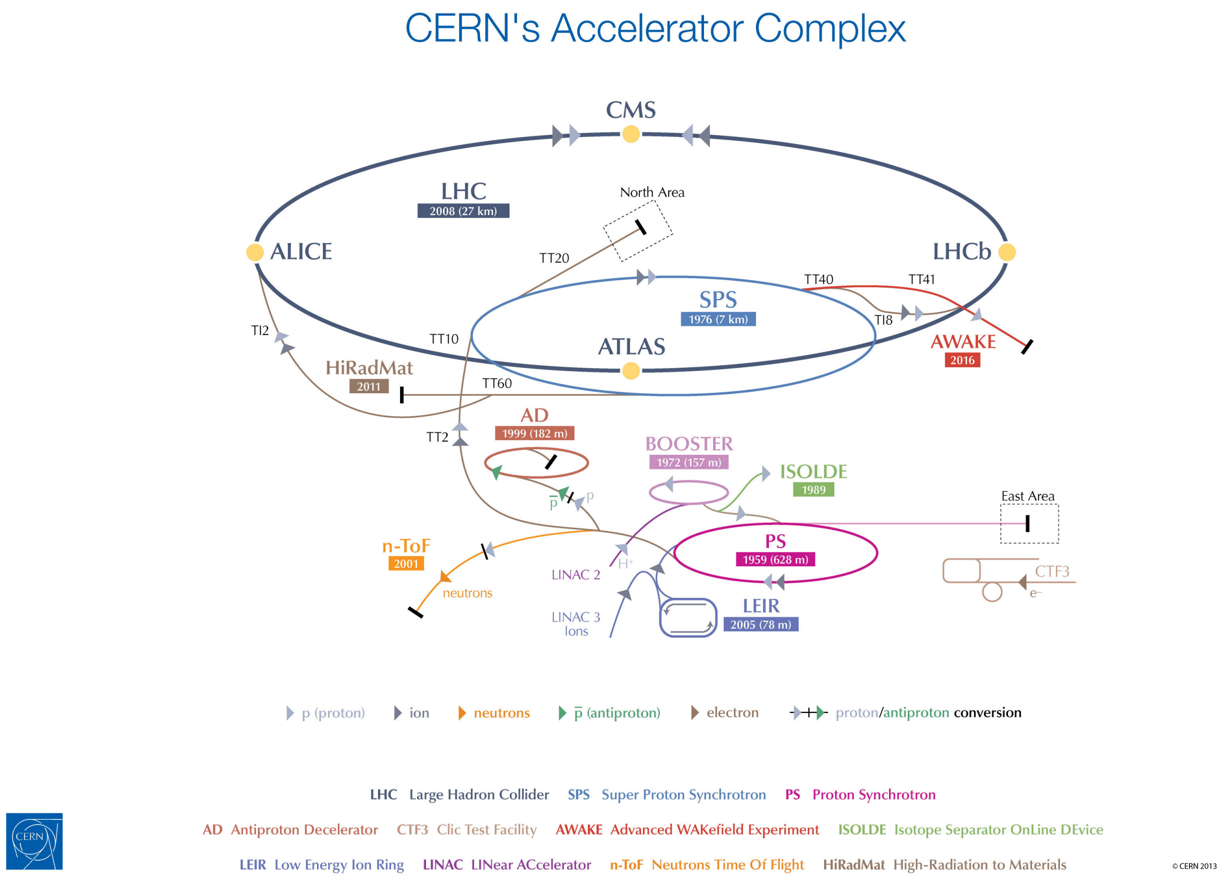

Figure 2.2.: Schematic view of the CERN accelerator complex [43].

Proton beams at the LHC are divided into 2808 bunches containing approximately 10^{11} protons each. The distance separating two consecutive LHC bunches, called bunch-spacing, is either 50 ns or 25 ns (depending on the operating year). As bunches contain a large number of protons, multiple pp collisions occur each bunch-crossing resulting in what is referred to as pile-up. The interaction of interest for physics analyses, generally chosen as the one with the highest energy, is called the hard-scatter.

There are 8 straight sections and arcs composing the LHC ring. In the straight sections, a total of 16 superconducting Radiofrequency chambers (RF) are placed in addition to particle detectors surrounding the interaction points. The RF cavities generate an electric field of 5 MV/m oscillating at 400 MHz which accelerates the protons to the desired energy.

The proton beams are maintained in a curved trajectory inside the beam pipes of the LHC using a variety of superconducting magnets which are cooled down to a temperature of 1.9 K using superfluid Helium. In particular, two main types of magnets are exploited: dipoles which are responsible for bending the proton beams in the arcs and quadrupoles which focus the beams keeping the protons away from the pipes walls. There are in total 1232 dipole magnets, around 15 m long each, generating a magnetic field of 8.3 T. Figure 2.3 shows a cross-section of an LHC dipole element: it has two beam pipes around which two opposite-sign magnetic fields are generated in order to accelerate the counter-rotating proton beams. As for quadrupoles, there are 858 of them, delivering a nominal gradient of 223 T/m and 241 T/m. These magnets are installed in pairs along the LHC ring so as to control both the width and the height of the beams. Additional magnetic multipoles (sextupoles, octupoles and decapoles) are also utilized in the LHC mainly to counteract divergence-inducing effects which result in imperfections in the proton beams.

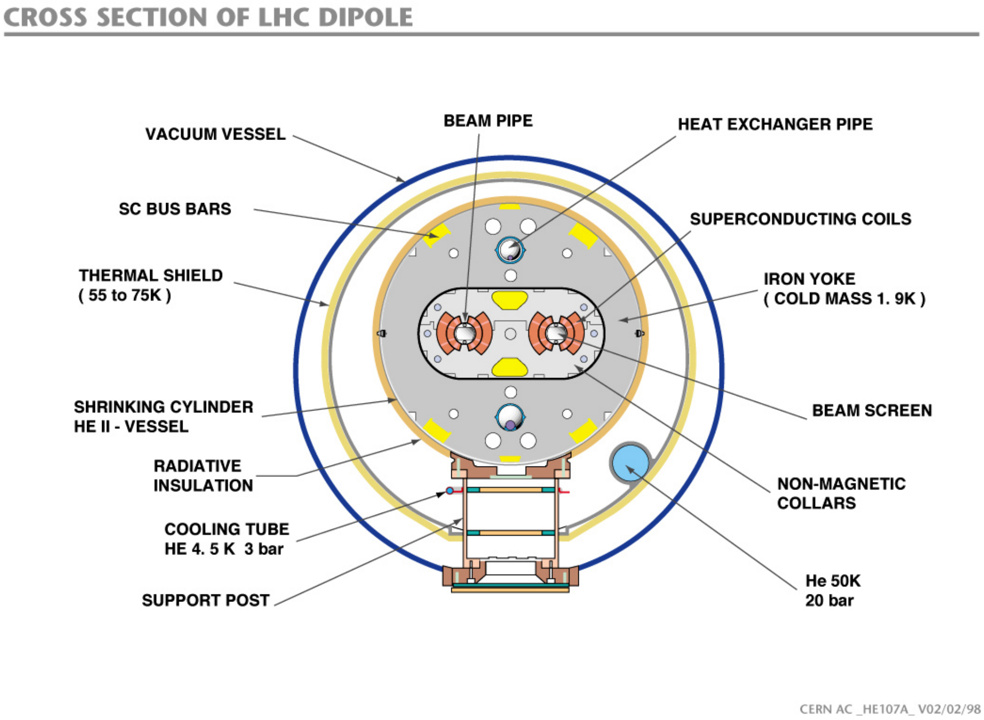

Figure 2.3.: Cross-section of an LHC dipole element [44].

The main operation parameters of the LHC machine are summarized in Table 2.1 for each data-taking period.

The collision rate at a collider can be described in terms of the *instantaneous luminosity* $\mathcal{L}$, defined as:

$$\mathcal{L} = \frac{N_p^2 n_b f_{\text{rev}}}{4\pi\sigma_x\sigma_y} F \tag{2.1}$$

where N_p is the number of protons per bunch, n_b the number of bunches per beam, f_{rev} the beam revolution frequency ($\sim$ 11 kHz), $\sigma_{x(y)}$ the beam dispersion in the transverse plane corresponding to

parameter	Run 1 2010—2011	 2012	Run 2 2015	 2016	 2017	 2018
Beam energy [TeV]	3.5	4	6.5	6.5	6.5	6.5
Bunch spacing [ns]	50	50	50-25	25	25	25
Max number of bunches	1380	1380	2244	2200	2556	2556
Protons per bunch $[10^{11}]$	1.45	1.6	1.15	1.15	1.15	1.15
Peak luminosity $[10^{33}\text{cm}^{-2}\text{s}^{-1}]$	3.7	7.7	5.0	13.6	20.6	20
Integrated luminosity $[1\text{fb}^{-1} = 10^{39}\text{cm}^{-2}]$	5.5	22.8	4.2	38.5	50	66
Mean pile-up	9	21	14	24	37.8	36.1

Table 2.1.: Operating parameters of the LHC for each data-taking period [45–49].

the size of the beamspot [a] ($\sim 10\ \mu m$ in 2016) and F a geometric correction factor encoding the effect of the beams crossing angle at the interaction point. The total amount of collision data delivered during a particular period is called the *integrated luminosity* given by $L = \int \mathcal{L}\ dt$. It is related to the total number of events obtained for a given process considered by an analysis, during a data-taking period, via $N = L\,\sigma\,\varepsilon$ where σ is the process cross-section and ε the event selection efficiency convoluting trigger, offline reconstruction and analysis phase space selection efficiencies.

2.1.3. LHC experiments

The main purpose of the LHC is to provide data allowing to answer some of the fundamental questions left unresolved in particle physics such as the origin of matter-antimatter asymmetry, the nature of dark matter (and possibly dark energy) and the unification of the fundamental forces. To this end, the LHC embarked on a rich physics program ranging from more precise measurements of the SM parameters to the search for new physics phenomena. This ambitious program is carried out by 4 main experiments deployed at the interaction points across the LHC ring:

- The ATLAS [50] (A Toroidal LHC ApparatuS) experiment: It is a multipurpose experiment covering a wide range of the LHC physics program. As such, it takes full advantage of the luminosity offered by the LHC. It is designed to identify most of pp collision products over a broad energy spectrum. The ATLAS detector is described in more details in section 2.2.
- The CMS [51] (Compact Muon Solenoid) experiment: It is a general purpose experiment with a similar physics program to ATLAS however it uses different detector technologies in terms of tracking and calorimetry. Having two independent experiments targeting the same physics analyses is beneficial as it allows to cross-check their findings. Furthermore, the datasets recorded by the two detectors can be combined for enhanced precision.
- The LHCb [52] (LHC beauty) experiment: It is an experiment dedicated to heavy flavor physics at the LHC. Its main goal is to look for indirect evidence of new physics via precision measurements of CP violation and rare decays of beauty and charm hadrons. With such a physics program, LHCb takes part in the efforts towards solving the matter-antimatter asymmetry riddle. The LHCb detector is designed as a single-arm spectrometer with a forward angular coverage ranging from approximately 10 mrad to 300 (250) mrad in the bending (non-bending) plane.

[a]The beamspot refers to the spatial region around the interaction point where the profiles of the two beams overlap.

This detector geometry choice is justified since at high energies both the b- and $\bar{b}$-hadrons are mostly produced in the same forward or backward region. LHCb operates at a lower luminosity compared to ATLAS and CMS ($\sim 10^{32}\text{cm}^{-2}\text{s}^{-1}$) without compromising the amount of data collected given the large cross-section of $b\bar{b}$ pair production.

- The ALICE [53] (A Large Ion Collider Experiment) experiment: It is a heavy-ion experiment focusing on the physics of strongly interacting matter and the quark-gluon plasma under extreme conditions of temperature and energy density.

Besides the above main detectors, there are three other small experiments installed around the LHC. For instance, LHCf [54] (Large Hadron Collider forward) is an independent experiment integrated in the ATLAS experimental area which measures the flux of neutral particles emitted in the very forward region close to the beam axis. These measurements provide data for calibrating the hadron interaction models used in the study of extremely high energy cosmic rays. TOTEM [55] (TOTal Elastic and diffractive cross-section Measurement) is another small detector placed in the CMS cavern targeting the measurement of the total pp cross-section and the study of elastic and diffractive scattering at the LHC. MoEDAL [56] (Monopole and Exotics Detector At the LHC) is the newest addition to the LHC experiments and its primary goal is the search for the magnetic monopole.

2.2. The ATLAS experiment

The ATLAS detector is one of the major four experiments at the LHC. It is operated by a huge collaboration of over 3000 scientists representing 38 countries. It was born conceptually in 1992 at the "*Towards the LHC Experimental Programme*" meeting held in Evian-les-Bains. The construction and installation of the detector took place over the period of 2001-2008 following a series of technical design and developments studies. ATLAS recorded its first pp collisions on the 23rd of November 2009 at a center-of-mass energy of 0.9 TeV .

ATLAS is a general-purpose experiment designed to test the predictions of the SM and perform precision measurements of its parameters, namely in the top quark sector, as well as to search for new phenomena beyond the SM at the TeV scale. It made headlines along side the CMS experiment when the discovery of the Higgs boson based on data collected during Run 1 was announced in July 2012. This achievement was an important milestone in the LHC physics program. After this discovery, the ATLAS experiment entered into an era of precision measurements in the Higgs boson sector marked by the start of the LHC Run 2 in 2015.

The ATLAS detector, depicted in Figure 2.4, is a cylinder 44 m long and 25 m high, forward-backward symmetrical with respect to the interaction point around which it is mounted. It is the most voluminous detector at the LHC as a result of the magnets configuration adopted (one solenoid magnet and three large superconducting toroids) and weighs around 7000 tons, about the same weight as the Eiffel tower. It consists of three main subsystems, each targeting a specific set of measurements, thanks to which the physics goals of the experiment are met. These subdetectors are arranged in an onion layers-like manner around the beam axis as illustrated in Figure 2.4, where going from the center outward we have:

- The **Inner Detector (tracker)** which is immersed in a 2 T axial field generated by a solenoid magnet. Its purpose is to provide measurements allowing to reconstruct the trajectories of charged particles, referred to as tracks later on, and precisely determine their origin i.e whether they stem from the interaction point or a displaced vertex. Additionally, the Inner Detector enables to measure the momenta of the charged particles making use of their tracks curvature in the magnetic field. This detector is described in more details in Section 2.2.1.

- The **electromagnetic and hadronic calorimeters**, described in Section 2.2.2, measure the energy deposited by the incoming particles through their destructive interaction with the detector material.
- The **muon chambers** described in Section 2.2.3, are used to detect muons and measure their momenta thanks to the toroidal magnet in which they are embedded.

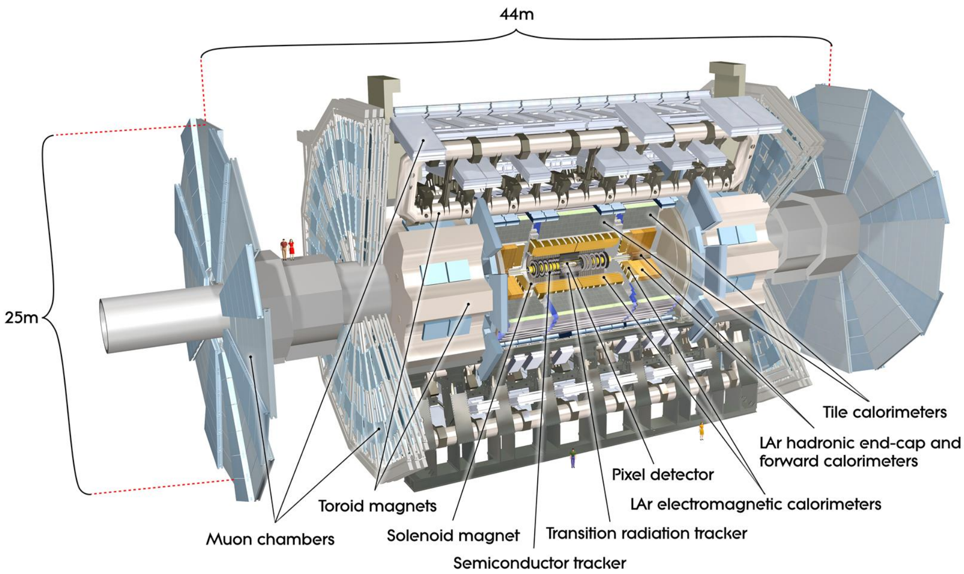

Figure 2.4.: The ATLAS detector overview.

The coordinate system adopted by ATLAS is described briefly hereafter and is used throughout this document. ATLAS uses a right-handed coordinate system, the origin being set at the nominal interaction point. The beam direction determines the z-axis while the x and y axes, defining the transverse plane, point towards the center of the LHC ring and upwards, respectively. The use of a spherical coordinate system (r,θ,ϕ) follows naturally from the cylindrical geometry of the ATLAS detector around the beam pipe. The azimuthal angle ϕ ($-\pi < \phi < \pi$) is defined with respect to the x-axis in the transverse plane and the polar angle θ ($0 < \theta < \pi$) with respect to the z-axis. The choice of variables which are boost-invariant along the z-axis is preferable since the z-component of the initial partons momentum is unknown. The distance in polar angle θ does not respect Lorentz-invariance therefore this angle is replaced by the rapidity y or pseudo-rapidity η (in the case of ultra-relativistic particles $E \gg mc^2$) defined as follows:

$$y = \frac{1}{2}\, ln\left(\frac{E + p_z}{E - p_z}\right) \xrightarrow{E \gg mc^2} \eta = -ln\left(\tan\frac{\theta}{2}\right) \tag{2.2}$$

The angular distance ΔR in the pseudorapidity-azimuthal plane is defined as $\Delta R = \sqrt{(\Delta\phi)^2 + (\Delta\eta)^2}$.

The richness of the physics program pursued by the ATLAS experiment imposes a set of requirements that need to be fulfilled by the detector. These requirements motivated the experiment design and involve primarily the following:

- Fast and radiation-hard electronics to cope with the high luminosity of the LHC.

- High detector granularity to attain a good position resolution and have a good separation among particles which are created in large fluxes at the LHC.

- Large acceptance in pseudorapidity combined with almost full azimuthal coverage to capture as much information as possible from the detector which is essential for the missing energy determination as well as the full reconstruction of events, namely those with complex final state topologies.

- Good charged-particle tracks identification in the inner detector with both high reconstruction efficiency and momentum resolution. This is particularly crucial for identifying jets stemming from the fragmentation of b-quarks, referred to as *b-tagging*.

- Very good electromagnetic and hadronic calorimetries with high energy resolution for the measurements of electrons, photons and jets which intervene in many of the targeted physics analyses.

- Good muon identification and momentum resolution over a broad momenta range.

- Fast and efficient triggers with enhanced selection of the low cross-section processes of interest and sufficient rejection of the large multijet background.

It is important to note that most of the above prerequisites have to be met over a large spectrum of energies, ranging from a few GeV to a few TeV . The performance requirements of the ATLAS detector components are summarized in Table 2.2.

Detector part	Resolution	η coverage	
		Measurement	Trigger
Inner detector	$\sigma_{p_T}/p_T = 0.05\%\ p_T \oplus 1\%$	±2.5	
EM calorimeter	$\sigma_E/E = 10\%/\sqrt{E} \oplus 0.7\%$	±3.2	±2.5
Hadronic calorimeter			
barrel and end-cap	$\sigma_E/E = 50\%/\sqrt{E} \oplus 3\%$	±3.2	±3.2
forward	$\sigma_E/E = 100\%/\sqrt{E} \oplus 10\%$	$3.1 < \lvert\eta\rvert < 4.9$	$3.1 < \lvert\eta\rvert < 4.9$
Muon spectrometer	$\sigma_{p_T}/p_T = 10\%$ at $p_T = 1$ TeV	±2.7	±2.4

Table 2.2.: Performance goals of the ATLAS sub-detectors [50]. The units for E and p_T are in GeV .

2.2.1. The inner detector

The Inner Detector (ID) is the innermost part of the ATLAS detector dedicated to tracking measurements. These measurements allow to reconstruct the charged particles tracks and determine their momenta in addition to reconstructing interaction vertices as well as secondary vertices from decaying particles. The ID is surrounded by the central solenoid which delivers an axial magnetic field of 2 T. The layout of the tracker is depicted in Figure 2.5.

The ID is able to achieve the required precision on the tracking measurements through the combination of three complementary subsystems which employ different technologies: the *pixel* and *Semi-Conductor Tracker (SCT)* close to the interaction point and a *Transition Radiation Tracker (TRT)* at

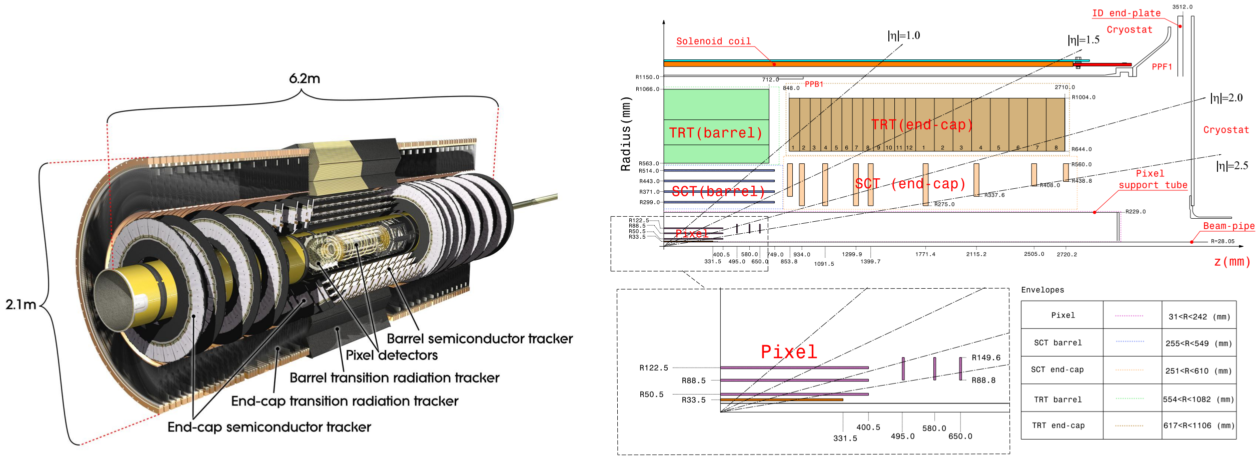

Figure 2.5.: (Left): Layout of the ATLAS inner detector depicting both the barrel and end-cap regions [50]. (Right): An (r, z) cross-section view of the ATLAS Inner Detector layout [57].

larger radii. The pixel detector exploits high-granularity silicon sensors to perform 3D track measurements whereas the SCT provides pseudo-3D spatial measurements (up to some ambiguities) making use of silicon strips crossing with a small angle. The TRT, on the other hand, utilizes straw tubes filled with gas to provide 1D track measurements.

Each ID subcomponent is split in two regions: the *barrel* part covers low pseudorapidities and is composed of concentric cylinders around the beam axis while the *end-caps* placed at high η are arranged in disks perpendicular to the beam axis. This setup allows to maximize the pseudorapidity coverage, up to $|\eta| = 2.5$ for the pixels and SCT systems and up to $|\eta| = 2$ for the TRT.

The pixel detector

The ATLAS pixel detector is the closest subdetector to the Interaction Point (IP). Its layout is depicted in Figure 2.6(a). It exploits the pixel technology allowing it to attain a high granularity, thanks to which it is able to meet the stringent specifications on radiation hardness in the vicinity of the IP. Up until the end of Run 1, the pixel detector consisted of three barrel layers and six end-cap disks. As part of the ID upgrade program, a fourth layer, referred to as the Insertable B-Layer (IBL), was added closer to the beamline during the first long shutdown. Figure 2.6(b) shows the IBL prior to insertion into the existing pixel detector. This upgrade was motivated by the eventual efficiency decrease of the former innermost layer due to radiation damage.

The pixel detector relies on the silicon semi-conductor technology. Each pixel collects the ionization charge deposited by a charged particle crossing a p-n junction, after which an electrical signal is output through proper electronics. The pixel area of 50×400 μm^2 (and 50×250 μm^2 for IBL) is dictated by the readout electronics pitch and was optimized to obtain the best physics performance namely in terms of b-tagging. The pixel detector provides 3D measurements with an excellent resolution: 10μm in r-ϕ and 115 μm in the z (R) direction in the case of the three outer layers (and end-cap disks) of the pixel detector. The resolution is even better with the smaller pixels of the IBL: 8 μm in r-ϕ and 40 μm in the z direction. This allows for an accurate reconstruction of the charged tracks, the interaction vertex as well as the secondary vertices originating from long-lived particles which is crucial for b-tagging (cf. Section 3.1).

Each pixel sensor is made of 47232 pixels which are bump-bonded to 16 frontend chips containing 2880 readout channels each. The sensor, the frontend chips along with power cables and services

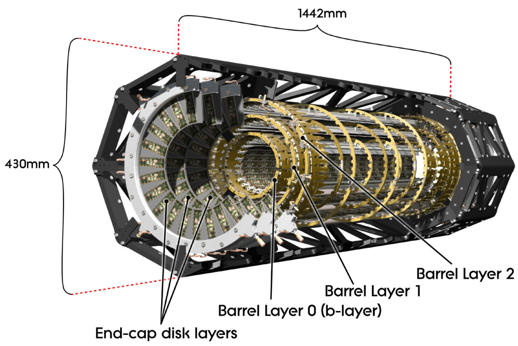

(a)

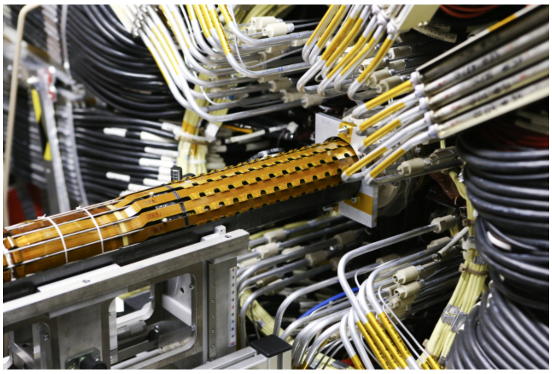

(b)

Figure 2.6.: (a) Schematic view of the ATLAS pixel detector consisting of barrel and end-cap layers [58]. (b) The IBL before insertion into the pixel detector [59].

compose what is called a module which is illustrated in Figure 2.7. These modules are loaded on barrel staves and disk sectors such that the detector hermeticity requirement is met. The number of modules per barrel layer and per disk are summarized in Table 2.3.

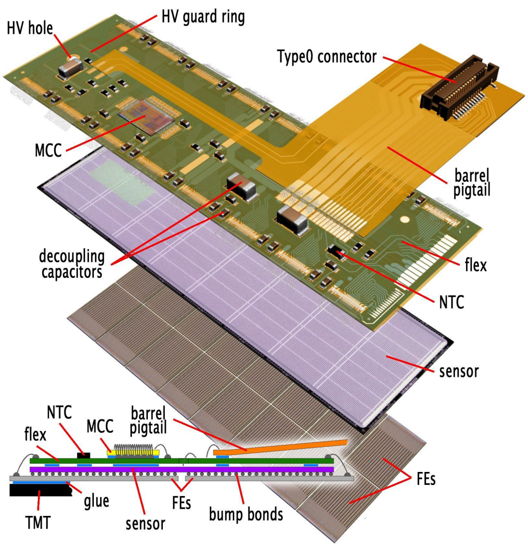

Figure 2.7.: Layout of an ATLAS pixel module [50].

The Semi-Conductor Tracker

The SCT occupies the intermediate volume between the pixel detector and the TRT. It comprises four barrel layers and 2 endcaps with nine disks each.

The SCT relies on the same detection principle as the pixel detector. Two 6 cm-long sensors are daisy-chained to make up the rectangular barrel sensor which consists of 768 p-n junctions strips of 80 μm pitch. For the endcap region, however, trapezoidal sensors with radially oriented strips of varying pitch ranging from 56.9 μm to 90.4 μm were adopted. A pair of these sensors, one on the top and one on the bottom, coupled with their readout electronics form a module as shown in

Barrel:	Radius (*mm*)	Staves	Modules
Insertable-B-Layer	33.2	14	280
Layer-0 (B-Layer)	50.5	22	286
Layer-1	88.5	38	494
Layer-2	122.5	52	676
End-cap (one side):	z(*mm*)	Sectors	Modules
Disk $\times$ 3	495, 580, 650	8	48

Table 2.3.: Parameters of the pixel detector components in the barrel and end-cap regions [50, 59].

Figures 2.8(a) and 2.8(b) for the barrel layers and endcap disks, respectively. The module sensors are rotated with respect to each other by 40 mrad in order to allow for 2D measurements in the module plane, through the intersection of the strips from both its sides. The barrel region consists of 2112 modules while the endcaps count 1976 modules.

The SCT system achieves an intrinsic accuracy of 17 μm in r-ϕ and 580 μm in z (R) for the barrel (end-cap disk) region. As such, the 3D measurements it provides (with some ambiguities when neighboring strips are hit, unlike for the pixels), contribute to the high precision measurement of the tracks impact parameters and their curvature together with the pixel detector and TRT respectively.

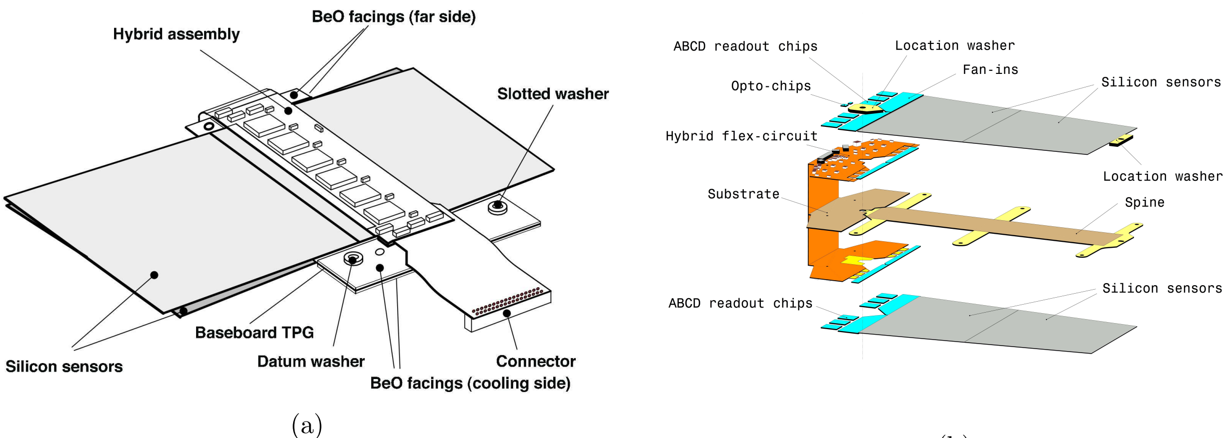

Figure 2.8.: Schematic layouts of the SCT (a) barrel and (b) endcap modules [50].

The Transition Radiation Tracker

The TRT constitutes the outer part of the ID. It provides tracking information at large radii which is crucial for precise tracks curvature measurements needed to attain the required momentum resolution. In contrast to the Pixel and SCT detectors, it was not designed for precise hit position measurements.

The basic elements composing the TRT are thin-walled proportional drift tubes, measuring 4 mm in diameter, commonly referred to as straws. The surface of the straw, which is kept at a negative potential of ~ -1.5 kV, plays the role of the cathode, whereas at its center a 31 μm diameter wide tungsten wire -coated with 0.5 to 0.7 μm of gold- acts as the anode being kept at ground potential. The straws are filled with a gas mixture of 70% Xe, 27% CO_2 and 3% O_2. A charged particle traversing the straws, ionizes the gas mixture and the resulting electrons and positive ions drift apart under the electric field effect. A detectable signal, proportional to the energy deposited by the particle, is then generated and collected at the wire end via proper electronics. The drift time can be computed and gives a spatial accuracy of ~ 130 μm in the plane perpendicular to the wire. The TRT does not provide tracking information in the direction parallel to the straw.

The TRT consists of three parts: a barrel and two endcaps. The barrel contains up to 73 layers of 144 cm-long straws oriented parallel to the beam axis. These straws are arranged within three rings made of 32 modules each. Figure 2.9(a) shows a picture of a TRT barrel module. In the TRT endcaps, a total of 245760 straws, 37 cm in length, are mounted on a set of 20 wheels per side. Each wheel (cf. Figure 2.9(b)) is composed of eight layers of 768 radially-oriented straws. Given this setup, a track with $p_T > 0.5$ GeV and $|\eta| < 2$ crosses a minimum of 36 straws except in the barrel-end-cap transition region of $0.8 < |\eta| < 1.0$, where a track traverses a minimum of 22 straws.

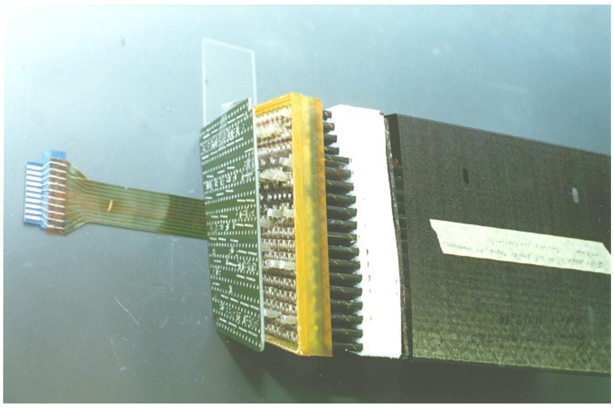

(a)

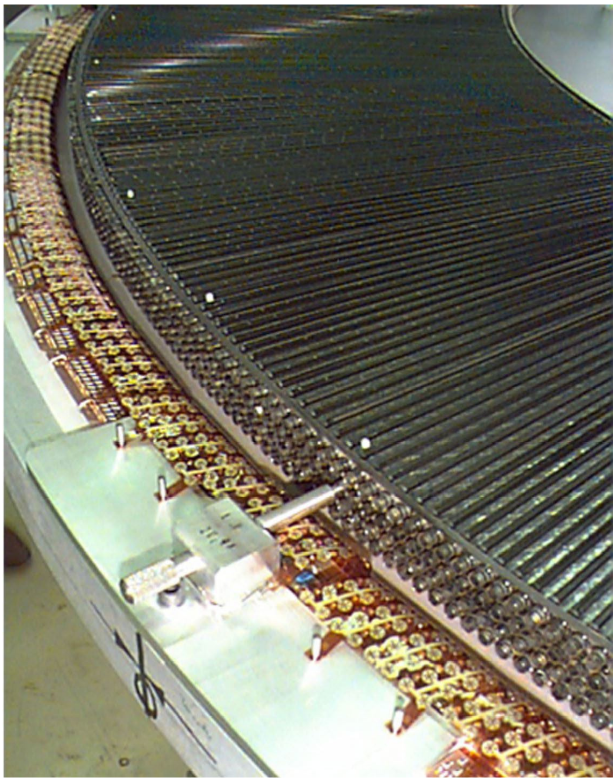

(b)

Figure 2.9.: Photographs of a TRT (a) barrel module [60] and (b) four-plane endcap wheel during assembly [50].

The TRT straw layers are interleaved with polypropylene fibers which act as a transition radiation material allowing to distinguish electrons from heavier charged particles such as pions. Electrons passing through the radiator generate a notably large amount of transition radiation (photons) due to their small mass. The transition photons emitted are then absorbed by the gas mixture inside the straws yielding a large signal amplitude. The TRT electronics provide two thresholds to identify these high amplitude signals: a passing electron, with $p_T > 2$ GeV , leads to at least 7 straws with a high-amplitude signal. Thus, the TRT plays a key role in electron identification.

2.2.2. Calorimeters

The ATLAS calorimeters are designed to stop the particles exiting the ID and measure precisely their energies with a good position accuracy. They cover the pseudo-rapidity range up to $|\eta| = 4.9$. To build the calorimetric system, different technologies which revolve around the concept of *sampling calorimetry* were utilized. Sampling calorimeters are made by alternating layers of a dense passive material and an active medium. The showering of particles passing through the passive material is triggered, whereby one particle produces a cascade of lower energy secondary particles. This induces a signal in the active medium which is proportional to the deposited energy.

Incident particles release their energy in the calorimeters through different processes. Photons and high energy electrons traversing matter deposit their energy via e^+e^- pair creation and Bremsstrahlung radiation respectively. Such processes are characterized by the material radiation length X_0[b]. Hadrons, however, typically lose energy by undergoing inelastic hadronic collisions in the crossed matter, governed by the nuclear interaction length λ. As such, the calorimeters must be conveniently large to fully contain the electromagnetic and hadronic showers which expand over several X_0 and λ in length, and thus reduce the amount of energy leaked into the muon spectrometer. Muons are not stopped in the calorimeters as they loose less energy via Bremsstrahlung compared to electrons given their larger mass and they are not strongly interacting particles. Neutrinos, on the other hand, do not interact with the calorimeters and their presence is manifested in the form of missing energy inside the detector.

The ATLAS calorimetry system is divided into three main parts: the electromagnetic, the hadronic and the forward calorimeters. The overall layout of the calorimeter system is illustrated in Figure 2.10.

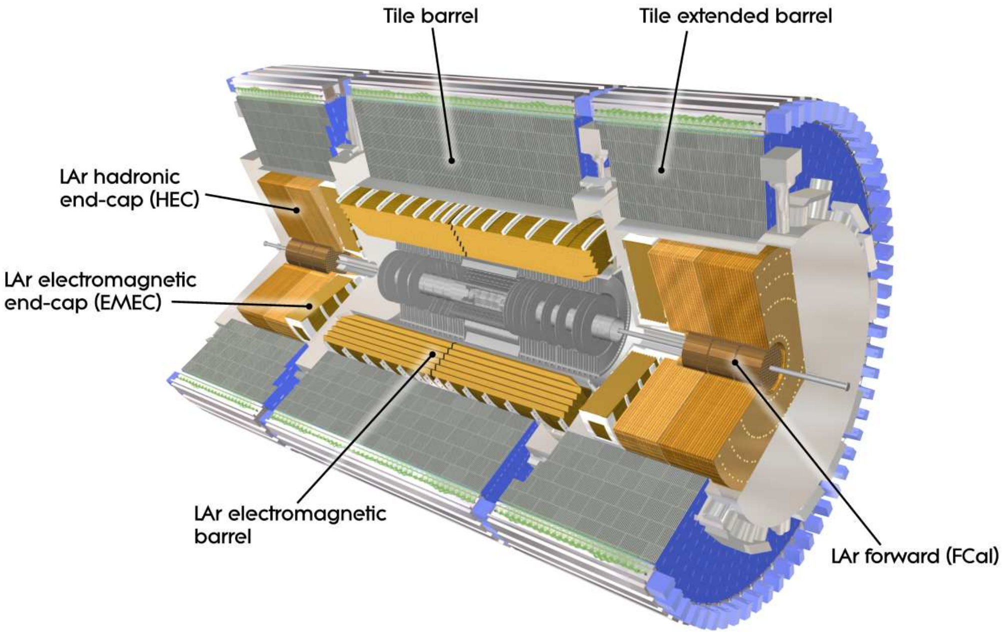

Figure 2.10.: General view of the ATLAS calorimetry system displaying the different parts of the electromagnetic, hadronic and forward calorimeters [50].

[b] The radiation length measures the absorption power of a material through electromagnetic processes. It is defined as the mean distance over which a high energy electron ($E > 10$ MeV) looses 63% of its energy predominantly through Bremsstrahlung radiation. It also corresponds to 7/9 of the mean free path for e^+e^- pair production by a high energy photon.

Electromagnetic calorimeters

The electromagnetic calorimeter (ECal) aims primarily at measuring the energy of electrons and photons with high precision. It is a sampling calorimeter composed of layers of lead plates absorbers interleaved with Kapton electrodes which are immersed in a Liquid Argon (LAr) active material as shown in Figure 2.11(a). An accordion geometry was adopted for the absorbers and electrodes to ensure a full coverage in ϕ without gaps.

The ECal consists of three parts: a barrel covering the region up to $|\eta| = 1.475$ and two endcaps (EMEC), each made of two wheels, covering the pseudorapidity range of $1.375 < |\eta| < 3.2$. Each of these parts is housed in its own cryostat which holds the Argon in a liquid state (89 K). LAr was chosen as an active medium given its resistance to radiation as well as its response stability over time.

The barrel and outer endcap wheels are longitudinally segmented into three layers: the strip layer, the middle and the back. The strip layer is finely granular in the η direction yielding the best η measurement of the calorimeter whereas the second and third layers provide a better granularity in the ϕ direction. A sketch view of the three layers is shown in Figure 2.11(b) for a barrel module. On the other hand, the endcaps inner wheels are segmented into two layers with a coarser granularity in both directions. The virtual calorimeter cells resulting from the above segmentation represent elementary energy deposits and are readout by proper electronics. An electromagnetic shower is recorded in the detector as a cluster of such cells and the corresponding energy is measured by summing over the energies deposited in each of these cells.

The region with $|\eta| < 1.8$ is equipped with a presampler placed in front of the electromagnetic calorimeter, the role of which is to help estimate the energy loss due to the material in front of the calorimeter.

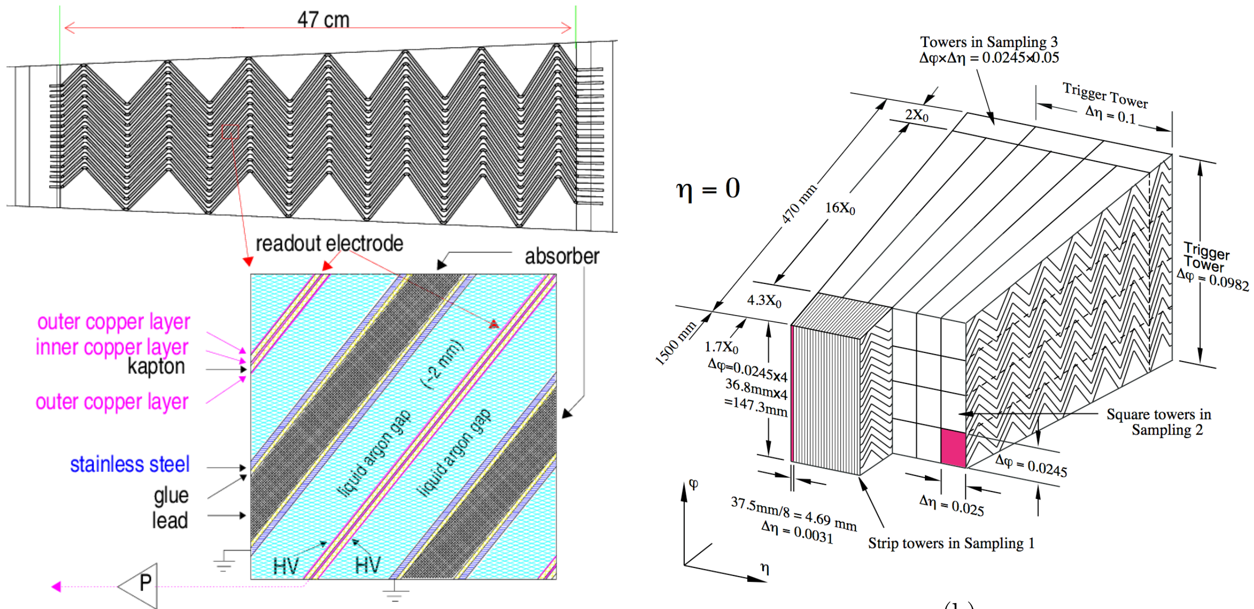

(a) (b)

Figure 2.11.: (a): A view of a small sector of the barrel calorimeter highlighting the accordion structure of the lead absorbers and electrodes [61]. (b): Sketch of a barrel module of the electromagnetic calorimeter highlighting the different layers with their corresponding granularities [50].

Hadronic calorimeters

The hadronic calorimeters system is designed to measure the energy of hadronic showers (jets). It is composed of a barrel and two endcaps.

The barrel consists of plastic polystyrene scintillating tiles acting as active material, interleaved with steel plates absorbers. It is further divided into three parts: a central part covering up to $|\eta| = 1$ and two extensions on each side with a coverage range of $0.8 < |\eta| < 1.7$. Each of these parts is segmented azimuthally into 64 wedge-shaped modules as shown on Figure 2.12. The passage of charged particles in the scintillating tiles produces ultraviolet light. The latter is then collected and converted into visible light via wavelength shifting fibers, before reaching photomultiplier tubes (PMTs) which output an amplified electrical signal.

For the hadronic endcap calorimeters (HEC), the liquid Argon technology is utilized whereby flat copper plates play the role of the absorber material instead of Lead. They are located behind the electromagnetic calorimeter endcaps and are housed in the same cryostats. Each of the endcaps consists of two independent wheels, covering the pseudo-rapidity range of $1.5 < |\eta| < 3.2$.

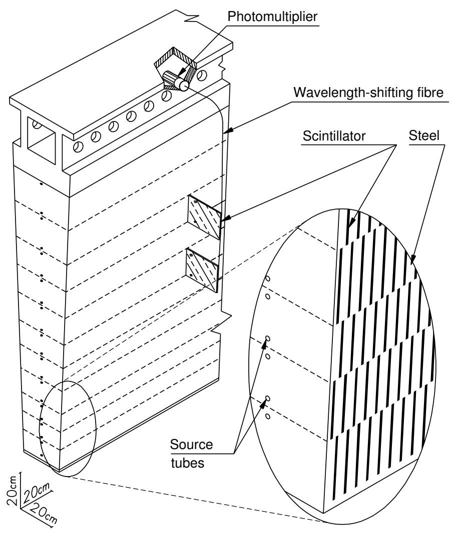

Figure 2.12.: Schematic view of a tile barrel module emphasizing the mechanical assembly and the different components of the optical readout namely the tiles, the fibers and the photomultipliers [50].

Forward calorimeters

Two forward calorimeters (FCal) are placed on each side of the ATLAS detector to measure forward jets and estimate better the missing energy. Additionally, they help to limit the backgrounds reaching the muon system. They cover the range of $3.1 < |\eta| < 4.9$. Each endcap is divided longitudinally into three modules. The first layer, which is the closest to the interaction point, uses copper as an absorber and is optimized for electromagnetic detection. The two remaining layers use tungsten as an absorber and are optimized for hadronic showers measurements. All three modules are housed in the same LAr cryostat with the other endcap calorimeters (EMEC and HEC).

2.2.3. The muon spectrometer

The muon spectrometer (MS), shown in Figure 2.13, is the outermost subdetector of the ATLAS experiment. It is devoted to the detection of muons which exit the calorimeters, the reconstruction of their tracks as well as the precise measurement of their momenta over the pseudorapidity range of $|\eta| < 2.7$.

To measure the particles momenta, the MS relies on the deflection of the corresponding tracks in the magnetic field generated by the air-core toroidal magnets system. This system provides a magnetic field with a strength of 0.5 up to 1 T which bends the muons in the (R,z) plane. The toroidal magnets system is composed of a large barrel part providing magnetic bending in the range of $|\eta|<1.4$ and two endcaps with a coverage of $1.6 < |\eta| < 2.7$. In the $1.4 < |\eta| < 1.6$ range, referred to as transition region, tracks are deflected by both barrel and end-cap toroids. Each of these toroids is formed of eight rectangular coils which are made of a mixture of Aluminium, Copper, Niobium and Titanium and are cooled using liquid Helium to 4.5 K. The muon p_T resolution achieved by the MS is limited by the non-uniformity of the toroidal magnetic field.

The MS is composed of three concentric layers in the barrel region, surrounding the beam axis and three endcap wheels perpendicular to it with a gap at $|\eta| \approx 0$ to allow for the passage of services to the different subsystems. These layers are instrumented with two groups of muon chambers. The first is designed for track precision measurements and involves two kinds of subdetectors: Monitored Drift Tubes (MDT) and Cathode Strip Chambers (CSC). The second group of chambers is dedicated to providing information to the ATLAS trigger system based on fast muon measurements and consists of a combination of Resistive Plate Chambers (RPC) and Thin Gap Chambers (TGC).

The MDT chambers cover all the region of $|\eta| < 2.7$ except for the part of the innermost endcap layer covering $2 < |\eta| < 2.7$ where CSC chambers are installed instead. An MDT chamber consists of three to eight layers of drift tubes $\sim$ 3 cm in diameter filled with a gas mixture of 93% Argon and 7% CO_2. Each tube is equiped with a tungsten-rhenium wire of 50 μm in diameter, placed at the center and operating at $\sim$ 3 kV. The drift time of the ionization charge produced by the incoming particles inside the tube is measured and used to derive the spatial hit coordinate in the bending plane. The typical spatial resolution achieved per tube is 80 μm which improves to about 35 μm per chamber.

The use of CSC chambers in the innermost endcap layer is motivated by the limited counting rate of the MDTs, which is around 150 Hz/cm^2. In contrast, the CSCs provide higher radiation tolerance and rate capability (up to 1000 Hz/cm^2) in accordance with the larger particle flux in the $2 < |\eta| < 2.7$ region. The CSCs are multi-wire proportional chambers using the same gas mixture as the MDTs. The multiple anode wires are oriented radially and held at a potential of 1.9 kV whereas the planar cathodes are segmented into strips in the orthogonal direction. This allows to reconstruct tracks in the (η, ϕ) space. The CSC system is arranged in two disks each composed of eight chambers. Each chamber consists of four planes enabling to perform four independent measurements in η and ϕ per track. The CSCs have a good time resolution with their maximum drift time for signal collection being 40 ns compared to 700 ns for the MDTs. The typical spatial resolution obtained with the CSCs is 40 μm in the bending η-plane and 5 mm in the non-bending ϕ-plane.

The remaining triggering chambers provide fast and coarse muon tracking information as well as bunch-crossing identification. Additionally, these chambers perform measurements in the non-bending ϕ plane, thus complementing those obtained from the MDTs.

The RPCs are arranged in three concentric layers around the beam axis, in the barrel region covering up to $|\eta| = 1.05$. They consist of two parallel resistive plates, 2 mm apart, filled with a gas mixture of $C_2H_2F_4$/Iso-C_4H_{10}/SF_6. They operate at a potential difference of 9.8 kV which allows for a very good timing resolution of $\sim$ 2 ns. The TGCs, however, are installed in the endcap wheels, covering the range of $1.05 < |\eta| < 2.7$ (2.4 for triggering). They consist in multi-wire proportional chambers filled with a gas mixture of CO_2 and n-C_5H_{12}. The cell geometry adopted features a wire-to-cathode distance (1.4 mm) which is smaller than the wire-to-wire distance (1.8 mm), thus allowing a fast signal collection reaching a timing resolution of the order of 4 ns.

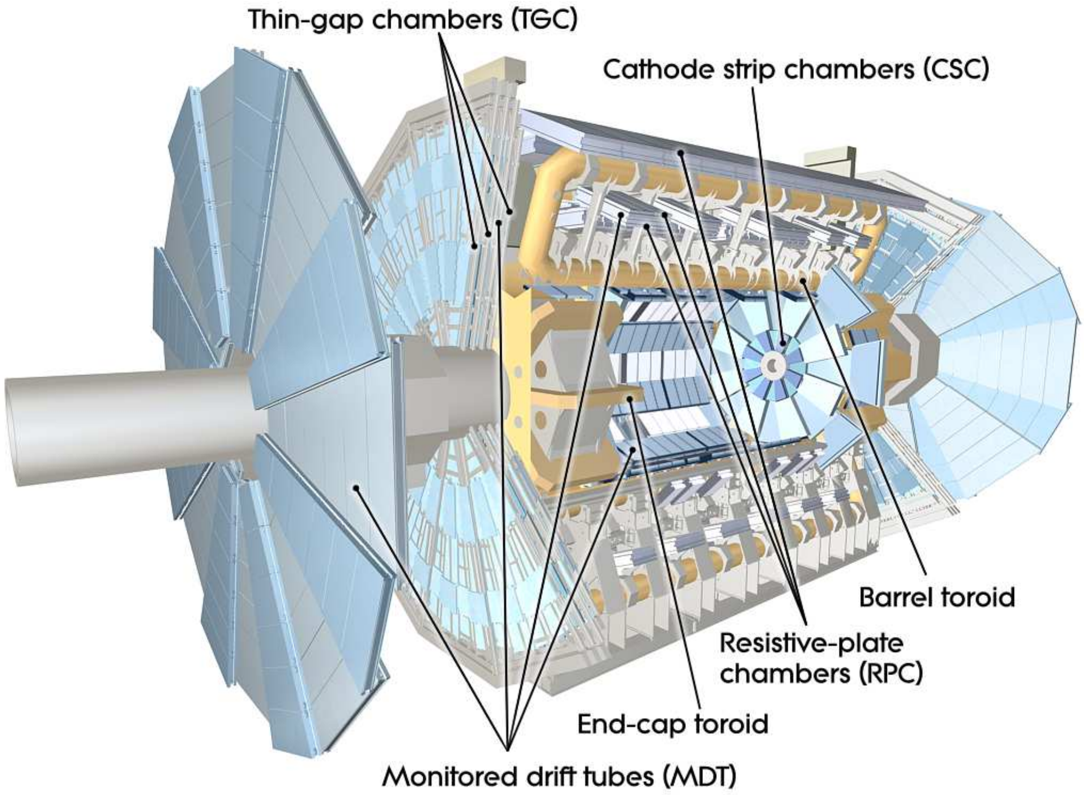

Figure 2.13.: Overview of the ATLAS muon spectrometer [50].

2.2.4. The ATLAS trigger system

The high luminosity of the LHC, with a bunch-crossing frequency of 40 MHz, results in a huge amount of data which is impossible to record fully given the current limitations on storage capacity and rates. This is why ATLAS put in place a trigger system to significantly reduce the size of the data to be processed. To this end, the trigger performs fast and effective events selection at run-time, allowing to reject most of the QCD background and save only events which are of interest for the experiment physics program.

The current ATLAS trigger system consists of a hardware-based level 1 trigger (L1) and a subsequent software-based high level trigger (HLT). A scheme of the ATLAS Trigger and Data Acquisition (TDAQ) systems is shown in Figure 2.14.

The L1 trigger performs the initial event selection relying on logical electronics. It uses coarse-granularity information obtained exclusively from the calorimetry system and the muon trigger chambers while data recorded by the remaining subdetectors wait in pipelines until the trigger decision is made. The L1 trigger searches for events with high energy leptons, photons and jets as well as high total transverse energy and large missing transverse energy. Detector areas with such objects are flagged as regions of interest (RoI) by the L1 trigger. The latter is optimized to make a fast decision, in at most 2.5 μs after the bunch crossing. It has an output event rate of $\sim$ 100 kHz being reduced

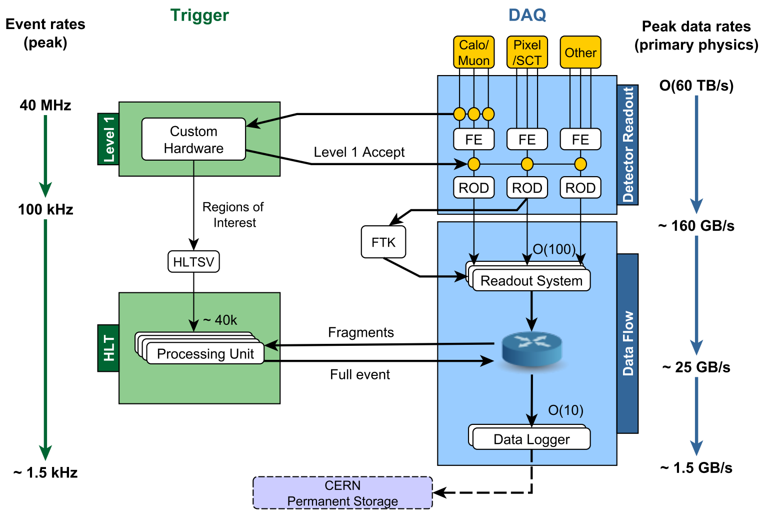

Figure 2.14.: Schematic overview of the ATLAS trigger system in Run 2 [62].

from the input rate of 40 MHz.

Once an event is accepted by the L1 trigger, it passes to the software based HLT trigger. At this stage, sophisticated reconstruction and selection algorithms are run in the L1 RoI using full granularity detector information in either these regions or the whole event. For instance, at this step, multivariate techniques are exploited to discriminate electrons and photons from hadrons thus enhancing particle identification and selection efficiency. The HLT reduces the event rate from the L1 input of 100 kHz to 1 kHz on average within a processing time of about 0.2 s. When an event is accepted by the HLT, its corresponding data is recorded.

Recorded data is periodically reprocessed to incorporate software updates and increased understanding of the detector conditions. The data quality of saved events is checked and those taken during periods of sub-detector malfunction are flagged not to be used for physics analyses.

2.3. Event simulation

The simulation of pp collision events is an essential input for ATLAS physics analyses. It is carried out through a chain of consecutive steps reflecting the high level of precision targeted by the experiment. The simulation procedure is primarily based on the Monte Carlo (MC) method in which repeated random sampling of variables described by complex probability density functions is used to model various physics processes which are considered in the analyses. Section 2.3.1 describes the successive stages involved in the event generation procedure. The latter is followed by the detector simulation step, presented in section 2.3.2, in which the interactions of the generated particles with the detector material are simulated as well as the subsequent electronic response of the detector to the deposited energy as a result of these interactions. This allows to perform direct comparisons between real and simulated data which are stored in the same format.

2.3.1. Event generation

The first link in the simulation chain is the event generation. The simulation of pp collision events requires a detailed description of physics processes taking place at different energy scales which can be treated separately according to the factorization theorem [63]. Thus, a physics event can be simulated through several consecutive steps which are illustrated in Figure 2.15: the extraction of partons from the incoming protons, the hard scattering, the parton shower and the hadronization followed by subsequent decay of hadrons.

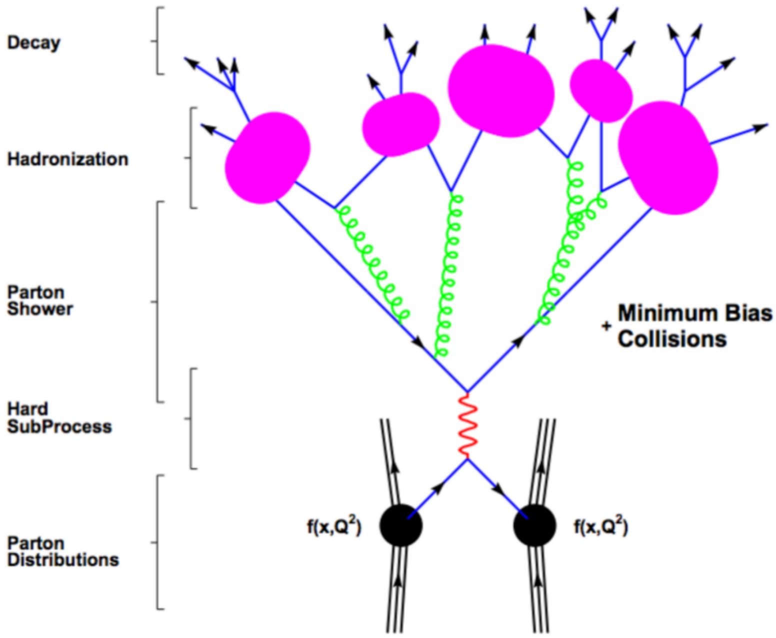

Figure 2.15.: Schematic overview of a pp collision event generation emphasizing the different steps involved [64].

The momenta of the hard-scatter partons within the colliding protons are extracted based on Parton Distribution Functions (PDFs). These determine the probabilities to find a parton of a certain flavor carrying a given fraction of the proton momentum. The partonic content of the proton cannot be described explicitly with the SM given its non-perturbative nature. Thus, PDFs are derived based on fits to experimental data obtained mainly from deep-inelastic scattering experiments and hadron colliders.

The hard-scatter step of the event generation is commonly referred to as the matrix element (ME) calculation. At this level, the kinematics and flavors of the partons extracted in the former step are used to compute the cross-section of the hard-scatter process within perturbative QCD. This is carried out by evaluating the Feynman diagrams corresponding to the process of interest where different orders of precision can be used depending on the complexity of the final state. This phase of the event simulation is accomplished by so-called parton-level generators (or ME generators). Some of these generators allow to add one or several additional partons to the main process. The ME generators used in the analyses presented in this thesis are Madgraph5_aMC@NLO [65], Powheg-Box [66–68] and Sherpa [69].

The parton shower (PS) brings corrections to the hard-scatter cross-section by approximating higher order contributions in order to mimic a complete final state. It is modeled by MC generators which simulate the successive emission of gluons, quarks and photons starting from the partons of the initial and final states. These generators evolve the event from the large energy scale associated with the hard scattering down to the PS cut-off scale where perturbation theory breaks down and hadronization models take over. The overlap taking place when generators with additional partons are coupled to parton showers is removed following dedicated procedures referred to as ME-PS matching schemes [70, 71].

The fragmentation and hadronization operate when the PS reaches non-perturbative energy scales. These processes are simulated using phenomenological models. At this stage, partons start to bind together forming colorless baryons and mesons. The hadrons produced in excited states are further decayed into more stable particles.

For the parton showering and hadronization steps, the ME generators used in the analyses presented in this document are interfaced with either PYTHIA [72, 73] or Herwig [74, 75]. Sherpa, however, has its own showering and hadronization models and does not need interfacing.

Soft processes such as pile-up and underlying event interactions involving mainly spectator partons from the colliding protons, are also simulated using phenomenological models whose parameters are tuned to match experimental data.

The output of the event generation sequence, also known as the MC history, is a list of four-vectors of all the produced particles in the event after the hadronization and decay of most of the intermediate unstable particles. The particles contained in the MC history record are commonly referred to as true or truth particles.

2.3.2. Detector simulation

At the second part of the event simulation procedure, a dedicated simulation of the ATLAS detector built based on the Geant 4 toolkit [76], is utilized to account for the energy deposited in the detector following the interactions of its material with the particles produced in the event generation step. The energy deposits, referred to as hits, are then digitized and converted into electronic signals simulating the detector response.

The detector simulation phase consumes most of the computational power used for the full event simulation. This is primarily due to the development of electromagnetic particles showers in the ATLAS calorimeter system which requires the longest time to simulate. For instance, for the full detector simulation (*Fullsim*) using a highly detailed detector description, a single $t\bar{t}$ event requires around 15 mn of CPU time [77]. As such, relying solely on standard *Fullsim* option would make it impossible to obtain the required number of simulated events for many physics studies. This is why a faster and less refined alternative simulation, referred to as *ATLFAST-II* (AFII) [77] was put in place to reduce the amount of CPU time needed to process an event. This is mainly achieved by using pre-simulated electromagnetic showers of low energy particles instead of developing them from scratch. The *Fullsim* samples generally provide higher precision and are used as the main samples for physics analyses whereas *AFII* samples are used for optimization studies as well as to evaluate theoretical systematic uncertainties.

The final step, referred to as reconstruction, is common to both simulated and real data events. At this stage, physics objects such as tracks and jets are built based on the digitized hit information in the subdetector systems (cf. Section 2.4).

2.4. Physics Objects reconstruction

The ATLAS experiment makes use of several dedicated algorithms developed to identify and reconstruct the properties of the various physics objects present in an event such as electrons, muons, photons and jets. Some of these objects as well as their signatures in the different detector subsystems are illustrated in Figure 2.16.

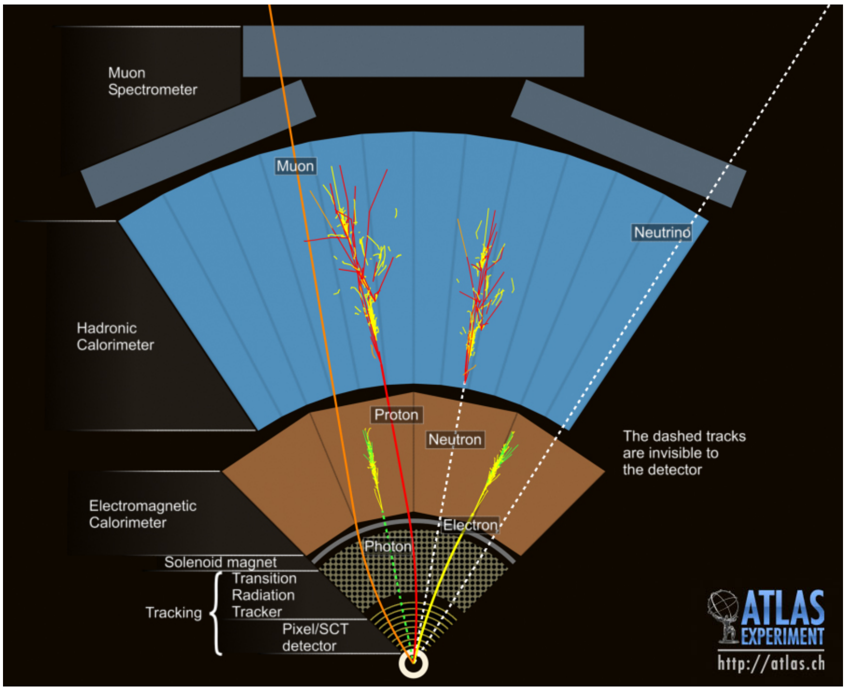

Figure 2.16.: Schematic cut-away of the ATLAS detector. The key features allowing to identify the different particles traversing the detector are highlighted [78]. The solid curves display the tracks of charged particles while the dashed ones correspond to neutral particles. The muon emerging from the interaction region traverses all detector layers and its track is determined by measurements from both the Inner Detector and Muon Spectrometer. The electron and photon are mainly stopped in the Electromagnetic calorimeter and are distinguished from one another by the presence or absence, respectively, of a track matching the corresponding energy deposit in the calorimeter. The proton and neutron are predominantly captured by the hadronic calorimeter with the former additionally leaving a track in the Inner Detector. Lastly, the neutrino goes through the whole detector without leaving any signature.

2.4.1. Tracks and vertices

The tracking [79, 80] and vertexing [81] algorithms both rely on the Inner Detector information (cf. Section 2.2.1). A charged particle traversing the subdetector generates hits in its layers which are combined into a track. The helices produced by tracks in the magnetic field require five parameters to be fully characterized as illustrated in Figure 2.17 in the case of the ATLAS coordinate system:

- **Transverse Impact Parameter d_0** is the signed distance of closest approach of the track to the primary vertex in the transverse plane.
- **Longitudinal Impact Parameter z_0** is the signed distance between the primary vertex and the point of closest approach of the track to it, along the beam axis.

- **Azimuthal angle ϕ** is the angle between the transverse momentum vector $\vec{p_T}$ and the x-axis in the transverse plane.

- **Polar angle θ** is the angle between the momentum vector $\vec{p}$ and the z-axis in the R-z plane.

- **Inverse transverse momentum q/p_T** is the electric charge divided by the track transverse momentum. This ratio is obtained using the track curvature R_{curv} as follows:

$$q/p_T = (0.3BR_{\text{curv}})^{-1} \tag{2.3}$$

  Where B is the magnetic field. B, q, p_T and R_{curv} are measured in units of T, e, GeV and m respectively.

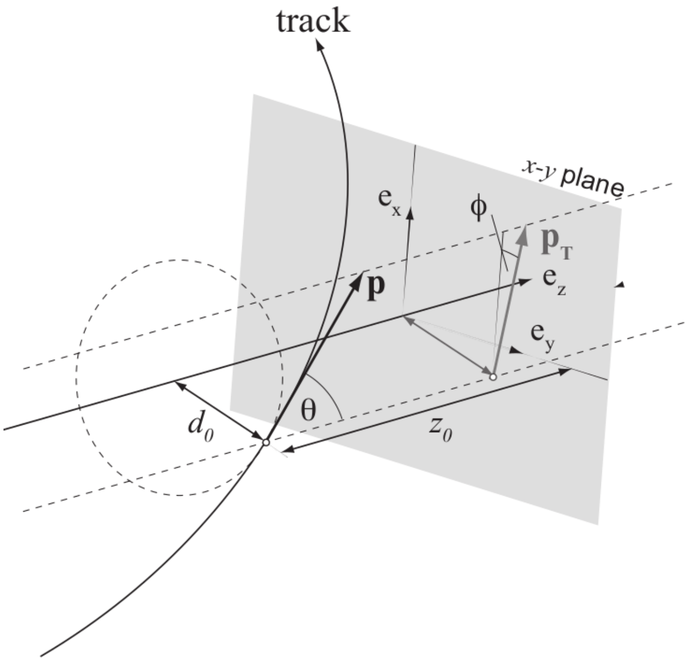

Figure 2.17.: Illustration of the track helix parameters [82].

Track reconstruction is carried out in two stages: track finding, also known as pattern recognition, which consists in combining the right hits to form tracks and track fitting whereby the helix parameters are fitted taking into account the errors on each hit and the passage of the corresponding particle through matter.

The main track finding algorithm used in ATLAS adopts an inside-out strategy where track seeds are first built from space points in the pixel and SCT detectors after which they are extended outwards to include measurements from the TRT. Most of tracks used in physics analyses are found based on this approach. In contrast, the outside-in or back-tracking pattern recognition algorithm takes into account hits that were not chosen by the former algorithm and starts by finding track segments in the TRT and then extrapolates them back to the silicon detectors. The latter strategy is well suited to reconstruct tracks originating from secondary vertices of long-lived particles such as Λ or K_S, photon conversions and material interactions taking place in the ID. A combinatorial Kalman filter [83] is used to build track candidates in the silicon detectors by extrapolating the chosen seeds. At this level multiple track candidates are obtained per seed if more than one compatible track extrapolation exists on the same layer.

To identify the best track candidates and reduce the rate of fake tracks, an ambiguity solving procedure is applied. The latter relies on a score-based ranking scheme for tracks which takes into account several kinematic and hit quality criteria in addition to the use of a dedicated neural network (NN) [84]. For instance, a bonus is given for each hit associated with the track whereas a penalty is imposed if the track contains holes[c]. Moreover, a hit can be associated to several tracks. This is referred to as a shared hit which can occur due to the presence of a fake track or in the case where the detector granularity is not enough to resolve close-by particles. The presence of such hits is also taken into account in the scoring scheme. Track candidates passing the ambiguity solving step undergo a high-resolution fit to enable the measurement of their parameters. The IP resolutions $\sigma(d_0)$ and $\sigma(z_0)$ of the reconstructed tracks are shown in Figure 2.18 for both 2012 and 2015 datasets. For Run 2, a transverse (longitudinal) IP resolution ranging from $\sim$ 150 μm ($\sim$ 220 μm) at low p_T to $\sim$ 20 μm ($\sim$ 80 μm) at high p_T is achieved. The significant improvement observed in Run 2 is primarily due to the installation of the IBL layer characterized by both a smaller radius and pixel pitch size.

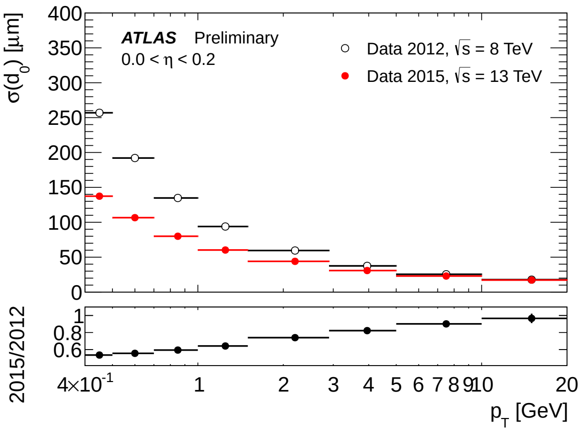

(a)

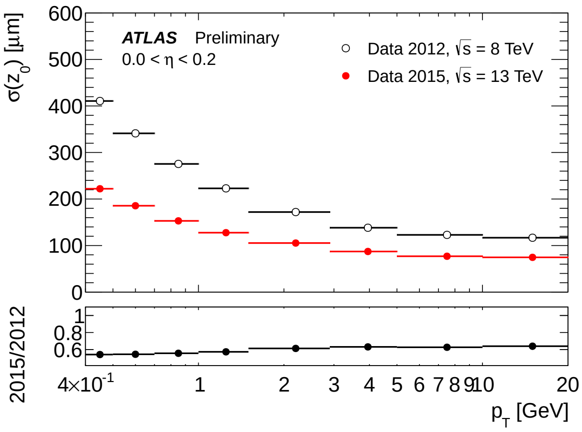

(b)

Figure 2.18.: Measured (a) transverse and (b) longitudinal impact parameter resolutions of tracks as a function of their transverse momentum comparing Run 1 (open black circles) and Run 2 (red full circles) configurations [85]. The gain observed in Run 2 is due to the insertion of the IBL.

Primary vertices (PV) are reconstructed with an adaptive vertex fitting algorithm using as inputs a set of reconstructed tracks passing some quality requirements cuts and the beamspot information. In particular, two steps are involved in this procedure. Firstly, in the vertex finding step, vertex seeds are selected looking for local maxima in the distribution of the z_0 parameter of the selected tracks. At this level, the tracks parameters are determined with respect to the beamspot center. In the second step, referred to as vertex fitting, the optimal vertex position is determined and the corresponding uncertainties are estimated. To do so, the seed position and the tracks around it are fed as input to the χ^2 fitting algorithm. At each fit iteration, tracks that are not likely to originate from the new seed are progressively downgraded and those which are incompatible with the vertex by more than 7 σ are used to seed a new vertex. This is repeated until no unassociated tracks are left or no additional

[c] A hole is defined as the intersection point of the reconstructed track trajectory with an active detector element which does not contain a matching cluster.

vertex is found.

The presence of pile-up in the event increases the number of reconstructed interaction vertices. The vertex corresponding to the hardest process in the event, to be considered as the main primary vertex, is chosen as the one having the highest sum of the squared p_T of its tracks. The remaining primary vertices are assumed to be associated with pile-up interactions. Vertices which are displaced from the beam collision region are considered as secondary vertices.

Once a primary vertex is chosen, the tracks parameters are refitted taken into account its coordinates to enhance their precision.

The vertex reconstruction is 100% efficient for events with at least five reconstructed tracks [86]. Figure 2.19 shows the vertex position resolution as a function of the number of tracks: typically, the vertexing algorithm achieves a resolution of 30 μm in the transverse plane and 50 μm along the z-axis.

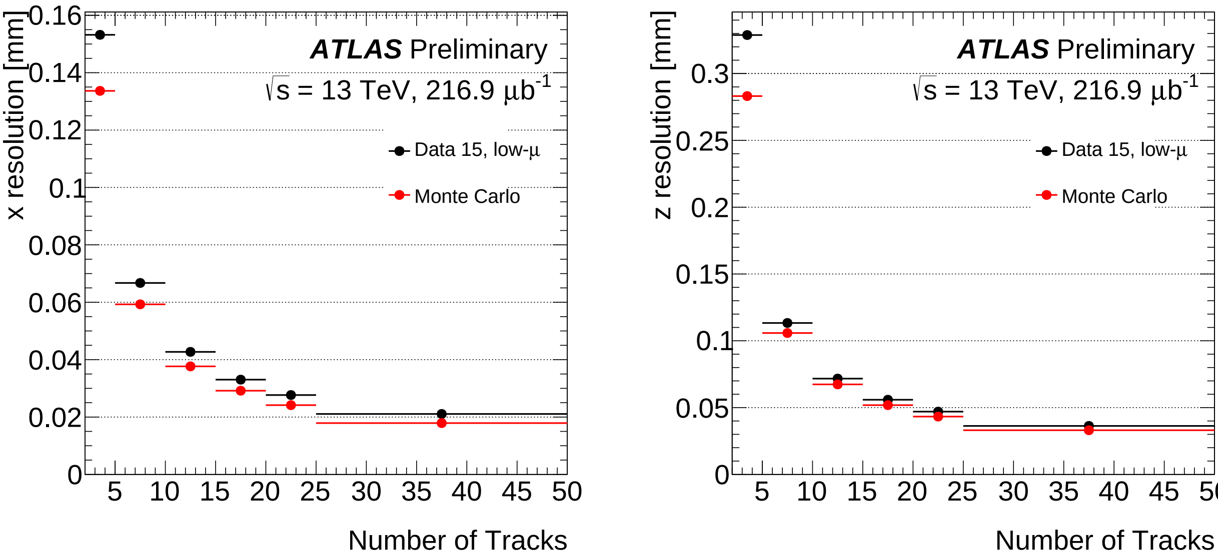

(a) (b)

Figure 2.19.: Primary vertex (a) x- and (b) z-resolution as a function of the number of tracks in a low-μ 2015 dataset [86].

2.4.2. Muons

At first, the muon reconstruction [87] is carried out independently in both the ID (cf. Section 2.4.1) and the MS (cf. Section 2.2.3). The individual subdetector measurements are then combined, in different ways, to obtain the muon tracks which are used in the physics analyses.

The muon reconstruction in the MS begins by forming local track segments in each of the muon chambers where hits are present. These segments are then combined into track candidates requiring at least two matching segments per track except in the barrel-endcap transition region where one segment can be used. A global χ^2 fit of the hits associated with each track candidate is performed and tracks with a χ^2 failing the selection criteria are dropped.

The combined muon reconstruction is performed based on various algorithms which take as input the information provided by the ID, the MS in addition to the calorimeters. Muons are classified into four types depending on which subdetector is involved in the reconstruction:

- **Combined muons**: muon tracks in this category result from the combination of both ID and MS tracks whereby a global refit is performed using the hits measured in both subdetectors. Combined muons have the best quality in terms of fakes rejection and momentum resolution.

- **Segment-tagged muons**: muons populating this category are those not falling in the combined muons category and which result from the association of an ID muon track with one local track segment from the MS. Such muons cross only one layer of the MS chambers, either due to their low p_T or because they fall in regions within the MS with reduced acceptance.

- **Calorimeter-tagged muons**: muons falling in this category are obtained by matching an ID muon track to an energy deposit in the calorimeter compatible with a minimum-ionizing particle. This type of muons recovers acceptance in the $|\eta| < 0.1$ region where the MS has a gap to allow for cabling and services to the calorimeters and the ID.

- **Extrapolated muons**: Muons of this category are reconstructed using only the MS information with a loose requirement on the compatibility with originating from the interaction point. Such muons are used to extend the acceptance for muon reconstruction into the $2.5 < |\eta| < 2.7$ region which is not covered by the ID.

Once muon candidates are reconstructed, an identification procedure is applied in order to suppress the contribution of background candidates originating mainly from pion and kaon decays, while enhancing the selection efficiency of prompt muons as well as guaranteeing a robust momentum measurement. At the time of writing, five levels of identification selections are provided to address the various needs of physics analyses: Medium, Loose, Tight, Low p_T and High p_T. The Medium working point which corresponds to the default selection is used in the analyses presented in this thesis.

Figure 2.20 shows the muon identification efficiency for both Medium and Loose muons categories exhibiting the outstanding performance of the ATLAS detector in terms of muon reconstruction.

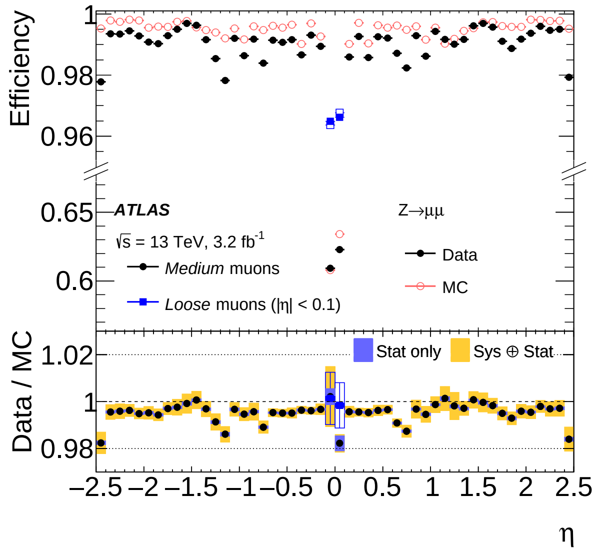

Figure 2.20.: Muon reconstruction efficiency as a function of η measured in $Z \to \mu\mu$ events for muons with $p_T > 10$ GeV shown for both Medium and Loose muon ($|\eta| < 0.1$) selections [87]. The Panel at the bottom shows the ratio of the measured to predicted efficiencies, with statistical and systematic uncertainties.

Furthermore, muons are required to be isolated from other detector activity in order to effectively reject those originating from heavy flavor semileptonic decays which take place inside jets. To this end, nine isolation selections or working points, are provided where each is optimized for specific physics analyses. These criteria rely on a track-based isolation variable depending on the momenta of the muon track as well as surrounding tracks, in addition to a calorimeter-based variable where energy deposits in a cone around the muon track are utilized.

Reconstruction, identification and isolation efficiencies are measured in both data and simulation using the tag-and-probe method on $Z \to \mu\mu$ events for muons with $p_T > 15$ GeV and $J/\Psi \to \mu\mu$ events for muons with $5 < p_T < 15$ GeV . Similarly, muon momentum scale and resolution are studied in these events. This allows to derive correction factors which can be applied to simulation to match the data measurements.

2.4.3. Electrons and photons

The electrons and photons reconstruction algorithms [88] proceed in a similar manner given their analogous signatures in the EM calorimeter (cf. Section 2.2.2).

For the reconstruction of electrons and photons in the central region of the ATLAS detector i.e within $|\eta| < 2.47$ excluding the barrel-endcap transition region ($1.37 < |\eta| < 1.52$), the combination of measurements from both the ID and the EM calorimeter is needed. The first step in this procedure is the seed-cluster reconstruction in the EM calorimeter [89]. The latter is split into a grid of towers of size 0.025×0.025 in the $\eta \times \phi$ space, which corresponds to the granularity of the middle EM calorimeter layer. For each tower, the contributions from all three EM calorimeter layers are summed together to evaluate the total energy within this element. A sliding-window algorithm with a window size of 3×5 towers is then used to search for cluster "seeds" with a total transverse energy above the detector background noise i.e 2.5 GeV . The sliding-window scans the full EM calorimeter acceptance and its position is adjusted so that the total transverse energy contained within, is a local maximum. The clusters are then built around the seeds using a clustering algorithm as described in ref [90].

Following the clusters reconstruction, an attempt to match them to well-reconstructed tracks in the ID is envisaged. These tracks are obtained after modifying the standard ATLAS tracking to account for possible energy loss through Bremsstrahlung which is expected to be larger for electrons. The matching makes use of the η and ϕ separation between the track and the cluster barycenter in the EM calorimeter. In the case where the matching fails, the cluster is tagged as an *unconverted photon*. However, if the matching is possible and the track in question is not compatible with originating from the primary vertex, the cluster is labeled as a *converted photon*[d], otherwise it is tagged as an *electron* candidate. Additional requirements on the tracks parameters are applied in order to reduce the contribution of backgrounds arising from conversions and secondary particles produced in long-lived particle decays as well as pile-up interactions. In the last stage of the reconstruction procedure, the clusters associated with the electron and converted photon candidates are rebuilt using a larger window size of 3×7 (5×5) units in the barrel (endcap) region of the calorimeter. Whereas, the same size of 3×5 is kept for the unconverted photons in the barrel region given their smaller lateral size. The clusters energy is then evaluated after applying a dedicated calibration scheme based on the full detector simulation.

Once electron reconstruction is finalized, identification algorithms are used to reject background-like objects misidentified as prompt electrons such as QCD jets and non-prompt electrons produced in photon conversions that were not flagged in the track-cluster matching step. These algorithms use as input a set of calorimeter-based and track-based discriminating variables such as calorimeter

[d]Photon conversions correspond to processes where a photon splits into a pair of e^+e^- as a result of its interaction with the detector material.

shower shapes, track-cluster association quantities, tracks quality information and variables sensitive to Bremsstrahlung effects. The identification procedure can be performed by imposing either independent requirements on the discriminating variables, referred to as *cut-based identification*, or a single requirement on a likelihood discriminant built based on the probability density functions of these variables for the signal and background hypotheses, known as *likelihood-based (LH) identification*. The latter approach is adopted as baseline for the electron identification in Run 2. Three working points are defined in increasing order of background rejection, based on the distribution of the likelihood discriminant: Loose, Medium and Tight. Figure 2.21 shows the electron identification efficiency as well as the efficiency of background misidentification for the aforementioned working points.

On the other hand, photon identification [91] is achieved using a *cut-based* approach whereby selection criteria are imposed on discriminating variables describing the shape and characteristics of the associated EM showers as well as the energy deposited in the hadronic calorimeter. In particular, two working points are provided: Loose and Tight. These are tuned separately for unconverted and converted photons.

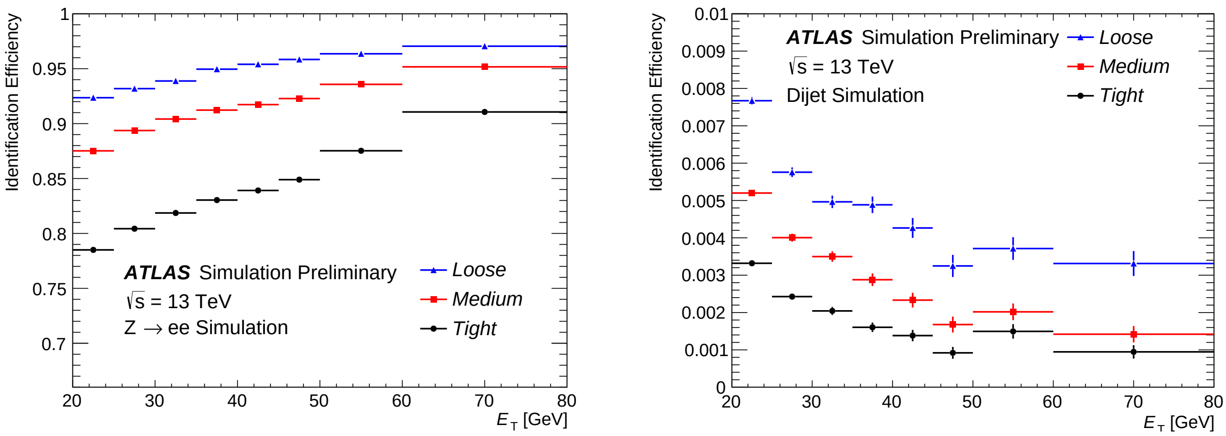

(a) (b)

Figure 2.21.: (a): Prompt electrons identification efficiency obtained based on simulated $Z \rightarrow ee$ events. (b): Fake electrons misidentification efficiency derived from a simulated multijet sample. These efficiencies are measured with respect to reconstructed electrons [89].

To further suppress background from non-prompt electrons produced in subsequent heavy flavor hadron decays or due to light hadrons misidentified as electrons, further isolation criteria as for muons, are applied. These requirements exploit both a track-based and a calorimeter-based variable associated with the tracks transverse momentum and the energy deposited in the calorimeters in a cone around the direction of the electron, respectively.

The electron reconstruction, identification and isolation efficiencies are estimated in both data and simulation using the tag-and-probe method on the $Z \rightarrow e^+e^-$ events for electrons with $E_T > 15$ GeV and $J/\Psi \rightarrow e^+e^-$ events for electrons with $7 < E_T < 20$ GeV . These measurements enable to derive scale factors as a function of η and E_T of the electron which can be applied to simulation in order to reproduce what is measured on data.

2.4.4. Jets

Gluons and quarks produced as final state partons in pp collisions cannot exist as free isolated particles and are not directly observed in the detector, due to the QCD color confinement. Instead, they hadronize creating collimated sprays of color-neutral particles bundled into special objects referred to as *jets*. These are observed in the detector as clusters of energy deposits in the calorimeter system which can be associated with charged particle tracks in the ID.

Jets initiated by b-quarks (b-jets) can be distinguished from other types of jets by exploiting the special characteristics of b-hadrons. The identification of b-jets, or b-tagging, is crucial for many physics analyses among which the ones presented in this thesis. b-tagging is described in detail in Chapter 3.

Jets reconstruction

The reconstruction of jets allows to build physics objects whose kinematics and properties are as close as possible to the initial partons from which they originated.

The first ingredients needed for jets reconstruction are *topoclusters* which are topologically adjacent clusters of calorimeter cells built using a dedicated clustering algorithm [90]. These are obtained via an iterative procedure starting from the cells with the most significant energy deposits which are flagged as seeds and carrying through by attaching the surrounding cells which have a signal-to-noise ratio above the set threshold.

The built clusters are then fed as input to the anti-k_t jet-finding algorithm, described in detail in ref [92]. This algorithm combines sequentially the topoclusters together into final jets, characterized by a radius parameter R representing their approximate size. The anti-k_t algorithm is adopted for the standard ATLAS jet reconstruction. The jets used for the analyses presented in this dissertation, are obtained with the above algorithm with $R = 0.4$.

Jets calibration

Reconstructed jets need to be calibrated in order to match the predictions of *truth-jets*. These correspond to jets which are not reconstructed from topoclusters found in the calorimeter, commonly referred to as *reco-jets*, but rather from stable particles generated in MC samples. The full chain of the jet calibration procedure adopted in Run 2 is illustrated in Figure 2.22.

The energy scale of the electromagnetic showers is used for the initial calibration of the calorimeter clusters. Once the jet four-momentum is reconstructed from the combined clusters, several corrections are applied accounting for different effects.

As a first step, the origin correction alters the jet direction so that it points to the hard-scatter PV instead of the detector center, without affecting the measured energy of the jet. This correction enhances the η resolution of jets.

Secondly, the pile-up correction adjusts the jet energy taking into account the in-time and out-of-time pile-up contributions. This is carried out in two stages: the area-based correction followed by the residual pile-up correction. The former method evaluates the pile-up contribution per event based on the median p_T density of jets in the η-ϕ plane and subtracts it from the p_T of each jet depending on its area. This calculation is performed in the central, lower occupancy region of the calorimeter and thus it does not effectively describe the pile-up in the forward region or in the high-occupancy core of high-p_T jets. This results in a jet p_T dependence on the pile-up after applying this correction. This is why, a complementary MC-based residual correction as a function of the number of PV and the number of interactions per bunch-crossing μ is subsequently applied.

After subtracting the pile-up contribution, MC samples without pile-up are used to derive the absolute jet energy scale (JES) calibration which allows to correct the jet four-momentum to the particle-level energy scale of truth-jets.

At the global sequential calibration step, the remaining differences in the distribution of energy within jets are addressed. The particle content and shower shape of a jet depends on the type of particle that initiated it. For instance, jets originating from quarks typically contain hadrons carrying a large fraction of the jet p_T which enables them to go further through the calorimeter and thus enhance the longitudinal profile of the jets. However, gluon-initiated jets usually consist of softer particles in p_T and consequently feature a wider transverse component. To account for these effects, a sequence of jet four-momentum corrections is derived. In particular, these corrections are applied to five jet observables (tracker-, calorimter- and MS-related variables) so that they match those of the corresponding truth-jets while preserving the overall energy scale.

Lastly, in-situ techniques are used to correct for the remaining differences between data and simulation. This calibration is applied to data and is based on comparing the p_T of a jet with well-measured physics objects such as photons and Z-bosons.

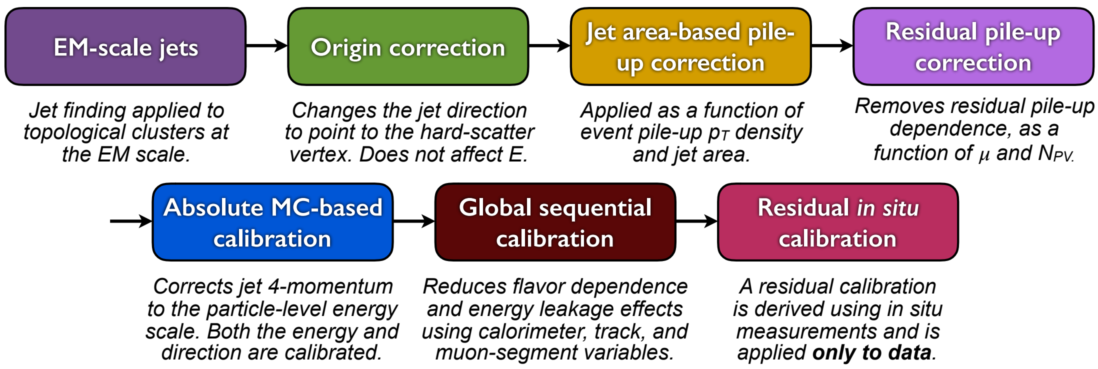

Figure 2.22.: Jet calibration chain [93].

Pile-up jets

The suppression of jets originating from pile-up interactions [94] is a key component for many physics analyses in order to properly measure the targeted hard scatter process.

The rejection of pile-up jets in Run 1 was performed by imposing a lower limit on the *jet vertex fraction* (JVF), defined as the fraction of the total momentum of tracks in the jet which is associated with the hard-scatter primary vertex.

However, in order to cope with the luminosity increase in Run 2, a more sophisticated technique was developed to identify jets from pile-up using the *jet-vertex-tagger* (JVT) discriminant. The latter is constructed from a likelihood function of two variables: a modified version of the JVF and the ratio of the sum of the p_T of tracks within the jet which originate from the hard-scatter PV to the fully calibrated jet p_T. The distribution of the JVT output for both jets originating from the hard-scatter interaction and pile-up is shown in Figure 2.23, demonstrating the separation power of this discriminant.

Pile-up jets are suppressed by applying a JVT>0.59 requirement for which a 92% selection efficiency for hard-scatter jets is achieved. This requirement is only applied to jets with a p_T below 60 GeV and with $|\eta| < 2.4$ given that the contribution of pile-up jets is negligible at high p_T. The efficiency and corresponding scale factors of the JVT cut on data and MC are derived using $Z \to \mu^{+}\mu^{-}$ events containing additional hard-scatter jets.

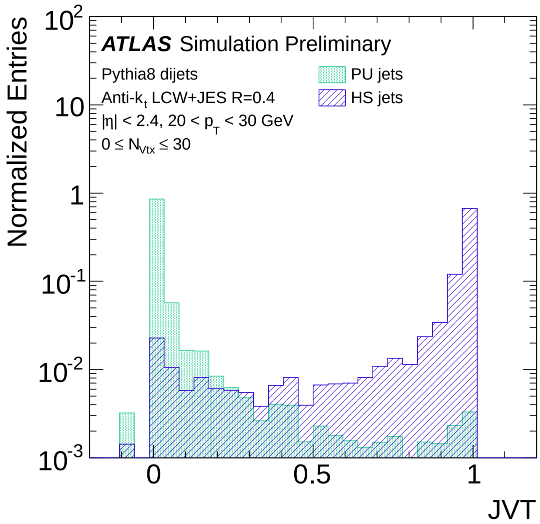

Figure 2.23.: JVT score distribution for hard-scatter (blue dashed histogram) and pile-up (green histogram) jets with $20 < p_T < 30$ GeV and $|\eta| < 2.4$ in simulated dijet events [94]. Jets with no tracks associated to them get a value of -0.1.

2.4.5. Taus

τ leptons decay leptonically in 35% of the time and hadronically in the rest of the cases with accompanying neutrinos in both decay modes. Given their short lifetime, it is very hard to distinguish between τ leptons decaying into electrons or muons and the prompt electrons and muons. Hence, only hadronically decaying τ candidates are reconstructed as described in ref [95].

2.4.6. Missing Transverse Energy

The presence of particles escaping detection, in the final state, can be inferred from an imbalance in the measured momentum of the detected particles, referred to as *missing energy*. The measurement of this quantity is of great importance for processes involving decays to neutrinos as well as for beyond the SM phenomena searches where additional weakly-interacting particles are predicted. It is practically impossible to measure the full missing energy since the initial partons momenta are inaccessible. These however can be assumed to be negligible in the transverse plane given that pp collisions occur along the z-axis. Thus, imposing momentum conservation gives access to the Missing Transverse Energy denoted by MET or E_T^{miss}.

The reconstruction of MET [96] is based on the energy deposits in the calorimeters, the tracks reconstructed by the Inner Detector and Muon Spectrometer. It is derived from the negative vector sum of the transverse momenta of all reconstructed and calibrated physics objects: electrons, photons, hadronically decaying τ-leptons, jets and muons. An additional term is considered to account for soft energy contributions that are not associated with any of these objects and which mostly result from underlying events and soft radiation. The x and y components of the E_T^{miss} are defined as follows:

$$E_{x(y)}^{\text{miss}} = E_{x(y)}^{\text{miss,e}} + E_{x(y)}^{\text{miss},\gamma} + E_{x(y)}^{\text{miss},\tau} + E_{x(y)}^{\text{miss,jets}} + E_{x(y)}^{\text{miss},\mu} + E_{x(y)}^{\text{miss,SoftTerm}} \tag{2.4}$$

The magnitude of E_T^{miss} is then given by:

$$E_T^{\text{miss}} = \sqrt{(E_x^{\text{miss}})^2 + (E_y^{\text{miss}})^2} \tag{2.5}$$

The soft term $E_{x(y)}^{\text{miss,SoftTerm}}$ is calculated using the momenta of tracks from the ID matching the hard scatter primary vertex and which are not associated to the reconstructed objects. This method is more robust against pile-up interaction contamination compared to the calorimeter-based approach adopted in Run 1 whereby energy deposits in the calorimeters not associated with the hard objects were used [97].

The MET measurement resolution attained in Run 2 in $Z \to \mu\mu$ events is illustrated in Figure 2.24 as a function of the number of primary vertices. This channel is particularly suited for this measurement as no genuine MET is expected in addition to the small background contamination and the possibility to precisely measure the Z boson kinematics.

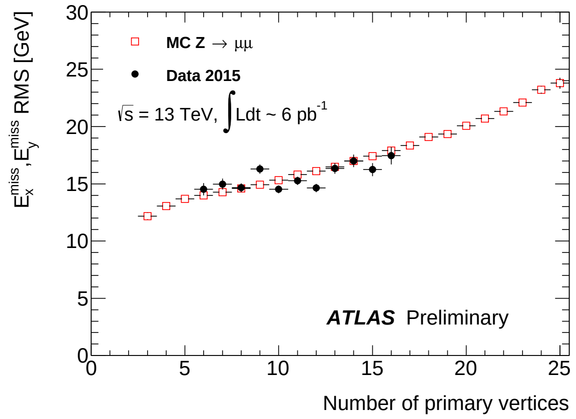

Figure 2.24.: E_x^{miss} and E_y^{miss} resolution as a function of the number of primary vertices in $Z \to \mu\mu$ selected events [96] . The Run 2 data (black circles) is compared to the MC simulation (red squares).

2.5. High-Luminosity LHC upgrade

The scientific program of the LHC stretches over the next 20 years encompassing an ambitious series of upgrades, culminating in the High-Luminosity LHC (HL-LHC) phase. The latter consists in increasing the LHC instantaneous luminosity to achieve a factor of 5-to-7 beyond its nominal design value, which will ultimately result in an accumulated integrated luminosity for proton-proton collisions of around 4 ab^{-1}. This will allow experiments to enlarge their datasets by one order of magnitude compared to what would be collected by the end of 2023 with the LHC baseline program.

The full exploitation of the large dataset to be collected during the HL-LHC phase, will enhance greatly the experimental precision of the SM measurements, namely in the Higgs sector, which is crucial as deviations of the Higgs boson properties from the SM expectations would indirectly hint at the existence of new physics. Furthermore, the HL-LHC will allow to probe the rarest phenomena that are beyond the reach of the current analyses. For instance, it will provide access for the first

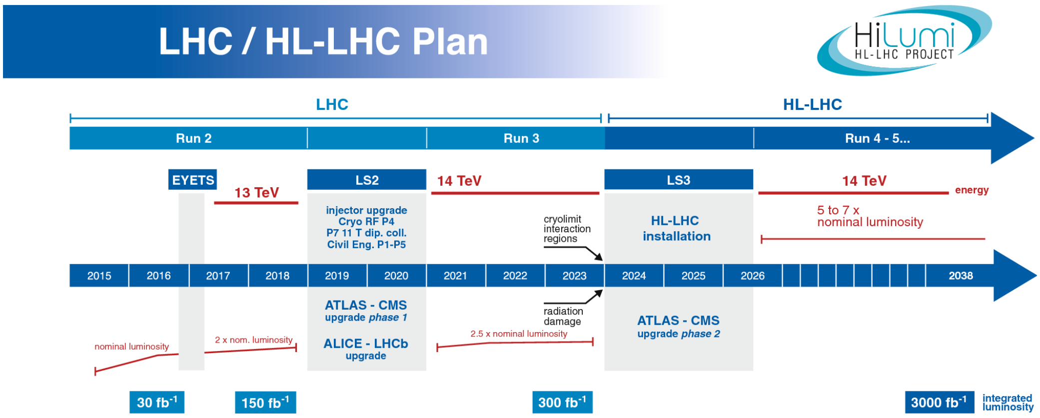

Figure 2.25.: Current timeline of the LHC program including the HL-LHC upgrade phase.

time to the Higgs boson couplings to the second generation fermions through studies of the rare H$\rightarrow \mu\mu$ decay mode. Moreover, evidence for the production of a pair of Higgs bosons may be attained enabling to probe the strength of the Higgs self-interaction and thus provide constraints on the Higgs mechanism (See section 1.3). In parallel, direct searches for new physics will carry on at the HL-LHC investigating several scenarios such as Supersymmetry and extra dimensions theories, and will benefit from an increased discovery potential and an enhanced sensitivity. The breadth of the measurements and searches foreseen at the HL-LHC phase consolidates the physics case for this upgrade leading to its adoption as the highest priority project by the high energy physics community worldwide.

The HL-LHC upgrade [98] is a challenging project relying on a number of key innovative technologies which involve namely cutting-edge 11-12 T superconducting magnets, compact superconducting crab cavities and new technology for beam squeezing. The installation of the necessary accelerator components as well as the first commissioning of the new machine configuration will take place during the so-called Long Shutdown 3 (LS3) in 2024-2026 as depicted in Figure 2.25 which illustrates the timeline for the LHC program followed by the HL-LHC phase.

The upgrade of the collider is complemented by upgrades of the experiments to enable the detectors to take full advantage of the physics potential granted by the HL-LHC. As a result of the higher luminosity at the HL-LHC phase and more specifically the higher number of protons per bunch, the ATLAS experiment will have to cope with 140 pile-up interactions on average with the possibility of extending up to 200 in the extreme scenario. To operate under this harsh environment, the ATLAS experiment will replace entirely its Inner Detector by a highly granular and more radiation-hard silicon tracker; this upgrade is described in more details in section 3.2. Moreover, a High-Granularity Timing Detector[99] covering the pseudo-rapidity region between 2.4 and 4 will be installed to help mitigate the effects of the pile-up using timing information to distinguish between collisions taking place very close in space but well separated in time. Additionally, major upgrades are also planned for the calorimeters and muon spectrometer readout electronics in line with the trigger and data acquisition system upgrade targeting a faster and more efficient online selection of the collision events.

3. b-tagging studies for the Inner Tracker phase II upgrade

The identification of b-flavored jets, stemming from the hadronization of b-quarks, is a cornerstone for many physics analyses, not only at the LHC but also at the foreseen HL-LHC. Such analyses cover the top-quark physics sector, the measurement of the Higgs boson couplings to heavy quarks, the Higgs boson self-coupling and searches for new physics where new heavy particles decay to heavy quarks. This is why, several algorithms for identifying b-jets, a procedure also known as b-tagging, were developed within ATLAS. These algorithms are briefly described in Section 3.1. Their performance rely heavily on the tracking information provided by the ATLAS Inner Detector (ID). However, this detector will be entirely replaced by the Inner Tracker (ITk), described in Section 3.2, to operate under the harsh pile-up conditions ($\langle\mu\rangle = 200$) of the HL-LHC phase. The ITk b-tagging performance is a key benchmark to design the detector. To this end, the b-tagging algorithms need to be reoptimized, in order to fully exploit the tracking ability of the ITk: indeed, suboptimal algorithms could mask the relative strengths of the various options considered for the layout. Section 3.3 reviews my studies targeting the optimization of these algorithms in the context of the ITk upgrade. Moreover, as part of the ITk layout characterization, it is necessary to assess the impact of various operating conditions on the detector performance namely in terms of b-tagging. In this regard, I gauged the robustness of the optimized algorithms response against multiple HL-LHC pile-up configurations and ITk dead pixel modules scenarios as presented in Section 3.4.

3.1. b-jet identification in ATLAS

The intrinsic properties of the b-hadrons, described in Section 3.1.1, are the essential ingredients based on which the b-tagging algorithms (called taggers in the following) are built. A brief overview of the main taggers exploited in ATLAS is given in Section 3.1.2. A special emphasis is put on the algorithms that were used for the optimization of b-tagging in the context of the ITk upgrade for HL-LHC.

3.1.1. b-hadrons properties

The most distinctive b-hadrons property, which is at the foundation of b-jet identification, is their relatively long lifetime ($\tau \sim 1.5$ ps). For instance, a b-hadron with a transverse momentum of $p_T = 50$ GeV and a mass around 5 GeV , will have a significant flight path length in the transverse direction $L_{xy} = \beta\gamma c\tau$[a], allowing it to travel a measurable distance of the order of 4 mm, before decaying. This results in two signatures which are directly exploitable by the b-tagging algorithms. Firstly, the b-hadron decay gives rise to at least one *secondary vertex* displaced w.r.t the primary vertex where the hard-scatter collision occurred. Secondly, the charged decay products of the b-hadron emerging from the displaced vertex, will be reconstructed as tracks having *large impact parameters*[b]. These signatures can be discerned by the ATLAS detector. Figure 3.1 illustrates the aforementioned properties.

Another property which is advantageous for b-tagging algorithms is the relatively high mass of b-hadrons ($\sim$ 5 GeV) compared to c- and light-hadrons. Consequently, b-hadrons decay producing a large number of charged particles leading to high track multiplicity within b-jets compared to c- and light-jets.

[a] β corresponds to the reduced velocity with respect to the speed of light in vacuum i.e $\frac{v}{c}$ and γ is the Lorentz factor given by $\frac{1}{\sqrt{1-\beta^2}}$

[b] Impact parameters measure the distance from the point of closest approach of a track to the primary vertex (cf. Section 3.1.2.1)

Additionally, a b-hadron can decay into leptons resulting in electrons or muons within the associated jet. This decay mode takes place either directly or through a subsequent c-hadron decay; the cumulated branching fraction is $\sim 20\%$ for each lepton flavor (electron or muon). Algorithms exploiting this semileptonic decay signatures inside jets are developed (e.g the Soft Muon Tagger) but will not be discussed in the scope of this thesis.

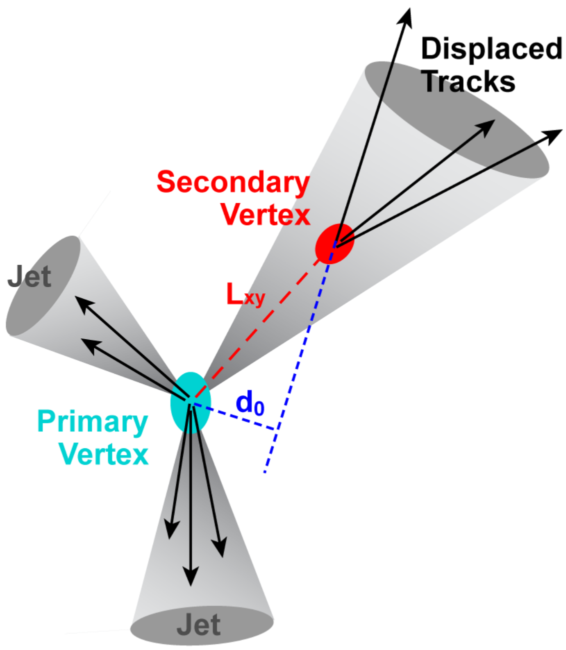

Figure 3.1.: A sketch illustrating the distinctive properties of a b-jet namely the presence of a secondary vertex inside the jet and the large impact parameters (d_0) of the tracks originating from the displaced vertex.

3.1.2. Main b-tagging algorithms

In order to label jets as being b, c-, τ- or light-flavor jets in the simulation, the jets are matched to b and c-hadrons as well as τ leptons within a cone of radius $\Delta R = 0.3$ around their axis. The transverse momenta of the matched particles are required to be larger than 5 GeV . The labeling procedure is performed by first searching for b-hadrons within the cone centered on the axis of the jet. If no b-hadron is found, the algorithm is repeated for c-hadrons, and for τ leptons. Ultimately the remaining jets which do not fall in the previous categories are considered as light-flavor jets. For simulation, this labeling method is used to define the genuine flavor of the jets, while in real data complex calibration analyses are performed in order to define samples enriched in jets of the required flavor.

The figure of merit for b-tagging performance relies on the following key quantities. The first one is the efficiency with which a b-jet is identified by a b-tagging algorithm. This is known as the *b-jet tagging efficiency*. The other necessary pieces of information are the probability of mistakenly tagging a c-,τ- and light-flavor jet as a b-jet and are referred to as the *c-jet tagging efficiency*, the *τ-jet tagging efficiency* and the *mistag rate*, respectively. These can also be expressed in terms of rejection factors defined as the inverse of the efficiencies. All these quantities are evaluated after applying a specific cut on the b-tagging discriminant distribution; this cut is commonly referred to as the *working point*. Jets containing τ leptons are not considered in the scope of this document.

The final discriminants that the physics analyses use in ATLAS to distinguish b-jets from c- and light-jets, are built in two steps. Firstly, low-level discriminants are developed exploiting directly different properties of the b-hadrons as presented in Sections 3.1.2.1 and 3.1.2.2. The outputs of these taggers are then combined to increase the separation among the different jet flavors as explained in Section 3.1.2.3.

3.1.2.1. Impact-parameter based algorithms

The Impact Parameter (IP) based algorithms exploit the *large impact parameters* signature of the tracks associated with the b-hadron decay products. The excellent spatial resolution of the tracks reconstructed by the ATLAS ID allows to distinguish these tracks from those stemming from the primary vertex. IP3D and IP2D are two tagging algorithms that take advantage of this property. In particular, the IP3D tagger is more widely used by ATLAS for the HL-LHC b-tagging upgrade studies (cf. Section 3.3.2).

The transverse impact parameter, d_0, is the distance of closest approach of the track to the primary vertex point, in the r-φ projection; it is schematically shown in Figure 3.1. z_0, is the difference between the z coordinates of the primary vertex and of the track at this point of closest approach; the longitudinal impact parameter is defined as $z_0 \sin\theta$. Since the b-hadron decay vertex must lie along its flight path, d_0 and z_0 are signed to further discriminate the tracks associated with the b-hadron products from those originating from the primary vertex. The sign is positive if the track intersects with the jet axis in front of the primary vertex with respect to the jet direction, and negative if the intersection takes place behind it (i.e opposite to the jet direction) as shown in Figure 3.2. The experimental resolution engenders a random sign for tracks incoming from the primary vertex, while the tracks associated with b- and c-hadron decays are more likely to have a positive sign as illustrated in Figure 3.3.

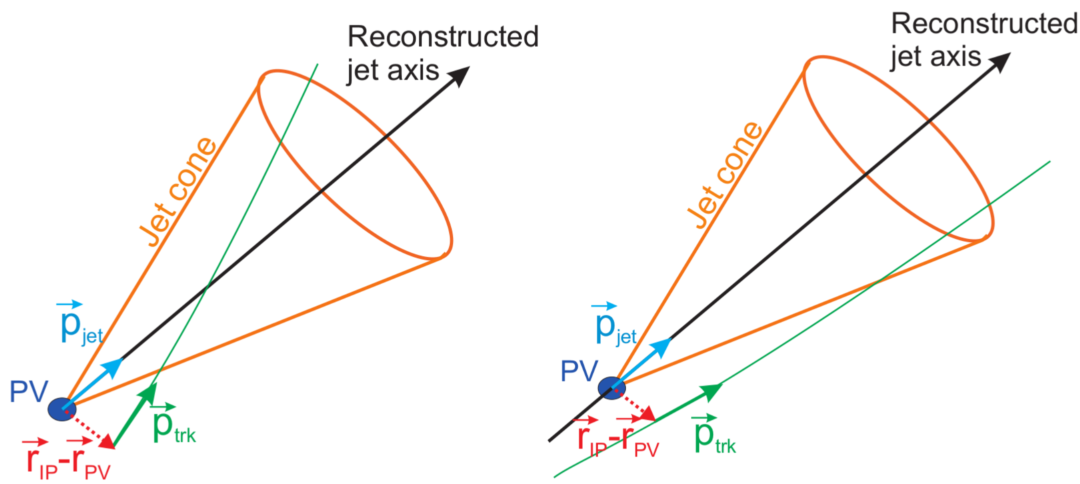

Figure 3.2.: Impact parameters sign definition: if a track (or its extrapolation) intersects with the jet axis (left) in front of the PV, the sign is positive whereas (right) if the intersection occurs behind the PV, the sign is negative [100].

IP3D is based on a log-likelihood ratio (LLR) method whereby for each track the measurement of the transverse and longitudinal significances $S \equiv (d_0/\sigma_{d_0}, z_0/\sigma_{z_0})$ is compared to pre-determined two-dimensional probability density functions (PDFs) obtained from simulation for both the b- and light flavor jet hypotheses; σ_{d_0} and σ_{z_0} are the uncertainties on the reconstructed d_0 and z_0 respectively.

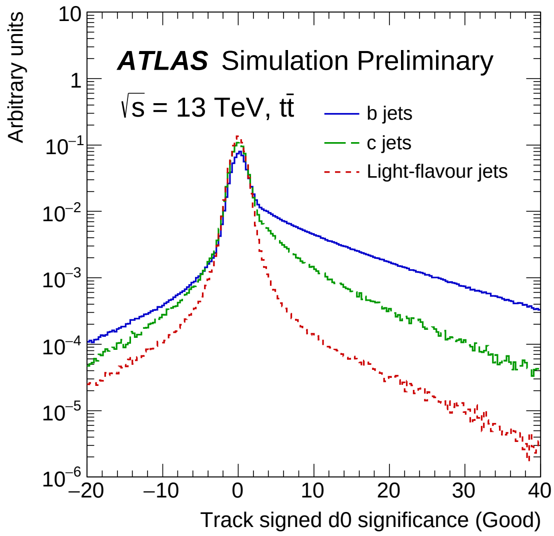

Figure 3.3.: The transverse signed impact parameter significance (see text) of good quality tracks in $t\bar{t}$ events for b-jets (blue), c-jets (green) and light-jets (red) [101].

These errors are introduced to have a larger contribution to the likelihood from high quality tracks. The track weight is defined as $w_{\text{track}} = \frac{p_b}{p_u}$ where p_b and p_u are the probability densities for the track originating from a b-jet and a light-jet, respectively. The jet weight is the sum of the logarithms of the individual track weights associated with the jet i.e $w_{\text{jet}} = \sum_{\text{tracks}} \log w_{\text{track}}$. Figure 3.4 shows the IP3D LLR distribution for the different jet flavors evaluated on a $t\bar{t}$ sample and corresponding to the LHC Run 2 conditions. IP2D is very similar to IP3D but uses only information in the r-φ projection which makes it significantly less powerful however more robust against pile-up.

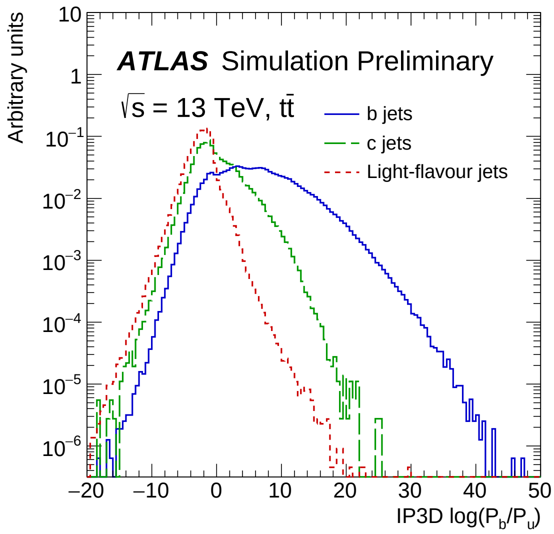

Figure 3.4.: The log-likelihood ratio distribution for IP3D for b-jets (blue), c-jets (green) and light-jets (red) evaluated in $t\bar{t}$ events [101].

3.1.2.2. Secondary vertex-based algorithms

This class of taggers is built upon algorithms targeting the reconstruction of the b-hadron decay vertex inside a jet. One such algorithm is the Single Secondary Vertex Finder (SSVF) [102] which aims to reconstruct an inclusive secondary vertex taking into account the subsequent decay of the c-hadron in the jet. The properties of this secondary vertex are then used as inputs to a likelihood ratio formalism similar to the one used for the IP3D tagger, known as the SV1 algorithm.

SV1 exploits three properties of the reconstructed secondary vertex: the vertex mass (*i.e.* the invariant mass of all charged-particle tracks used to reconstruct the vertex, assuming that all tracks are pions), the ratio of the sum of the energies of these tracks to the sum of the energies of all tracks in the jet (charged energy fraction), and the number of two-track vertices (N2T) which are formed by searching for two-track pairs that yield a good vertex among the tracks present in the jet. In addition, the angular distance ΔR between the jet axis and the direction of the line joining the primary and secondary vertices is used in the LLR. SV1 relies on a two-dimensional distribution of the first two variables and on two one-dimensional distributions of the latter variables. Figure 3.5 illustrates some of the properties of secondary vertices reconstructed by the SSVF algorithm. SV1 typically provides better performance in terms of mistag rate since it is relatively unlikely to vertex random tracks of different origins. However, the algorithm exhibits a limited secondary vertex finding efficiency e.g of the order of 75-85% in real b-jets for the $t\bar{t}$ sample used for the ITk b-tagging upgrade studies (cf. Section 3.3.1).

JetFitter [103] is another vertexing algorithm which tries to reconstruct the full decay chain of the b-hadron, exploiting the weak b- and c-hadrons decay topologies inside the jet. The properties of the resulting vertices are then combined through an artificial neural network to obtain the b-tagging discriminant.

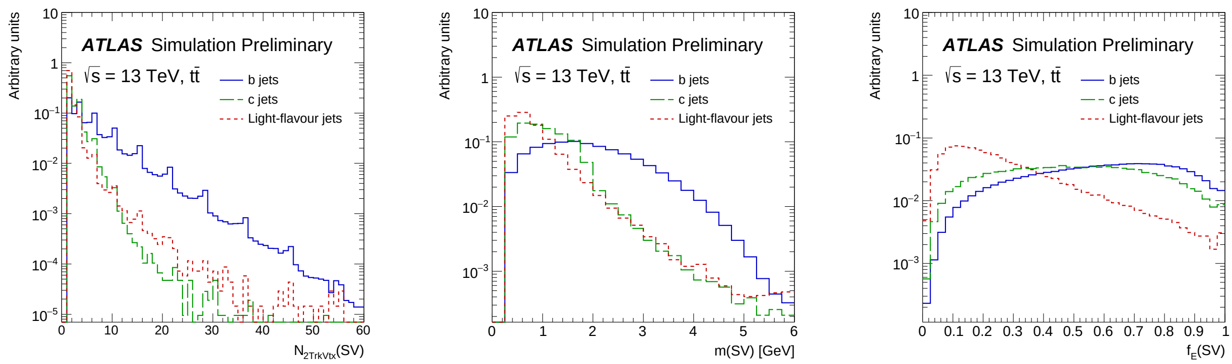

(a) (b) (c)

Figure 3.5.: A selection of the properties associated with the secondary vertices reconstructed by the SSVF algorithm for b-jets (blue), c-jets (green) and light-flavor jets (red) in simulated $t\bar{t}$ events: (a) The number of two-track vertices reconstructed within the jet, (b) invariant mass and (c) the energy fraction defined as the ratio of the energy of tracks associated with the SV relative to the energy of all tracks reconstructed within the jet [101]. The $t\bar{t}$ sample used corresponds to the LHC Run 2 conditions.

3.1.2.3. Combined tagging algorithms

The secondary vertex-based algorithms exhibit lower mistag rates than the impact parameter-based ones, but their efficiency for tagging b-jets is limited by the secondary vertex finding efficiency. Both approaches are therefore combined, in multiple ways, to define versatile and powerful b-tagging discriminants maximizing the separation between b-jets and other jet flavors.

The LLR-based IP3D and SV1 algorithms, for instance, can be combined in a straightforward manner by summing their respective weights: this is the so-called IP3D+SV1 algorithm.

The properties of the reconstructed SV and the IPxD (IP2D and IP3D) LLRs can also be combined using MultiVariate Analysis (MVA) techniques to provide the final b-tagging discriminant. During Run 1 of the LHC, the three intermediate MVA taggers: IP3D and SV1 LLRs as well as JetFitterCombNN [c] [104] output were combined in a neural network yielding the MV1 discriminant as output; this tagger was the official algorithm supported for all the analyses of Run 1.

During Run 2, the secondary vertex properties reconstructed by both SSVF and JetFitter algorithms, are directly combined with the IPxD LLRs in a Boosted Decision Tree (BDT) producing the MV2 discriminant. Three variations of the MV2 tagger are available MV2c00, MV2c10, MV2c20 based on the fraction of c-jets included in the training sample (respectively 0%, 7% and 15% and the rest are light-jets for the background definition, the signal being b-jets). As of 2016, the MV2c10 variant was chosen by ATLAS as the standard b-tagging discriminant for the physics analyses as documented in [101]. Figure 3.6 shows the MV2c10 BDT distribution for the three jet flavors evaluated on simulated $t\bar{t}$ events.

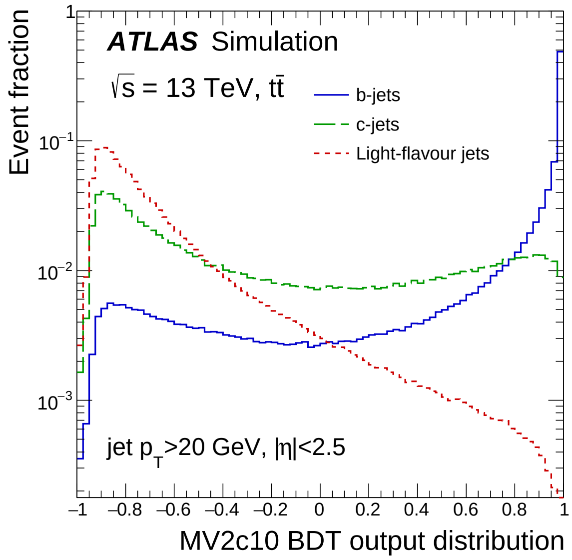

Figure 3.6.: The MV2c10 BDT distribution for b-jets(blue), c-jets (green) and light-jets (red) evaluated in simulated $t\bar{t}$ events [101].

[c] JetFitterCombNN -also known as IP3D+JetFitter- is defined in the same way as the JetFitter algorithm, the main difference being the use of the IP3D LLR as an additional input node in the corresponding neural network.

3.2. ATLAS Inner Tracker upgrade

The identification of b-jets in the ATLAS experiment relies heavily on the tracking information provided by the ID. However, this tracker will be completely replaced by the ATLAS collaboration in preparation for the HL-LHC era (cf. Section 2.5). In the following, the phase II ATLAS tracker upgrade is presented along with its motivation and the various layouts considered at the time of writing.

3.2.1. Motivation for the tracker upgrade

The current ATLAS ID (cf. Section 2.2.1) was designed for 10 years of operation under the nominal LHC running conditions. Therefore, it will not be able to cope with the extreme conditions of the HL-LHC phase (cf. Section 2.5) featuring very high pile-up (up to 200 collisions per bunch-crossing) which results in large radiation doses, occupancies and data transmission rates. This is why, the ATLAS collaboration decided to replace entirely the ID with a new all-silicon Inner Tracker (ITk) to maintain and possibly improve the tracking performance despite the harsher environment. The necessary detector upgrades (Phase II) to operate under HL-LHC will take place during the Long Shutdown 3, starting in 2024.

The phase II physics program requirements are used as input to inform the ITk design. The latter combines central tracking precision in presence of 200 pile-up events with the ability to extend the tracking coverage to a pseudo-rapidity η of ± 4 [d] with excellent tracking efficiency and performance. The main motivation for the extended pseudo-rapidity coverage stems from the need to use tracking information in order to reject forward pile-up jets whose tracks mostly originate from pile-up vertices rather than the hard-scatter vertex. This is crucial, for instance, for the measurements of vector boson fusion (VBF) production of the Higgs boson which is based on the selection of forward jets populating $|\eta| > 2.5$. This process is one of many used as benchmarks to develop the ITk design.

3.2.2. The ITk layout

The ITk is an all-silicon tracker comprising two subsystems: an inner Pixel and outer Strip detectors [105, 106]. Similarly to the ID, each subdetector consists of a barrel region with multiple concentric layers around the beam direction and an endcap part composed of disks (for the strip detector) or rings (for the Pixel detector) placed perpendicularly to the beamline. The layout of the ITk is displayed in Figure 3.7. The ITk is surrounded by the same 2T solenoid magnet as for the current ID for the momentum measurements.

3.2.2.1. The ITk Strip detector

The Strip detector consists of a four-layer barrel section and two six-disks endcaps on each side (cf. Figure 3.7(b)). It covers up to $|\eta| = 2.7$ in pseudo-rapidity. Each strip barrel layer is 2.8 m long extending from -1.4 m to +1.4 m along the z-axis. The radii at which the barrel layers are placed and the z-positions of the end-cap disks are chosen to optimize the number of hits on a track and the p_T resolution. The two inner (outer) barrel layers are instrumented with strip sensors 300-320 μm thick and 24.1 mm (48.2 mm) long whereas the endcaps are equipped with strips whose length varies between 19 and 60.1 mm depending on the radius. Each barrel layer (endcap disk) consists of pairs of detectors mounted back-to-back and with a stereo angle of ± 26 mrad (± 20 mrad) with respect to the beam (radial) direction yielding a total stereo angle of 52 mrad (40 mrad). The implementation of the stereo angles allows to provide 2D hit position measurements.

[d] was ± 2.5 for the Inner Detector

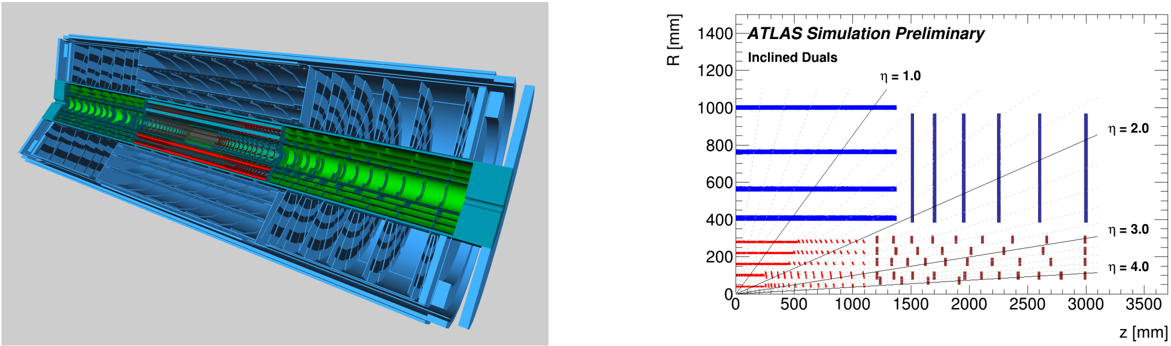

(a) (b)

Figure 3.7.: (a): Display of the Inner Tracker layout for the HL-LHC phase of ATLAS and (b): schematic layout of ITk with strip (blue) and pixel (red) detectors showing only one quadrant and only active detector elements; the horizontal axis is along the beam line with zero being the interaction point and the vertical axis is the radius measured from the interaction region [105].

3.2.2.2. The ITk Pixel detector

The Pixel detector is composed of five barrel layers and five endcap ring layers where the number of rings depends on the pseudo-rapidity (cf. Figure 3.7(b)). It provides hermetic tracking coverage up to $|\eta| = 4$. The pixel layout makes use of two novel design concepts compared to a classical pixel design. The first one consists of prolonging a conventional flat barrel section, where the sensors are mounted horizontally, with a section equipped with inclined modules tilted at an oblique angle ($\sim 56\,°$) with respect to horizontal. This allows to minimize the material induced performance deterioration in the barrel/endcap transition region. Additionally, this option enables to reduce the amount of silicon needed as the inclined modules have a larger angular coverage in this region. However, the conventional flat barrel design referred to as the "*Extended layout*" was also studied in parallel and was found to underperform compared to the "*Inclined layout*" [106]. The second novel concept utilized in the ITk pixel layout is the endcap ring system where the layers of pixel rings extending the coverage in z allow for routing services separately along each ring layer. The Pixel system is designed so that the combined Pixel and Strip detectors supply a minimum of 13 hits per track in the central region.

The baseline pitch size for the pixel sensors is 50×50 μm^2, however having some layers with a pixel pitch of 25×100 μm^2 is still being discussed at the time of writing. Given the harsh radiation environment foreseen for HL-LHC, the two innermost barrel layers and the innermost ring are replaceable, while the remaining outer layers and rings are designed to operate for the entire lifetime of the ITk.

While the Strip system remained unchanged since the design described in the Strip TDR [106], the pixel detector layout underwent several developments within the time frame of the studies presented in Section 3.3. These developments aim to further improve the detector performance, reduce costs and incorporate engineering constraints. In particular, two Pixel ITk layouts are featured in this document. The layout reported in the Strip TDR, referred to as Step 1.6 and previously known as *Inclined layout*, was used to design the new track categories for b-tagging as explained in Section 3.3.2. Later on, the b-tagging performance results were updated considering the most recent geometry layout available at the time, referred to as Step 2.2 and also known as *Inclined Duals*. These two Pixel layouts are depicted in Figure 3.8. The structural differences between them are detailed in the Pixel TDR [105]. Some of these modifications include:

- Changing the required minimal number of hits from 13 to 9 for $|\eta| > 2.7$ without affecting significantly the detector performance.
- Reducing the number of modules in the barrel layers as well as the endcap rings.
- Improving the hermiticity in the flat/inclined barrel transition region.
- Changing the modules inclination angle to 75 °in barrel layers 0 and 1.

Further changes to the detailed design of the Pixel detector are still expected. At the time of writing, the Pixel layout referred to as *Step3* became available.

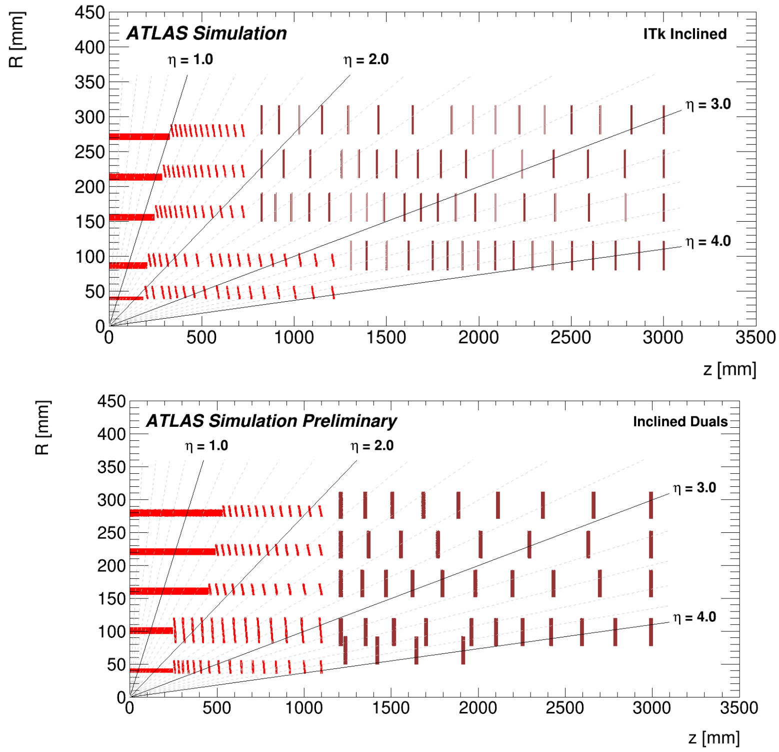

Figure 3.8.: Schematic layouts of the ITk pixel detectors. The upper part corresponds to the layout used for the Strip TDR [106] and referred to as Step 1.6 (also known as the Inclined layout). The lower part corresponds to the layout used for the Pixel TDR [105] and referred to as Step 2.2 (also known as the Inclined Duals layout). Only one quadrant and only active detector elements are shown for both diagrams. The horizontal axis is along the beam line with zero being the interaction point. The vertical axis is the radius measured from the interaction region.

3.3. *b*-tagging optimization for the ITk upgrade

Undoubtedly, *b*-tagging is also key to many physics analyses at HL-LHC. Therefore it is essential to at least maintain and possibly improve the current Run 2 *b*-tagging performance while extending it to larger rapidities in accordance with the ITk geometry (described in Section 3.2). Hence, the *b*-tagging performance is a key benchmark for the ITk layout definition.

In this section, I present the studies performed to optimize the *b*-tagging algorithms in order to take advantage of the ITk geometry, and summarize the overall performance of the main tagging algorithms obtained after implementing these optimizations.

3.3.1. Samples and physics objects selections

The studies presented in this section, are performed using a simulated Monte Carlo sample of half a million $t\bar{t}$ events produced in proton-proton collisions generated at a center-of-mass energy of $\sqrt{s} = 14$ TeV . This sample is simulated with POWHEG [66–68] interfaced with PYTHIA 6 [107] for parton shower and hadronization. The baseline simulation used for the optimization studies is generated with an average of 200 pile-up interactions per event ($\langle\mu\rangle$) in line with the HL-LHC operating environment (cf. Figure 3.9(a)). Additional $t\bar{t}$ samples were generated with different amount of pile-up in order to check the robustness of the response of the tagging algorithms: $\langle\mu\rangle = 0, 60, 140$.
To simulate the detector response, the $t\bar{t}$ sample is propagated through a GEANT4 [76] simulation of the ATLAS detector adapted to incorporate the ITk. The simulated energy deposits were then digitized into the detector readout format after which the event reconstruction process starts.

The vital objects for *b*-tagging are: the tracks reconstructed in the ITk, the signal primary vertex of the hard-scattering collision of interest and the jet direction usually obtained from calorimeter jets.

Tracks are reconstructed from clusters of signals in the silicon pixel and strip sensors, collectively referred to as hits. For the studies shown henceforth, the pixels hits are clustered using the so-called *digital clustering* algorithm, for which the center of the cluster is the geometrical mean of the hits: the charge information in each pixel provided by the time-over-threshold (ToT) is not used as a weight to compute the center of the cluster. This approach, which is the least sophisticated, is the baseline for ITk studies performed for the Strip and Pixel TDRs [105, 106].

The reconstructed tracks that make it to the final list of selected good tracks must satisfy the tracking requirements summarized in Table 3.1. Moreover, baseline level of *b*-tagging quality requires tracks to have at least 7 silicon hits, of which at least two must be in the pixel detector and one in the innermost pixel layer. Further quality criteria are applied to the selected tracks depending on the *b*-tagging algorithm and will be discussed in more details where relevant.
The primary and pile-up interaction vertices are reconstructed using the Adaptive Multi-Vertex Finder (AMVF) algorithm [108]. The use of this algorithm was motivated by the increased pile-up as well as the significantly improved tracking performance with ITk. The inputs to the AMVF along with the procedure employed to reconstruct vertices are described in details in the Pixel TDR [105]. The vertex reconstruction efficiency achieved is close to 100%. The reconstructed vertex with the largest sum of the squared transverse momenta of the associated tracks ($\sum p_T^2$) is chosen as the signal primary vertex. Simulation studies indicate that the probability to identify the correct signal primary vertex, applying this criterion, is around 95% in $t\bar{t}$ events [105].

Following the prescriptions used consistently in ATLAS for previous estimations of the expected *b*-tagging performance for future detectors, such as for the IBL TDR [109] and more recently for the Phase II Strip TDR [106], some events are rejected based on the true position of the hard scatter vertex. The aim is to focus on the *b*-tagging performance and factor out primary vertex finding and/or

[e] See Section 2.4.1

Requirement	$\|\eta\| < 2$	$2 < \|\eta\| < 2.6$	$2.6 < \|\eta\| < 4$
Si hits	≥ 9	≥ 8	≥ 7
Pixel hits	≥ 1	≥ 1	≥ 1
Holes[e]	< 2	< 2	< 2
Double holes	< 2	< 2	< 2
Pixel holes	< 2	< 2	< 2
Strip holes	< 2	< 2	< 2
p_T [MeV]	> 900	> 400	> 400
$\|d_0\|$	≤ 2 mm	≤ 2 mm	≤ 10 mm
$\|z_0\|$	≤ 20 cm	≤ 20 cm	≤ 20 cm

Table 3.1.: Summary of the tracking selection criteria applied to reconstructed tracks in different η regions in the ITk detector [105]. Further cuts are applied for b-tagging quality selection (cf. text).

resolution issues. Events where the reconstructed signal primary vertex (PV_0) is not within 0.1 mm from the true position of the hard scatter vertex along the beam axis, make up around 7% of the $t\bar{t}$ baseline sample and are discarded. In Figure 3.9(b), the local pile-up density [f] calculated within a window of ±2 mm around the reconstructed signal PV_0 along the beam axis, is shown for both events that pass and fail the above resolution cut on PV_0.

Jets are reconstructed by clustering energy deposits in the calorimeter with the anti-k_t algorithm [92] with a radius parameter of 0.4. The jet selection adopted for the studies hereafter is consistent with the b-tagging recommendations for Run 2 analyses apart from the extended acceptance of the tracker to $|\eta| = 4$ which is the only difference w.r.t the Run 2 configuration. Only jets with $p_T > 20$ GeV and $|\eta| < 4.5$ [g] are selected. Furthermore, in order to reject jets originating from pile-up interactions, and again building on the previous studies used for layout definition and performance assessment of future detectors, the selected jets are required to be matched to true quarks from the $t\bar{t}$ system based on an angular separation requirement ($\Delta R < 0.3$). Therefore, for the studies to be shown, light-flavor jets originate only from light quarks produced in the W from top decays and do not comprise gluon jets from radiation nor pile-up induced jets. However, inside the considered jets, the overlay of energy deposits and tracks coming from pile-up is present.

The transverse momentum and pseudo-rapidity distributions of the selected jets from the $t\bar{t}$ system as well as of light-jets from pile-up interactions are shown in Figure 3.10. Because of the kinematics of the $t\bar{t}$ events, the number of jets in the forward region is relatively low. While the large size of the $t\bar{t}$ MC sample used provides enough events for a first pass of the optimization studies, an additional sample populating more this region could be useful for further studies.

[f] The local pile-up (PU) density is defined as $\frac{N_{PV}(|PV_z - PV_{0,z}| < \Delta Z)}{2\Delta Z}$, where N_{PV} is the number of primary vertices reconstructed within a ΔZ window of 2 mm around the reconstructed hard scatter vertex PV_0.

[g] The $|\eta| < 4.5$ cut is applied instead of $|\eta| < 4$ (ITk coverage) as jets passing the cut may contain tracks with $|\eta| < 4$ and so can be used to assess the b-tagging performance.

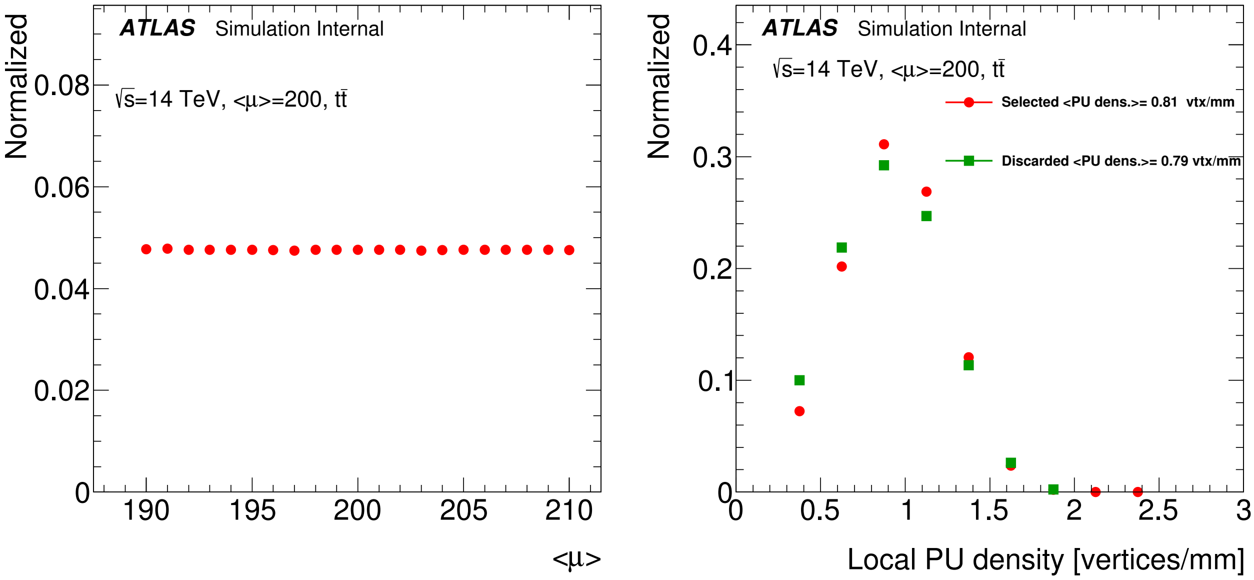

(a) (b)

Figure 3.9.: (a) Average number of pile-up interactions per event and (b) local pile-up density, computed with respect to the signal primary vertex within a 2 mm window along the z-axis shown separately for selected (red) and discarded (green) events by the PV_0 cut (cf. text). Both distributions are obtained from the $t\bar{t}$ sample used as baseline for all the ITk performance studies shown in this document. This sample is generated at a center-of-mass energy ($\sqrt{s}$) of 14 TeV and with an average number of interactions per event of 200, in line with the HL-LHC operating conditions.

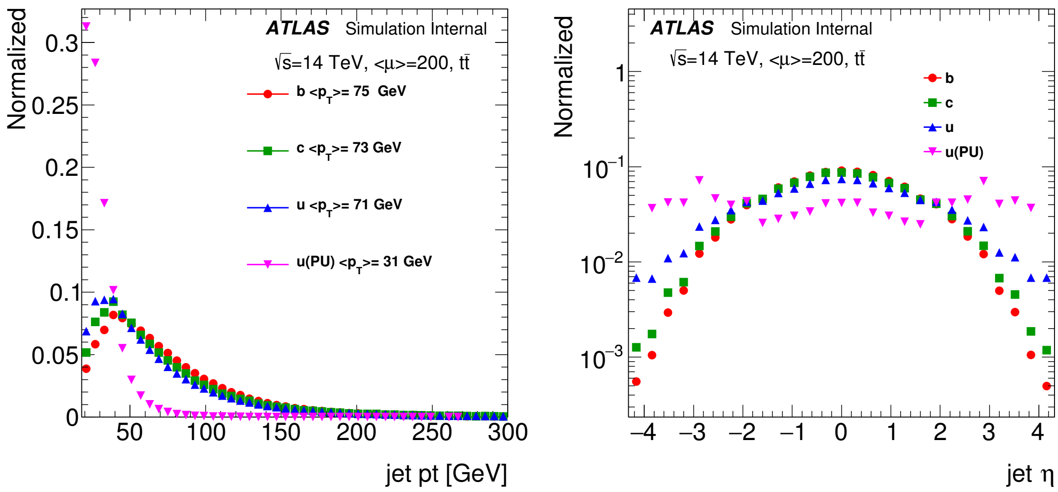

Figure 3.10.: Distributions of (left) the transverse momentum and (right) pseudo-rapidity of jets from the $t\bar{t}$ signal (b-jets in red, c-jets in green and light-jets in blue) as well as of light-jets from pile-up (magenta). The $t\bar{t}$ sample is generated at a center-of-mass energy of 14 TeV and with an average pile-up of 200, in line with the expected HL-LHC operating conditions for the ITk.

3.3.2. Impact parameter-based algorithms optimization and performance

As described in Section 3.1.2.1, the IPxD taggers are based on an LLR method. This formalism allows track categories to be used by defining different dedicated PDFs for each of them depending on the quality of the tracks. This maximizes the use of the available information and is more powerful than for instance rejecting some of these tracks. These categories are designed to be exclusive: a track belongs to one category and only one. Only tracks with $p_T > 1$ GeV are considered. The transverse and longitudinal impact parameters with respect to the primary vertex must fulfill $|d_0| < 1$ mm and $|z_0| \sin\theta < 1.5$ mm, where θ is the polar angle of the track .

The first step towards optimizing the IPxD taggers, in the context of the ITk upgrade, is to redefine the track categories to take advantage of the new tracker geometry since the Run 2 categories designed based on the ID geometry will become obsolete. Several categorizations were developed as will be described in the following. My work was to mainly assess the b-tagging performance obtained with each of these configurations through the derivation of dedicated PDFs to be used for the LLR estimation. The new ITk categories were chosen based on these comparisons.

It is important to note that these categories were initially defined for the Step 1.6 geometry (cf. Section 3.2.2.2). The PDFs were then updated with simulated events based on the Step 2.2 layout defined for the Pixel TDR, but the actual definition of the track categories was not changed, while the boundaries between regions with different structures have moved a bit. Thus, it would be interesting to revisit slightly the definition of categories to take that into account, in particular with the next iteration of the ITk layout, the so-called Step 3.

3.3.2.1. Figures of merit for defining track categories

For b-tagging purposes and more specifically for defining the track categories in what follows, the quality of a track is determined by the resolution with which its impact parameters are measured and is inherently dependent on its hit contents. Since the transverse impact parameter d_0 is the main parameter driving the b-tagging performance, it is the primary parameter of interest here. The behavior of the longitudinal projection z_0, is used as a cross-check.

The impact parameters are computed with respect to the primary vertex position. The impact parameters resolution is defined as the difference between the reconstructed and true values, Δd_0 and Δz_0. The measured values are determined after refitting the primary vertex position without using the track in question as input in order not to bias the resolutions measurement. For simplicity, only tracks from light-jets (including those from pile-up) are considered in the context of defining tracks categories, as they should not have large values of impact parameters, but in practice tracks from b-jets could have been used as well since the true usually non-zero impact parameter value is subtracted.

To study the behavior of a category, the quality of all its tracks is assessed by looking at their impact parameter resolution, mostly in the transverse plane (d_0). The impact parameter residual distribution Δd_0 is fitted using a simple approach relying on a double-Gaussian fit: $\mathcal{G}_1(\mu_1, \sigma_1) + \mathcal{G}_2(\mu_2, \sigma_2)$, where $\mu_1 \equiv \mu_2 \equiv 0$ is forced by construction. This permits to quantify the Gaussian core σ_1 of the resolution while being able to accommodate non-Gaussian tails, roughly described by σ_2, that can be large for specific categories with badly measured tracks. These two parameters σ_1 and σ_2 are the ones used to compare candidate track categories. It is important to note that these fits are used only to construct categories and possibly decide to merge some of them, it is not an attempt to parametrize the resolution, therefore the fact that the goodness of the fits is actually rather low has no further consequence. The ITk detector layout is quite complex resulting in the hit contents of tracks depending heavily on the pseudo-rapidity (cf. Figure 3.11). One can observe:.

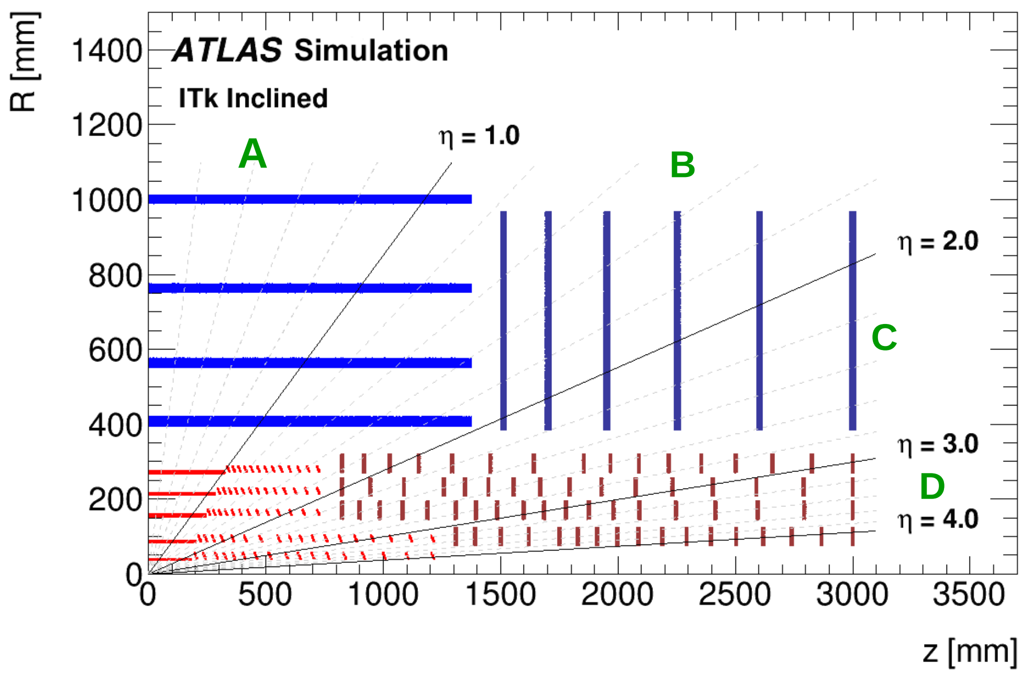

Figure 3.11.: Schematic view of the Inclined layout for ITk (Step 1.6).

- A homogeneous central region ($|\eta| < 1$), referred to as region A in the following, in which variations in pseudo-rapidity have no influence over the hit contents of the tracks. The layout of this region is rather similar to the one of the current detector, for which the track categories had been defined for Run 2 based solely on hit contents. Therefore the first option is to evaluate whether the pre-existing Run 2 track categories are still relevant for this region of ITk.

- The forward region beyond $|\eta| = 1$ is much more complex: there are many detector layers and thus many measurement points. Figure 3.12 illustrates clearly this situation, representing the number of hits in the pixel and the strip layers as a function of the pseudo-rapidity of the tracks for single muons with $p_T = 10$ GeV . The hit contents depend heavily on the pseudo-rapidity for $|\eta| > 1$. For these regions, defining the categories solely based on the hit contents may be too complicated, and an η-based definition has to be considered.

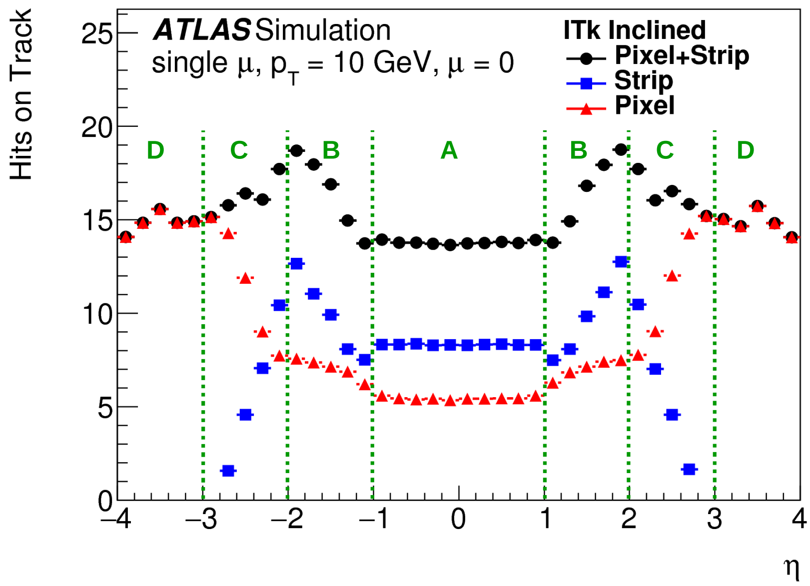

Figure 3.12.: Mean number of pixel (red triangles) and strip (blue squares) hits on a track as a function of pseudo-rapidity for single muons with $p_T = 10$ GeV, for the Step 1.6 layout [106]. The four regions defined for the track categorization are shown.

Due to the strong dependence of the hit contents on the pseudo-rapidity in the forward regions, testing the Run 2 categories here would be to a large extent pointless. Therefore it was decided to define differently the track categories in the central and forward regions.

3.3.2.2. Central region ($|\eta| < 1$): tuning of Run 2 track categories for ITk

As mentioned previously, the categories for Run 2 were defined solely based on the hit pattern, as summarized in Table 3.2. Tracks are assigned to only one category, by testing their compatibility with the category requirements following the order of the table. Tracks of the worst quality are in category #01, while the best quality tracks belong to category #14.

For a track, having a first measured hit at low radius in the detector is crucial for having a good accuracy when extrapolating the track trajectory back to the primary vertex. If tracks do not have this measurement in the first pixel layer (innermost), or worse, in the first two layers, their impact parameter resolution will be poor (categories #01 to #08 in Table 3.2), and so handling them separately improves the performance. Furthermore, knowing whether the hit is expected or not in the innermost and next to innermost layers is an additional quality criterion. The expectations of whether hits should be present are derived from the study of the detector geometry: a hit is expected in a given layer if the extrapolation of the helix in that layer is crossing an active part of the silicon sensor [101]. Category #01, for which the tracks have no hit in both the first and second pixel layers, while they were expected, contains the tracks with the worst quality, and we are interested in singling it out to assign better quality tracks to other categories. Other hit content parameters have an influence on the quality of a track. A hit is considered split if it was identified as being created by several charged particles (the decision is made partly by looking at its typical cluster shape). If a Pixel or Strip hit is associated to more than one track, and is not already marked as split, it is regarded as shared, and this is often an indication of a pattern-recognition issue arising from the high density of tracks in the local neighborhood. The requirement that a track has a low fraction of shared measurements is a very strong handle to suppress duplicate and fake tracks[h]. However, tracks are allowed to have a small fraction of shared measurements to avoid compromising the track reconstruction efficiency. Shared measurements typically provide a worse position estimate and hence degrade the quality of the reconstructed track.

Category #	**Description**
01	No hit in 1st pixel layer; no hit in 2nd pixel layer; expected hits in both layers
02	No hit in 1st pixel layer; no hit in 2nd pixel layer; expected hit in 1st layer but not in 2nd
03	No hit in 1st pixel layer; no hit in 2nd pixel layer; expected hit in 2nd layer but not in 1st
04	No hit in 1st pixel layer; no hit in 2nd pixel layer; no expected hit in either layers
05	No hit in 1st pixel layer but expected
06	No hit in 1st pixel layer and not expected
07	No hit in 2nd pixel layer but expected
08	No hit in 2nd pixel layer and not expected
09	Shared hits in 1st pixel layer > 0; shared hits in 2nd pixel layer > 0
10	Total number of shared hits in pixel layers > 0
11	Total number of shared hits in SCT layers > 2
12	Split hits in 1st pixel layer > 0; split hits in 2nd pixel layer > 0
13	Total number of split hits in pixel layers > 0
14	All other tracks

Table 3.2.: Description of the Run 2 track categories used by the IP2D and IP3D algorithms [101]. Tracks are assigned to only one category, by testing their compatibility with the requirements following the order of this table, based on increasing quality. Tracks not fulfilling any of those requirements are considered as well-measured tracks and are assigned to the last (#14) category. A hit is expected when the track extrapolation crosses an active detector element of a given layer.

Despite the similarities between the ID and ITk in region A, the Run 2 track categories were revisited in order to assess whether all categories were still relevant for the ITk geometry and if it was possible to reduce the number of categories, without over-simplifying and compromising the performance of the *b*-tagging algorithms.

For instance, around 0.02 ‰ only of the tracks have shared hits in the second pixel layer in the ITk

[h]Tracks which are not associated with real particles.

configuration, leading to a very depleted category #09. The choice was eventually made to discard it, meaning redistribute its contents among the other categories. Dropping the restrictive condition, however, made category #09 included in category #10. The two categories were then merged in a new category labeled 09+10. Similar analyses led to redistribute the contents of categories #02, #03, #04 among #05, #06, #07 and #08 whereas the contents of categories #11, #12 and #13 were merged into #14. Moreover, category #14 was further subdivided based on the number of hits in the first pixel layer for additional precision on the behavior of the tracks it contained.

The final new eight track categories that were defined for the ITk central region A are:

- **Category A01** : No hit in 1st pixel layer; no hit in 2nd pixel layer
- **Category A05** : No hit in 1st pixel layer but expected
- **Category A06** : No hit in 1st pixel layer and not expected
- **Category A07** : No hit in 2nd pixel layer but expected
- **Category A08** : No hit in 2nd pixel layer and not expected
- **Category A09+10** : Total number of shared hits in pixel layers > 0
- **Category A14A** : All other tracks; number of hits in 1st pixel layer $= 1$
- **Category A14B** : All other tracks; number of hits in 1st pixel layer ≥ 2

Figures 3.13 and 3.14 show the resolutions in d_0 and z_0 for these 8 categories defined for region A. The distributions are fitted by a double Gaussian as explained in Section 3.3.2.1.

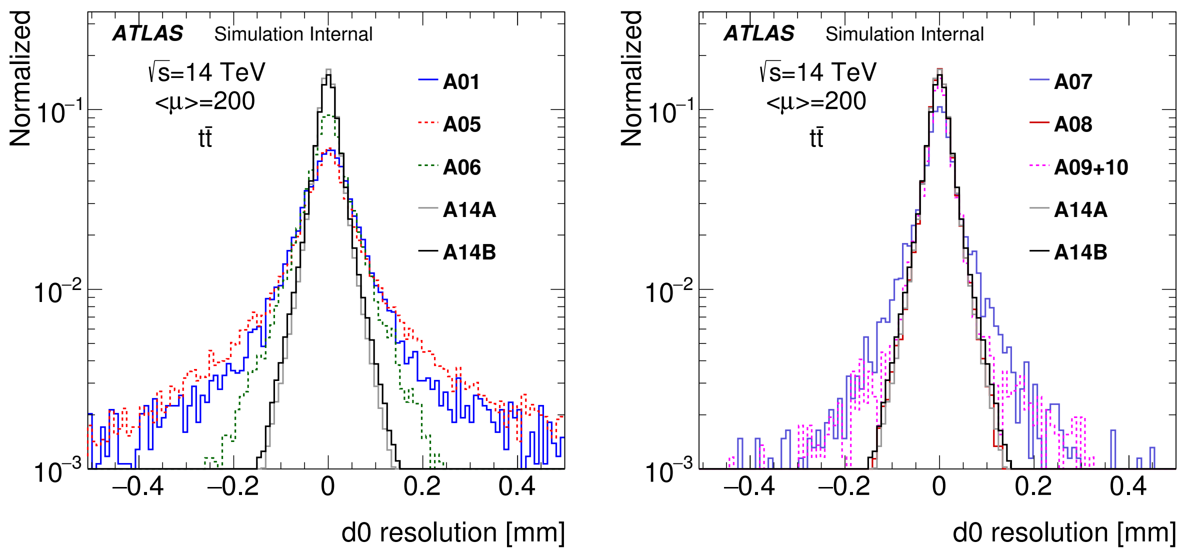

Figure 3.13.: Resolution distributions in d_0 for the 8 track categories defined for ITk region A ($|\eta| < 1$), for tracks with $p_T > 1$ GeV in light-jets. Tracks from pile-up jets are not included in these plots however they were taken into account when fitting the d_0 resolution distributions. Fits results are summarized in Table 3.3.

From Figure 3.13, we can see that the categories have quite different resolutions. Comparing the resolution of category A01 to categories A14A or A14B highlights these differences. Overall, the resolutions tend to get better going from category A01 to A14A or A14B as expected. Categories A01, A05 and A07 for instance, illustrate the occurrence of tails for mismeasured tracks. For the z_0 resolutions in Figure 3.14, a similar behavior to d_0 is observed.

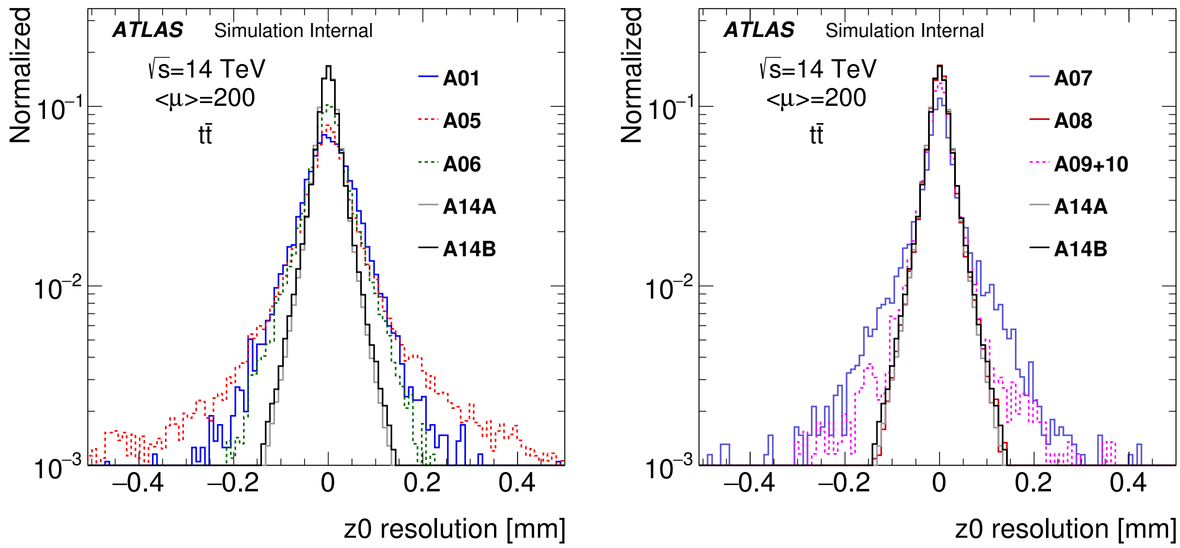

Figure 3.14.: Resolution distributions in z_0 for the 8 track categories defined for ITk region A ($|\eta| < 1$), for tracks with $p_T > 1$ GeV in light-jets. Tracks from pile-up jets are not included in these plots however they were taken into account when fitting the z_0 resolution distributions. Fits results are summarized in Table 3.3.

The results of d_0 and z_0 resolution fits are presented in Table 3.3. The bold columns contain the values of the core Gaussian widths σ_1 obtained from the fits in d_0 and z_0. The values of the Gaussian widths σ_2 describing the distributions tails as obtained from these fits are also shown in the table. The main conclusion that was reached from this study is that the resolutions are different enough between the categories, and thus, this subset of categories inspired from Run 2 is still meaningful in this region. The relative fraction of tracks in each category is also indicated in the table, with respect to the total number of tracks selected in the central region A. Even though some of the categories contain a very small number of tracks (~ 0.3‰ for A07 for instance), they can be just as important as more populated categories when it comes to the effect they have on the discriminating power of the algorithms. In addition, for different kind of events these categories could be more populated.

3.3.2.3. Track categories investigated for ITk forward region

As previously noted, the forward region has a much more complex behavior than the central region, as the hit contents of the tracks depend strongly on the pseudo-rapidity. For this reason three different configurations were devised and analyzed for the forward region such that each is complemented with the same central region categorization defined in the previous section. The first one is a simple separation of the region in η, defining regions corresponding more or less to the transition regions visible on the layout of the detector (Figure 3.11). The second is similar but further subdivides each η region according to the tracks hit contents. The third approach attempts to define categories based

Category	% tracks	d_0 fit				z_0 fit			
		χ^2 / ndf	RMS (μm)	Core: σ_1 (μm)	Tails: σ_2 (μm)	χ^2 / ndf	RMS (μm)	Core: σ_1 (μm)	Tails: σ_2 (μm)
A01	0.216	115 / 50	171	**64 ± 2**	238 ± 5	120 / 22	148	**61 ± 1**	197 ± 4
A05	0.171	432 / 50	133	**39 ± 1**	176 ± 5	424 / 22	113	**34 ± 1**	127 ± 4
A06	0.040	137 / 37	78	**29 ± 1**	98 ± 4	61 / 19	69	**23 ± 1**	75 ± 3
A07	0.031	201 / 50	167	**27 ± 3**	207 ± 16	96 / 22	178	**25 ± 1**	225 ± 11
A08	0.044	115 / 36	53	**16 ± 0.7**	49 ± 1	41 / 15	46	**19 ± 0.6**	54 ± 2
A09+10	0.110	311 / 49	76	**34 ± 0.6**	127 ± 5	213 / 22	74	**35 ± 0.8**	121 ± 6
A14A	44.818	2.7e+04 / 52	47	**24 ± 0.1**	57 ± 0.1	3.0e+04 / 52	46	**23 ± 0.1**	57 ± 0.1
A14B	54.542	2.9e+04 / 52	56	**32 ± 0.1**	69 ± 0.1	2.7e+04 / 52	55	**32 ± 0.1**	70 ± 0.1

Table 3.3.: Summary of fits results for d_0 and z_0 resolutions of tracks in the 8 categories defined for ITk central ($|\eta| < 1$) region A (see text for details). The fractions of tracks are relative to the total number of tracks selected in region A. Tracks from pile-up jets were taken into account in the fits.

on the expected worsening of the impact parameters resolution for low momentum tracks depending on the amount of material crossed by the particles.

First configuration for the forward region: rapidity-based categories

The tracks separation in η in the forward region, corresponding to the first configuration, yields 3 categories which are called B, C and D (cf. Figure 3.11), in addition to the 8 categories defined for region A :

- **Category B** : $1 < |\eta| < 2$
- **Category C** : $2 < |\eta| < 3$
- **Category D** : $3 < |\eta| < 4$

Figure 3.15 shows the resolutions in d_0 and z_0 for the 3 η-based categories covering the forward region of ITk. Both the resolutions in d_0 and z_0 are different among the three categories, meaning the tracks have a different behavior inside the detector based on their pseudo-rapidity.

The results of the fits for this configuration are presented in Table 3.4. The 2nd column shows the fraction of the tracks within each category with respect to the total number of tracks contained in the detector.

Category	% tracks	d_0 fit				z_0 fit			
		χ^2 / ndf	RMS (μm)	Core: σ_1 (μm)	Tails: σ_2 (μm)	χ^2 / ndf	RMS (μm)	Core: σ_1 (μm)	Tails: σ_2 (μm)
B ($1 < \|\eta\| < 2$)	20.96	7.8e+04 / 52	79	**42 ± 0.1**	102 ± 0.1	9.4e+04 / 24	76	**38 ± 0.1**	94 ± 0.1
C ($2 < \|\eta\| < 3$)	27.77	4.1e+04 / 52	111	**68 ± 0.1**	145 ± 0.2	1.5e+05 / 106	140	**60 ± 0.1**	140 ± 0.1
D ($3 < \|\eta\| < 4$)	32.69	1.3e+04 / 52	160	**99 ± 0.1**	217 ± 0.0	6.0e+05 / 106	190	**79 ± 0.1**	192 ± 0.1

Table 3.4.: Summary of fits results for d_0 and z_0 resolutions for the 3 track categories B, C and D of the 1st *η-based* configuration defined for the ITk forward region (see text). The fractions of tracks are relative to the total number of tracks in regions A+B+C+D. Tracks from pile-up jets are taken into account in the fits.

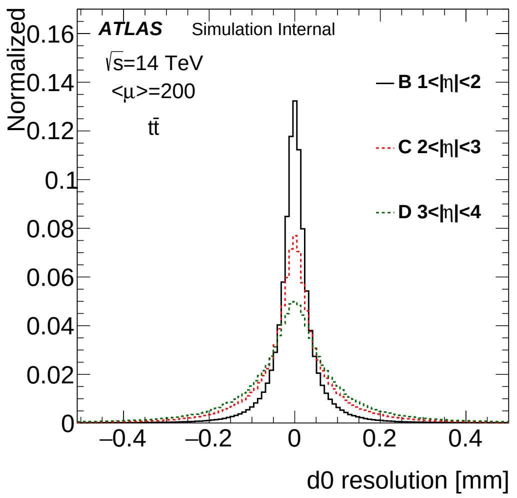

(a)

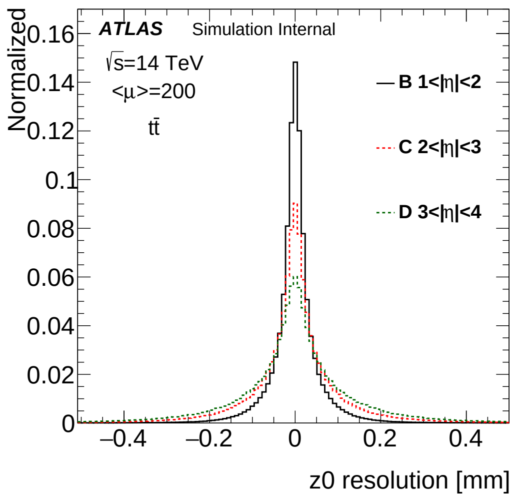

(b)

Figure 3.15.: Resolutions in (a) d_0 and (b) z_0 for the 3 track categories B, C and D of the 1st η-*based* configuration (referred to as V01 later) defined for the ITk forward region (see text). Tracks from pile-up jets are not included in these plots.

Second configuration for the forward region: rapidity and hit pattern-based categories

The second configuration goes beyond the simple separation in η in the forward region, subdividing each resulting region (B, C and D) based on the hit contents of the tracks, in the same way categories were defined in region A (cf. Section 3.3.2.2).

In region B ($1 < |\eta| < 2$), only 5 relevant sub-categories based on hit contents were kept:

- **Category B01** : No hit in 1st pixel layer; no hit in 2nd pixel layer
- **Category B05** : No hit in 1st pixel layer but expected
- **Category B09+10** : Total number of shared hits in pixel layers > 0
- **Category B11** : Total number of shared hits in strip layers > 1
- **Category B14** : All other tracks

Figure 3.17 illustrates the resolutions in d_0 and z_0 for the 5 sub-categories of region B of the second configuration. The resolutions for the different categories are different from one another and getting narrower as the quality of the tracks increases. Tracks in this region thus still behave somewhat similarly to tracks from region A, even though the Run 2 categories start to become less relevant in this region and only a subset could be kept.

Based on the same approach followed to define track categories for regions A and B, only 3 and 2 sub-categories were defined in regions C ($2 < |\eta| < 3$) and D ($3 < |\eta| < 4$) respectively:

- **Category C09+10** : Total number of shared hits in pixel layers > 0
- **Category C11** : Total number of shared hits in Strip layers > 1
- **Category C14** : All other tracks

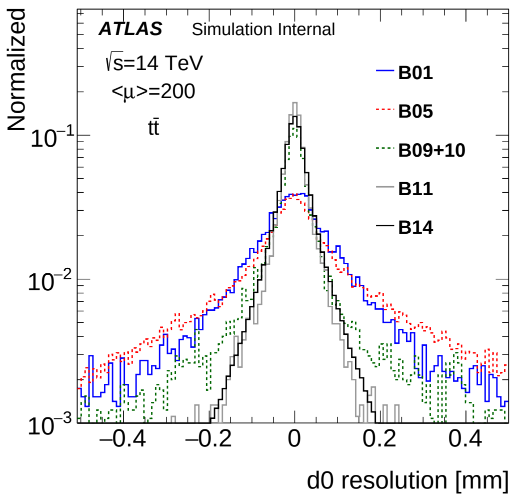

(a)

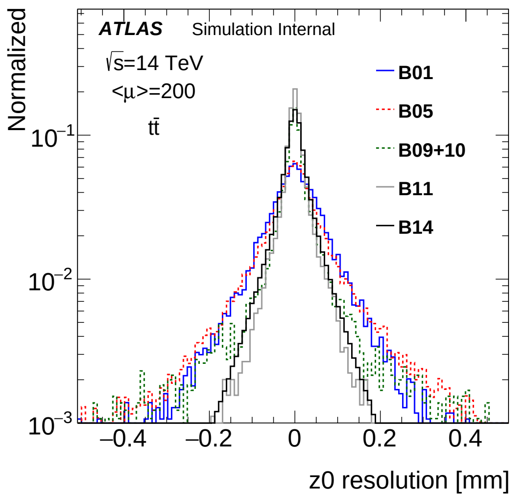

(b)

Figure 3.16.: Resolutions in (a) d_0 and (b) z_0 (b) for the five sub-categories defined in region B ($1 < |\eta| < 2$) of the 2$^{\text{nd}}$ track categories configuration for the ITk forward region (see text). Tracks from pile-up jets are not included in these plots.

- **Category D09+10** : Total number of shared hits in pixel layers > 0
- **Category D14** : All other tracks

Figures 3.17 and 3.18 illustrate the resolutions in d_0 and z_0 for the 5 (3+2) sub-categories of regions C and D of the second configuration.

At this stage, one can conclude that the categories defined for region A become less relevant as the most forward regions of ITk are explored. This is due to the fact that for regions C and D (i.e $|\eta| > 2$), the information about the hits in the first and second pixel layers which is crucial to a good track quality, was not provided due to technical limitations in the tracking event data model. Thus categories separating the tracks with poor quality from those with good quality could not be exploited. However, tracks categorization in these forward regions can be revisited when the tracking event data model is adjusted to accommodate the new ITk layout.

The results of the d_0 and z_0 resolution fits of the 2$^{\text{nd}}$ configuration for the forward region are presented in Table 3.5. The second column shows the relative fraction of tracks in each category with respect to the total number of tracks contained in their respective regions.

Third configuration for the forward region: multiple scattering-based categories

A charged particle moving through the material of the detector suffers from numerous deflections in the Coulombian field of the nuclei therein, altering its helical trajectory in the magnetic field. This Multiple Scattering (MS) effect is proportional to the amount of material crossed by the particle which is illustrated for ITk in Figure 3.19, in terms of radiation length X_0 (see Section 2.2.2). The amount of material traversed by particles in the forward region of ITk ($|\eta| > 1$) is considerably higher (up to ~ 6 times) than that in the central region A; compared to the ID however, the ITk utilizes significantly less material across nearly the full η coverage. For a uniform part like the sensors, the crossed amount of material scales as the sine of the polar angle θ and is inversely proportional to the

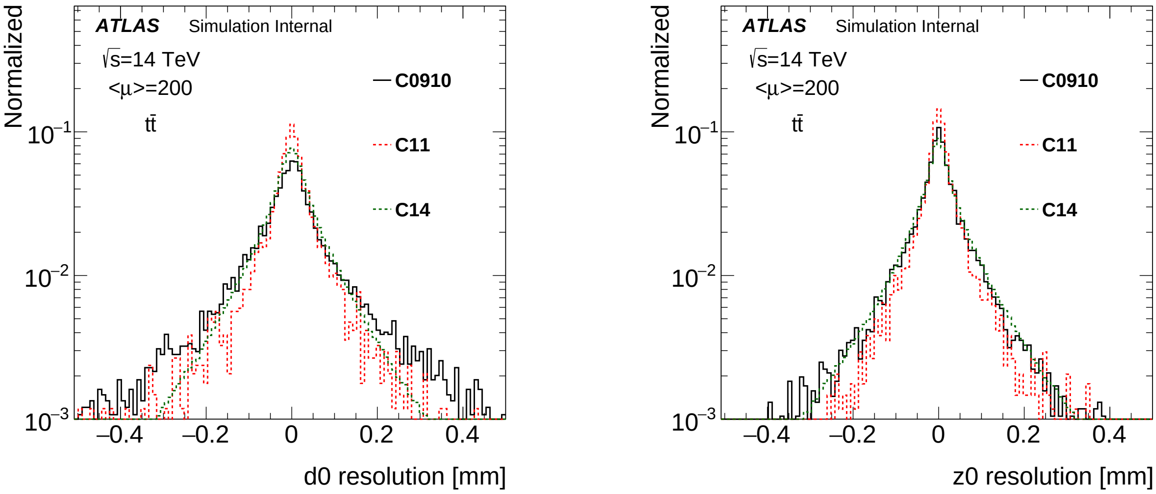

(a) (b)

Figure 3.17.: Resolutions in (a) d_0 and (b) z_0 for categories in region C ($2 < |\eta| < 3$) of the 2nd configuration of track categories for the ITk forward region (see text). Tracks from pile-up jets are not included in these distributions.

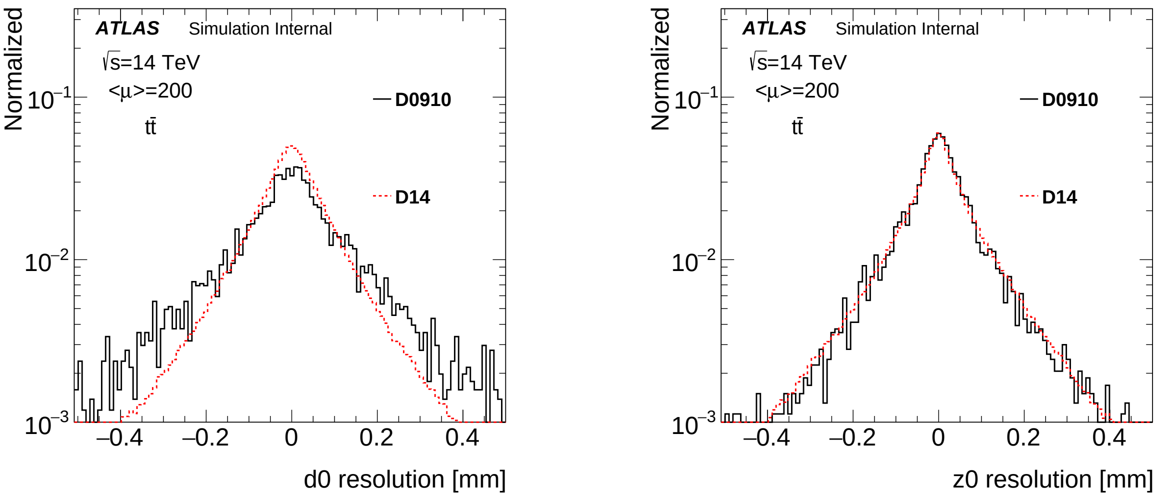

(a) (b)

Figure 3.18.: Resolutions in (a) d_0 and (b) z_0 for categories in region D ($3 < |\eta| < 4$) of the 2nd configuration of track categories for the ITk forward region (see text). Tracks from pile-up jets are not included in these plots.

Category	% tracks	d_0 fit				z_0 fit			
		χ^2 / ndf	RMS (μm)	Core: σ_1 (μm)	Tails: σ_2 (μm)	χ^2 / ndf	RMS (μm)	Core: σ_1 (μm)	Tails: σ_2 (μm)
B01	0.32	178 / 52	215	**92 ± 3**	365 ± 14	108 / 24	180	**78 ± 2**	206 ± 1
B05	0.22	332 / 52	170	**52 ± 1**	231 ± 4	662 / 24	127	**44 ± 1**	200 ± 5
B09+10	0.16	580 / 52	145	**47 ± 1**	234 ± 6	450 / 24	142	**44 ± 1**	254 ± 6
B11	0.12	240 / 44	73	**22 ± 1**	76 ± 1	160 / 21	73	**21 ± 0.5**	83 ± 1
B14	99.18	7.2e+04 / 52	78	**41 ± 0.1**	100 ± 0.1	8.9e+04 / 24	75	**38 ± 0.1**	93 ± 0.1
C09+10	0.19	550 / 52	121	**74 ± 2**	177 ± 6	822 / 80	189	**50 ± 1**	133 ± 2
C11	0.04	201 / 48	98	**31 ± 2**	103 ± 2	209 / 48	165	**23 ± 1**	102 ± 2
C14	99.78	4.0e+04 / 52	111	**67 ± 0.1**	145 ± 0.2	1.4e+05 / 106	140	**60 ± 0.1**	140 ± 0.1
D09+10	0.52	440 / 52	173	**105 ± 2**	227 ± 4	1615 / 104	160	**85 ± 1**	233 ± 3
D14	99.48	1.3e+04 / 52	160	**99 ± 0.1**	217 ± 0.1	5.7e+05 / 106	191	**79 ± 0.1**	192 ± 0.1

Table 3.5.: Summary of fits results for d_0 and z_0 resolutions for the 2nd *η- and hit contents-based* configuration of the track categories defined for the forward region of ITk (see text). The fractions of tracks are relative to the respective total number of tracks in each of the regions B, C and D. Tracks from pile-up jets are taken into account in the fits.

total momentum of the particle. Therefore the MS effect is particularly important for low momentum tracks, for which both the momentum and the impact parameter resolutions are indeed dominated by multiple scattering effects.

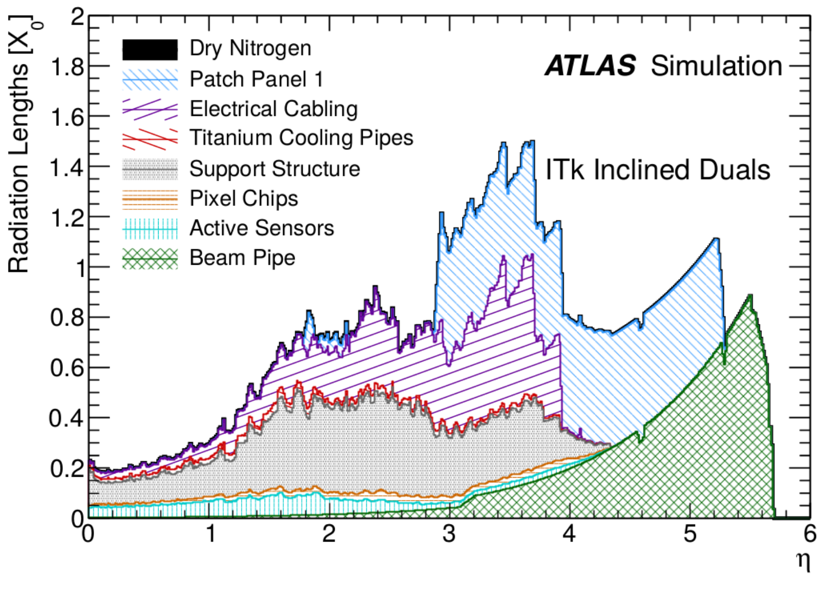

Figure 3.19.: Cumulative material thickness of the ITk in terms of radiation length X_0 as a function of η [105]. Only positive η is shown in the figure while negative η is expected to look the same.

The impact parameter resolution can be parametrized as proportional to a γ factor (cf. Equation 3.1 below), the value of which is used to best account for this phenomenon. The distribution of γ for tracks outside of region A is shown in Figure 3.20.

The third configuration of track categories for the ITk forward region is defined in terms of this γ

parameter. In particular, 4 categories were arbitrarily defined:

- **Zone 1** : $\gamma \leq 0.001$ MeV $^{-1}$
- **Zone 2** : $0.001 < \gamma \leq 0.002$ MeV $^{-1}$
- **Zone 3** : $0.002 < \gamma \leq 0.003$ MeV $^{-1}$
- **Zone 4** : $\gamma > 0.003$ MeV $^{-1}$

$$\text{where} \quad \gamma \equiv \frac{1}{p_T\sqrt{\sin(\theta)}} \tag{3.1}$$

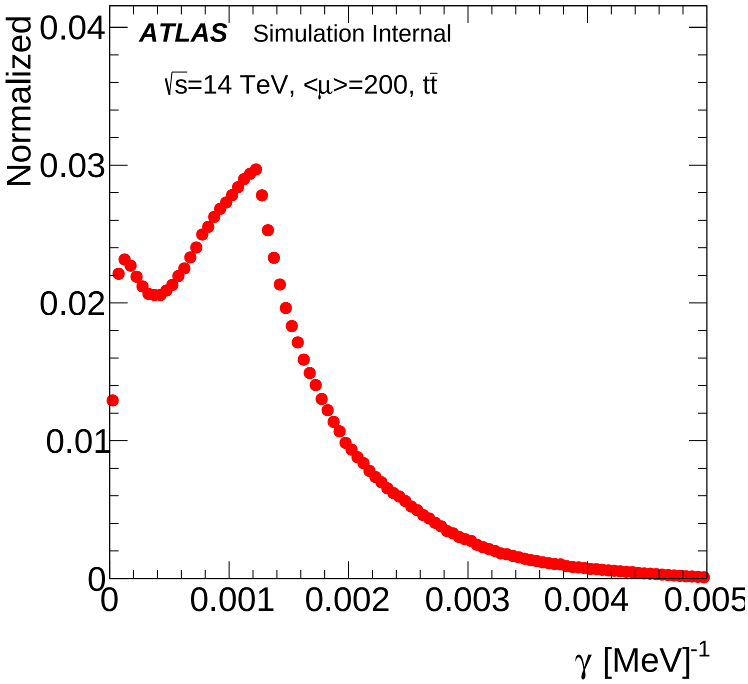

Figure 3.20.: Distribution of $\gamma \equiv \left(p_T\sqrt{\sin(\theta)}\right)^{-1}$ for tracks outside the ITk central region A; i.e $|\eta| > 1$. Tracks from pile-up jets are not included in this plot.

Figure 3.21 illustrates the resolutions in d_0 and z_0 for the 4 categories of the third configuration.

In this configuration, the impact parameters resolution worsens going from zone 1 to zone 4 categories which is expected since the tracks in the last categories are those suffering the most from multiple scattering.

The results of d_0 and z_0 resolutions fits for the categories of the third configuration are presented in Table 3.6.

3.3.2.4. Optimal track categories configuration

In order to decide on the tracks categorization to adopt as baseline for the ITk flavor-tagging studies, I evaluated the IP3D performance obtained with each of the configurations defined in the previous section. To do so, I built a framework to derive configuration-dedicated PDFs based on the $t\bar{t}$ sample and used them to recompute the jets IP3D discriminant in each case.

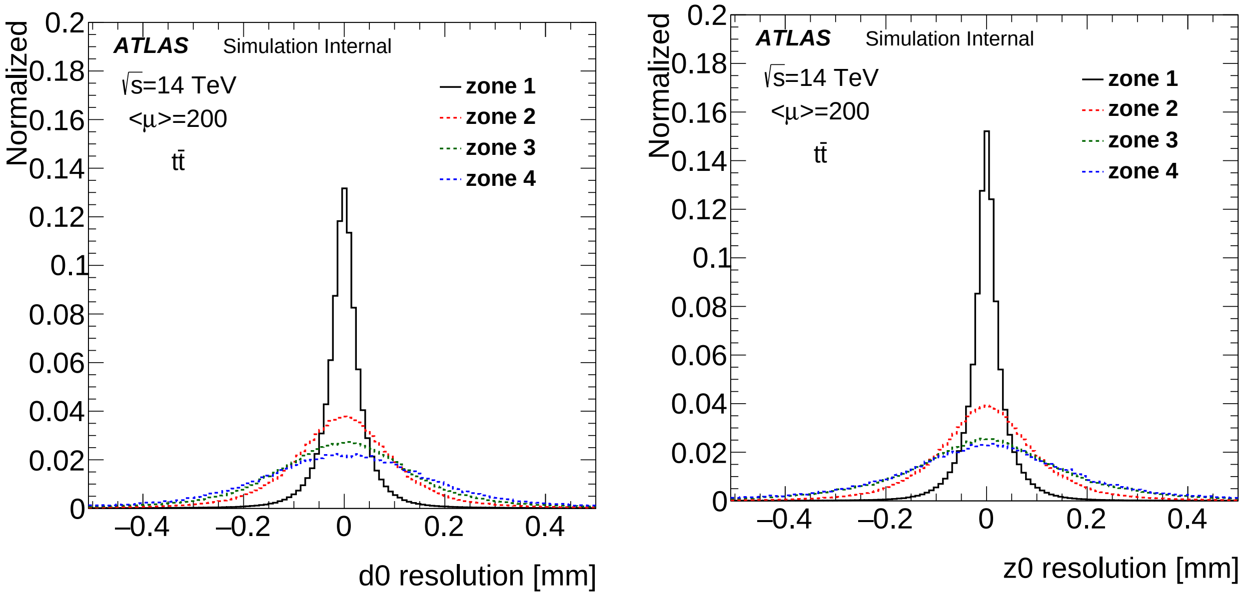

Figure 3.21.: Resolutions in (left) d_0 and (right) z_0 for the 4 track categories of the 3rd configuration for the forward region of ITk ($|\eta| > 1$). Tracks from pile-up jets are not included in these plots.

Category	% tracks	d_0 fit				z_0 fit			
		χ^2 / ndf	RMS (μm)	Core: σ_1 (μm)	Tails: σ_2 (μm)	χ^2 / ndf	RMS (μm)	Core: σ_1 (μm)	Tails: σ_2 (μm)
Zone 1 $\gamma \leq 0.001$	20.96	1.0e+05 / 52	67	**38 ± 0.1**	93 ± 0.2	1.1e+05 / 106	88	**28 ± 0.1**	65 ± 0.1
Zone 2 $0.001 < \gamma \leq 0.002$	38.64	1.3e+04 / 52	107	**81 ± 0.1**	180 ± 0.3	3.3e+05 / 24	98	**62 ± 0.1**	118 ± 0.1
Zone 3 $0.002 < \gamma \leq 0.003$	24.50	1717 / 52	145	**118 ± 0.1**	223 ± 0.7	7.0e+04 / 106	177	**103 ± 0.1**	203 ± 0.1
Zone 4 $\gamma > 0.003$	15.90	654 / 52	187	**163 ± 0.5**	347 ± 7	3.8e+04 / 106	222	**148 ± 0.1**	347 ± 10

Table 3.6.: Summary of the fits results for d_0 and z_0 resolutions for the 4 track categories of the 3rd *MS-based* configuration defined for the forward region of ITk (see text). The fractions of tracks are relative to the total number of tracks with $|\eta| > 1$. Tracks from pile-up are taken into account in the fits.

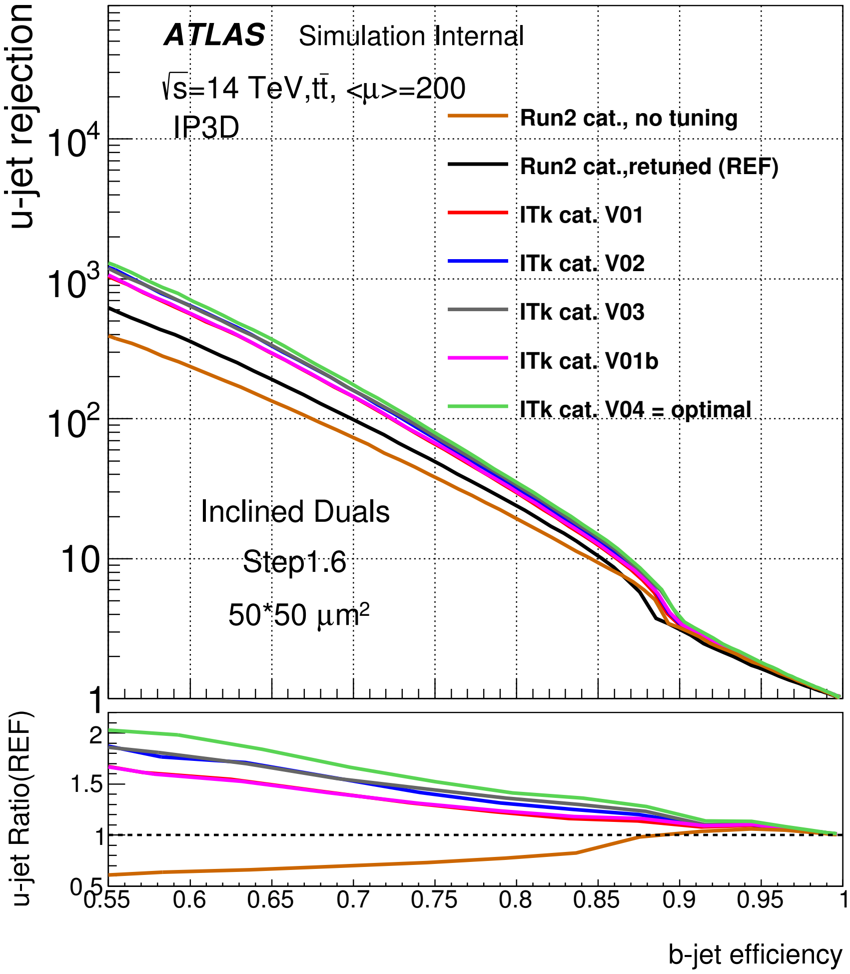

Figure 3.22.: Light-jet rejection Vs b-tagging efficiency of IP3D evaluated in $t\bar{t}$ events with 200 pile-up for the ITk layout. The performances obtained with the different proposed categorizations (see text) are compared: *rapidity-based* configuration (V01) in red, *hit-pattern based* configuration (V02) in blue, *multiple-scattering based* configuration (V03) in grey, a variant of the rapidity-based configuration using the full Run 2 track categories instead of the reduced list of 8 in the central region (V01b) in magenta which gives as expected the same performance as V01. The performance obtained with the optimal configuration (V04) defined based on the above configurations (see text) is shown in green. Additionally, the performances obtained with the Run 2 PDFs out-of-the-box (no tuning) as well as in the case where the references are retuned to take into account the ITk geometry are overlaid on the figure. On the bottom pad, the ratios with respect to the performance obtained with the retuned Run2 PDFs are shown for each tested configuration.

In Figure 3.22, a comparison of the b-tagging performance of IP3D in terms of light-jet rejection *vs* b-jet efficiency, is shown for three configurations:

- V01: the 8 categories for the central region A (cf. Table 3.3) and the 3 categories from the 1st

forward configuration (cf. Table 3.4),

- V02: the 8 categories for the central region A and the 10 categories from the 2nd forward configuration (cf. Table 3.5),

- V03: the 8 categories for the central region A and the 4 categories from the 3rd forward configuration (cf. Table 3.6).

These results are based on the Step 1.6 layout of the ITk (cf. Section 3.2.2.2). For completeness, the performances obtained with the Run 2 categories when using the Run 2 PDFs out-of-the-box (referred as "no tuning") as well as when the PDFs are updated to take into account the new geometry of the ITk (referred to as "retuned") are overlaid on the figure. Furthermore, an additional configuration labeled V01b was tested, as a variation of the V01 configuration, where the full list of Run 2 categories was used in the central region to check that no loss in performance is induced when using the reduced list of Run 2 categories as was decided for the ITk configurations. The obtained results show an enhancement in the IP3D performance when using any of the new ITk configurations (V01, V02, V03) compared to the Run 2 categories (both with retuned and non-tuned PDFs); *e.g.* a gain of around 40-60 % is achieved in the light-jet rejection at the 70% b-tagging efficiency working point. In particular, the multiple scattering-based configuration (V03) exhibits the best performance with respect to the remaining configurations. However, more detailed checks examining the performance in exclusive η regions led to conclude that the rapidity and hit pattern-based configuration (V02) gives the best performance in the $1 < |\eta| < 2$ region whereas configuration V03 performs the best for $|\eta| > 2$.

These conclusions motivated the idea of combining the three configurations in a manner to optimize the performance in all regions, *i.e.* to define an optimal categorization that adopts in each $|\eta|$ region the configuration with the best performance. The optimal configuration, labeled V04, consists of 17 categories: the 8 categories of region A in $|\eta| < 1$, the 5 categories of region B ($1 < |\eta| < 2$) from configuration V02 and the 4 γ categories from configuration V03 for $|\eta| > 2$ (cf. Table 3.7). The b-tagging performance achieved with the optimal configuration is also shown on Figure 3.22. As expected, the optimal configuration leads to the best performance inclusively in $|\eta|$. Thus, it is adopted as the baseline tracks categorization for IP3D in the context of the flavor-tagging studies for ITk.

η region	Category	Description	% tracks
$\lvert\eta\rvert < 1$	A01	No hit in 1st pixel layer; no hit in 2nd pixel layer	0.22
	A05	No hit in 1st pixel layer but expected	0.63
	A06	No hit in 1st pixel layer and not expected	0.39
	A07	No hit in 2nd pixel layer but expected	0.14
	A08	No hit in 2nd pixel layer and not expected	0.43
	A09+10	Total number of shared hits in pixel layers > 0	0.11
	A14A	All other tracks; number of hits in 1st pixel layer = 1	31.12
	A14B	All other tracks; number of hits in 1st pixel layer ≥ 2	7.64
$1 < \lvert\eta\rvert < 2$	B01	No hit in 1st pixel layer; no hit in 2nd pixel layer	0.22
	B05	No hit in 1st pixel layer but expected	0.64
	B09+10	Total number of shared hits in pixel layers > 0	0.14
	B11	Total number of shared hits in strip layers > 1	0.10
	B14	All other tracks	28.37
$\lvert\eta\rvert > 2$	Zone 1	$\gamma \leq 0.001$ MeV $^{-1}$	15.17
	Zone 2	$0.001 < \gamma \leq 0.002$ MeV $^{-1}$	8.47
	Zone 3	$0.002 < \gamma \leq 0.003$ MeV $^{-1}$	4.27
	Zone 4	$\gamma > 0.003$ MeV $^{-1}$	1.94

Table 3.7.: Description of the optimal configuration (V04) of track categories used by IP2D and IP3D algorithms for the ITk layout. The last column shows the relative fraction of tracks in each category, for selected tracks in light-jets coming from the $t\bar{t}$ system in the sample under consideration.

3.3.3. Impact of the new track categories on the IP3D and IP2D performances

In Figure 3.23, the b-tagging performance in terms of light-jet and charm-jet rejections for the IP3D tagger is shown, comparing the performance obtained with the Run 2 categories (out-of-the-box PDFs) to that with the ITk optimal configuration categories, with the reference histograms derived based on simulations of Step 2.2 layout. Globally, using the new ITk categories enhances the b-tagging performance. A gain of around 100% in the light-jet rejection is achieved at the 70% b-tagging efficiency working point. As for the charm-jet rejection, the gain is more modest, below 5%.

Figures 3.24 and 3.25 depict the b-tagging performance of IP3D in exclusive p_T and η regions respectively, comparing the performance obtained with the optimal ITk categories with respect to the one obtained with the Run 2 categories. An enhancement in performance is observed in all p_T regions when making use of the ITk categories, however, it is most pronounced in the low p_T region ($20 < p_T < 70$ GeV). As for the performance versus the different η regions, most of the enhancement is showing up in the most forward region ($3 < \lvert\eta\rvert < 4$). This is expected as the Run 2 template PDFs are not constructed taking into account tracks beyond $\lvert\eta\rvert = 2.5$.

Similar results were obtained for the IP2D tagger (cf. appendix A) except that the improvement induced by using the new ITk categories was found to be less pronounced compared to the IP3D case e.g around 10% gain in the light-jet rejection was achieved at the 70% working point.

Figure 3.26 compares the IP3D performance, in terms of light-jet and charm-jet rejections, obtained with the new ITk categories to that achieved by the current ATLAS Inner Detector. The performance of the latter is obtained for an average amount of pile-up of 30, and can be compared directly for the same η range with ITk (dashed line). These results illustrate clearly that the ITk not only is capable of restoring the b-tagging performance of the current detector despite the high pile-up environment (around 200) but also outperforms it.

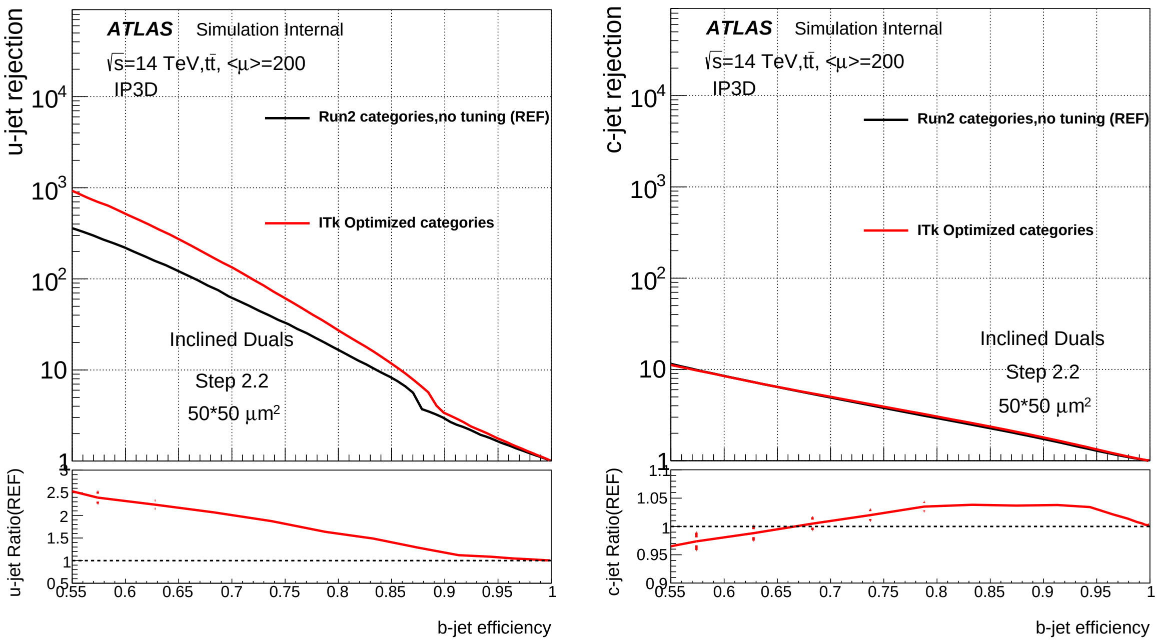

Figure 3.23.: Light-jet (left) and charm-jet (right) rejection *vs* b-tagging efficiency for the IP3D algorithm, evaluated in $t\bar{t}$ events with 200 pile-up events for the ITk layout. The results obtained with the out-of-the-box Run 2 categories (black) and the new ITk ones (red) are compared and their ratio is shown on the bottom pad.

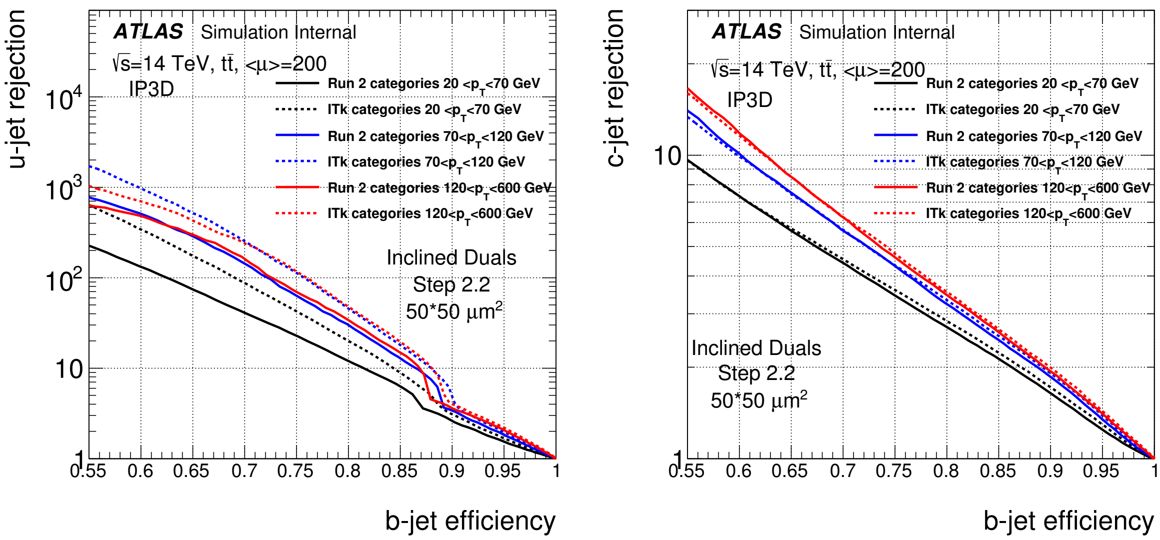

Figure 3.24.: Light-jet (left) and charm-jet (right) rejection *vs* b-tagging efficiency for the IP3D tagging algorithm, evaluated in $t\bar{t}$ events with 200 pile-up events for the ITk layout. The results obtained with the out-of-the-box Run 2 categories (solid line) and the new ITk ones (dashed line) are compared in different p_T regions: $20 < p_T < 70$ GeV (black), $70 < p_T < 120$ GeV (blue) and $120 < p_T < 600$ GeV (red).

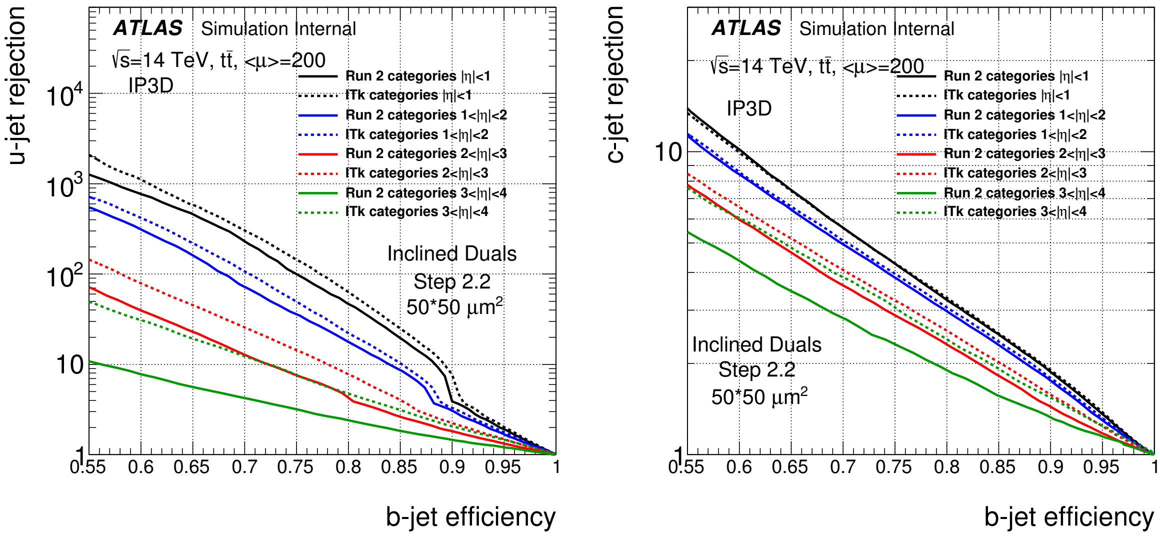

Figure 3.25.: Light-jet (left) and charm-jet (right) rejection *vs* b-tagging efficiency for the IP3D tagging algorithm, evaluated in $t\bar{t}$ events with 200 pile-up events for the ITk layout. The performances obtained with the out-of-the-box Run 2 (solid lines) and the new ITk (dashed lines) PDFs are compared in different η regions: $|\eta| < 1$ (black), $1 < |\eta| < 2$ (blue), $2 < |\eta| < 3$ (red) and $3 < |\eta| < 4$ (green).

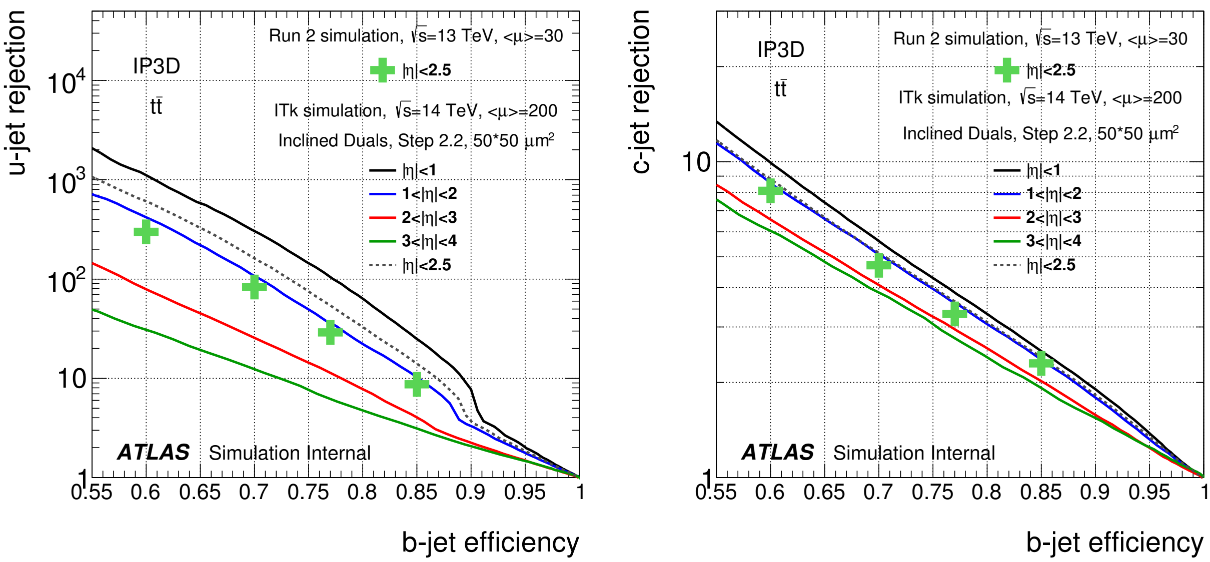

Figure 3.26.: Light-jet (left) and charm-jet (right) rejection *vs* b-tagging efficiency for the IP3D algorithm evaluated in $t\bar{t}$ events with 200 pile-up events for the ITk layout Step 2.2. The performance is depicted in different η regions and assessed making use of the new ITk categories, as explained in the text. For comparison, the performance obtained with the current Run 2 Inner Detector with an average pile-up of 30 is also shown as green crosses for the 60%, 70%, 77% and 85% b-tagging efficiency working points. Modulo a cosmetic change, these plots are the ones appearing in the Phase II ITk Pixel TDR [105].

3.3.4. SV1 performance

The SV1 b-tagging algorithm, as explained in Section 3.1.2.2, is based on the reconstruction of the secondary vertex formed by the decay products of the b-hadron and also relies on an LLR formalism. This algorithm adopts looser requirements for the tracks selection not to compromise the displaced vertices reconstruction efficiency: tracks with $p_T > 400$ MeV and transverse impact parameter fulfilling $|d_0| < 3.5$ mm are taken into account in the considered jets; no cut on the longitudinal impact parameter z_0 is applied.

In the context of the ITk phase II upgrade, the SV1 algorithm needs to be optimized to exploit fully the capabilities of the new tracker. However, given the timescale of these studies, only a few modifications were made to the algorithm itself. In this respect, my work consisted in deriving the reference distributions needed for the SV1 LLR taking into account the modifications made and the new geometry of the ITk. In the following, these modifications with respect to the Run 2 configuration are discussed as well as their impact on the algorithm performance.

3.3.4.1. SV1 software changes for ITk

Minor modifications were made to the SV1 tagging software for the ITk upgrade studies. Forward tracks with $|\eta| > 2$ are no longer subjected to tighter conditions on the number of silicon hits which are applied as a mean to reject bad quality tracks at an early stage of the selection in the case of the current ID. The minimum requirement on the number of Strip hits is removed. Additionally, the requirements on the secondary vertex position allowing to reject vertices from hadronic interactions in the detector material, random crossing of two-tracks and photon conversion, were lifted as the tagging software was not updated to take into account the new geometry of the detector. There is, therefore room for improved performance once a specific and detailed SV1 optimization is conducted for ITk.

3.3.4.2. Updated reference histograms

The reference histograms used for the SV1 LLR formalism were updated based on the ITk $t\bar{t}$ sample with an average pile-up amount of 200. The software changes mentioned above were applied. The distributions of the main observables related to secondary vertices are shown for illustration in Figure 3.27 in the case of the ITk $t\bar{t}$ sample: the vertex mass (M), the jet charged energy fraction (E fraction) carried by the secondary vertex tracks and the number of two-track vertices. To build the reference histograms, the correlation of the first two variables is used after applying some transformations as shown in equation 3.2, and specific binnings are used for the histograms. Neither the transformations nor the binnings were reoptimized for ITk.

$$\begin{aligned} \text{M} &\longrightarrow \frac{\text{M}}{\text{M+1}} \text{ where M is in GeV} \\ \text{E fraction} &\longrightarrow (\text{E fraction})^{0.7} \end{aligned} \tag{3.2}$$

These updated reference histograms are also compared with the original Run 2 reference histograms, obtained with the Run 2 geometry and software, on the same $t\bar{t}$ sample but with an average pile-up of 30 and a center-of-mass energy of $\sqrt{s} = 13$ TeV . Figures 3.28, 3.29 and 3.30 show a comparison between the Run 2 and the ITk distributions for the number of two-track vertices (N2T), ΔR between the jet axis and the direction of the line joining the PV and SV and the transformed energy fraction *vs* the vertex mass distributions, respectively. Overall, the distributions are not extremely different. For the N2T distributions, the Run 2 sample tends to have slightly more two-track vertices on

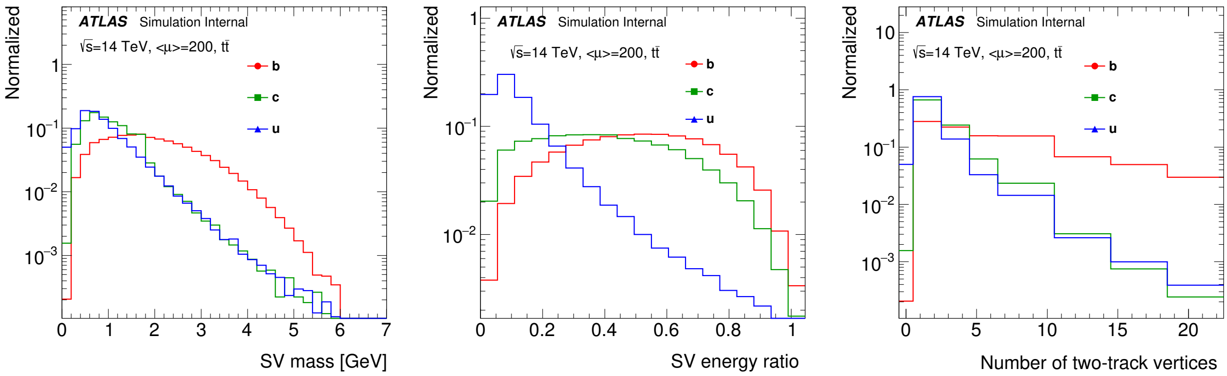

Figure 3.27.: Distributions of the main vertex properties exploited by the SV1 tagging algorithm for light-, b- and c-jets in the ITk $t\bar{t}$ sample: (left) vertex mass, (middle) jet charged energy fraction carried by the secondary vertex tracks and (right) number of two-track vertices.

average compared to the ITk sample for b-jets whereas it is the opposite for light-flavor jets. As for the ΔR distributions, the jet axis and the line joining the PV and SV seem closer in the ITk sample for b-jets with respect to the Run 2 sample, however, the situation is reversed for light-flavor jets. The two-dimensional distributions in Figure 3.30 illustrate that secondary vertices tend to be less energetic in the ITk sample, due to the contribution from forward jets. For clarity, a projection of those two-dimensional distributions is shown on Figure 3.31.

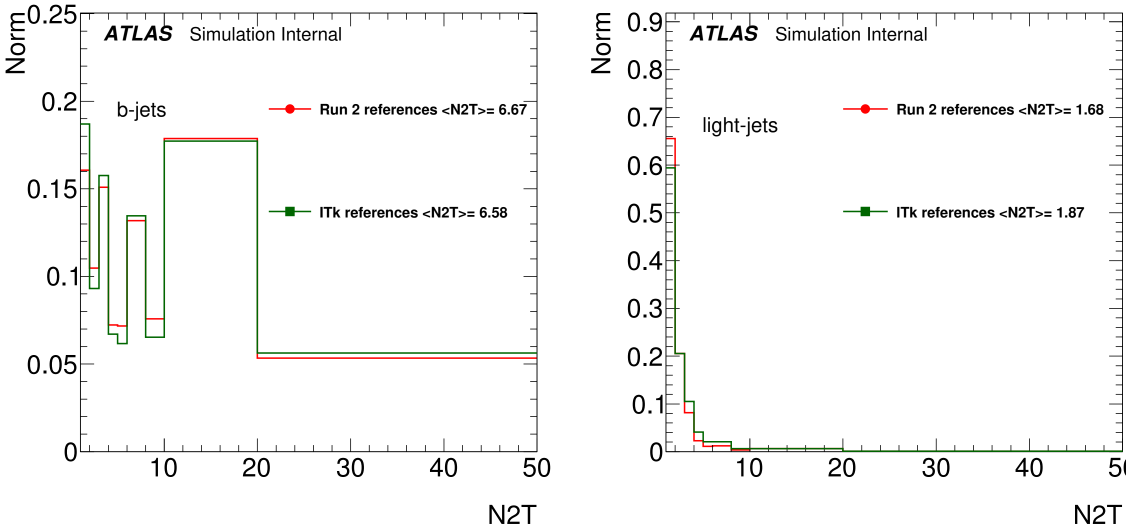

Figure 3.28.: Number of two-track vertices (N2T) exploited by the SV1 algorithm in (left) b-jets and (right) light-flavor jets. The distributions from Run 2 (red) and the new ITk (green) SV1 PDFs are compared.

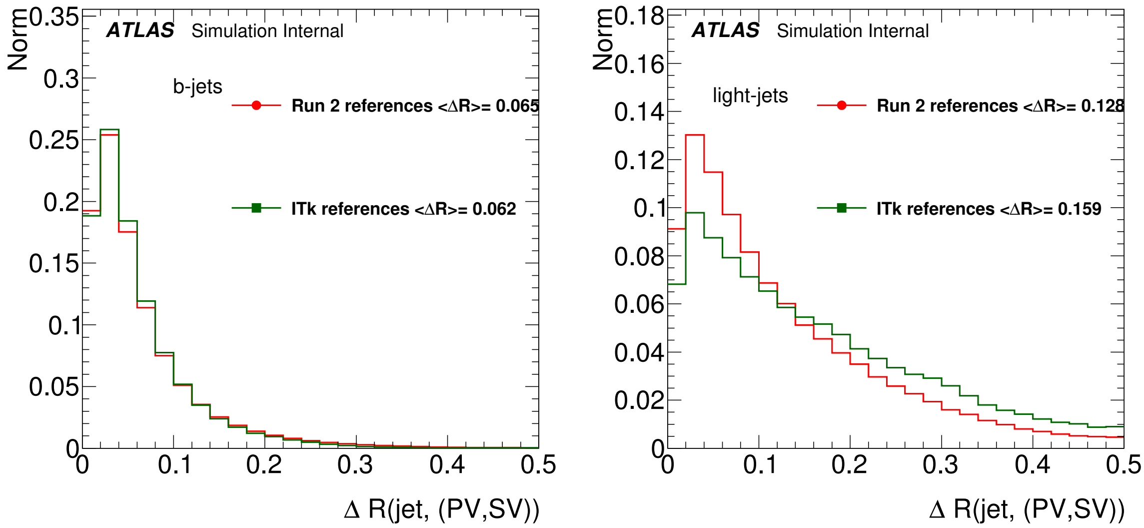

Figure 3.29.: ΔR separation between the jet axis and the line joining the primary vertex (PV) and secondary vertex (SV) for (left) b-jets and (right) light-flavor jets. The distributions from Run 2 (red) and the new ITk (green) SV1 PDFs are compared.

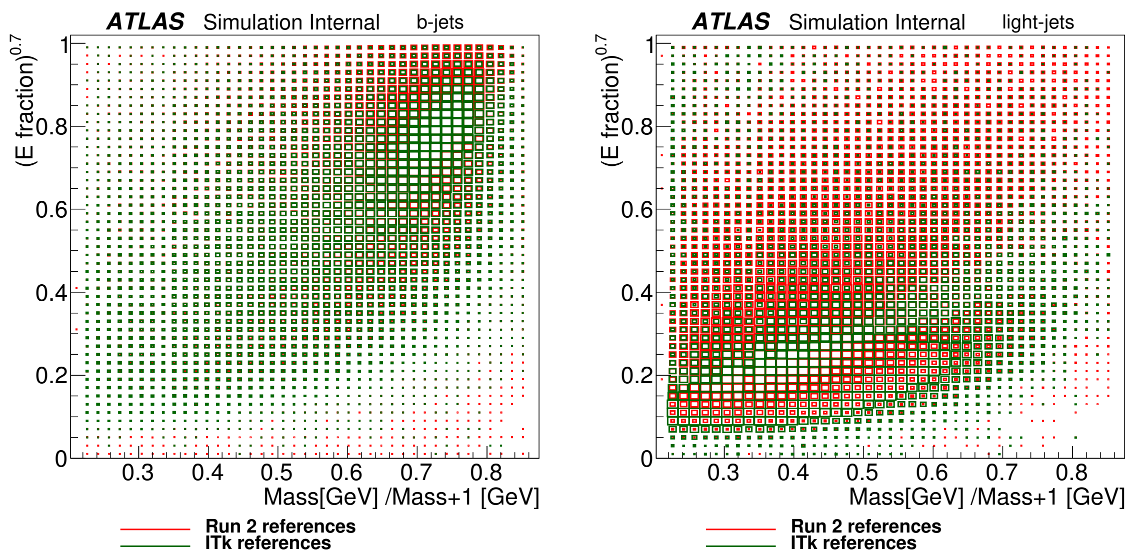

Figure 3.30.: Energy fraction, defined as the energy of the tracks in the secondary vertex (SV) relative to the energy of all tracks reconstructed within the jet, *vs* the SV invariant mass for (left) b-jets and (right) light-flavor jets. The distributions from Run 2 (red) and the new ITk (green) SV1 PDFs are compared. The variables transformation explained in the text is applied.

3.3.4.3. Impact on the SV1 performance

The impact of using the new ITk SV1 reference histograms on the performance of the tagger was assessed. Figure 3.32 depicts the SV1 performance, in terms of light-jet and charm-jet rejections *vs* b-tagging efficiency, when using the Run 2 references out-of-the-box and the new ITk references.

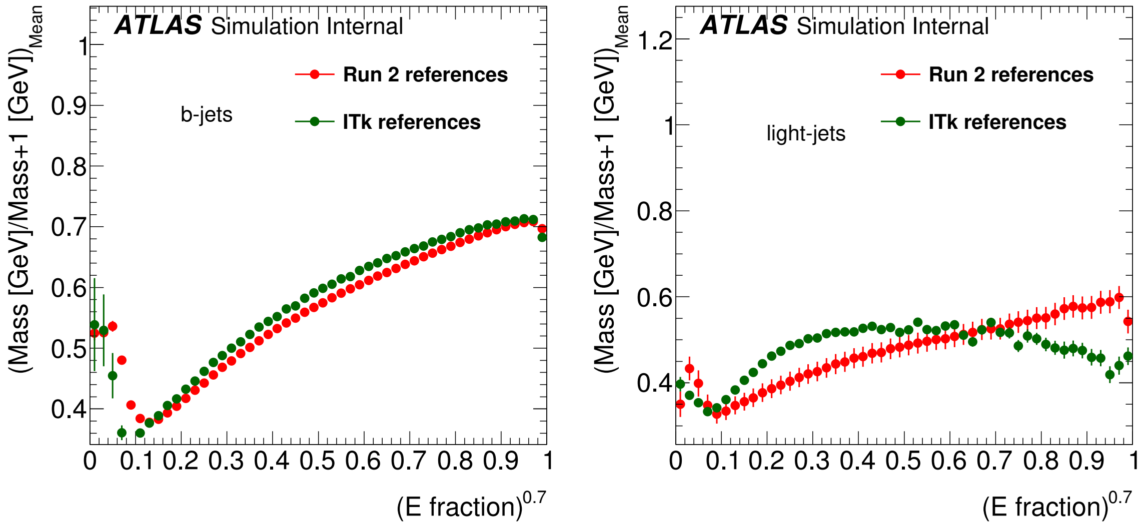

Figure 3.31.: Profile histogram of the bi-dimensional distributions of the transformed energy fraction *vs* vertex mass, for (left) b-jets and (right) light-flavor jets. The distributions from Run 2 (red) and the new ITk (green) SV1 PDFs are compared.

Making use of the updated ITk references leads to a better performance in terms of light-jet rejection. For instance, a gain of $\sim$ 30% in light-jet rejection at the 70% b-tagging efficiency working point is obtained using the ITk reference distributions. However, the charm-jet rejection is slightly worse with the ITk references, e.g a loss of $\sim$ 10% is observed at the 70% working point.

In Figures 3.33 and 3.34, the SV1 performance in different p_T and η regions is shown, comparing what is obtained with the ITk references with respect to using the Run 2 SV1 references. In terms of light-jet rejection, most of the improvement is obtained in the low p_T region (p_T < 70 GeV) as well as in the most forward regions ($|\eta| > 2$); the gain in the forward region is expected as the Run 2 references do not account for jets in that region. As for the charm-rejection, a degradation in performance is observed across all regions except for the most forward region ($3 < |\eta| < 4$).

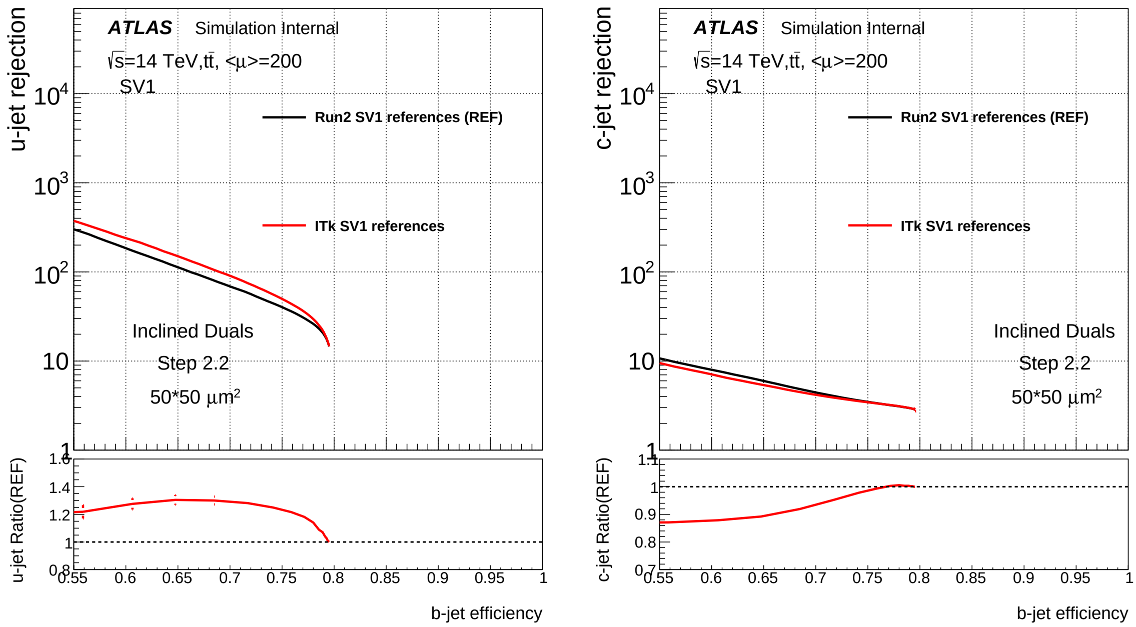

Figure 3.32.: Light-jet (left) and charm-jet (right) rejection *vs* b-tagging efficiency for SV1 evaluated in $t\bar{t}$ events with 200 pile-up for the ITk layout. The results obtained with the out-of-the-box Run 2 (black) and with the new ITk (red) PDFs are compared and their ratio is shown on the bottom pad.

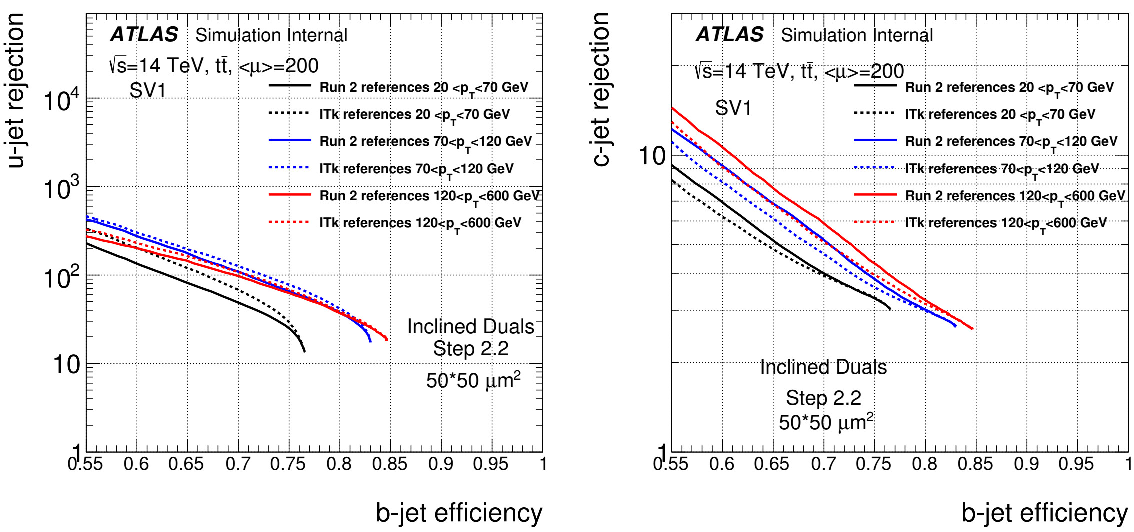

Figure 3.33.: Light-jet (left) and charm-jet (right) rejection *vs* b-tagging efficiency for SV1 evaluated in $t\bar{t}$ events with 200 pile-up for the ITk layout. The results obtained with the out-of-the-box Run 2 (solid line) and with the new ITk (dashed line) PDFs are compared in different p_T regions: $20 < p_T < 70$ GeV (black), $70 < p_T < 120$ GeV (blue) and $120 < p_T < 600$ GeV (red).

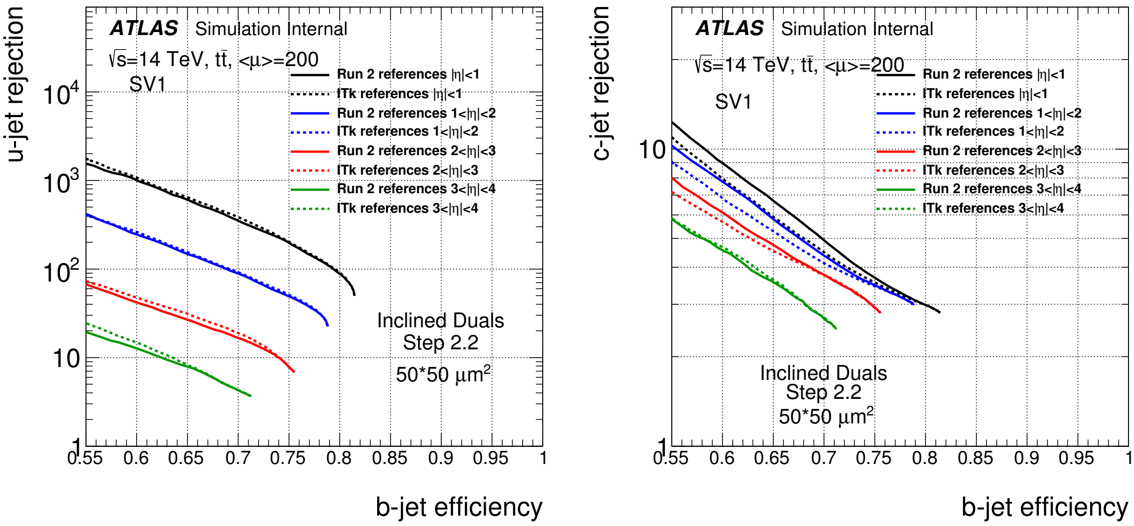

Figure 3.34.: Light-jet (left) and charm-jet (right) rejection *vs* b-tagging efficiency for SV1 evaluated in $t\bar{t}$ events with 200 pile-up for the ITk layout. The results obtained with the out-of-the-box Run 2 (solid line) and with the new ITk (dashed line) PDFs are compared in different η regions: $|\eta| < 1$ (black), $1 < |\eta| < 2$ (blue), $2 < |\eta| < 3$ (red) and $3 < |\eta| < 4$ (green).

3.3.5. MV2 optimization and performance

The MV2 BDT algorithm, as described in Section 3.1.2.3, combines the output of the basic taggers in order to achieve a better discrimination among the different jet flavors. To optimize MV2 for ITk, only the IP-based taggers optimization whereby the new ITk track categorization is adopted as baseline (cf. Section 3.3.2) is exploited, since the secondary vertex-based LLRs are not used by the BDT. The list of input variables in the algorithm has not been modified with respect to the set used for Run 2 b-tagging analyses, documented in Ref. [110].

The training of the multivariate discriminant is performed on b-, c- and light-flavor jets stemming from $t\bar{t}$ events. The transverse momentum and pseudo-rapidity of the jets are also included in the training but are reweighted in order to avoid differences in the kinematics being interpreted as discriminating by the training. The reweighting procedure is applied at the training stage of the classifier and is done in such a way as to match the spectrum of the light-flavor jets. The c-fraction included in the MV2 training has been set to 7% such that the training is performed by assigning b-jets as signal and a mixture of 93% of light-flavor jets and 7% of c-jets as background (MV2c10 setup). This choice is in line with the tagging algorithm available for Run 2 studies. It is possible to modify such a fraction in the training in order to enhance the light-flavor or the c-jet rejection. The training parameters characterizing the BDT network have not been optimized with respect to the configuration used for the Run 2 MV2 tagger algorithm, i.e. the minimum node size parameter defining the minimal fraction of jets in a leaf over the total number of jets in the training is set to 0.05%, the number of decision trees in the BDT forest is set to 1000 and their depth is 30. The MV2 training is performed on the Step 2.2 $t\bar{t}$ sample accounting for the ITk geometry and the HL-LHC operating conditions.

Figure 3.35 displays the results of the MV2 performance in terms of light-jet and c-jet rejections vs b-tagging efficiency obtained on the Step 2.2 sample. The performance achieved using the ITk setup is compared to that of Run 2 ($|\eta|$ coverage up to 2.5 with $\sim$ 30 interactions per bunch-crossing on average), depicted as green crosses, for the 60%, 70%, 77% and 85% b-tagging working points. The gain in performance with respect to Run 2 configuration in the region $|\eta|$ <2.5 is significant both for light-flavor and c-jet rejections. Although a small drop in rejection power is observed in the forward and very-forward η regions (2< $|\eta|$ <3 and 3< $|\eta|$ <4), the MV2 optimization for the ITk conditions allows to provide a remarkable discrimination power also in this very forward topology, as expected.

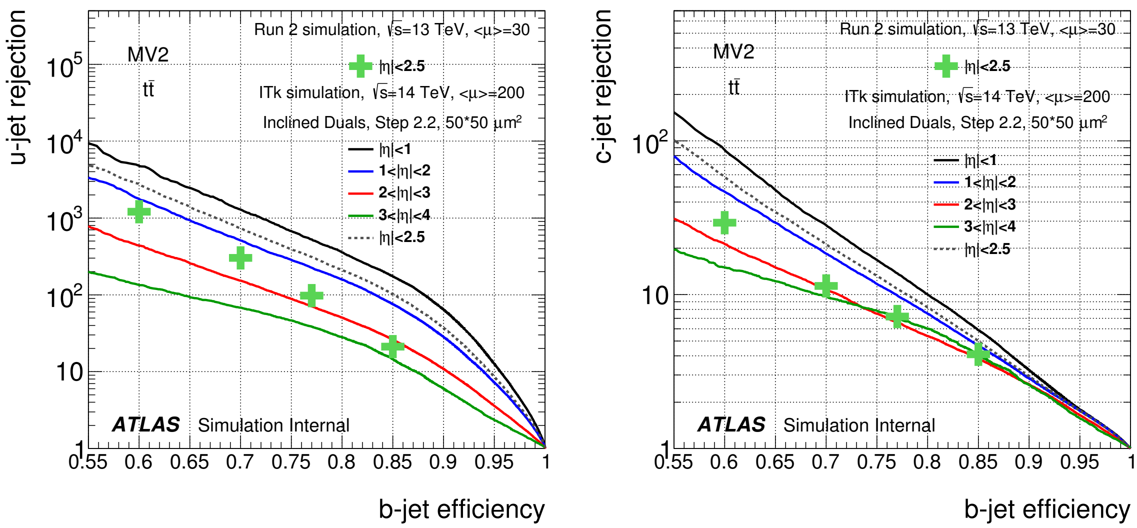

Figure 3.35.: Performance of the MV2 b-tagging algorithm for (left) light-jet and (right) c-jet rejection as a function of the b-jet efficiency in $t\bar{t}$ events with $\langle\mu\rangle$=200 pile-up using the Inclined Duals ITk geometry layout. For comparison purposes, the current performance for ATLAS Run 2 b-tagging (using Run 2 geometry layout with track pseudo-rapidity coverage up to $|\eta|$=2.5 and $<\mu>$=30) is shown as green crosses. Modulo a cosmetic change, these plots are the ones appearing in the Phase II ITk Pixel TDR [105].

.

3.4. *b*-tagging robustness checks for ITk

Assessing the impact of different operating conditions on the ITk performance, namely in terms of b-tagging, is an essential input to characterize the detector layout under consideration. In what follows, the studies that I performed to gauge the robustness of the optimized b-tagging algorithms response against various HL-LHC pile-up configurations and ITk dead pixel modules scenarios, are presented.

3.4.1. *b*-tagging performance for different pile-up scenarios

To assess the dependence of the b-tagging algorithms performance on pile-up, three additional ITk $t\bar{t}$ samples with lower pile-up ($\langle\mu\rangle$ = 140, $\langle\mu\rangle$ = 60 and $\langle\mu\rangle$ = 0) have been generated and utilized for this study. In Figure 3.36(a), the b-tagging performance of the IP3D tagger is shown for the different pile-up scenarios available: the performance is evaluated applying the template histograms built from the baseline $t\bar{t}$ sample with $\langle\mu\rangle$ = 200, *i.e* no dedicated training was applied for the lower pile-up samples. Noticeably, the light-jet rejection seems to degrade with the decreasing pile-up: for instance for $\langle\mu\rangle$ = 0, the light-jet rejection drops by ~ 30% at the 70% b-tagging efficiency working point, with respect to the case at $\langle\mu\rangle$ = 200. This loss in performance is in fact due to the reference histograms being inconsistent with the lower pile-up scenarios. Therefore it is important to employ dedicated reference histograms on each pile-up configuration in order to check the level of performance degradation attained by the algorithms. The results obtained with the dedicated templates are shown in Figure 3.36(b). As expected, the artificial loss in performance in the lower pile-up samples is mitigated by the use of the pile-up dedicated reference histograms. In particular, the lower pile-up samples exhibit a slightly better performance w.r.t the $\langle\mu\rangle$ = 200 baseline sample, as it should be.

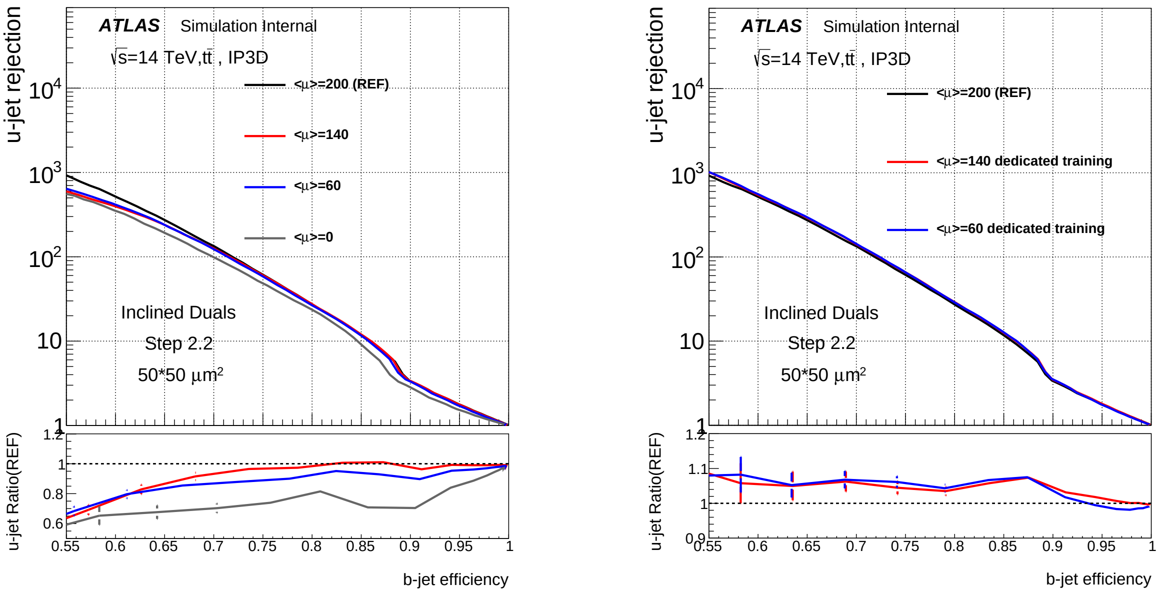

(a) (b)

Figure 3.36.: Light-jet rejection *vs* b-tagging efficiency of IP3D evaluated in $t\bar{t}$ samples, for the ITk layout, with different pile-up: $\langle\mu\rangle$ = 200 (black), $\langle\mu\rangle$ = 140 (red), $\langle\mu\rangle$ = 60 (blue) and $\langle\mu\rangle$ = 0 (grey). The performances are assessed making use of (a) the new ITk PDFs derived from the $t\bar{t}$ sample with 200 pile-up events and (b) using pile-up dedicated PDFs. The bottom pads show the ratio of the performances w.r.t the one obtained in the $t\bar{t}$ sample with a pile-up of 200.

Similar checks have been performed for MV2 in the context of the Run 2 b-tagging optimization campaign [110] and it was found that the BDT algorithm exhibits a 25% and 30% drop in light-flavour jet rejection at the 77% b-jet efficiency working point for $\langle\mu\rangle$=60 and $\langle\mu\rangle$=80 respectively. This behavior is confirmed with the ITk samples where the magnitude of the performance degradation was found to be even larger. The loss in MV2 performance is however mitigated when performing a dedicated training for the pile-up scenario considered.

Based on the above results, we concluded that the performance of the b-tagging algorithms optimized for ITk is resilient against different HL-LHC pile-up scenarios as long as dedicated reference histograms and BDT trainings are used.

3.4.2. b-tagging performance for different dead pixel modules scenarios

To test the robustness of the b-tagging algorithms response against the failures of the ITk Pixel Detector components, I checked several scenarios with different fractions of dead pixel modules for which samples were generated. In the following, three dead pixel modules scenarios are examined: 5%, 10% and 15% of random dead modules in the pixel volume.

The IP3D performance was evaluated for each of the above scenarios using the template PDFs derived considering the fully operational Pixel detector hypothesis *i.e* based on the nominal ITk $t\bar{t}$ sample with $\langle\mu\rangle$ = 200 (cf. Section 3.3.1). Figure 3.37 shows the IP3D performance obtained for each scenario compared to the nominal one where all pixel modules are active. As expected, the IP3D performance degrades with the increasing fraction of dead pixel modules. Particularly, the light-jet rejection worsens by around 65% at the 70% b-tagging efficiency working point in the case where 15% of the pixel modules are not operational. Figure 3.38, depicts the degradation of the IP3D performance in the central and forward η regions for each of the considered scenarios. Interestingly, the degradation is more pronounced in the central region ($|\eta| < 2.5$) compared to the forward region. This is explained by the fact that the IP3D algorithm relies on the tracks hit information in the central region of the detector to categorize them and eventually compute the LLR whereas the multiple scattering parameter γ is used in the forward region.

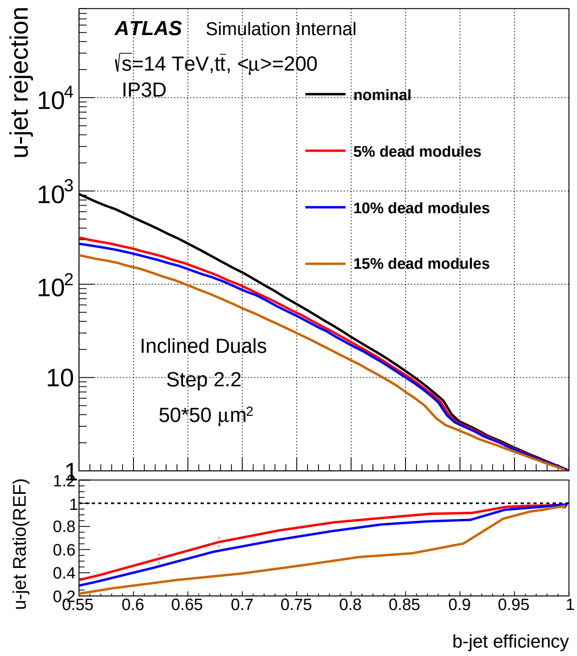

Figure 3.37.: Light-jet rejection Vs b-tagging efficiency of IP3D evaluated in $t\bar{t}$ events with 200 pile-up for the ITk Step 2.2 layout. The performance obtained for different dead pixel modules scenarios is compared to the nominal case (black) where the ITk pixel detector is fully operational; three dead pixel modules scenarios are considered: 5% (red), 10% (blue) and 15% (brown) dead modules. The bottom pad shows the ratios with respect to the performance obtained in the nominal case, for each of the tested scenarios.

The MV2 performance obtained for each of the considered dead pixel modules scenarios was also assessed and compared to the nominal one as shown in Figure 3.39. Similarly, the MV2 performance degrades with the increasing fraction of dead pixel modules e.g for the 15% dead modules case, the effect on the MV2 is significant: the light-jet rejection degrades by ~ 80% at the 70% b-tagging efficiency working point. Unlike IP3D, the performance degradation for MV2 does not depend on η and is quite significant everywhere as illustrated in Figure 3.40.

To see if the degradation in b-tagging performance can be partially restored if the algorithms are retrained taking into account the modified pixels configuration, I produced dedicated IP3D template PDFs based on the 10% dead pixel modules sample and used them to reassess both the IP3D and MV2 performances on this sample. Figure 3.41 shows that making use of these dedicated PDFs helps mitigating the drop in IP3D performance: the light-jet rejection degradation w.r.t the nominal case (fully operational detector) lessens, going from around 40% to 20% at the 70% b-tagging efficiency working

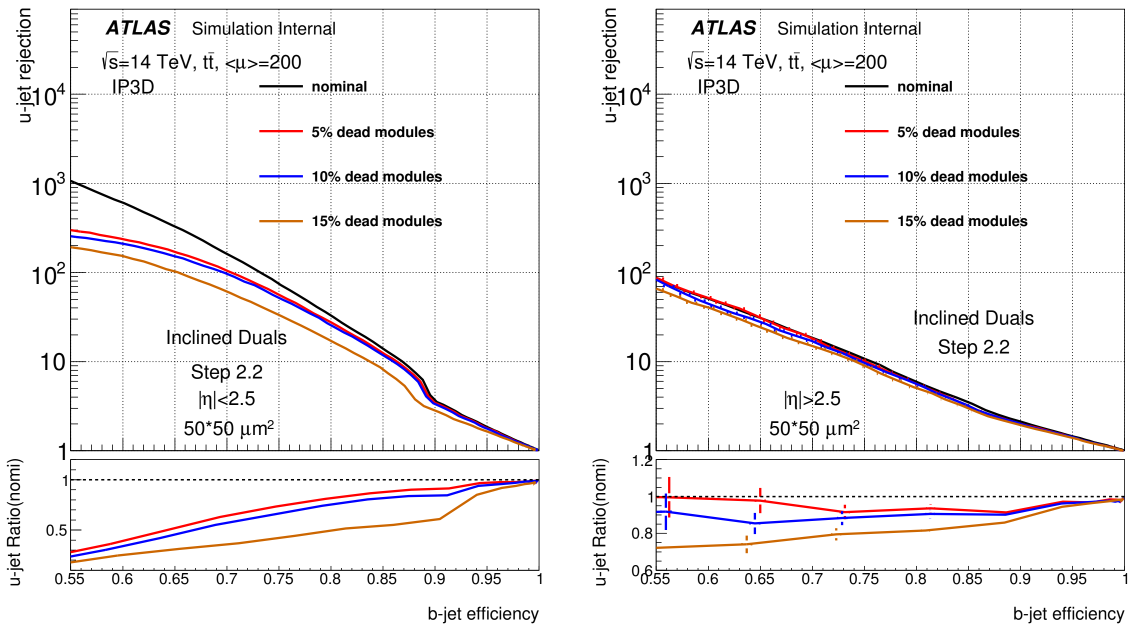

Figure 3.38.: Light-jet rejection Vs b-tagging efficiency of IP3D evaluated in $t\bar{t}$ events with 200 pile-up for the ITk Step 2.2 layout. The performance obtained for different dead pixel modules scenarios is compared to the nominal case (black) where the ITk pixel detector is fully operational. The comparisons are depicted in different η regions: (left) $|\eta| < 2.5$ and (right) $|\eta| > 2.5$. Three dead pixel modules scenarios are considered: 5% (red), 10% (blue) and 15% (brown) dead modules. The bottom pad shows the ratio for each of the tested scenarios performance with respect to that obtained in the nominal case.

point. For completeness, Figure 3.42 depicts the IP3D performance obtained using the dedicated PDFs compared to the case where the baseline PDFs were used, in exclusive η regions. As for MV2, the dedicated retraining on the updated pixel conditions largely mitigates the performance degradation and reduces the drop in the MV2 rejection power down to a level of approximately 10% at the 77% b-jet efficiency working point as shown in Figure 3.43.

The results of the above checks confirm that the expected performance degradation of the optimized b-tagging algorithms, resulting from potential failures in the ITk pixel detector components, can be partially mitigated when using dedicated reference histograms and BDT trainings which take into account the detector conditions.

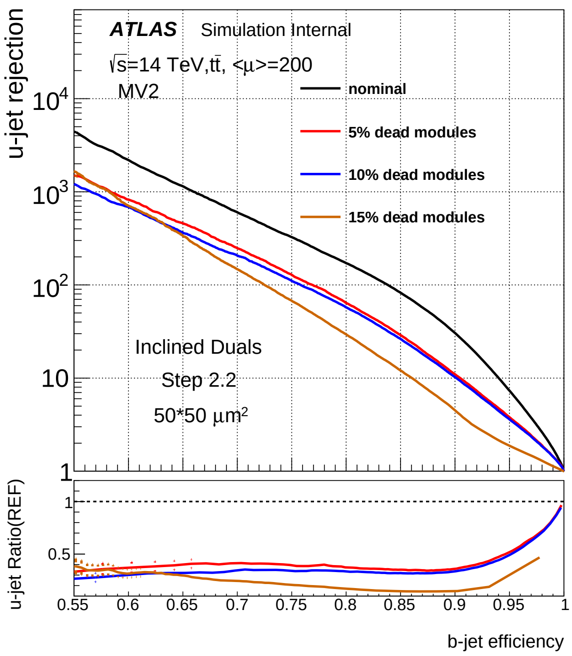

Figure 3.39.: Light-jet rejection Vs b-tagging efficiency of MV2 evaluated in $t\bar{t}$ events with 200 pile-up for the ITk Step 2.2 layout. The performance obtained for different dead pixel modules scenarios is compared to the nominal case (black) where the ITk pixel detector is fully operational; three dead pixel modules scenarios are considered: 5% (red), 10% (blue) and 15% (brown) dead modules. The bottom pad shows the ratio for each of the tested scenarios performance with respect to that obtained in the nominal case.

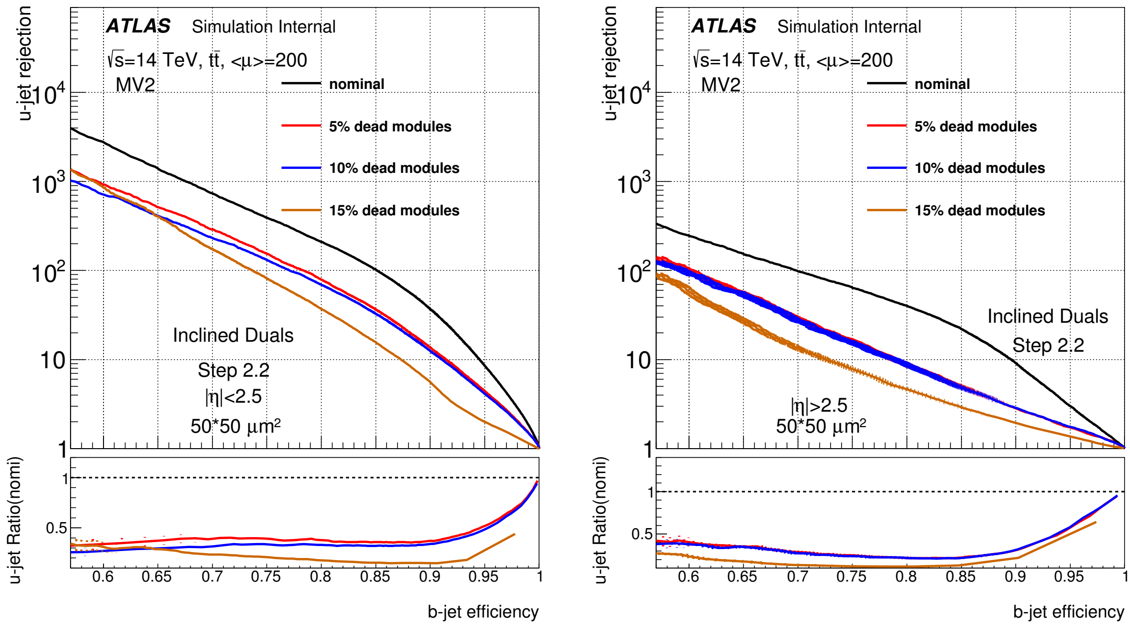

Figure 3.40.: Light-jet rejection Vs b-tagging efficiency of MV2 evaluated in $t\bar{t}$ events with 200 pile-up for the ITk Step 2.2 layout. The performance obtained for different dead pixel modules scenarios is compared to the nominal case (black) where the ITk pixel detector is fully operational. The comparisons are depicted in different η regions: (left) $|\eta| < 2.5$ and (right) $|\eta| > 2.5$. Three dead pixel modules scenarios are considered: 5% (red), 10% (blue) and 15% (brown) dead modules. The bottom pad shows the ratio for each of the tested scenarios with respect to that obtained in the nominal case.

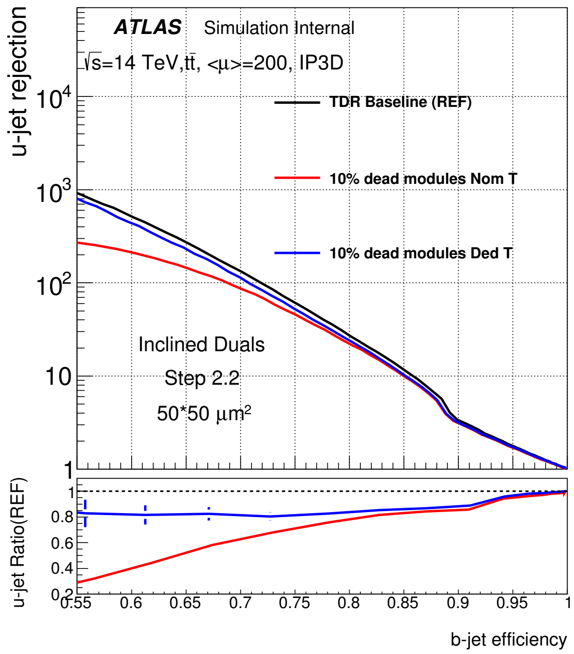

Figure 3.41.: Light-jet rejection Vs b-tagging efficiency of IP3D evaluated in $t\bar{t}$ events with 200 pile-up for the ITk Step 2.2 layout. The performances obtained in the case where 10% of the pixel modules are turned off, using the baseline PDFs (red), derived in the case of a fully operational detector, and the dedicated PDFs (blue) generated based on the 10% dead pixel modules sample are compared to the nominal case (black) where the ITk pixel detector is fully operational. The bottom pad shows the ratio of each of the above cases performance with respect to that obtained in the baseline configuration.

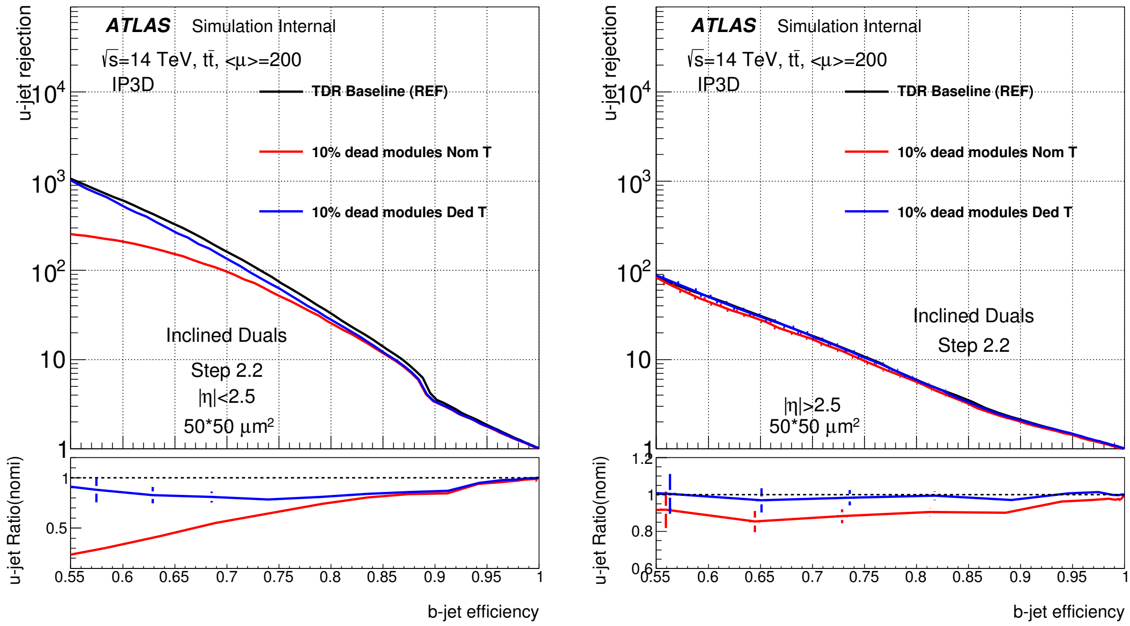

Figure 3.42.: Light-jet rejection Vs b-tagging efficiency of IP3D evaluated in $t\bar{t}$ events with 200 pile-up for the ITk layout. The performances obtained in the case where 10% of the pixel modules are turned off, using the baseline PDFs (red), derived in the case of a fully operational detector, and the dedicated PDFs (blue) generated based on the 10% dead pixel modules sample are compared to the nominal case (black) where the ITk pixel detector is fully operational. The comparisons are shown in different η regions: (left) $|\eta| < 2.5$ (left) and (right) $|\eta| > 2.5$. The bottom pad shows the ratio of each of the above cases performance with respect to that obtained in the baseline configuration.

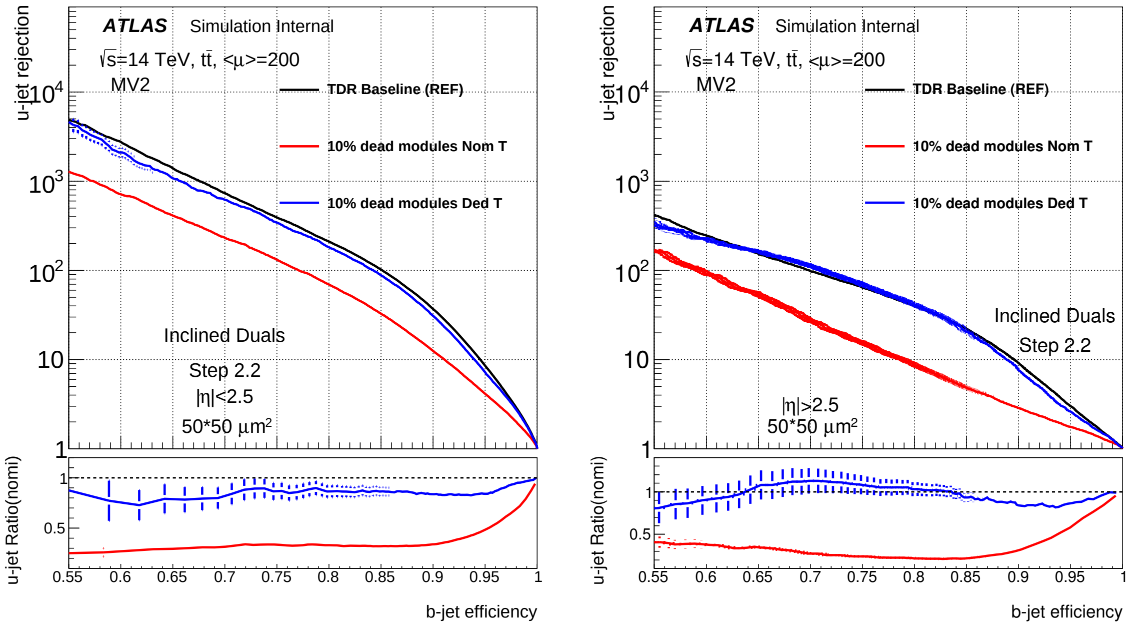

Figure 3.43.: Light-jet rejection Vs b-tagging efficiency of MV2 evaluated in $t\bar{t}$ events with 200 pile-up for the ITk layout. The performances obtained in the case where 10% of the pixel modules are turned off, using the nominal training (red), derived in the case of a fully operational detector, and the dedicated training (blue) generated based on the 10% dead pixel modules sample are compared to the nominal case (black) where the ITk pixel detector is fully operational. The comparisons are shown in different η regions: (left) $|\eta| < 2.5$ and (right) $|\eta| > 2.5$. The bottom pad shows the ratio of each of the above cases performance with respect to that obtained in the baseline configuration.

3.5. Summary

b-tagging plays a crucial role in many physics analyses, not only at the LHC but also at the foreseen HL-LHC. Within ATLAS, *b*-tagging algorithms rely heavily on the tracking information provided by the Inner Detector and were optimized based on its layout. However, the ID will have reached its lifetime by the end of Run 3 in 2024 and will not be able to operate under the extreme conditions of HL-LHC. This is why, it will be entirely replaced by the Inner Tracker (ITk) as part of the Phase II upgrade program. The ITk will employ novel design technologies to improve the tracking efficiency and performance under harsh pile-up conditions ($\langle\mu\rangle = 200$) and will extend the tracking coverage to large pseudorapidities ($|\eta| = 4$). *b*-tagging is one of the key benchmarks used to inform the design of the ITk layout since it is essential to at least maintain and possibly improve on the Run 2 *b*-tagging performance. To this end, the current *b*-tagging algorithms need to be reoptimized in accordance with the new ITk geometry.

The impact-parameter based algorithms rely on an LLR formalism exploiting tracks categories with dedicated PDFs derived based on simulation in order to compute the *b*-tagging discriminant. The first step towards optimizing these taggers in the context of the ITk upgrade, is to redefine the track categories to reflect the new tracker geometry since the Run 2 categories which were designed based on the ID geometry will become obsolete. In this respect, I first assessed the *b*-tagging performance obtained with three preliminary configurations of track categories defined for ITk. To do so, I built a framework allowing to extract PDFs for each of these configurations and used them to compute the *b*-tagging discriminant in each case. I quantified the gain in IP3D performance achieved with the ITk tracks configurations compared to that obtained when using out-of-the-box Run 2 PDFs. Based on these comparisons, I proposed a new track categorization which combines features from the preliminary ones in order to maximize the attained gain in performance. Utilizing the new categorization enhances significantly the *b*-tagging performance of the IP3D algorithm (around 100% gain in light-jet rejection at the 70% *b*-tagging efficiency working point) compared to using out-of-the-box Run 2 categories configuration. This optimal ITk track categorization was adopted as baseline for the IP taggers within the scope of the *b*-tagging upgrade studies. Moreover, I compared the performance of the IP3D tagger achieved with ITk after the dedicated optimization to that obtained with the current ATLAS ID with the Run 2 setup. This illustrated that the ITk is not only able to restore the performance of the current detector despite the harsher pile-up conditions but also outperforms it.

The optimization of the secondary-vertex finding algorithm is needed as well to exploit fully the capabilities of the new tracker. The SV1 algorithm, similarly to the IP taggers, utilizes simulation-based reference distributions to evaluate the *b*-tagging LLR discriminant. Although no dedicated optimization was conducted for this tagger at the time of performing these studies, minor modifications were made to the secondary-vertex finding software to take the ITk geometry into account. I generated the SV1 reference distributions incorporating these updates and used them to assess the tagger performance under the ITk scenario. The use of the ITk PDFs allows to enhance the light-jet rejection by around 30% at the 70% *b*-tagging efficiency working point compared to that obtained with the Run 2 references. There is room for more improvement once a dedicated optimization of this tagger takes place.

The optimization of the MV2 tagger for ITk was realized through the retraining of its BDT with the input IP taggers utilizing the optimal ITk track categorization for the LLR discriminant evaluation. I characterized the performance of the tagger after this optimization and compared it to that attained with Run 2 configuration. A significant gain is achieved in the background rejection in the central region of the ITk in comparison with the Run 2 setup. Even though the rejection power is lower in the ITk forward regions, the optimized tagger still provides a notable discrimination power in these regions.

To characterize the ITk layout, it is necessary to probe the impact of different operating conditions on the detector performance especially in terms of *b*-tagging. In this regard, I gauged the robustness of the optimized *b*-tagging algorithms response against various HL-LHC pile-up configurations and ITk dead pixel modules scenarios. I found the performance of the *b*-tagging algorithms to be resilient against the different tested pile-up conditions provided that dedicated reference histograms and MV2 BDT training are employed. Moreover, the expected degradation in performance induced by potential failures in the ITk pixel detector components can be partially mitigated if these detector conditions are accounted for in the reference histograms extraction and MV2 BDT training.

4. Measurement of $t\bar{t}$ pair production in association with heavy flavor jets with ATLAS

The Measurement of the top quark pair production in association with additional heavy flavor jets ($t\bar{t}$ + HF), especially b-jets ($t\bar{t} + b\bar{b}$) is of great importance in the top quark physics sector as well as in the search for the Standard Model (SM) Higgs boson and new physics phenomena. Inclusive and differential cross-section measurements of $t\bar{t} + b\bar{b}$ production performed using data recorded by the ATLAS detector in 2015 and 2016, are presented in Section 4.1. The measurements are unfolded to the particle level in a well defined fiducial volume. Particular emphasis is put on the simulation studies that I conducted to assess the purity of the $t\bar{t} + b\bar{b}$ data sample in the single lepton channel, prior to the unfolding step. The measured cross-sections are in agreement with the various QCD predictions available for the process within uncertainties but are not sensitive enough at this stage, to indicate which of these predictions is best at describing data. This is why, I propose a new approach in Section 4.2, to further enhance the sensitivity of these measurements. The novel technique that I developed to implement this approach, based on the use of a boosted decision tree, is also presented.

4.1. Overview of the Run 2 measurement of the $t\bar{t}$ + HF production

4.1.1. Motivation

The measurements of the $t\bar{t}$ pair production in association with additional jets play a key role in testing the SM QCD predictions. Particularly, the process where the $t\bar{t}$ pair is produced with additional b-jets ($t\bar{t} + b\bar{b}$), depicted in Figure 4.1, is quite essential to measure as large theoretical uncertainties intervene in its computation.

State-of-the-art QCD calculations provide predictions for the cross-section of the $t\bar{t}$ production with up to two additional massless partons (so-called five flavor scheme, 5FS) at the next-to-leading-order (NLO) accuracy in the Matrix Element (ME) in QCD, matched to a parton shower. Moreover, dedicated calculations of QCD production of $t\bar{t} + b\bar{b}$ at NLO in the ME where the additional b-quarks are massive (so-called four flavor scheme, 4FS), are also available. Significant modeling differences are seen among these various calculations especially in the kinematic distributions characterizing the additional $b\bar{b}$-system. This is why inputs from experimental measurements of the $t\bar{t} + b\bar{b}$ process are highly anticipated to confront these MC models with data, allowing to constrain them and subsequently improve the $t\bar{t}+b\bar{b}$ modeling namely in terms of the additional b-jets properties. A better understanding of the QCD production of $t\bar{t} + b\bar{b}$ as predicted by the SM would benefit greatly the analyses in which the background is overwhelmed by this process as it is the case for the $t\bar{t}H(H \to b\bar{b})$ analysis where the sensitivity to the signal is primarily limited by the mismodeling of $t\bar{t} + b\bar{b}$ (see Chapter 5).

In the following, an overview of the analysis conducted to measure the inclusive and differential production cross-sections of the $t\bar{t}+b\bar{b}$ process [111] based on the data collected by the ATLAS detector in 2015 and 2016, is given. It is worth noting that in this analysis, no attempt is made to distinguish between additional b-jets and those originating from the $t\bar{t}$ system. To this end, a proposal to improve further on the sensitivity of these measurements by taking advantage of the explicit identification of the b-jets origin is presented in Section 4.2.3.

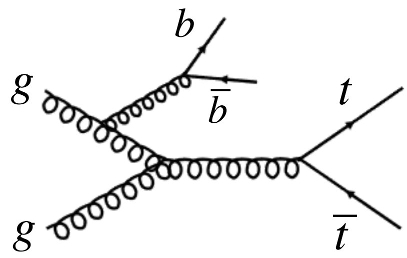

Figure 4.1.: An example leading order Feynman diagram of the QCD $t\bar{t}+b\bar{b}$ production.

4.1.2. Data and Monte Carlo simulation samples

The data used for the $t\bar{t}+b\bar{b}$ measurements presented in this document were recorded by the ATLAS detector in 2015 and 2016 during pp collisions at a center-of-mass energy of $\sqrt{s}$ = 13 TeV corresponding to an integrated luminosity of 36.1 fb^{-1}.

The Monte Carlo (MC) samples used to predict the signal and background composition of the selected data sample, to derive corrections for detector and acceptance effects and to estimate systematic uncertainties are presented below.

The nominal $t\bar{t}$ MC sample was produced using the Powheg-Box generator [66–68] at NLO accuracy in QCD with the NNPDF3.0NLO set of parton distribution functions (PDF) [112] in the ME computation. The modeling of the parton shower, fragmentation and the underlying event was performed using Pythia 8 with the NNPDF2.3LO PDF sets and the corresponding A14 set of tuned parameters [113]. The h_{damp} parameter which regulates the transverse momentum of the hardest additional parton emission beyond the $t\bar{t}$ system was set to 1.5 times the top quark mass [114]. In this sample, additional jets including b-jets, come from the hardest additional parton emission and parton showering. In what follows, the nominal sample is referred to as *PWG+PYT8* .

Processes where the W, Z or the Higgs boson is produced with a $t\bar{t}$ pair were modeled using the Madgraph5_aMC@NLO generator [115, 116] at NLO in QCD for the ME calculation. The parton shower, fragmentation and underlying event were simulated using Pythia 8 with the A14 set of tuned parameters. The NNPDF3.0NLO PDF set was used in the ME while the NNPDF2.3LO PDF set was used in the parton shower. The Higgs boson mass was set to 125 GeV in the case of the $t\bar{t}H$ sample and all decay modes were allowed based on the latest branching ratios available [29]. The $t\bar{t}W$ and $t\bar{t}Z$ samples are normalized to the cross-sections calculated to the NLO in QCD while the $t\bar{t}H$ sample is normalized to a cross-section computed to NLO accuracy in QCD including electroweak corrections [28].

Although the aim of this analysis is to improve the modeling of the QCD production of the additional b-jets in $t\bar{t}$ events, the production of these jets via $t\bar{t}$, $t\bar{t}H$ and $t\bar{t}V$ modes is treated collectively as the signal process without separating among them.

Alternative $t\bar{t}$ samples were also generated to estimate the uncertainties associated with a given choice of QCD MC model describing the b-jets properties, and to compare with data. The effect of the parton shower choice is estimated using a MC sample generated by interfacing Powheg-Box with HERWIG 7 using the H7UE set of tuned parameters [75]. This sample is referred to as *PWG+HW7* in the following. The uncertainties associated with the choice of the QCD scales, the NLO matching algorithm used in the $t\bar{t}$ ME calculation and the parton shower to predict additional b-jets, are assessed using a MC sample generated with the Sherpa 2.2.1 generator [117] which models the zero and one additional parton process at NLO accuracy and up to four additional partons at LO accuracy using the MEPS@NLO prescription [69]. In this case, the ME calculation is interfaced with a dedicated parton shower. This sample is referred to as *SHERPA* hereafter. Furthermore, a $t\bar{t}$ sample was generated using the Madgraph5_aMC@NLO generator interfaced to Pythia 8 and is referred to as aMC@NLO+PYT8 below. This sample is used to evaluate the fraction of $t\bar{t}$ +V/H events in selected $t\bar{t}$ events and to compare with the data (see Section 4.1.7). All $t\bar{t}$ samples are normalized to a cross-section of 832^{+46}_{-51} pb calculated at the next-to-next-to-leading-order (NNLO) in QCD including resummation of next-to-next-to-leading-log (NNLL) soft gluon terms [118].

The remaining $t\bar{t}$ samples used for systematics as well as for comparisons with data are described in details in ref [111]. Furthermore, the MC samples set-ups used to model the considered background processes (single top quark, Z/W+jets and diboson production) are also described therein.

4.1.3. Detector and particle-level objects

In the following, a brief description of the reconstruction and identification criteria applied to the detector-level (also referred to as reco-level) electrons, muons, jets and b-jets used in the analysis, is given together with the definitions adopted for their particle-level (or truth-level) counterparts.

Detector-level muons and electrons are reconstructed based on the ATLAS standard procedures described in sections 2.4.2 and 2.4.3, respectively. Electron candidates are required to have $p_T > 25$ GeV and $|\eta| < 2.47$; those falling in the barrel-endcap calorimeter transition region i.e $1.37 < |\eta| < 1.52$ are poorly measured and thus are discarded in this analysis. Candidate muons are subjected to the following kinematic cuts: $p_T > 25$ GeV and $|\eta| < 2.5$. Electrons and muons must satisfy the tight and medium identification criteria, respectively. Both are required to be isolated using the gradient isolation working point. Cuts are applied on the charged leptons longitudinal impact parameter, $|z_0 \sin\theta| < 0.5$ mm, and on the transverse impact parameter significance, $|d_0|/\sigma_{d_0} < 5(3)$ for electrons (muons), to ensure that the associated tracks are consistent with originating from the hard scatter vertex. For the particle-level leptons, only those not coming from hadron decays are considered in the analysis; the muons and electrons from τ decays are hence included. For the fiducial phase space definition, they are required to pass $p_T > 25$ GeV and $|\eta| < 2.5$.

Reco-jets are built using the topoclusters in the calorimeters as inputs to the anti-k_t algorithm with a distance parameter of 0.4 as described in section 2.4.4. They are required to have $p_T > 25$ GeV and $|\eta| < 2.5$ in accordance with the detector acceptance. Jets with $p_T < 60$ GeV and $|\eta| < 2.4$ are required to be identified as originating from the primary vertex using the JVT algorithm. For the truth-jets, stable particles[a] except for those identified as electrons or muons using the corresponding particle definitions above and the neutrinos not from hadron decays, are used as inputs to the anti-k_t algorithm with the same distance parameter as the reco-jets. Particles from pile-up events are not included in the truth-jets while those from the underlying event are considered; the decay products of the hadronically decaying τ lepton are also included. Truth-jets are subjected to the same kinematic cuts as the reco-jets for the fiducial phase space definition.

Reco-jets containing b-hadrons are identified based on the multivariate discriminant, MV2c10 (cf. Section 3.1.2.3). Four working points are defined with different thresholds on the b-tagging discriminant output, corresponding to efficiencies of 85%, 77%, 70% and 60% for b-jets in simulated $t\bar{t}$ events with $p_T > 20$ GeV and to rejection factors from 3-35 for c-jets and 30-1500 for light flavor jets. On the other hand, truth-jets are identified as b-jets by requiring that at least one b-hadron with $p_T > 5$ GeV is matched to the jet by ghost association [119]. This procedure includes b-hadrons in the jet clustering after scaling their p_T to an infinitely small value. A similar approach is followed for c-jets with the b-jets definition checked first. Jets that were not matched to either a b-hadron or a c-hadron are considered to be light-flavor jets. This definition is used for the cross-section measurements presented in Section 4.1.7. However, for the studies presented in sections 4.1.6.1, 4.2.1 and 4.2.2, the labeling of b-jets is based on a ΔR matching to hadrons instead; the difference between the two procedures was

[a]Stable particles, in the scope of this document, are particles that have a proper lifetime greater than 30 ps.

found to be negligible based on previous studies [120]. For the ΔR matching procedure, the flavor of a jet is determined by counting the number of b- or c-hadrons within $\Delta R < 0.4$ of the jet axis.

4.1.4. Event selection

Data events are selected using single lepton triggers requiring a $p_T > 20(26)$ GeV for muons and $p_T > 24(26)$ GeV for electrons for the 2015 (2016) dataset with additional lepton quality and isolation criteria. These triggers are combined with others with higher p_T thresholds but loosened isolation requirements.

Two channels are considered in this analysis depending on how the W bosons originating from the top quarks decay: the eμ (dilepton) channel in which both W bosons decay leptonically, one into a muon and muon neutrino and the other into an electron and electron neutrino, and the lepton+jets (single lepton) channel where one W boson decays leptonically and the other hadronically. The detector-level cuts adopted in each of these channels which are designed to select events with at least one additional b-jet, are presented below.

In the dilepton channel, events are required to have exactly one electron and one muon of opposite electric charge and with $p_T > 27$ GeV each. For the baseline selection, events are further required to have at least two jets, two of which at least are b-tagged at the 77% working point. The measurements of the inclusive cross-sections with one and two additional b-jets are performed requiring at least three and at least four b-tagged jets, respectively. For the differential cross-section measurements, at least three jets of which at least three must be b-tagged are required, except for the b-jet multiplicity distribution where the baseline selection is considered.

In the single lepton channel, events must have exactly one lepton with $p_T > 27$ GeV , at least five jets of which two at least must be b-tagged at the tighter 60% working point[b] for the baseline selection. For the measurement of the inclusive cross-section with one (two) additional b-jets, events must have at least five (six) jets, of which at least three (four) are b-tagged. The measurement of the differential cross-sections requires at least 6 jets, four of which at least are b-tagged. More emphasis is put on this channel in the remainder of this chapter.

4.1.5. Background estimation

After the baseline selection of events with a least two b-tagged jets, a small amount of backgrounds from non-$t\bar{t}$ processes persists; these do not include the $t\bar{t}V$ and $t\bar{t}H$ productions which are treated as signal. Section 4.1.5.1 gives a brief description of the non-$t\bar{t}$ backgrounds considered in this analysis. On the other hand, backgrounds arising from $t\bar{t}$ production in association with additional light-flavor or c-jets are estimated based on a template fit to data as explained in section 4.1.5.2.

4.1.5.1. Non-$t\bar{t}$ backgrounds

The non-$t\bar{t}$ backgrounds can be divided into two types. The first one corresponds to those with prompt leptons from single top, W or Z decays (including those arising from leptonic τ decays). The single top background intervenes in both single lepton and dilepton channels and is estimated from MC predictions. A small number of events from the Z/γ^* + jets background enters the two channels under consideration and its estimation also relies on the MC predictions. However, in the dilepton channel, the predictions are scaled to data with scale factors derived from $Z \to ee/\mu\mu$ events. A small background from W+jets events remains in the single lepton channel after the event selection and it is obtained directly from MC simulation.

[b] A tighter working point is adopted in this channel to better suppress c-jets from W boson decays.

The second type of non-$t\bar{t}$ backgrounds concerns those where at least one of the reconstructed lepton candidates is either non-prompt (i.e lepton from b-/c-hadrons decay, electron from photon conversion) or fake (i.e from hadronic jet activity misidentified as an electron). In the dilepton channel, the normalization of this background is estimated from data using same sign dilepton events scaled by a transfer factor derived from simulation as described in ref [121]. In the single lepton channel however, a fully data-driven approach based on the matrix method [122] is used to estimate this background.

4.1.5.2. $t\bar{t}$-related backgrounds

The fiducial cross-sections are extracted from detector-level data distributions obtained after applying the event selections described in section 4.1.4 and subtracting the non-$t\bar{t}$ backgrounds presented in section 4.1.5.1. However, even after the latter step, the resulting data sample is not pure in $t\bar{t}$ events with additional b-jets ($t\bar{t}b$) and is still contaminated by backgrounds from $t\bar{t}$ processes with additional light-flavor ($t\bar{t}l$) or c-jets ($t\bar{t}c$) misidentified as b-jets by the b-tagging algorithm. The MC predictions of these backgrounds are affected by large uncertainties. This is why, correction factors for $t\bar{t}b$, $t\bar{t}c$ and $t\bar{t}l$ are measured in data and applied to the corresponding predictions prior to the unfolding procedure presented in section 4.1.6.2.

The correction factors for the yields of the $t\bar{t}b$ signal and $t\bar{t}c/t\bar{t}l$ backgrounds are extracted based on template fits to data. The templates for these processes are constructed from $t\bar{t}$, $t\bar{t}V$ and $t\bar{t}H$ MC samples since the signal takes into account the contributions of $t\bar{t}V$ and $t\bar{t}H$. The analysis regions considered for the template fits consist of events with at least three b-tagged jets at the 77% working point among those selected in the dilepton channel while events with at least 5 jets and at least two b-tagged jets at the 60% working point are used in the single lepton channel. The latter suffers from an additional background arising from $W^+ \rightarrow c\bar{s}$ or the corresponding W^- decays in the inclusive $t\bar{t}$ process where the c-jet is misidentified as a b-jet. Events with only one particle-level c-jet are attributed to this background and are grouped into a $t\bar{t}l$ class to separate its contribution from $t\bar{t}$ + c-jet events. The $t\bar{t}c$ class is then built with events having at least two particle-level c-jets in the single lepton channel. The $t\bar{t}$ event classes definitions for which templates are made in both channels are summarized in table 4.1.

Category	$e\mu$	lepton + jets
$t\bar{t}b$	$\geq$3 b-jets	$\geq$3 b-jets
$t\bar{t}c$	$<$ 3 b-jets and $\geq$ 1 c-jet	$<$ 3 b-jets and $\geq$ 2 c-jets
$t\bar{t}l$	events that do not meet above criteria	events that do not meet above criteria

Table 4.1.: Definition of the $t\bar{t}$ event categories used to build MC templates (see text) for the fits to data. This categorization is based on the particle-level selections of b-jets, c-jets and light-jets [111].

The templates are built using the b-tagging discriminant value of the jet with the third-highest b-tagging discriminant in the dilepton channel, and of the two jets with the third- and fourth-highest b-tagging discriminant values in the single lepton channel. The discriminant values are divided into five bins defined by the working points, such that each bin corresponds to a certain range of b-tagging efficiencies. Particularly, the bins range from 1 to 5, corresponding to efficiencies of 100%-85%, 85%-77%, 77%-70%, 70%-60% and <60%, respectively. In the dilepton channel, three bins corresponding to efficiencies between 77% and 0% are used for the b-tagging discriminant value of the jet ranked third in b-tagging. In the single lepton channel, however, two-dimensional templates are created using the b-tagging discriminant values of the two jets ranked third and fourth in b-tagging exploiting all five bins. In both channels, one template is constructed from the sum of all non-$t\bar{t}$ backgrounds and three templates are created for the $t\bar{t}b$, $t\bar{t}c$ and $t\bar{t}l$ event classes. These are fitted to data using a binned maximum-likelihood fit with a Poisson likelihood:

$$\mathcal{L}(\vec{\alpha}|x_1, ..., x_n) = \prod_k^n \frac{e^{-\nu_k(\vec{\alpha})}\nu_k(\vec{\alpha})^{x_k}}{x_k!}$$

where x_k is the number of events in bin k of the data template and $\nu_k(\vec{\alpha})$ is the expected number of events depending on a number of free parameters denoted by $\vec{\alpha}$.

In the dilepton channel, two free parameters are used as follows:

$$\nu_k(\alpha_b, \alpha_{cl}) = \alpha_b N^k_{t\bar{t}b} + \alpha_{cl}\left(N^k_{t\bar{t}c} + N^k_{t\bar{t}l}\right) + N^k_{non-t\bar{t}}$$

where $N^k_{t\bar{t}b}$, $N^k_{t\bar{t}c}$, $N^k_{t\bar{t}l}$ and $N^k_{non-t\bar{t}}$ are the number of events in bin k of the $t\bar{t}b$, $t\bar{t}c$, $t\bar{t}l$ and non-$t\bar{t}$ templates, respectively.

In the single lepton channel, three free parameters are utilized, such that the expected number of events is given by:

$$\nu_k(\alpha_b, \alpha_c, \alpha_l) = \alpha_b N^k_{t\bar{t}b} + \alpha_c N^k_{t\bar{t}c} + \alpha_l N^k_{t\bar{t}l} + N^k_{non-t\bar{t}}$$

Figure 4.2 shows the distributions of the templates before and after the fit to data as well as the obtained values of the scale factors in both channels. For clarity, the two-dimensional single lepton templates are flattened into a single dimension. Figure 4.3 shows the good agreement between data and predictions for the b-tagged jet multiplicity in both channels after injecting the corresponding correction scale factors.

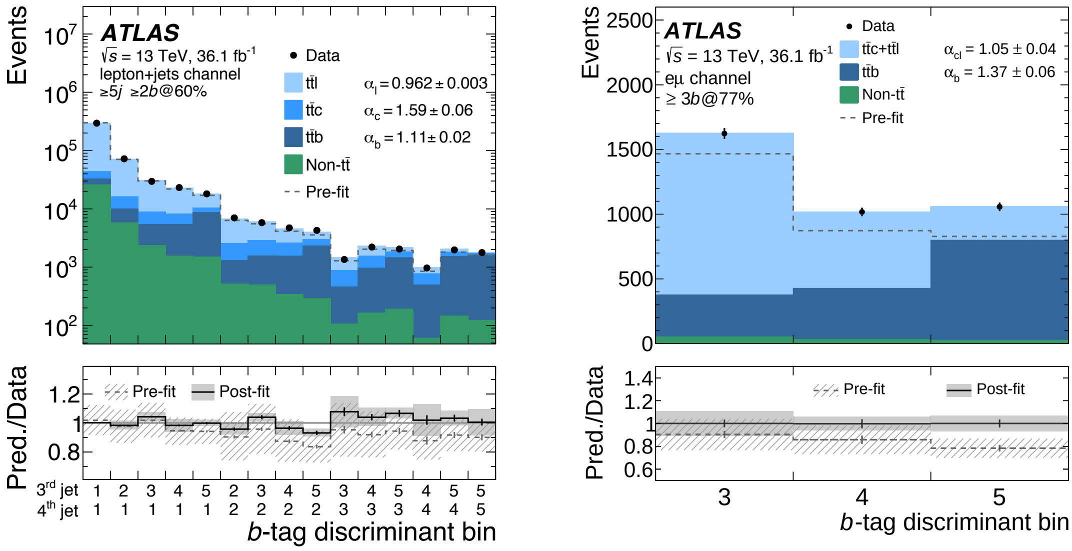

Figure 4.2.: The b-tagging discriminant distribution of the third and fourth ranked jet in b-tagging in (left) the single lepton channel and of the third ranked jet in (right) the dilepton channel [111]. For clarity, the two-dimensional single lepton templates have been flattened into one dimension. The ratios of total predictions before and after the fit to the data are shown in the lower panel. The extracted scale factors α_b, α_c, α_l, α_{cl} are given considering only statistical uncertainties.

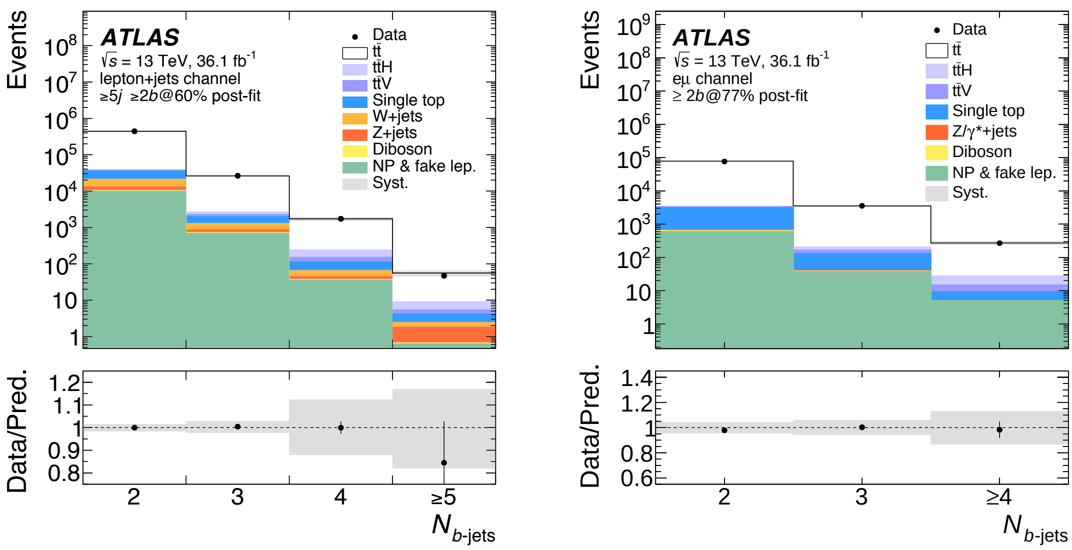

Figure 4.3.: Comparison of the data distributions with predictions, after applying the correction scale factors, for the number of b-tagged jets, in events with at least 2 b-tagged jets in (left) the single lepton channel and (right) the dilepton channel [111].

4.1.6. Fiducial phase space definition for unfolding in the single lepton channel

For the cross-section measurements, the data distributions obtained after the event selection and the non-$t\bar{t}$ backgrounds subtraction, are unfolded to the particle level in the fiducial volume. This procedure allows to correct for resolution effects and detector efficiencies and acceptances. The fiducial volume in each channel is defined using truth-level objects required to satisfy similar kinematic requirements to those placed on the reco-objects in the event selection. As already alluded to in Section 4.1.5.2, the obtained data sample after the non-$t\bar{t}$ backgrounds subtraction is not pure in events falling within the fiducial phase space with additional b-jets. Since the cross-sections measurements need to be performed in the fiducial volume, the contamination of the selected data sample needs to be investigated and studied using $t\bar{t}$ simulation to derive correction factors. For these studies, the $t\bar{t}$ samples take into account the $t\bar{t}c$ and $t\bar{t}l$ contributions since these components are not subtracted from the selected data sample but corrected for as part of the unfolding procedure. The extracted correction factors can then be applied to the kinematic distributions of the data sample to only retain events falling within the fiducial phase space. In Section 4.1.6.1, I present the detailed studies that I performed in the single lepton channel to explore the different sources of contamination affecting the selected $t\bar{t} + b\bar{b}$ data sample (≥ 6 jets, ≥ 4 b-tagged jets). The unfolding procedure allowing to correct for these sources of contamination and extracting the differential and inclusive cross-sections is then explained in Section 4.1.6.2.

4.1.6.1. Sources of contamination after the event selection

To identify the various sources contaminating the selected $t\bar{t} + b\bar{b}$ data sample, the particle level composition of simulated $t\bar{t}$ + jets events passing the $t\bar{t} + b\bar{b}$ event selection was thoroughly examined in the case of the single lepton channel across different b-tagging working points. In Particular, the truth-level composition was checked in the following $t\bar{t}$ + jets MC samples: PWG+PYT8 , PWG+HW7 , aMC@NLO+PYT8 and SHERPA . For these samples, the generators configuration and setups are overall similar to those described in section 4.1.2 except for few differences such as the value of the h_{damp} parameter which is set to the top quark mass for the above POWHEG samples.

For these studies, reco-jets are matched to the corresponding truth jets geometrically requiring ΔR(reco-jet, truth-jet)< 0.4. The achieved matching efficiency is around 98%. The transverse momenta of the reco-jets and the corresponding truth jets are depicted in Figure 4.4.

Firstly, the kinematics of the particle level objects within the selected events were broadly checked. Figure 4.5 shows the transverse momenta distributions of the truth b-jets matched to b-tagged reco-jets, truth electrons and truth muons in events passing the reco-level based $t\bar{t}+b\bar{b}$ event selection using the 85% working point. The fraction of selected events which contain particle-level objects that do not satisfy the kinematic requirements applied to their detector-level counterparts i.e truth b-jets with $p_T < 25$ GeV or truth leptons with $p_T < 27$ GeV , is quite small.

To examine more closely the truth composition of the $t\bar{t} + b\bar{b}$ phase space defined by the detector-level selection, a categorization of the selected events based on their particle level topology and the kinematics of the truth objects (leptons, jets and b-jets) they contain was carried out. Concretely, the event categories were constructed in such a way as to allow to study the phase space contamination arising from lepton related migration at a first stage, and then that associated with jets migration and b-tagging effects at a later stage. As such, events are first classified based on the multiplicity and kinematics of the truth leptons (e, μ and τ). The Single Lepton “SL” category contains events with exactly one truth lepton whereas events having exactly two truth leptons fall into the Dilepton “DL” category. Events within these categories are further scrutinized checking for the presence of a truth τ lepton to quantify their contribution to the $t\bar{t} + b\bar{b}$ phase space. In particular, two new categories are

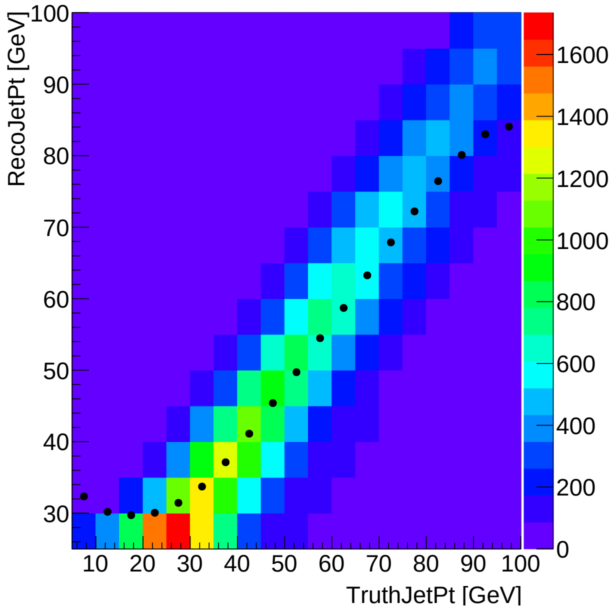

Figure 4.4.: Reco-jet p_T vs the truth jet p_T to which it was matched in the case of the PWG+PYT8 $t\bar{t}$ sample. The mean reco-jet p_T per truth-jet p_T bin is also overlaid in black dots.

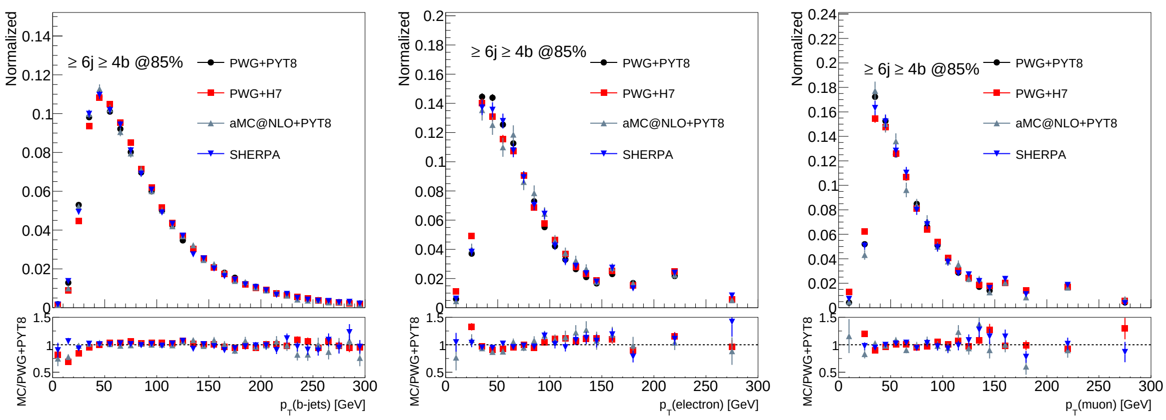

Figure 4.5.: p_T distribution of (left) truth b-jets matched to b-tagged reco-jets in addition to that of (middle) the truth electrons and (right) truth muons. Only events passing the detector-level $t\bar{t} + b\bar{b}$ event selection (≥ 6 jets, ≥ 4 b-tagged jets) at the 85% working point are considered.

defined "SL, no τ" and "DL, no τ" accounting for events in the "SL" and "DL" categories, respectively, which do not contain a truth τ lepton[c]. The subset of events in the "SL, no τ" category, where the truth electron or muon also passes the fiducial cuts (i.e the kinematic cuts applied on the reco-level leptons for the event selection) form a new category referred to as Single Lepton Fiducial "SL, Fid". The fractions of events entering each of the above categories are summarized in Table 4.2 for the

[c]The exclusion of the τ lepton events was performed in the context of these studies. However, these events are taken into account in the analysis but have a small contribution.

considered $t\bar{t}$ + jets samples in the case of the 60% b-tagging working point. The uncertainties on these fractions vary between 1% and 2%.

Samples \ Category	SL	SL, no τ	SL, Fid	DL	DL, no τ
PWG+PYT8	89	84	84	11	3
aMC@NLO+PYT8	91	88	88	9	2
PWG+HW7	91	88	84	9	3
SHERPA	89	84	82	11	3

Table 4.2.: Fractions of events in the various particle-level categories, defined based on the number and flavor of the truth leptons and their kinematics (see text), for the different $t\bar{t}$ + jets samples under consideration. These fractions are computed with respect to the total number of events passing the $t\bar{t}+b\bar{b}$ selection ($\geq$ 6 jets, $\geq$ 4 b-tagged jets) at the 60% b-tagging efficiency working point. The fractions values are quoted in percentage (%).

The fraction of events in the "SL, Fid" category, with respect to the total number of events passing the reco-level based single lepton selection, ranges between 82% and 88% depending on the $t\bar{t}$ sample. The contribution of events having exactly one truth τ lepton to the selected $t\bar{t}+b\bar{b}$ sample, where either an electron or a muon at reco-level are required, results from the subsequent leptonic decay of the τ lepton and amounts to 5% at most. The contamination in true dilepton events (DL) reaches 10% approximately. These are mainly dominated by events with one electron or muon and one hadronically decaying τ lepton resulting in a single lepton event topology. Furthermore, events having two truth leptons such that one of the leptons is reconstructed outside of the detector level phase space volume, also contribute to the "DL" category but to a lesser extent: up to 3% excluding dilepton events containing τ's. The above event fractions were also checked at looser b-tagging working points and yield consistent results as expected.

The particle-level composition of events in the "SL, Fid" category was further examined, checking the multiplicity and kinematics of the truth jets present in these events, as summarized in Table 4.3 in the case of the PWG+PYT8 sample. Events having at least 6 truth jets passing the fiducial cuts form the "≥6 jets, Fid" category and make up around 70% of the selected events compared to around 80% which make it to the "SL, Fid" category. The difference is due in part to detector resolution effects allowing for truth jets, in events with at most 5 truth jets passing the fiducial cuts, to migrate when reconstructed and pass the reco-level event selection.

Within the "≥6 jets, Fid" category, events which have at least 4 truth b-jets passing the fiducial cuts and matched to b-tagged reco-jets enter the "Pure $t\bar{t}+b\bar{b}$" category. The latter defines the $t\bar{t}+b\bar{b}$ fiducial volume where the particle-level objects pass the same kinematic requirements as those applied to the corresponding detector-level objects. The contribution of this category depends closely on the considered b-tagging working point: for instance, it constitutes 56% of the selected sample at the 60% working point while it reduces to 12% at the loosest working point. This stresses the importance of operating at the tightest working point in the single lepton channel to achieve the best accessible purity.

The contribution of three sources of contamination in the "≥6 jets, Fid" category, associated with particle-level event topologies which do not satisfy the "Pure $t\bar{t}+b\bar{b}$" category definition, were additionally assessed. The first one corresponds to events with at least four truth matched b-tagged jets however one of them at least is matched to a b-jet lying outside of the fiducial space, labeled as "≥4 b-tags, $\geq$ 1 b-jet not Fid". It represents $\sim$ 4% of the selected sample. Events in this category arise from detector resolution effects. The second contamination category, labeled as "≥4 b-tags, ≥ 1 mis-tag ($t\bar{t}+b\bar{b}$)", corresponds to events where at least one of the four b-tagged jets is matched to a c- or a light-jet instead of a b-jet even though the events in question have at least four truth b-jets. The contribution of this category amounts to ~ 3%. Lastly the "≥4 b-tags, ≥ 1 mis-tag (non-$t\bar{t}+b\bar{b}$)" category is populated by events which either have exactly one additional truth b-jet or $t\bar{t}c$ and $t\bar{t}l$ events, where at least one of the b-tagged jets originates from a c- or a light truth jet passing the fiducial cuts. The contribution of the latter depends on the b-tagging working point going from 8% at the 60% working point up to 51% at the 85% working point. The last two sources of contamination arise from the mis-tagging of c- and light-jets as b-jets.

Category \ b-tagging WP	60	70	77	85
≥ 6 jets, Fid	72	71	69	67
Pure, $t\bar{t}+b\bar{b}$	56	41	27	12
≥ 4 b-tags, ≥ 1 b-jet not Fid	5	4	3	1
≥4 b-tags, ≥ 1 mis-tag ($t\bar{t}+b\bar{b}$)	2	3	3	2
≥4 b-tags, ≥ 1 mis-tag (non-$t\bar{t}+b\bar{b}$)	8	21	34	51

Table 4.3.: Fractions of events in the various categories defined based on the multiplicity and kinematics of the truth jets (see text). These fractions are computed with respect to the total number of events passing the $t\bar{t}+b\bar{b}$ event selection at different b-tagging working points in the case of the PWG+PYT8 sample. The fractions values are quoted in percentage (%).

The detailed studies above allowed to probe and assess the different sources of contamination affecting the selected $t\bar{t}+b\bar{b}$ data sample in the single lepton channel. These checks showed that the designed $t\bar{t}+b\bar{b}$ event selection (see Section 4.1.4) results in a sample purity of ~ 56% accounting for events passing the fiducial cuts at the particle level. Similar conclusions were obtained in the dilepton channel. To measure the $t\bar{t}+b\bar{b}$ cross-section in the fiducial phase space, the distributions of interest are corrected for the various sources of contamination namely the mis-tagging efficiency and the detector resolution, through the unfolding procedure as explained in the following section.

4.1.6.2. Unfolding

The successive simulation-based corrections applied to the detector-level data distributions prior to their unfolding to the particle level are presented below.

Firstly, the number of non-$t\bar{t}$ background events in the j^{th} bin of the considered distribution ($N^j_{\text{non}-\text{t}\bar{\text{t}}-\text{bkg}}$) is subtracted from the data distribution in the same bin (N^j_{data}). Since the remaining events are a mixture of the signal and $t\bar{t}$-related backgrounds, a series of corrections are applied. These are derived from the nominal $t\bar{t}$ as well as the $t\bar{t}H$ and $t\bar{t}V$ simulations as the last two processes are also considered as signal in this analysis.

The first correction factor that regards the mis-tagged events is derived as follows:

$$f^j_{\text{t}\bar{\text{t}}\text{b}} = \frac{N^j_{\text{t}\bar{\text{t}}\text{b,reco}}}{N^j_{\text{t}\bar{\text{t}}\text{b,reco}} + N^j_{\text{t}\bar{\text{t}}\text{c,reco}} + N^j_{\text{t}\bar{\text{t}}\text{l,reco}}}$$

where $N^j_{\text{t}\bar{\text{t}}\text{b,reco}}$, $N^j_{\text{t}\bar{\text{t}}\text{c,reco}}$ and $N^j_{\text{t}\bar{\text{t}}\text{l,reco}}$ are the numbers of detector-level $t\bar{t}b$, $t\bar{t}c$ and $t\bar{t}l$ events reconstructed in bin j. These numbers are obtained after scaling the predicted MC yields by the data-driven correction factors derived based on the template fits to data presented in Section 4.1.5.2.

The second correction applied, f^j_{accept}, allows to correct for the fiducial acceptance. It is defined as the probability of a $t\bar{t}b$ event passing the reco-level selection in a bin j ($N^j_{\text{t\bar{t}b,reco}}$) to end up in the particle-level fiducial phase space ($N^j_{\text{t\bar{t}b,reco}\wedge\text{part}}$). It is evaluated as:

$$f^j_{\text{accept}} = \frac{N^j_{\text{t\bar{t}b,reco}\wedge\text{part}}}{N^j_{\text{t\bar{t}b,reco}}}$$

For the fiducial phase space definition, the detector-level objects are required to be matched with $\Delta R = 0.4$ to the corresponding particle-level objects. As such, a matching correction factor, f^j_{matching}, is applied next and is estimated as:

$$f^j_{\text{matching}} = \frac{N^j_{\text{t\bar{t}b,reco}\wedge\text{part}\wedge\text{matched}}}{N^j_{\text{t\bar{t}b,reco}\wedge\text{part}}}$$

where $N^j_{\text{t\bar{t}b,reco}\wedge\text{part}\wedge\text{matched}}$ is the subset of reconstructed events falling in the fiducial volume and where the detector-level objects are matched to their particle-level counterparts.

Once the above corrections are applied, the remaining steps in the unfolding procedure consist in effectively inverting the migration matrix $\mathcal{M}$ which allows to correct for the resolution effects followed at last by detector inefficiencies correction. The matrix $\mathcal{M}$ represents the probability for a particle-level event in bin i to be reconstructed in bin j. The effective inversion of this matrix is performed based on the iterative Bayesian unfolding technique [123] as implemented in the RooUnfold software package [124]. After the matrix inversion, a factor f^i_{eff} is applied to correct for the reconstruction efficiency and is defined as:

$$f^i_{\text{eff}} = \frac{N^i_{\text{t\bar{t}b,part}\wedge\text{reco}\wedge\text{matched}}}{N^i_{\text{t\bar{t}b,part}}}$$

where $N^i_{\text{t\bar{t}b,part}}$ is the number of $t\bar{t}b$ events passing the particle-level selection in bin i while $N^i_{\text{t\bar{t}b,part}\wedge\text{reco}\wedge\text{matched}}$ is the number of $t\bar{t}b$ events at particle level in bin i passing the detector-level selection and containing matched objects.

For an observable X at particle level, the unfolding procedure can be summarized in the following expression:

$$\frac{d\sigma^{\text{fid}}}{dX^i} = \frac{N^i_{\text{unfold}}}{\mathcal{L}\Delta X^i} = \frac{1}{\mathcal{L}\Delta X^i f^i_{eff}} \sum_{\text{j}} \mathcal{M}^{-1}_{ij} f^j_{\text{matching}} f^j_{\text{accept}} f^j_{\text{t\bar{t}b}} (N^j_{\text{data}} - N^j_{\text{non-t\bar{t}-bkg}})$$

where ΔX^i is the bin width, N^i_{unfold} is the number of events in bin i of the unfolded distribution and $\mathcal{L}$ is the integrated luminosity. The inclusive fiducial cross-section σ^{fid} can be derived from:

$$\sigma_{\text{fid}} = \int \frac{d\sigma^{\text{fid}}}{dX} dX = \frac{\sum N^i_{\text{unfold}}}{\mathcal{L}}$$

4.1.7. Results

The measurements of the inclusive fiducial cross-sections for $t\bar{t}$ production in association with at least one and at least two additional b-jets are summarized in Figure 4.6 where various $t\bar{t}$+$b\bar{b}$ MC predictions (both 5FS and 4FS) are overlaid for comparison. The measured cross-sections are found to be higher than the predictions but compatible within uncertainties. The most precise of these measurements are obtained in the $\geq 3b$ phase space in the dilepton channel with an uncertainty of 13%, and the $\geq 6j$, $\geq 4b$ phase space in the single lepton channel with an uncertainty of 17%. These uncertainties are dominated by the systematic component arising mainly from uncertainties associated with the $t\bar{t}$ modeling, b-tagging and the jet energy scale as detailed in ref [111].

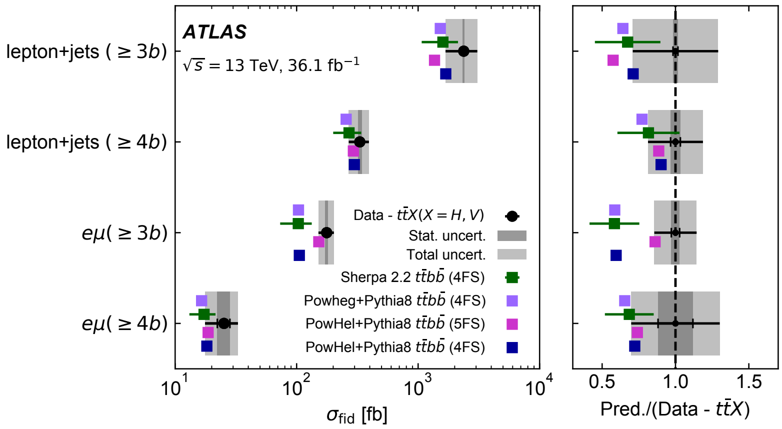

Figure 4.6.: The measured fiducial cross-sections compared with various $t\bar{t}+b\bar{b}$ predictions (5FS and 4FS) [111]. The $t\bar{t}H$ and $t\bar{t}V$ contributions are subtracted from the unfolded data.

The normalized fiducial cross-section as a function of the b-jet multiplicity is shown in Figure 4.7, compared with predictions from different MC generator set-ups. Those that calculate the matrix element of the $t\bar{t}$ pair production at the NLO but rely on the parton shower for high jet multiplicities such as the nominal PWG+PYT8 and PWG+HW7 , predict too few events with three and four b-jets indicating that the parton shower in these setups is not optimal. On the other hand, SHERPA which models one additional parton process at NLO and up to four additional partons at LO is the only one among the considered generators that describes the b-jet production well across the full phase space.

The p_T distributions of the third and fourth leading b-jets in p_T in the single lepton channel are shown in Figure 4.8. These distributions are assumed to be dominated by additional b-jets produced via gluon splitting as these have the tendency to be softer. These observables exhibit little variation among the predictions and a good agreement with data.

Figure 4.9 shows the distributions of the angular distance ΔR between the two highest-p_T b-jets and between the closest b-jets in ΔR in the single lepton channel. A good agreement between these models and data is obtained for both distributions.

The rest of the measured distributions in both the single and dilepton channels can be found in ref [111] along with a quantitative assessment of their agreement with predictions.

4.2. Prospective studies for a better $t\bar{t}$ + HF measurement

Based on the results of the $t\bar{t}+b\bar{b}$ measurements presented in the previous section, the various predictions available for this process agree with data within uncertainties. However these measurements, namely the differential cross-section distributions, are not sensitive enough to provide a clear indication on which generator (or class of generators) describes data better. To this end, I investigated the feasibility of improving the sensitivity of the $t\bar{t}+b\bar{b}$ differential measurements by explicitly identifying

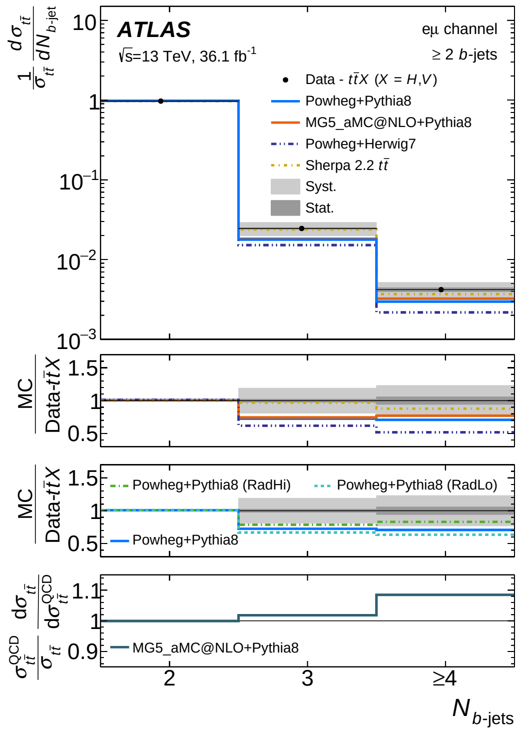

Figure 4.7.: Normalized differential cross-section as a function of the b-jet multiplicity in events with at least two b-jets in the dilepton channel compared with multiple MC generators [111]. The $t\bar{t}H$ and $t\bar{t}V$ contributions are subtracted from the unfolded data. The first two ratio panels show the ratios of different predictions to data. The third ratio pad shows the ratio of predictions of normalized differential cross-sections from aMC@NLO+PYT8 including (numerator) and excluding (denominator) the contributions from $t\bar{t}V$ and $t\bar{t}H$ production.

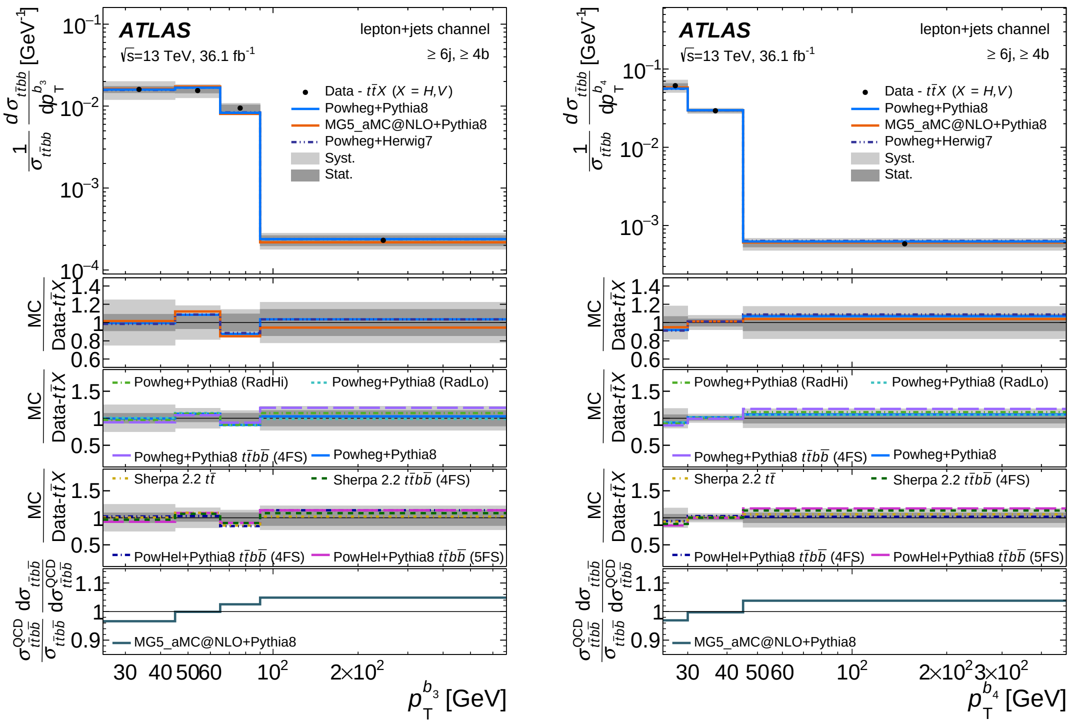

Figure 4.8.: Normalized differential cross-sections as a function of the p_T of (left) the third and (right) fourth leading b-jets in p_T in events with at least four b-jets in the single lepton channel [111].

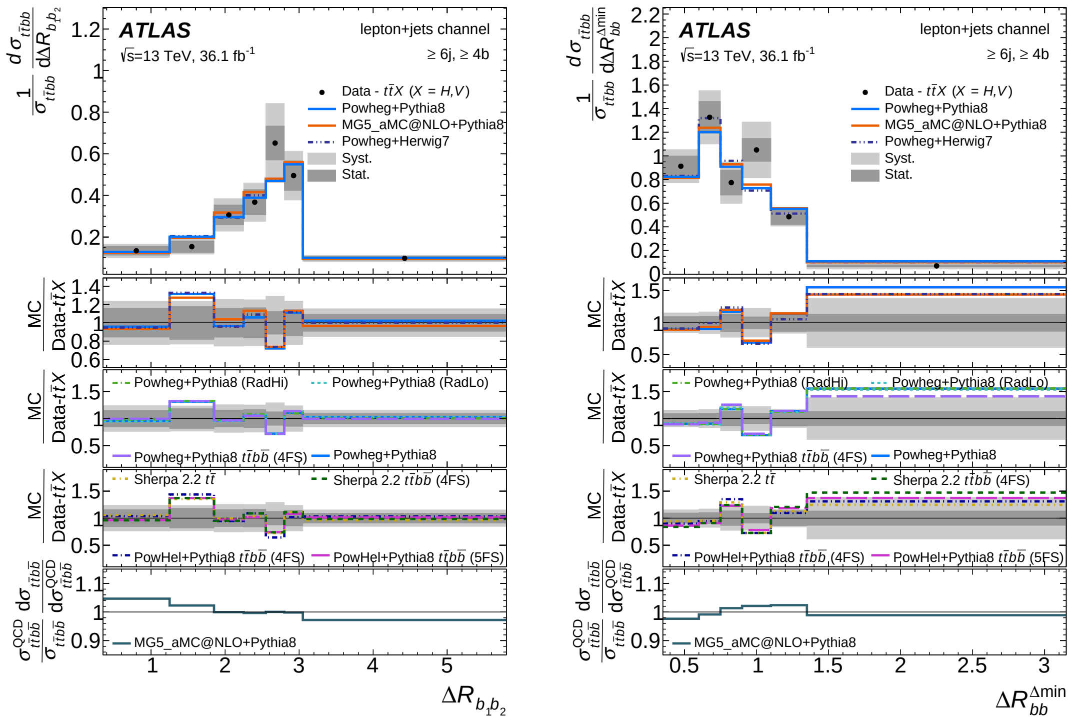

Figure 4.9.: Normalized differential cross-section as a function of the angular distance ΔR between (left) the two highest-p_T b-jets and between (right) the closest b-jets in ΔR in events with a least four b-jets in the single lepton channel [111].

the origin of the b-jets present in the events and separating between the b-jets from the $t\bar{t}$ system and those which are additional. This would allow to measure better defined and more specific distributions for the b-jets properties since for instance the pair of the b-jets with the highest p_T does not correspond in all cases to b-jets from the $t\bar{t}$ system and similarly for the b-jets pair with the smallest angular separation which is not always made of true additional b-jets; these assumptions do not account for the phase space region where the additional b-jets are produced at high p_T or with large angular separation. In particular, I checked the validity of assigning the b-jets origin based on their p_T ordering in $t\bar{t}$ events with at least one additional b-jet selected at particle level in the single lepton channel as explained in Section 4.2.1. In Section 4.2.2, I show the advantages of explicitly identifying the origin of these b-jets compared to the case where the origin is assumed based on their p_T ordering. Lastly, I discuss in Section 4.2.3, a possible way to separate the b-jets based on their origin using a Boosted Decision Tree (BDT).

4.2.1. The origin of p_T-ordered b-jets in $t\bar{t}$+≥1b events

For the studies presented in the following, only $t\bar{t}$ events in the single lepton channel with at least one additional b-jet identified based on the ΔR labeling procedure introduced in Section 4.1.3 are selected. Truth b-jets are arranged in descending order in p_T such that bj1 denotes the highest p_T b-jet while bj4 corresponds to the fourth leading b-jet in p_T for events with ≥ 4 b-jets. The origin of these b-jets is checked applying different thresholds on their p_T: 15 GeV , 20 GeV and 25 GeV .

The $t\bar{t}$ samples used in these studies are similar to those considered in Section 4.1.6.1 except for the HERWIG++ [74] parton shower, labeled as HERWIGpp in the following, being used instead of HERWIG 7. Furthermore, two additional samples are checked: PWG+PYT6 where the PYTHIA 6 [107] parton shower is interfaced to POWHEG and the aMC@NLO+HWpp sample with HERWIGpp interfaced to Madgraph5_aMC@NLO.

The fraction of events where the n^{th} b-jet ($n = 1, \ldots, 4$) either originates from the $t\bar{t}$ system or the additional $b\bar{b}$ system, are shown in Figure 4.10 in the case of the PWG+PYT8 sample for different thresholds on the jets p_T. The statistical uncertainties on the obtained fractions are $< 1\%$ and therefore are neglected. These fractions are consistent across the different p_T cuts. A comparison of the fractions among different $t\bar{t}$+≥1b samples is also shown in Figure 4.11 in the case of the $p_T > 25$ GeV cut for b-jets.

The leading (subleading) b-jet is produced through top quark decays around 70% (65%) of the time. Moreover, about 50% of the events with ≥ 3 b-jets, have their third b-jet also coming from the $t\bar{t}$ system. This means that considering only the two highest p_T b-jets to characterize b-jets production from the $t\bar{t}$ system in these events would neglect a significant contribution from the third b-jet to the process. On the other hand, the fourth leading b-jet is an additional jet about 70% of the time. Overall, the harder the b-jet the more likely it originates from the $t\bar{t}$ system.

The origin of the leading (bj1,bj2) and subleading (bj3,bj4) pairs of b-jets was also checked in the case of $p_T > 25$ GeV threshold. The fraction of events where these b-jets pairs are either produced in top quark decays or originating from gluon splitting are summarized in tables 4.4 and 4.5, respectively. The contribution of the $t\bar{t}$ system to the leading b-jets pair amounts to 40% approximately. This indicates that the measured leading b-jets pair distributions are only pure up to about 40% and are mostly dominated by events where at least one of the b-jets in the pair is not produced from a top quark decay. On the other hand, the contribution of gluon splitting production mode to the subleading b-jets pair distributions make up for about 30%. Similarly, these are mostly contaminated by events where at least one of the b-jets in the pair does not originate from a gluon splitting.

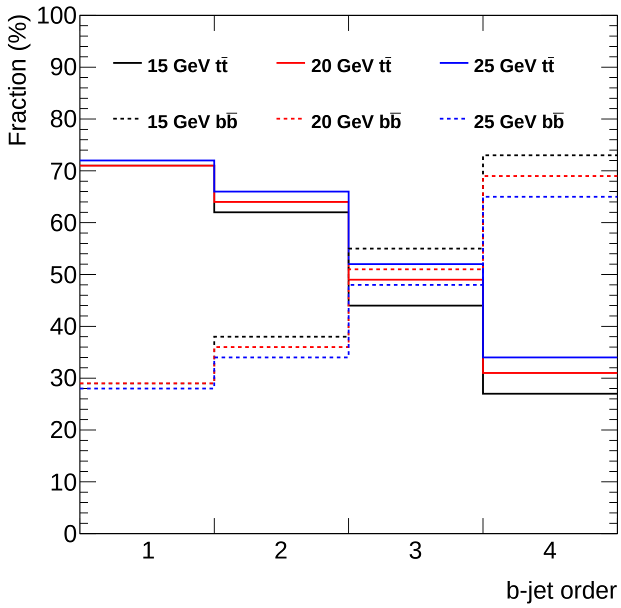

Figure 4.10.: Fraction of events where the n$^{\text{th}}$ ($n = 1, \ldots, 4$) b-jet originates from the $t\bar{t}$ (solid line) or $b\bar{b}$ (dotted line) systems for different thresholds on the b-jets p_T: 15 GeV (black), 20 GeV (red) and 25 GeV (blue) in the case of the PWG+PYT8 sample.

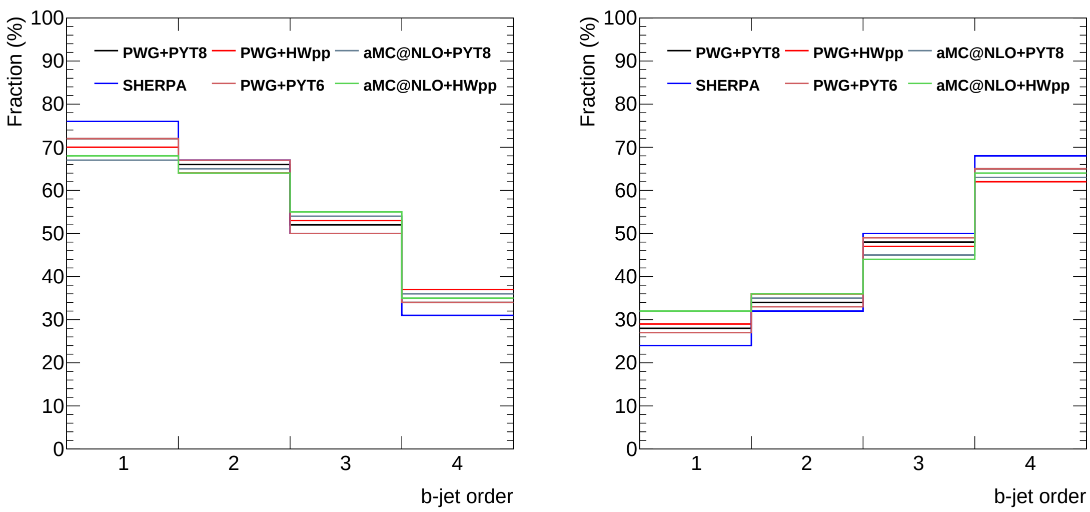

Figure 4.11.: Fraction of events where the n$^{\text{th}}$ ($n = 1, \ldots, 4$) b-jet originates from (left) the $t\bar{t}$ or (right) $b\bar{b}$ systems for different $t\bar{t}+\geq 1b$ samples. b-jets are required to have $p_T > 25$ GeV .

b-jets pair / $t\bar{t}$ sample	(bj1,bj2) (%)	(bj3,bj4) (%)
PWG+PYT8	40	9
PWG+HWpp	36	10
aMC@NLO+PYT8	34	10
SHERPA	44	7
PWG+PYT6	41	8
aMC@NLO+HWpp	34	9

Table 4.4.: Fraction of events where both the leading and subleading b-jets pair originate from the $t\bar{t}$ system. b-jets are required to have $p_T > 25$ GeV . The fractions values are quoted in percentage (%).

b-jets pair / $t\bar{t}$ sample	(bj1,bj2) (%)	(bj3,bj4) (%)
PWG+PYT8	2	29
PWG+HWpp	2	26
aMC@NLO+PYT8	3	26
SHERPA	1	31
PWG+PYT6	2	28
aMC@NLO+HWpp	2	27

Table 4.5.: Fraction of events where both the leading and subleading b-jets pair originate from the gluon splitting (additional b-jets). b-jets are required to have $p_T > 25$ GeV . The fractions values are quoted in percentage (%).

4.2.2. Impact of b-jets origin identification on the $t\bar{t} + b\bar{b}$ differential distributions

Kinematic distributions characterizing b-jet pairs originating either from the $t\bar{t}$ system or gluon splitting are of great importance for measurements in order to improve the MC modeling of the challenging $t\bar{t} + b\bar{b}$ process. However, the measurements presented in Section 4.1.7, were performed without the explicit identification of the b-jets origin. In the following, I check the impact of identifying the b-jets origin on the kinematic distributions which are interesting for measurements.

In Figure 4.12, kinematic distributions characterizing the leading b-jets pair are compared to those which correspond to the b-jets pair originating from the top quarks decays. The shapes in the latter distributions, where only b-jets from top quarks decays are used to build the variables, are fairly similar to the case where b-jets from the leading pair are used. Additionally, the sensitivity of these distributions to the differences among generators, which is key to identify which generator describes data the best, is of the same level. Thus, the assumption that the leading b-jets pair distributions are dominated by the $t\bar{t}$ production mode which is valid with a probability of up to 40% approximately, does not have a significant impact on the level of sensitivity achieved by the measured distributions.

In Figures 4.13 and 4.14, the kinematic distributions characterizing the subleading b-jets pair are compared to those obtained using additional b-jets to build the distributions. On one hand, the shapes in these distributions are heavily dependent on whether or not the b-jets are matched to their origin. For instance, the two additional b-jets tend to be very close in terms of angular distance (ΔR). This property, however, is not fully captured if one considers the subleading pair of b-jets as corresponding to the additional jets. In the latter distribution, two peaks can be distinguished: the one at small ΔR (around 0.4) corresponding to the additional jets contribution and another peak at large ΔR values (around 3) which is due mainly to the contamination with events where one of the b-jets in the subleading pair originates from the $t\bar{t}$ system. On the other hand, the sensitivity to the differences among generators is more pronounced for pure distributions where the used b-jets are explicitly identified as not originating from the top quarks decays. This effect can be exploited in order to determine which MC prediction is favored by data measurements assuming a good experimental precision is achieved. However, this level of sensitivity attained with variables characterizing the additional b-jets is diluted if no explicit matching is done as can be seen in the ΔR distribution for the subleading b-jets pair and the p_T distribution of the third leading jet where the differences among the various predictions are mitigated.

These studies led to the conclusion that it is important to identify the origin of the b-jets present in the event and distinguish between those which are additional and the ones produced in top quarks decays, to enhance the sensitivity of the $t\bar{t}$ + HF measurements. An MVA technique based on the use of a Boosted Decision Tree (BDT) is presented in the following as a potential way to achieve this separation.

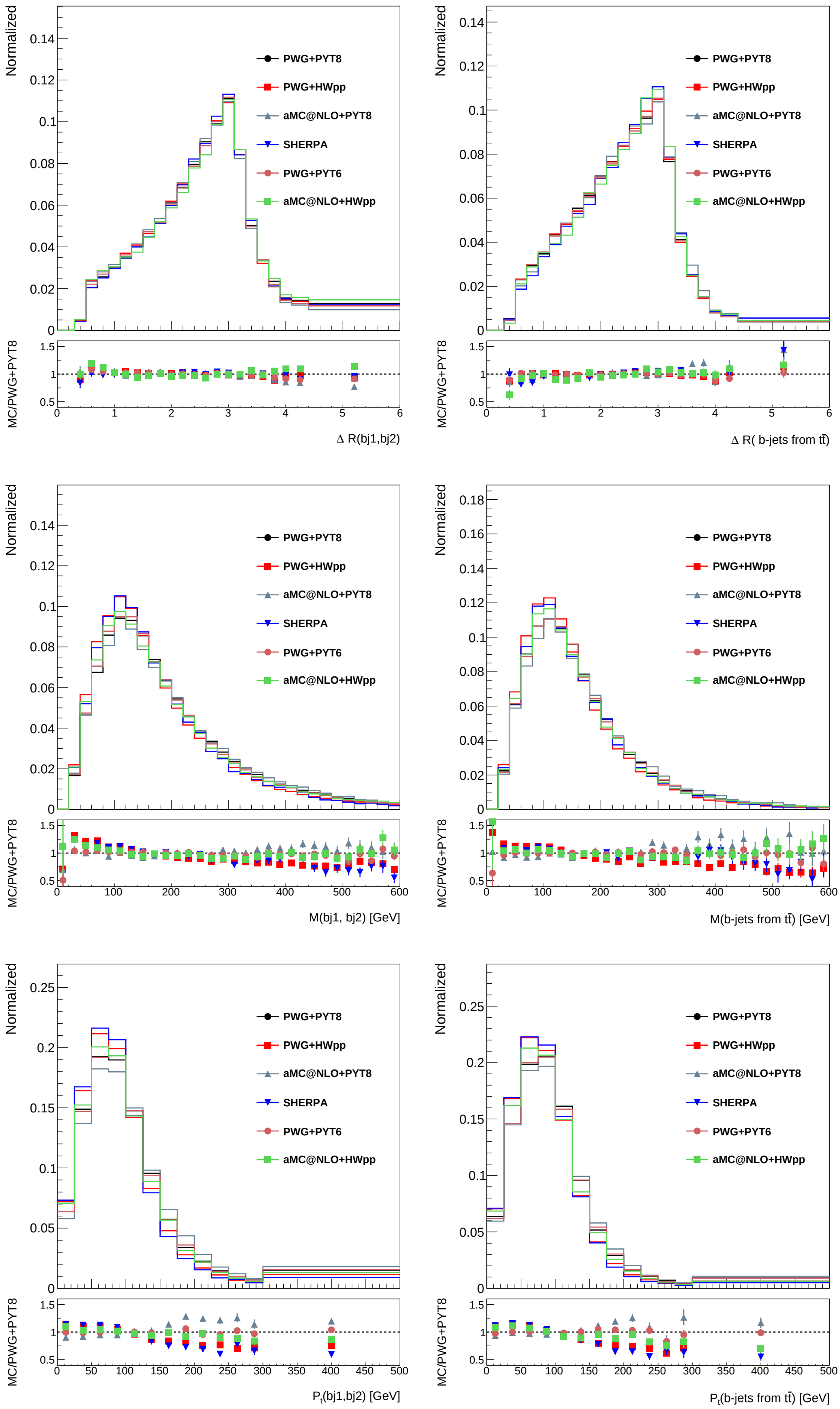

Figure 4.12.: Distributions of the ΔR separation (up), invariant mass (middle) and transverse momentum (bottom) characterizing (left) the leading b-jets pair (bj1, bj2) and (right) the b-jets pair originating from the top quarks decays for various $t\bar{t}+\geq 1b$ MC samples.

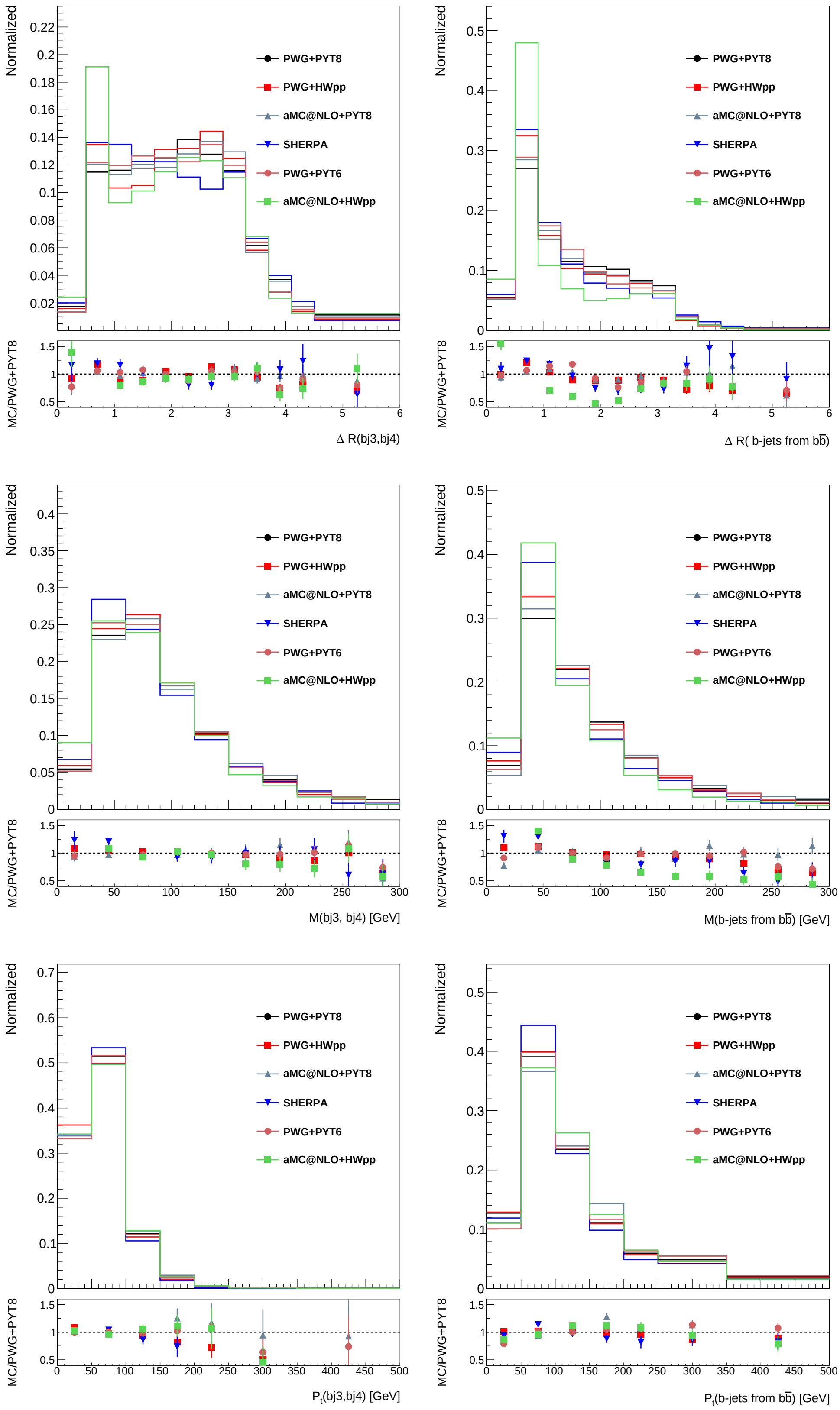

Figure 4.13.: Distributions of the ΔR separation (up), invariant mass (middle) and transverse momentum (bottom) characterizing (left) the subleading b-jets pair (bj3, bj4) and (right) the b-jets pair originating from gluon splitting i.e additional b-jets for various $t\bar{t}+\geq 1b$ MC samples.

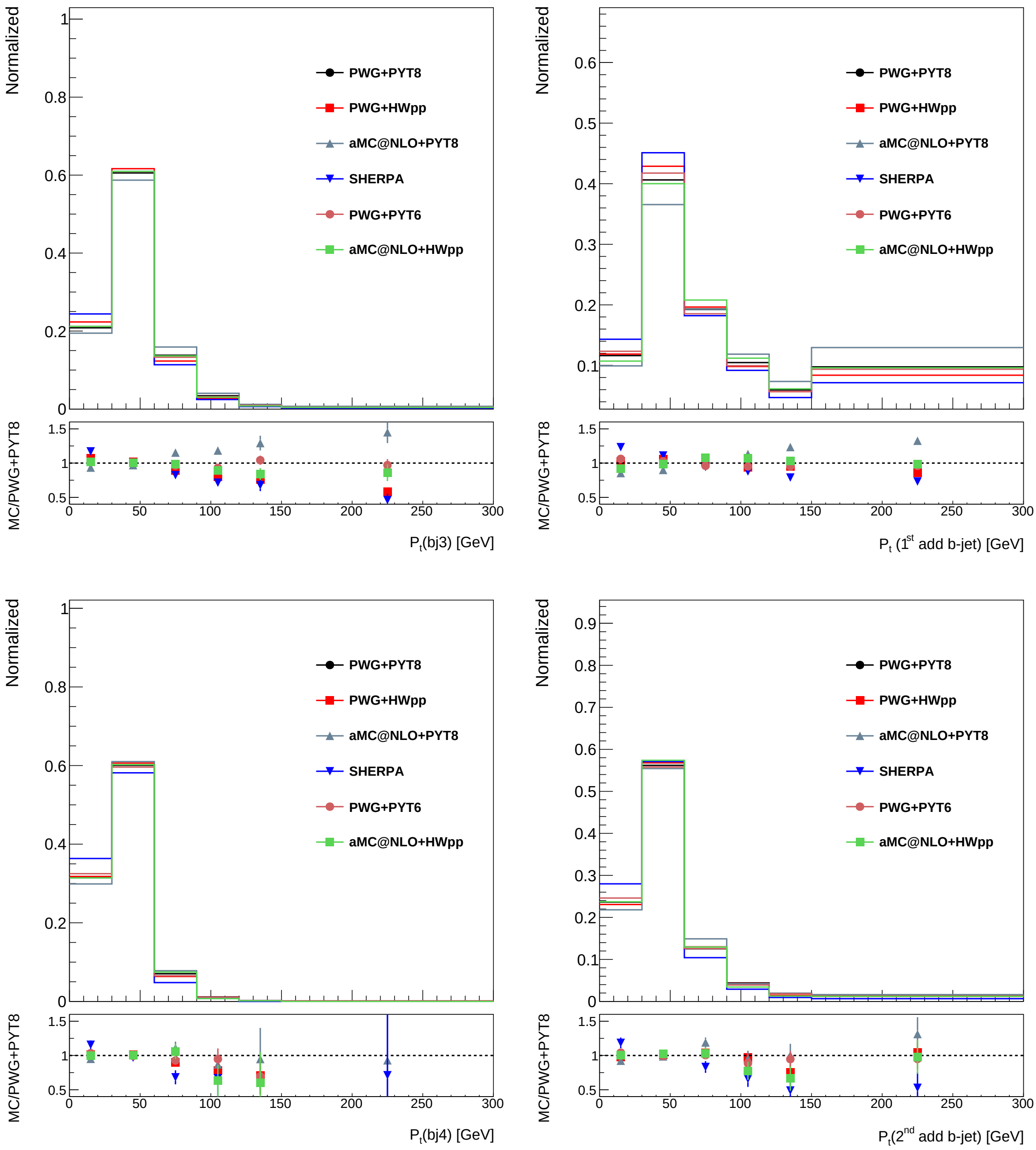

Figure 4.14.: Transverse momenta of (left) the 3rd and 4th leading b-jet and (right) the 1^{st} and 2nd additional b-jet for various $t\bar{t}+\geq 1b$ samples.

4.2.3. Reconstruction of the $t\bar{t}$ system via a BDT

The identification of the origin of jets produced in $t\bar{t}$ + jets events can be achieved through the reconstruction of the $t\bar{t}$ system: jets which are not assigned to build the top quarks can be identified as being additional jets. However, reconstructing the top quarks in events having the $t\bar{t} + b\bar{b}$ topology (at least 6 jets, 4 of which at least are b-tagged) can be quite challenging due to the high jet multiplicity and thus the many possibilities for the jet-parton assignments combinations. To deal with this challenge, I explored the possibility of using a BDT to find the best correspondence between the observed jets and the final state partons originating from the $t\bar{t}$ system, in single lepton events which have the $t\bar{t} + b\bar{b}$ topology. This is similar to what is done in the $t\bar{t}H(H \to b\bar{b})$ analysis (see Section 5.2.3.2) for reconstructing the final state objects except for not requiring to build the Higgs boson. The training as well as the performance of the $t\bar{t}$ reconstruction BDT is presented in the following.

4.2.3.1. Truth matching

The association of reconstructed jets to quarks from the $t\bar{t}$ system is realized through a geometric matching, with $\Delta R = \sqrt{(\Delta\eta)^2 + (\Delta\phi)^2} < 0.3$. Each jet can only be associated to one parton. The lepton is correctly selected in most events and thus it is not required to be truth matched.

Table 4.6 summarizes the fractions of selected events (at least 6 jets and at least 4 b-tagged jets) satisfying the different matching requirements in the case of the PWG+PYT8 $t\bar{t}$ sample; the fractions in the table are quoted at four different b-tagging working points. These fractions correspond to the maximum achievable efficiencies for the reconstruction BDT assuming it provides the correct jet-parton assignments. The matching schemes shown in the table are defined as follows:

- bHadTop: one jet is matched to the b-quark from the hadronic top which refers to the top quark resulting in a hadronically decaying W boson.
- bLepTop: one jet is matched to the b-quark from the leptonic top which corresponds to the top quark producing a leptonically decaying W boson.
- wj1: one jet is matched to the leading quark in p_T, from the hadronically decaying W boson.
- wj2: one jet is matched to the subleading quark in p_T, from the hadronically decaying W boson.
- allb: two jets are matched to the two b-quarks from the top quarks decay.
- hadW: two jets are matched to the two quarks from the hadronically decaying W boson.
- All Match: four jets are matched to the four final state partons from the $t\bar{t}$ system i.e the b-quarks from the top quarks decay as well as the two quarks from the hadronically decaying W boson.

4.2.3.2. $t\bar{t}$ reconstruction algorithm

For the reconstruction method, I used a subset of all possible jet permutations in the selected events to build the $t\bar{t}$ combinations. In particular, jets are ranked by their binned b-tagging weight (see Section 4.1.5.2) such that the leading four jets are allowed to be assigned to the b-quarks from top quarks decay while the leading two jets in b-tagging weight are not allowed to be used as the jets from the hadronic W. The number of $t\bar{t}$ combinations to be built can be reduced profiting from this pseudo-continuous b-tagging information without a significant loss of purity from the excluded combinations. This can be concluded from Figure 4.15 which shows the origin of the jets sorted in decreasing order

Matching Pattern \ Fractions	@ 85WP	@ 77WP	@ 70WP	@ 60WP
bHadTop	89	89	88	88
bLepTop	97	98	98	99
wj1	89	87	85	83
wj2	66	63	59	56
allb	86	87	87	87
hadW	64	61	57	53
All Match	59	58	54	52

Table 4.6.: Fraction of selected events satisfying the different matching requirements (see text) in a sample with ≥ 6 jets and ≥ 4 b-tagged jets at the following b-tagging working points: 85%, 77%, 70% and 60%. The fractions values are quoted in percentage (%).

of their discrete b-tagging weight: the fraction of events where the b-quarks from the top quarks decay lead to a jet ranked fifth or below is quite small and similarly for the contribution of events where the quarks from the hadronic W give rise to jets ranked first or second.

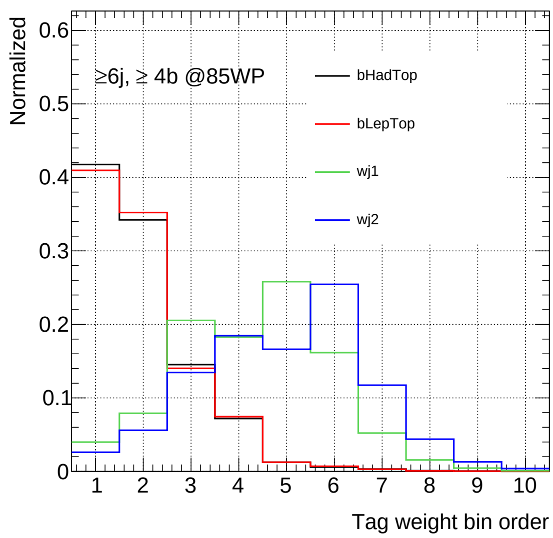

Figure 4.15.: Origin of the jets, sorted in decreasing order of their binned b-tagging weight, in events passing the ≥ 6 jets and ≥ 4 b-tagged jets selection at the 85% b-tagging efficiency working point.

In addition to jets, the reconstruction algorithm also uses the lepton and the event missing transverse momentum E_T^{miss} to build the leptonic W boson. The reconstruction of the latter in addition to the hadronic W and the top quarks is explained in more details in the following.

The reconstruction of the leptonic W boson requires the full neutrino momentum. The transverse component of the latter is taken from the event E_T^{miss}. However, the longitudinal component of the neutrino momentum ($p_{z\nu}$) is not accessible for measurement. It is derived by assuming that the lepton and E_T^{miss} originate exclusively from a W boson decay and consequently constraining the invariant mass of the system to that of the W boson. This results in a quadratic equation with two possible solutions:

$$p_{z\nu}^{\pm} = \frac{1}{2}\frac{p_{z\ell}\beta \pm \sqrt{\Delta}}{E_\ell^2 - p_{z\ell}^2}$$

where:

$$\beta = m_W^2 - m_\ell^2 + 2p_{x\ell}p_{x\nu} + 2p_{y\ell}p_{y\nu}$$
$$\Delta = E_\ell^2\left(\beta^2 + (2p_{z\ell}p_{\mathrm{T}\nu})^2 - (2E_\ell p_{\mathrm{T}\nu})^2\right).$$

If the quadratic equation does not have a real solution, its discriminant is set to zero ($\Delta = 0$). On the other hand, if there are two solutions, two different leptonic W bosons are considered.

As for the hadronic W, it is built using all combinations of 2 jets in the selection other than the leading and subleading jets in b-tagging weight as mentioned above. Lastly, the top quarks are reconstructed by pairing a W boson and one of the four leading jets in the b-tagging weight. The remaining jets which were not used to build the $t\bar{t}$ system are considered as additional jets.

4.2.3.3. BDT training

To train the BDT on reconstructing the $t\bar{t}$ system, I used the toolkit for multivariate analysis (TMVA) [125]. The training is performed on a $t\bar{t}$ PWG+PYT8 sample where I selected only the single lepton events with ≥ 6 jets and ≥ 4 b-tagged at the 85% working point. The $t\bar{t}$ combinations used as input for the training are divided into signal and background classes fed to the BDT so that it learns to distinguish among them. The former class corresponds to $t\bar{t}$ combinations where all the jets are correctly assigned to the partons from which they originate while the latter refers to the rest of the combinations where at least one jet is not properly matched to the parton to which it was assigned. I also tested another version of the BDT where the signal class also includes combinations where only one of the jets associated with the hadronic W is properly matched to a quark from the W boson decay but this configuration resulted in a worse performance and therefore it was not used further for the $t\bar{t}$ system reconstruction.

The selected sample is randomly divided into two subsamples for training and testing and the BDT trained on one of the subsamples is then applied on the other and vice versa. Additionally, to maximize the size of the training sample, the absolute value of the event weight is taken, so that events with negative weights which TMVA does not handle properly, are also used. This approach does not affect the shape of the input variables as it is in agreement between events with positive and negative weights.

The TMVA training parameters used for the $t\bar{t}$ reconstruction BDT are summarized in Table 4.7. These are the same as the ones used for the reconstruction BDT of the $t\bar{t}H$ system in the $t\bar{t}H(H \to b\bar{b})$ analysis (see section 5.2.3.2) and no attempt to optimize them was made in the context of these studies.

BoostType	AdaBoost
AdaBoostBeta	0.15
NTrees	250
MaxDepth	5
nCuts	80
MinNodeSize	4%

Table 4.7.: TMVA parameters for the $t\bar{t}$ reconstruction BDT.

The full list of variables used in the training of the $t\bar{t}$ reconstruction BDT is shown in Table 4.8. Some of these variables are shown for the signal and background $t\bar{t}$ combinations in Figure 4.16.

Variable	Definition
t_{lep} mass	Leptonic top mass
t_{had} mass	Hadronic top mass
W_{had} mass	Hadronic W mass
Mass of W_{had} and b from t_{lep}	Mass of the hadronic W and b-jet from the leptonic top
Mass of W_{lep} and b from t_{had}	Mass of the leptonic W and b-jet from the hadronic top
$\Delta R(W_{\mathrm{had}}, b \text{ from } t_{\mathrm{had}})$	ΔR distance between the hadronic W and b-jet from the hadronic top
$\Delta R(W_{\mathrm{had}}, b \text{ from } t_{\mathrm{lep}})$	ΔR distance between the hadronic W and b-jet from the leptonic top
$\Delta R(\mathrm{lep}, b \text{ from } t_{\mathrm{lep}})$	ΔR distance between the lepton and b-jet from the leptonic top
$\Delta R(\mathrm{lep}, b \text{ from } t_{\mathrm{had}})$	ΔR distance between the lepton and b-jet from the hadronic top
$\Delta R(b \text{ from } t_{\mathrm{lep}}, b \text{ from } t_{\mathrm{had}})$	ΔR distance between the b-jet from leptonic top and the b-jet from hadronic top
$\Delta R(q_1 \text{ from } W_{\mathrm{had}}, q_2 \text{ from } W_{\mathrm{had}})$	ΔR distance between the two jets from the hadronic W
$\Delta R(b \text{ from } t_{\mathrm{had}}, q_1 \text{ from } W_{\mathrm{had}})$	ΔR distance between the b-jet from hadronic top and the leading jet from the hadronic W
$\Delta R(b \text{ from } t_{\mathrm{had}}, q_2 \text{ from } W_{\mathrm{had}})$	ΔR distance between the b-jet from hadronic top and the subleading jet from hadronic W
min. $\Delta R(b \text{ from } t_{\mathrm{had}}, q \text{ from } W_{\mathrm{had}})$	ΔR distance between the b-jet from hadronic top and the jet from hadronic W with the smallest ΔR separation
min. $\Delta R(b \text{ from } t_{\mathrm{had}}, q \text{ from } W_{\mathrm{had}}) - \Delta R(\mathrm{lep}, b \text{ from } t_{\mathrm{lep}})$	Difference between smallest ΔR between the b-jet from hadronic top and the jet from hadronic W and the ΔR distance between the b-jet from leptonic top and the lepton
$qqhadW_{angle}$	Angle between the jets from hadronic W
$\Delta R(t_{\mathrm{lep}}, t_{\mathrm{had}})$	ΔR distance between the hadronic and leptonic top quarks

Table 4.8.: Input variables to the $t\bar{t}$ reconstruction BDT in the single lepton channel with ≥ 6 jets and ≥ 4 b-tagged jets at the 85% working point.

4.2.3.4. BDT Performance

The BDT is evaluated on each of the $t\bar{t}$ combinations constructed in a selected event. The jet-parton assignment is assumed to be correct in the combination with the highest BDT score. This combination is used in the following to gauge the BDT performance in terms of separating between the b-jets from the $t\bar{t}$ system and the additional jets.

Table 4.9 summarizes the matching fractions obtained using the $t\bar{t}$ reconstruction BDT; both absolute and relative fractions are shown, with the latter being computed with respect to the maximum achievable efficiencies (see Table 4.6). The BDT is able to correctly identify the b-jets from the top quarks decay in 35% of the selected events, amounting to 41% when considering only events where

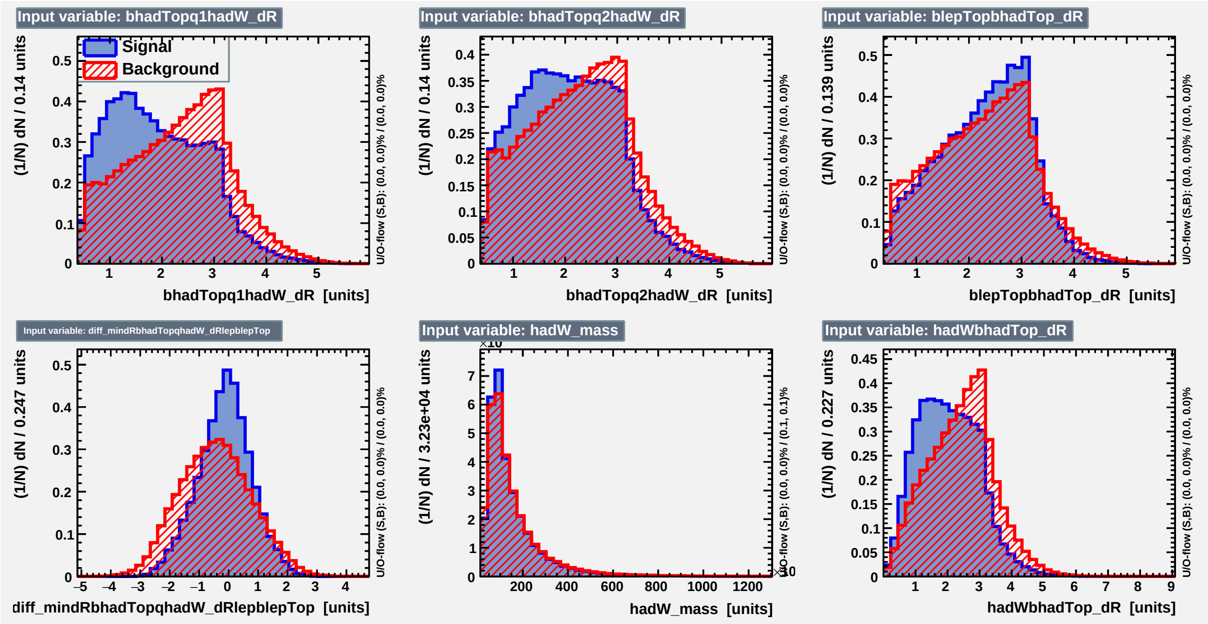

Figure 4.16.: A selection of the input variables to the $t\bar{t}$ reconstruction BDT (see Table 4.8) for for both signal (blue) and background (red) $t\bar{t}$ combinations.

jets matching the b-quarks from top quarks decays are present. The two leading additional jets in b-tagging, are correctly assigned by the BDT in 45% of the selected events.

Matching Pattern	Absolute matching fractions	Relative matching fractions
bHadTop	48	54
bLepTop	62	64
allb	35	41
wj1	52	59
wj2	44	67
hadW	30	48
All Match	19	32
add jet 1	56	-
add jet 2	79	-
add jets	45	-

Table 4.9.: Absolute and relative matching fractions accounting for events where the different objects from the $t\bar{t}$ system and additional jets are correctly assigned by the $t\bar{t}$ reconstruction BDT. The absolute fractions are computed with respect to the total events selected with $\geq$ 6 jets and $\geq$ 4 b-tagged jets at the 85% working point while the relative fractions are obtained considering only those where the jets matching the different objects are present. The fractions values are quoted in percentage (%).

To determine the source of the wrong jet assignments for each parton in the combination with the highest BDT score, the truth origin of the jets used to build the $t\bar{t}$ system in this combination in addition to that of the two leading additional jets in b-tagging was closely examined as depicted in Table 4.10. This allows to assess the combinatorial background introduced by the use of the BDT. The label "non-$t\bar{t}$" in the table, refers to jets which are not truth matched to the partons from the $t\bar{t}$ system.

In cases where jets are wrongfully assigned to the b-quarks from the $t\bar{t}$ system decay, they are mostly taken from the "non-$t\bar{t}$" jets. Particularly, additional jets are used as the b-jet from the hadronic (leptonic) top quark decay in 24% (21%) of the selected events. Furthermore, the additional jets are incorrectly associated to the leading and subleading quark from the hadronic W boson decay in 40% and 50% of the cases, respectively. However, a better purity is achieved in the additional jets system identified in the combination with the highest BDT score. At most, the leading additional jet in b-tagging is incorrectly taken from jets which are matched to the partons from the $t\bar{t}$ system in 44% of the cases while for the subleading additional jet it occurs less often in around 21% of the selected events.

BDT label \ truth origin	bHadTop	blepTop	wj1	wj2	non-$t\bar{t}$
bHadTop	48	15	9	5	24
bLepTop	11	62	4	2	21
wj1	4	3	40	12	40
wj2	3	3	13	31	50
add jet 1	19	16	6	4	56
add jet 2	3	4	9	6	79

Table 4.10.: Fraction of events accounting for the various truth origins of jets used in the $t\bar{t}$ reconstruction and of the additional jets in the combination with the highest BDT score in selected events with ≥ 6 jets and ≥ 4 b-tagged jets at the 85% working point. The fractions values are quoted in percentage (%).

The *purity* of a selected sample in a given parton or object (hadronic W, leptonic and hadronic top) from the $t\bar{t}$ system or in the additional jets, is defined in the following as the fraction of events where jets are correctly assigned to the object in question in the combination with the highest BDT score. I investigated the possibility of selecting a sample with an increased purity in these objects by introducing a cut on the BDT score of the combination. The cut on the BDT is parameterized in these studies in terms of the fraction of selected events passing this cut, referred to as the "efficiency". This parameter reflects the size of the sample obtained after applying the BDT cut (together with additional criteria where relevant) compared to that of the initial sample where no BDT cut is applied i.e that for which the efficiency is 100%.

Figure 4.17 illustrates how the purity of the selected sample in the different considered objects evolves with the efficiency. Both absolute and relative purities with respect to the maximum achievable matching fractions are shown. For the absolute purities plots, the efficiencies are computed with respect to the sample of events containing ≥ 6 jets and ≥ 4 b-tagged jets at the 85% working point while in the relative purities plots, they are calculated relative to the subsample of events where jets matching the object in question are present (maximum matching fraction). The sample purity is enhanced with the tightening of the BDT cut or equivalently the decrease in the efficiency, as expected. For instance, if the value of the cut on the BDT score is chosen such that 50% of the initially selected events are kept, the purity of the resulting subsample in the b-quarks from the $t\bar{t}$ system would increase by around 8% while it would be enhanced by 4% for the additional jets; similar conclusions can be derived in terms of the relative purities. Essentially, the cut on the BDT score can be adjusted taking into account the trade-off between the sample size and its targeted level of purity. Additional gain in the b-quarks from the $t\bar{t}$ system purity can be achieved by further requiring the jets assigned to them to pass the 60% working point as shown in Figure 4.18; in these plots, the relative purities are shown and the efficiencies are obtained with respect to the sample of events where the jets matching the b-quarks are present and those assigned to them by the BDT pass either the 85% or 60% working points.

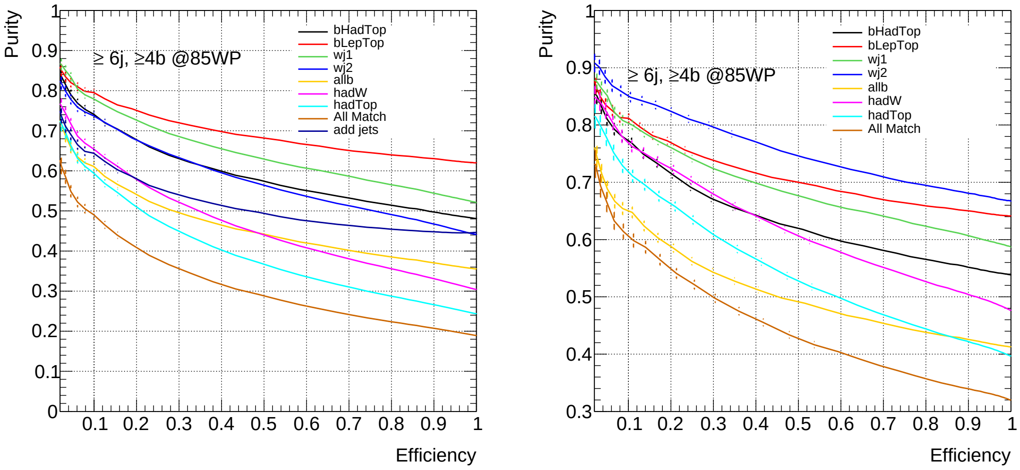

Figure 4.17.: Absolute (left) and relative (right) purities in the different objects from the $t\bar{t}$ and the additional jets systems as a function of the BDT cut efficiency (see text). The 100% efficiency corresponds to the selected sample with ≥ 6 jets and ≥ 4 b-tagged jets at the 85% working point for the absolute purities, and to the same sample with the further requirement of the jets matching the object in question to be present in the events, for the relative purities.

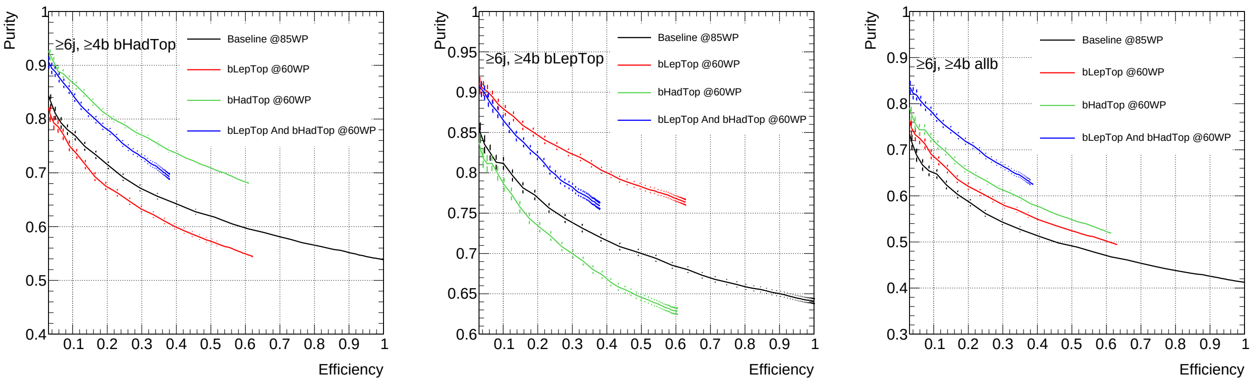

Figure 4.18.: Relative purity in the b-quark from hadronic top (left), b-quark from leptonic top (middle) and both b-quarks from the $t\bar{t}$ system (right), as a function of the BDT cut efficiency (see text). The impact of requiring the jets assigned to either one or both b-quarks to be b-tagged at the 60% working point is shown. The maximum efficiencies are computed with respect to the sample of events with ≥ 6 jets and ≥ 4 b-tagged jets at the 85 % working point where the jets matching either one or both b-quarks from $t\bar{t}$ are available (depending on the purity in question) and the jets assigned to them pass either the 85% or 60% working point.

Figure 4.19 shows the transverse momenta of the reconstructed hadronic top, leptonic top and the $t\bar{t}$ system for events with ≥ 6 jets and ≥ 4 b-tagged jets at the 85% b-tagging efficiency working point. The ΔR separation between the two b-jets from the top quarks decays, the transverse momenta of the leading and subleading additional jets in b-tagging are shown in Figure 4.20 for the same events. These variables are decently well modeled by the $t\bar{t}$ MC sample in the probed phase space region. Some discrepancies however, can be observed at low top quarks p_T, high additional jets p_T and low ΔR separation beween the b-quarks from the $t\bar{t}$ system.

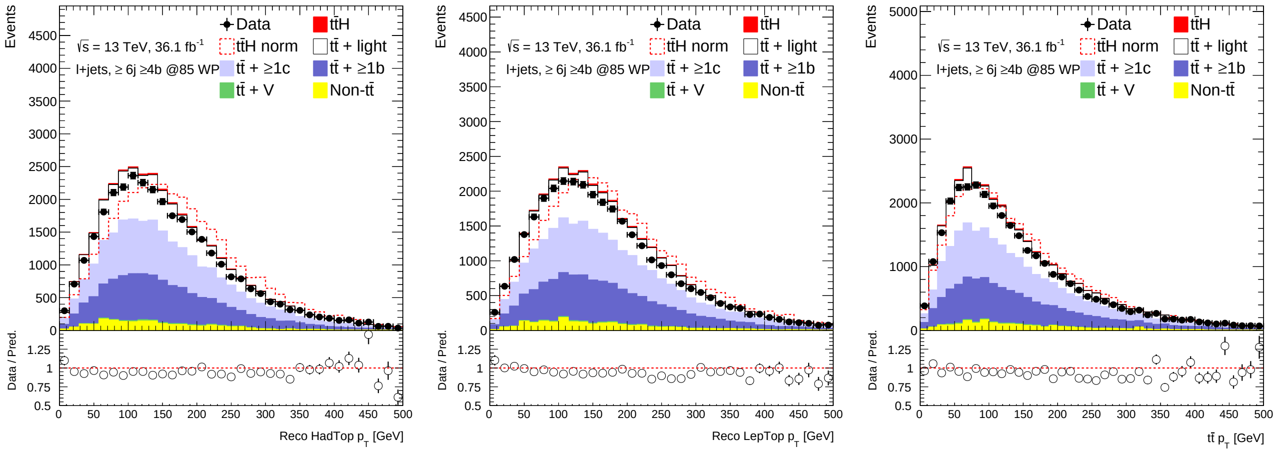

Figure 4.19.: Comparison of the predicted transverse momentum distribution of (left) the hadronic top, (middle) the leptonic top and (right) the $t\bar{t}$ system to that observed in data for events with ≥ 6 jets and ≥ 4 b-tagged jets at the 85% working point. The normalization of the $t\bar{t}+\geq 1b$ and $t\bar{t}+\geq 1c$ backgrounds was scaled based on the results of the $t\bar{t}H(H \to b\bar{b})$ search presented in Chapter 5.

4.3. Summary

The $t\bar{t}+b\bar{b}$ production evokes a lot of interest not only in the top-quark physics sector where it allows to perform important tests for the QCD predictions, but also in the search for the SM Higgs boson or BSM phenomena at the LHC. In particular, it intervenes as an overwhelming and irreducible background in the $t\bar{t}H(H \to b\bar{b})$ channel which gives a unique access to both the top and bottom quark Yukawa couplings. The $t\bar{t}+b\bar{b}$ process is challenging to model as reflected by the various MC predictions which exhibit large differences in its description. Thus, measurements of the $t\bar{t}+b\bar{b}$ production cross-section are highly anticipated to help identify which prediction best describes data and to use as inputs for improving the MC modeling of this process in the long term.

Measurements of inclusive and differential fiducial cross-sections of $t\bar{t}+b\bar{b}$ production using 36.1 fb^{-1}of data collected by the ATLAS detector during 2015 and 2016 are presented in this chapter. These measurements are performed in the single lepton and dilepton channels requiring one and two isolated leptons, respectively; further detector-level selection criteria in accordance with the $t\bar{t}+b\bar{b}$ signature in each channel are applied. The measured differential distributions are unfolded to the particle level in a well defined fiducial volume. I performed detailed simulation studies to assess the purity of the selected $t\bar{t}+b\bar{b}$ sample in terms of events falling within the fiducial volume in the single lepton channel. Around half of the selected $t\bar{t}+b\bar{b}$ events fall within the fiducial volume while the remaining half stems from various contamination sources. These were identified to be due to leptons

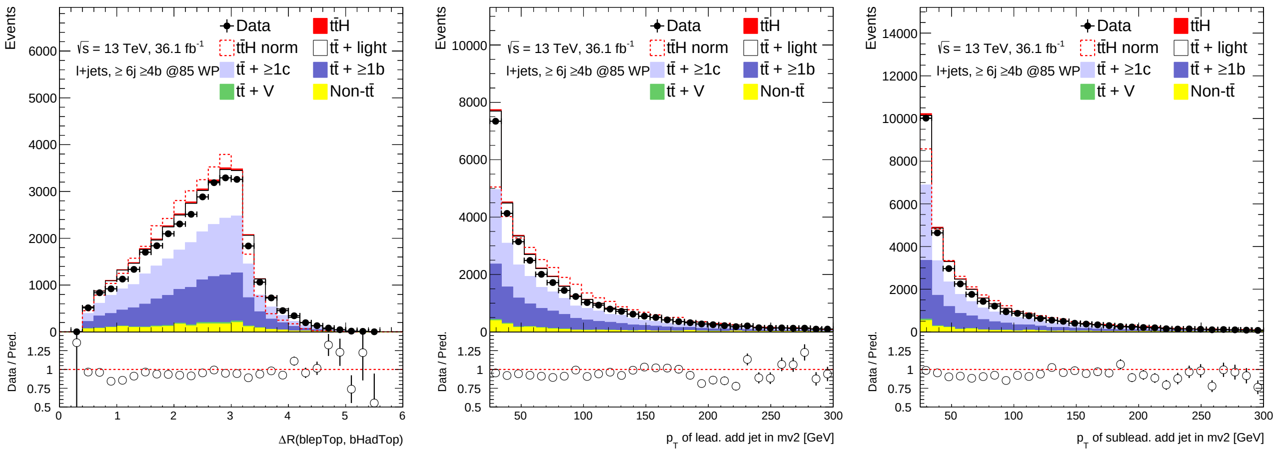

Figure 4.20.: Comparison of the predicted distribution of (left) the ΔR separation between the b-jets from top quarks decays, (middle) the p_T of the leading additional jet in the b-tagging score and (right) the p_T of the subleading additional jet in the b-tagging score to that observed in data for events with ≥ 6 jets and ≥ 4 b-tagged jets at the 85% working point. The normalization of the $t\bar{t}+\geq 1b$ and $t\bar{t}+\geq 1c$ backgrounds was scaled based on the results of the $t\bar{t}H(H \to b\bar{b})$ search presented in Chapter 5.

and jets migrations induced by the detector resolution in addition to the mis-identification of c- and light-jets as b-jets. These backgrounds are removed from the selected $t\bar{t} + b\bar{b}$ data sample prior to the unfolding step. The predicted inclusive and differential cross-sections are all in agreement with data within uncertainties. Particularly, the considered differential distributions do not yield enough differences for the data to indicate by which MC prediction it is best described.

In this thesis, I propose a method to enhance the sensitivity of the measured differential distributions namely those characterizing the additional b-jets which are the most challenging to describe by the MC models. I showed that the explicit identification of the b-jets origin will enhance the differences between the various predictions in the distributions corresponding to these jets, compared to the approach followed in the 36.1 fb^{-1}$t\bar{t} + b\bar{b}$ measurements where the b-jets origin is assumed based on their p_T ordering or ΔR separation; the validity of these assumptions was closely checked in the case of the p_T ordering. To achieve the separation between b-jets from the top quarks decays and additional b-jets, I developed a method based on the reconstruction of the $t\bar{t}$ system using a BDT. The latter was trained in the single lepton $t\bar{t} + b\bar{b}$ phase space, which suffers from large jet combinatorics, to find the best correspondence between partons from the $t\bar{t}$ system and the observed jets in the selected events; jets which were not assigned by the BDT to the $t\bar{t}$ system are identified as additional. A good performance is achieved for the $t\bar{t}$ reconstruction BDT even though no dedicated optimization was carried out. For instance, the BDT is able to correctly identify both b-jets from the $t\bar{t}$ system in 35% of the selected events in the $t\bar{t} + b\bar{b}$ phase space, and both leading additional jets in b-tagging in 45% of the events. Ways to further enhance the purities in the b-jets from $t\bar{t}$ were checked. There is a great room for improvement in the BDT performance with dedicated optimization namely in terms of input variables choice. This technique would be a great asset in the next iteration of the $t\bar{t} + b\bar{b}$ differential measurements.

5. Search for the Higgs boson in the $t\bar{t}H(H \to b\bar{b})$ channel

The top quark Yukawa coupling is the strongest in the Standard Model (SM) and plays a major role in the SM stability at high energies. It is also regarded as one of the best probes to unravel new physics phenomena. Section 5.1 presents the $t\bar{t}H(H \to b\bar{b})$ channel which grants direct access to this coupling in addition to that of the bottom quark Yukawa coupling. An overview of the $t\bar{t}H(H \to b\bar{b})$ search performed using 36.1 fb^{-1}of 13 TeV data recorded by the ATLAS detector in 2015 and 2016 is presented in Section 5.2. The main challenge of this analysis is the overwhelming background of the $t\bar{t}$ production with additional jets and more importantly with b-jets. This background is poorly described by the available MC predictions which leads to large uncertainties on its modeling. Particular emphasis is put on the studies that I performed to compare the modeling of this background among the various MC predictions. These studies are an essential input for the complex systematic model of this background. Section 5.3 presents the methods that I developed to enhance the sensitivity of the search using the full Run 2 data. The studies that I conducted to assess the sensitivity of the Higgs boson p_T measurement in the $t\bar{t}H(H \to b\bar{b})$ channel are also presented in Section 5.3.4.

5.1. The $t\bar{t}H(H \to b\bar{b})$ channel

The Higgs boson production in association with a $t\bar{t}$ pair ($t\bar{t}H$) accounts for only 1% of the total Higgs boson production cross-section at the LHC. Despite its relatively small cross-section, this production mode (see Section 1.5.1) is of great importance since it provides, at leading order, a unique direct access to the measurement of the top quark Yukawa coupling. The latter plays a key role in assessing the SM behavior of the observed Higgs boson in addition to its potential to constrain Beyond the SM (BSM) models which predict different coupling strengths.

For a 125 GeV Higgs boson, the $H \to b\bar{b}$ decay channel has the largest branching fraction of around 58% and thus it is experimentally attractive as a final state for the $t\bar{t}H$ search. Moreover, this decay mode allows to access the b-quark Yukawa coupling which is the second largest fermion coupling in the SM.

In the $t\bar{t}H(H \to b\bar{b})$ analysis, three different channels are explored depending on the decay mode of the W bosons originating from the top quarks decays:

- The **all-hadronic channel** which corresponds to events where both W bosons decay hadronically. Even though it exhibits the highest branching fraction of about 46%, it is the most challenging to exploit experimentally. This is due to the absence of leptons (electrons or muons) in the final state in addition to the presence of a high number of jets rendering it difficult to distinguish from the large multijet background which is hard to model accurately. The analysis probing this channel is optimized independently from the rest and will not be covered in the scope of this thesis.

- The **dilepton channel** which hosts events where both W bosons decay leptonically. It has the lowest branching ratio of around 10%. The two neutrinos from the W boson decays contribute both to the event missing transverse momentum (E_T^{miss}) which makes the reconstruction of the event kinematics less precise. However, it offers the cleanest signature with a very high separation from the multijet background.

- The **single lepton** channel which contains events where one W boson decays hadronically while the other decays leptonically. It is the most sensitive channel combining a high branching ratio of 44%[a] (close to that of the all-hadronic channel) and a relatively clean topology with one lepton in the final state allowing to suppress the multijet background. Moreover, the presence of only one neutrino in the final state allows for its kinematics to be determined fully from the event E_T^{miss} thus enabling a more precise event reconstruction compared to the dilepton channel. A Feynman diagram depicting the single lepton channel is shown in Figure 5.1(a).

In what follows, the term lepton refers to either an electron or a muon. Electrons and muons from τ leptons decay are also included. The single lepton and dilepton channels encounter similar challenges and thus follow the same strategy. However, they are analyzed separately and combined in the final fit to extract the signal strength μ.

Despite the benefits of targeting the $H \to b\bar{b}$ decay mode, the $t\bar{t}H(H \to b\bar{b})$ channel faces several challenges arising mainly from the complexity of the final state topology with the presence of multiple jets and b-tagged jets in addition to the overwhelming background from $t\bar{t}$ + jets events and most importantly the irreducible component of $t\bar{t}$ plus additional b-jets ($t\bar{t}+b\bar{b}$), depicted in Figure 5.1(b). The latter suffers from large theoretical uncertainties in the probed phase space and is poorly constrained by the existing data measurements (See Chapter 4).

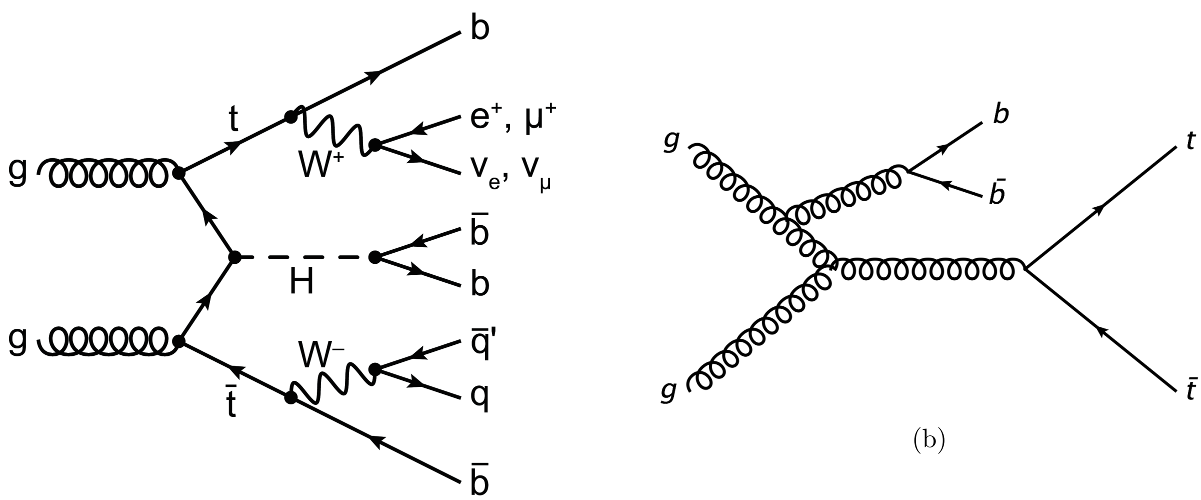

(a) (b)

Figure 5.1.: Feynman diagram representation at tree-level for: (a) the Higgs boson production in association with a $t\bar{t}$ pair and its subsequent decay to a pair of bottom quarks, in the single lepton channel (see text), (b) the main $t\bar{t}$ + $b\bar{b}$ background.

Searches for the $t\bar{t}H(H \to b\bar{b})$ production were performed by ATLAS [126] and CMS [127] in Run 1 using roughly 5 fb^{-1}of data at 7 TeV and 20 fb^{-1}at 8 TeV . The combination of ATLAS and CMS measurements [30] led to observed (expected) significances of 4.4 (2.0) σ for the $t\bar{t}H$ production and 2.6 (3.7) σ for the $H \to b\bar{b}$ decay mode. These processes were not yet established at the end of Run 1.

In Run 2, the analysis strategy for the ATLAS $t\bar{t}H(H \to b\bar{b})$ search was updated, implementing several improvements at various stages of the analysis chain to enhance its sensitivity. Results based on the updated strategy were published in [128] using the full 2015 and 2016 data corresponding to an

[a]The branching ratio of the single lepton channel becomes ~ 29% when excluding decays to τ leptons.

overall integrated luminosity of 36.1 fb^{-1}. In the first part of this chapter, the full analysis chain yielding these results is described with more emphasis on the single lepton channel. Since these results, a new round of the analysis started (and is currently ongoing), targeting results with the full Run 2 dataset amounting to an integrated luminosity of 139 fb^{-1}. The analysis strategy updates as well as its prospectives for measuring the Higgs boson p_T are presented in the second part of this chapter.

5.2. Overview of the $t\bar{t}H(H \to b\bar{b})$ analysis

5.2.1. Object and event selections

The analysis is performed using data events from pp collisions at $\sqrt{s}$ = 13 TeV recorded by the ATLAS detector during 2015 and 2016. Only events for which all relevant detector subsystems were operational are considered which amounts to an integrated luminosity of 3.2±0.1 fb^{-1}in 2015 and 32.9±0.7 fb^{-1}in 2016. The number of pp interactions per bunch crossing, or pile-up, in this data set ranges from 8 to 45 interactions. Only events containing at least one vertex with two or more tracks associated to it with p_T>0.4 GeV , are kept. The vertex with the largest sum of the squares of the transverse momenta of the associated tracks is chosen as the primary vertex of interest i.e the hard scatter vertex.

Events are selected with unprescaled single-lepton triggers with different p_T thresholds, combined in a logical "OR" to ensure higher selection efficiency. In particular, the lower p_T threshold triggers have additional lepton isolation criteria. Different triggers are used for the 2015 and 2016 datasets due to changes in the data-taking conditions, in order to maintain the same level of selection rate at the higher instantaneous luminosities in 2016. The selection criteria required by the adopted triggers are listed in table 5.1.

Reconstructed object	p_T threshold [GeV]	Identification menu	Isolation menu
2015(2016) data-taking period			
Electrons	≥24(26) ≥60 ≥ 120 (140)	Medium(Tight) Medium Loose	Gradient None None
Muons	≥20(26) ≥ 50	Loose(Medium) None	Gradient None

Table 5.1.: Single-lepton triggers used in the $t\bar{t}H(H \to b\bar{b})$ analysis.

Muons and electrons are reconstructed based on the standard ATLAS algorithms described in Sections 2.4.2 and 2.4.3, respectively. Loose selection requirements which are common to all $t\bar{t}H$ decay channels across the various final states, are applied first to avoid overlap when combining results from these channels at a later stage. Events with at least one lepton with p_T>27 GeV , passing these selections are kept for the $t\bar{t}H(H \to b\bar{b})$ analysis. Cuts on the leptons longitudinal impact parameter, $|z_0 \sin\theta| < 0.5$ mm, and on the transverse impact parameter significance, $|d_0|/\sigma_{d_0} < 5(3)$ for electrons (muons), are applied to ensure that leptons tracks are consistent with originating from the hard scatter vertex. Events are split based on the number of leptons into two channels: the dilepton and the single-lepton channels. To enter the dilepton channel, events must have exactly two leptons with opposite electric charge. The subleading lepton p_T must be above 15(10) GeV in the ee($e\mu/\mu\mu$) channel. Moreover, in the same lepton flavor channels ($\mu\mu$/ee), the dilepton invariant mass must be above 15 GeV and outside of the Z boson mass window (83-99) GeV . Dilepton events containing at least one hadronically decaying τ lepton candidate are vetoed to maintain orthogonality with other $t\bar{t}H$ search channels. On the other hand, events enter the single-lepton channel if they contain exactly one lepton and not more than one hadronic τ candidate. To improve the purity of events passing the above selections, selected leptons are required to satisfy additional identification and isolation criteria, otherwise the corresponding events are discarded. For electrons, the tight likelihood identification criterion is used whereas the medium working point is used for muons. Both electrons and muons are required to pass the Gradient isolation criterion.

Jets used in the $t\bar{t}H(H \to b\bar{b})$ analysis, are reconstructed with the anti-k$_T$ algorithm with a radius parameter of 0.4 using topological calorimeter clusters as inputs, corrected by the JES calibration as described in Section 2.4.4. They are required to have $p_T > 25$ GeV and $|\eta| < 2.5$. Additional quality criteria are imposed on jets to identify those originating from non-collision sources or detector noise and any event containing such a jet is removed. To reduce the contribution of jets from pile-up, jets with low transverse momenta ($p_T < 60$ GeV) in the central detector region ($|\eta| < 2.4$) are rejected if their corresponding JVT score is below 0.59. Moreover, an overlap removal procedure between jets and leptons is employed to avoid the double counting of a single detector response as more than one physics object in an event. At the preselection level, events are required to have at least 5 (3) selected jets in the single-lepton (dilepton) channel.

The identification of b-jets plays a crucial role in this analysis given the complexity of the $t\bar{t}H(H \to b\bar{b})$ final state with 6 jets expected, 4 of which being b-jets, for instance in the single lepton channel. To this end, the MV2c10 algorithm described in details in Section 3.1.2.3 is used. Four working points are defined depending on the threshold applied on the MV2c10 weight (discriminant output) and are referred to as *loose*, *medium*, *tight* and *very tight*. The corresponding efficiency for b-jets, with $p_T > 20$ GeV in simulated $t\bar{t}$ events, to pass these working points are: 85%, 77%, 70% and 60% respectively and the associated rejection factors for c-jets are in the range 3-35 whereas for light-jets, the factors are in the range of 30-1500. Each jet is assigned a discrete b-tagging discriminant value according to the tightest working point it passes, varying from 1 for a jet which does not satisfy any of the working points criteria up to 5 for a jet tagged at the very tight working point. The b-tagging efficiencies for each jet flavor in MC simulations are corrected to match data through scale factors. These factors as well as their corresponding uncertainties are measured independently for each of the considered working points and later combined in the so-called *pseudo-continuous* calibration allowing the simultaneous exploitation of multiple working points. Selected events are required to have at least two b-tagged jets at the very tight working point or at least three b-tagged jets at the medium working point in the single-lepton channel. As for the dilepton channel, events must have at least 2 b-tagged jets at the medium working point.

Large R-jets objects are used in the single-lepton channel to identify top quarks and Higgs bosons when these are produced with large transverse momenta (i.e boosted) and decay into collimated hadronic final states in signal events. These jets are built by reclustering standard jets with the anti-k$_T$ algorithm but with a radius parameter of 1 [129]. Events in the single lepton channel are split into boosted and resolved categories with the latter covering events which do not pass the boosted selection. To enter the boosted category, an event must contain at least one standard jet and at least two large-R jets with $p_T > 200$ GeV , $|\eta| < 2$ and an invariant mass above 50 GeV . Furthermore, at least one of the large-R jets must be identified as a Higgs boson candidate and one of the remaining large-R jets as a hadronically decaying top quark candidate. Boosted Higgs boson candidates are defined as large-R jets with at least two constituent jets, of which two at least are b-tagged at the loose working point. If more than one boosted Higgs candidate is found, the one with the highest sum of the constituent jets b-tagging discriminants is chosen. The boosted top is defined as the large-R jet with the highest mass which was not selected as a boosted Higgs boson candidate and satisfying $p_T > 250$ GeV . Exactly one constituent b-tagged jet at the loose working point and at least one additional constituent jet which is not b-tagged are required for the boosted top.

The missing transverse energy is reconstructed as described in Section 2.4.6 and it is not used for event selection. However, it contributes to the event reconstruction to account for the neutrino from the leptonic decay of the W boson.

5.2.2. Signal and background modeling

All the MC samples used in the $t\bar{t}H(H \to b\bar{b})$ analysis are generated through the standard ATLAS simulation software described in Section 2.3. Samples used for the nominal predictions of all considered processes are produced following the Fullsim procedure in order to ensure the best precision for data modeling. The faster simulation (ATLFAST-II) was adopted for some of the alternative samples used to define modeling systematic uncertainties. MC samples are subjected to the same reconstruction algorithms and analysis chain as data. The effects of pile-up are simulated based on its expected profile in the LHC runs. Simulated events are then reweighted to match the pile-up conditions observed in data. Heavy-flavor hadron decays were performed by EvtGen [130] except in samples simulated with Sherpa.

5.2.2.1. $t\bar{t}H$ MC simulation

The Madgraph5_aMC@NLO [65] package was used to model the $t\bar{t}H$ signal process at the NLO accuracy in QCD for the matrix element calculation. For the parton shower and hadronization modelling, Pythia 8 was used with the A14 set of tuned parameters [113]. The NNPDF3.0NLO parton distribution function set [112] was used. The Higgs boson mass was set to 125 GeV and all decay modes were included using the latest branching ratios calculations [29]. The $t\bar{t}H$ cross-section of 507^{+35}_{-50} fb was computed at the NLO accuracy in QCD including NLO electroweak corrections and is used to normalize the sample.

5.2.2.2. $t\bar{t}$ + jets background MC simulation

The nominal sample used to model the $t\bar{t}$+jets background is the same as the one used as the nominal prediction in the $t\bar{t}$+$b\bar{b}$ cross-section measurements, described in Section 4.1.2. This sample in referred to as PWG+PYT8 in the following.

The $t\bar{t}$ production in association with additional heavy flavor jets, namely b-jets, is the most challenging background in the $t\bar{t}H(H \to b\bar{b})$ analysis. This is why the $t\bar{t}$ + jets sample is divided into three orthogonal components such that the contribution from the different flavors of additional jets, not originating from the $t\bar{t}$ system, are separated. This division is based on the presence of additional truth jets in the event required to have $p_T > 15$ GeV and $|\eta| < 2.5$. The flavor of a jet is determined based on the ΔR labeling scheme described in Section 4.1.3. Jets matched to exactly one b-hadron with $p_T > 5$ GeV are labeled single b-jets, while those matched to more than one b-hadron are labeled B-jets such that no p_T requirement is imposed on the subleading b-hadrons. Single c-jets and C-jets are defined analogously if they are not already matched to b-hadrons. Events that have at least one additional single b- or B-jet are labeled as $\boldsymbol{t\bar{t}+\geq 1b}$. Events which are not already labeled as $t\bar{t}+\geq 1b$ and have at least one additional single c- or C-jet are labeled as $\boldsymbol{t\bar{t}+\geq 1c}$. Lastly, the remaining events which do not contain any additional heavy flavor jets, are labeled as $\boldsymbol{t\bar{t}}$ **+ light**. $t\bar{t}+\geq 1b$ and $t\bar{t}+\geq 1c$ samples are collectively referred to as $t\bar{t}$ + HF.

The $t\bar{t}$ + HF samples are further subdivided into sub-components in order to apply correction factors on the relevant sub-categories and estimate systematic uncertainties. The $t\bar{t}+\geq 1b$ is split into four sub-categories. Events with exactly one single b-jet are labeled as $\boldsymbol{t\bar{t}+b}$, those with exactly two single b-jets are labeled as $\boldsymbol{t\bar{t}+b\bar{b}}$ and events with exactly one B-jet are referred to as $\boldsymbol{t\bar{t}+B}$. The remaining events in the $t\bar{t}+\geq 1b$ background are labeled as $\boldsymbol{t\bar{t}+\geq 3b}$. Events containing additional b-jets entirely originating from multiparton interactions (MPI) or from gluon radiation from $t\bar{t}$ decay products (FSR) are considered in a separate subcategory labeled as $\boldsymbol{t\bar{t}+b}$ **(MPI/FSR)**. The latter accounts for a small fraction of the $t\bar{t}+\geq 1b$ events (few % after event selection) and is not present in all $t\bar{t}$ MC samples. The $t\bar{t}+\geq 1c$ sample is divided analogously.

In order to describe the dominant $t\bar{t}+\geq 1b$ background with the highest available precision, an NLO $t\bar{t}b\bar{b}$ sample including parton shower and hadronization, generated with Sherpa+OpenLoops [117, 131] was used. It was produced with Sherpa version 2.1.1 and the CT10 4FS PDF set [132, 133] which allows to use massive b-quarks. This sample, referred to in the following as SHERPA4F , provides a matrix element description for the two additional b-jets at NLO in QCD in contrast to the nominal PWG+PYT8 simulation where the additional b-jets are coming from the parton shower. Since there is no clear theoretical prescription on how to merge the $t\bar{t}b\bar{b}$ sample with the inclusive $t\bar{t}$ + jets 5FS samples and remove the overlap with $t\bar{t}$ production with additional b-jets, the former cannot be used as the nominal prediction for the $t\bar{t}+\geq 1b$ background in a straightforward manner. Instead, the relative contributions of the $t\bar{t}+\geq 1b$ subcategories in the PWG+PYT8 sample are scaled to match those predicted by the SHERPA4F sample; events in the $t\bar{t}+b$ (MPI/FSR) subcategory are not scaled as they are not included in this sample. The differences between the two predictions in the fractions of the $t\bar{t}+\geq 1b$ subcategories are shown in Figure 5.2.

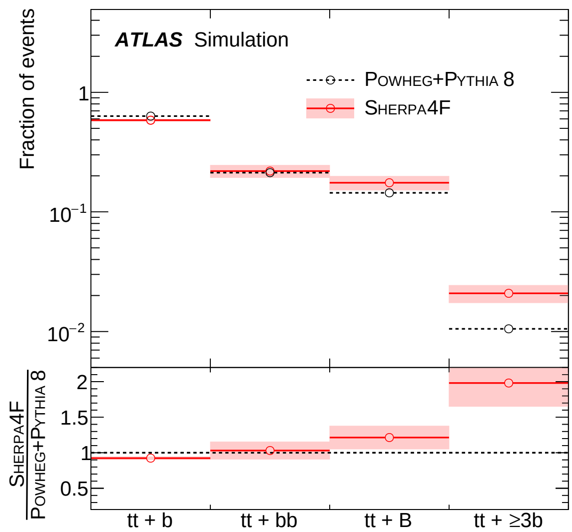

Figure 5.2.: The predicted fractions of the $t\bar{t}+\geq 1b$ subcategories in both the inclusive PWG+PYT8 and the SHERPA4F samples. The shaded area corresponds to the systematic uncertainties on the SHERPA4F sample (see Section 5.2.5.1). The fractions are normalized to the sum of the four contributions shown here, excluding the $t\bar{t}+b$ (MPI/FSR) subcategory [128].

The particular choice of parameters for the heavy flavor jets definition described above, i.e the threshold cuts on the transverse momentum of the truth jets being 15 GeV and that of the leading hadrons associated to them being 5 GeV , was adopted as the baseline in the $t\bar{t}H(H \to b\bar{b})$ analysis. In this respect, I performed studies to ensure that this choice of $t\bar{t}$ + HF definition does not introduce any bias in the analysis in terms of the differences among $t\bar{t}$ generators in the corresponding fractions of $t\bar{t}$ + jets components. The $t\bar{t}$ + jets generators used in these studies include the nominal and the SHERPA4F samples presented above in addition to three other samples: PWG+HW7 , SHERPA and aMC@NLO+PYT8 . The MC setups allowing to generate the first two samples, used to estimate $t\bar{t}$

related modeling uncertainties, are detailed in Section 5.2.5.1; the third sample uses the same setup as the $t\bar{t}H$ signal.

To gauge the impact of the HF definition choice, I assessed the fractions of $t\bar{t}$ + jets components for several HF jets definitions which I devised by performing a scan of one of the following parameters while the others are kept at their baseline value: the threshold cut on the truth jet p_T, on the leading hadron p_T and on their ratio. In the case of the $t\bar{t}+\geq 1b$ sample definition, these parameters are displayed for the additional b-jets and the b-hadrons matched to them in Figure 5.3. The p_T spectra of the additional b-jets and the leading b-hadrons are harder in the SHERPA4F sample compared to the 5FS generators. The largest discrepancies between the 4FS and 5FS samples and among the latter ones, arise at low b-hadrons p_T (< 14 GeV): the amount of low p_T b-hadrons present in the 5FS samples is significantly higher, especially in the PWG+HW7 sample, with respect to that in the 4FS sample. Furthermore, the fraction of b-jets where the leading b-hadron matched to them grabs a small fraction of their p_T (up to 30%) is larger in the 5FS samples compared to the SHERPA4F sample. This discrepancy is more pronounced when harder p_T cuts are applied on the additional b-jets (see Section 5.2.5.1).

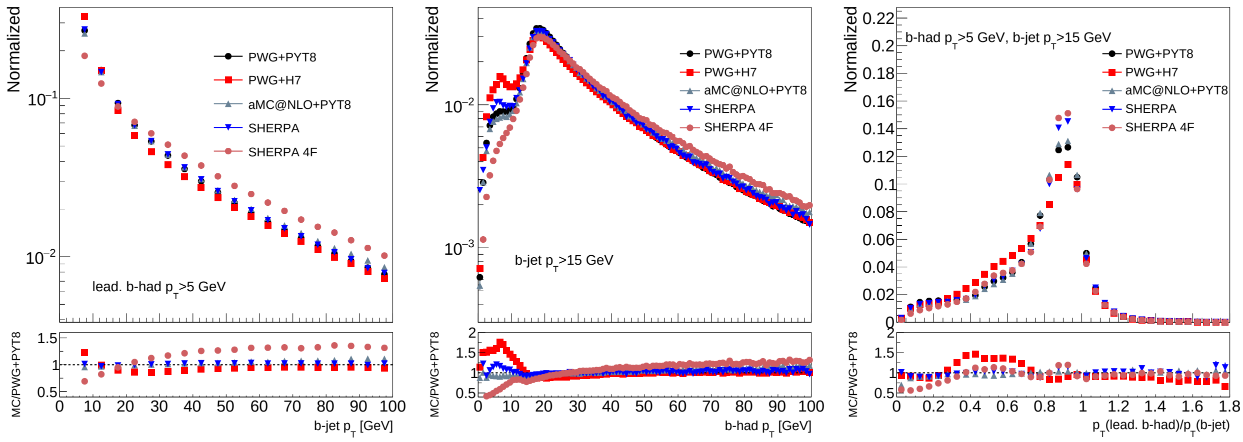

Figure 5.3.: Key parameters used in the $t\bar{t}+\geq 1b$ sample definition: additional b-jets p_T matched to b-hadrons with $p_T > 5$ GeV (left), additional b-hadrons p_T matched to truth jets with $p_T > 15$ GeV (middle) and p_T ratio of the leading b-hadron ($p_T > 5$ GeV) with respect to the additional b-jet ($p_T > 15$ GeV) to which it was matched (right). For these distributions, no reco-level event selection is applied.

The impact of the various HF definitions inspected on the $t\bar{t}+\geq 1b$ fraction in the considered $t\bar{t}$ + jets predictions is shown in Figure 5.4. As expected, the $t\bar{t}+\geq 1b$ fraction decreases when the p_T and p_T ratio thresholds are increased. However, the differences among the various $t\bar{t}$ + jets samples remain relatively stable with respect to the systematic uncertainties assigned in Section 5.2.5.1, across the different HF jets definitions. This also holds for the $t\bar{t}+\geq 1b$ subcategories definitions as shown in Figures 5.5 and 5.6 for the $t\bar{t} + b\bar{b}$ and $t\bar{t} + B$ subcomponents, respectively. Similar conclusions were achieved regarding the generators differences in the $t\bar{t}+\geq 1c$ and $t\bar{t}$ + light fractions.

These checks allowed to establish the choice of the nominal HF definition parameters used in the $t\bar{t}H(H \to b\bar{b})$ analysis.

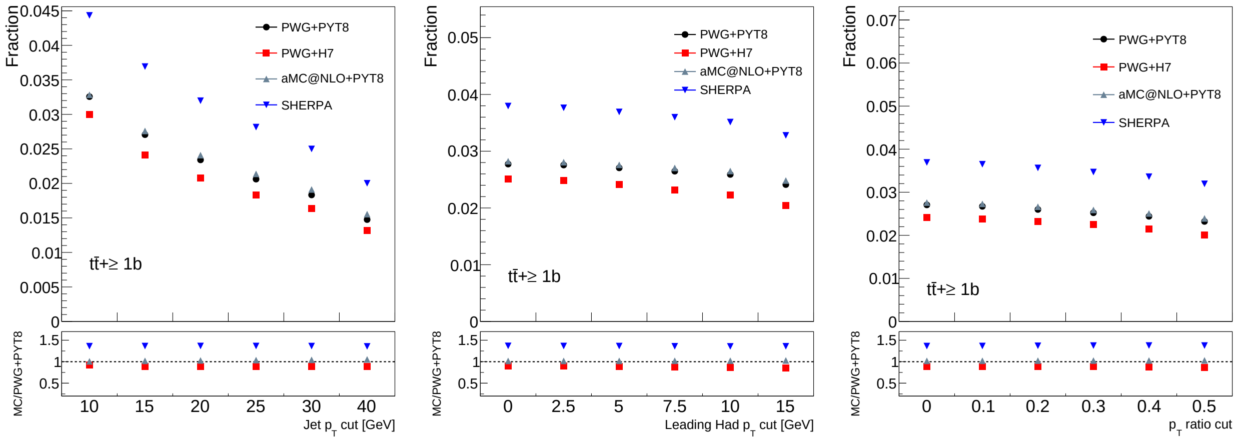

Figure 5.4.: Impact of varying the truth jet p_T (left), the leading hadron p_T (middle) and the p_T ratio cuts in the HF jets definition, on the $t\bar{t}+\geq 1b$ fraction. No reco-level event selection is applied.

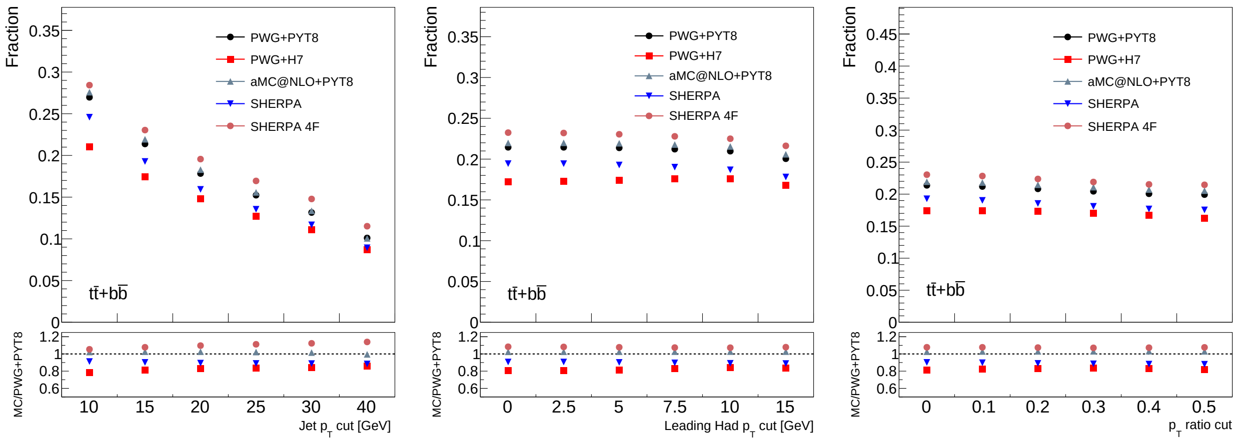

Figure 5.5.: Impact of varying the truth jet p_T (left), the leading hadron p_T (middle) and the p_T ratio (right) cuts in the HF jets definition, on the $t\bar{t}+b\bar{b}$ fraction normalized to that of the $t\bar{t}+\geq 1b$ category.

5.2.2.3. Other backgrounds

$t\bar{t}W$ and $t\bar{t}Z$ samples, collectively referred to as $t\bar{t}V$, were generated using the same setup as the $t\bar{t}H$ signal.

Samples of W/Z boson produced in association with jets were generated using Sherpa 2.2.1. The Comix [134] and OpenLoops matrix elements were used, computed for up to two additional partons at NLO and up to four additional partons at LO. These were merged with the Sherpa parton shower [135] using the ME+PS@NLO prescription. The W/Z+jets events are normalized using the NNLO cross-sections [136]. Additionally, the Z+heavy-flavor-jets contribution was corrected by a factor of 1.3, derived from dedicated Z+jets control regions in data. The diboson+jets samples were generated using Sherpa 2.1.1.

Single-top quark background processes were all modeled using Powheg-Box matrix element at the NLO accuracy with the CT10 PDF set, interfaced to the Pythia 6 parton shower with the Perugia

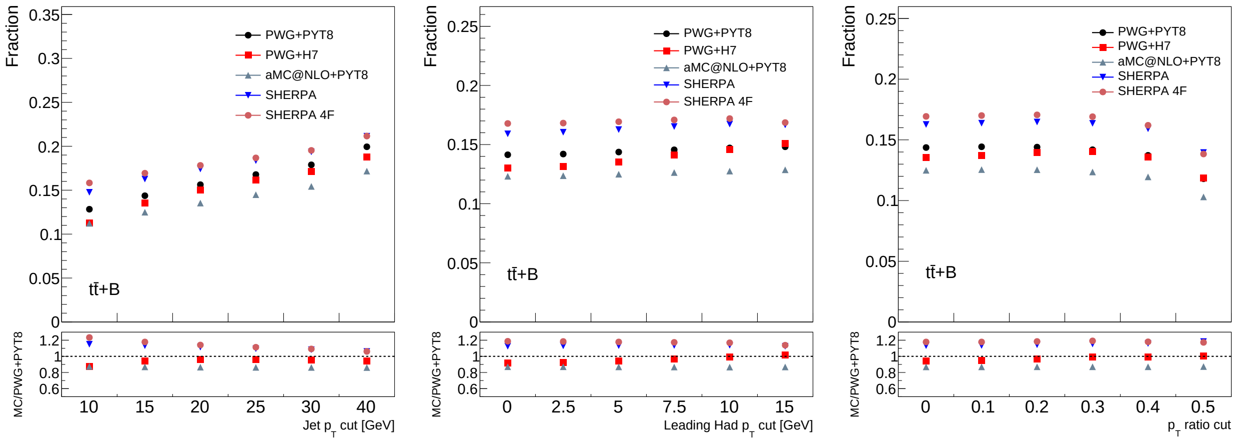

Figure 5.6.: Impact of varying the truth jet p_T (left), the leading hadron p_T (middle) and the p_T ratio (right) cuts in the HF jets definition, on the $t\bar{t}+B$ fraction normalized to that of the $t\bar{t}+\geq 1b$ category.

2012 set of tuned parameters [137]. Other sources of tops from $t\bar{t}WW$, tZW, tZ and 4-top production modes were also considered. These were generated with Madgraph5_aMC@NLO. The tZ sample was obtained using the Pythia 6 parton shower with the Perugia 2012 tune. The other three processes were generated using Pythia 8 for the parton shower modeling with the A14 set of tuned parameters.

The Higgs boson production in association with a single top quark is rare in the SM and has a negligible contribution in the $t\bar{t}H(H \to b\bar{b})$ analysis. However, it is considered in the analysis and treated as a background. The WtH sample, where the Higgs boson is produced in association with a single top quark and a W boson, was generated using Madgraph5_aMC@NLO interfaced to Herwig++ [74] with the CTEQ6L1 PDF set [138]. Samples of single top quarks plus Higgs boson plus jets, tHqb, were produced with Madgraph5_aMC@NLO interfaced to Pythia 8 using the CT10 4F scheme PDF set.

In the single lepton channel, the background originating from events with a jet or a photon misidentified as a lepton (fake lepton) or non-prompt lepton is hard to model theoretically and therefore it is estimated directly from data using the matrix method [122]. The latter is based on measuring in data, the efficiencies of fake or non-prompt leptons and real prompt leptons to pass a loose identification requirement and the tight criteria adopted in the $t\bar{t}H(H \to b\bar{b})$ analysis. For real prompt leptons, the efficiency is measured in $Z \to ll$ events based on the tag-and-probe method while for fake and non-prompt leptons, it is estimated in multijet enriched regions. The fake background contribution was found to be very small in the most sensitive single lepton signal regions (see Section 5.2.3.1) and thus it was neglected.

In the dilepton channel, the fake background is estimated based on simulation and is normalized to data in a control region with same-sign leptons.

All background samples described above, except for $t\bar{t}V$, are referred to as non-$t\bar{t}$. The contribution of the latter to the total background prediction varies between 4% and 15% depending on the considered analysis region [128].

5.2.3. Analysis strategy

Events passing the selection criteria described in section 5.2.1 are dominated by the $t\bar{t}$ background. These events are classified into exclusive analysis categories based on the total number of jets as well as that of the b-tagged jets at the four working points considered in the analysis. MVA techniques are then utilized to further improve the $t\bar{t}H(H \to b\bar{b})$ analysis sensitivity in the categories enriched in signal.

5.2.3.1. Event categorization

Events in the single lepton boosted category are not further subdivided given the small number of selected events entering in this category.

Single lepton resolved events are first classified based on the jet multiplicity into two categories: one with exactly 5 jets and one with at least 6 jets. In each of these categories, events are further subdivided depending on the discrete b-tagging discriminant value of the four leading jets in MV2c10 score. The latter are used as inputs to design b-tagging requirements enabling to devise analysis categories which are enriched in one of the relevant sample components: $t\bar{t}H$ and $t\bar{t}+b\bar{b}$, $t\bar{t}+b$, $t\bar{t}+\geq 1c$ and $t\bar{t}$ + light. Categories with an enhanced contribution of $t\bar{t}H$ and $t\bar{t}+b\bar{b}$ with respect to the other backgrounds are labeled as *signal* regions whereby MVA techniques are put in place to further separate the $t\bar{t}H$ signal from the dominating $t\bar{t}+b\bar{b}$ background. The remaining analysis categories are referred to as *control* regions. These are not subjected to further separation between the signal and background however they provide stringent constraints on the backgrounds and systematic uncertainties in a simultaneous fit with the signal regions (see section 5.2.4).

For the single lepton channel, five signal regions are defined with different levels of purity in $t\bar{t}H$ and $t\bar{t}+b\bar{b}$, three of which require $\geq$ 6 jets and are referred to as $\mathrm{SR}_1^{\geq 6\mathrm{j}}$, $\mathrm{SR}_2^{\geq 6\mathrm{j}}$and $\mathrm{SR}_3^{\geq 6\mathrm{j}}$while the remaining two require exactly 5 jets and are labeled as $\mathrm{SR}_1^{5\mathrm{j}}$and $\mathrm{SR}_2^{5\mathrm{j}}$. $\mathrm{SR}_1^{\geq 6\mathrm{j}}$and $\mathrm{SR}_1^{5\mathrm{j}}$have the highest signal purity and they both require four b-tagged jets at the very tight working point while the other signal regions apply looser b-tagging requirements. The boosted category forms the sixth signal region referred to as $\mathrm{SR}^{\mathrm{boosted}}$. The remaining events with $\geq$ 6 jets are then categorized into three control regions enriched in $t\bar{t}+b$, $t\bar{t}+\geq 1c$ and $t\bar{t}$ + light labeled as $\mathrm{CR}_{t\bar{t}+b}^{\geq 6\mathrm{j}}$, $\mathrm{CR}_{t\bar{t}+\geq 1c}^{\geq 6\mathrm{j}}$and $\mathrm{CR}_{t\bar{t}+\mathrm{light}}^{\geq 6\mathrm{j}}$, respectively. Similarly, events with exactly 5 jets are categorized into 3 control regions labeled as $\mathrm{CR}_{t\bar{t}+b}^{5\mathrm{j}}$, $\mathrm{CR}_{t\bar{t}+\geq 1c}^{5\mathrm{j}}$and $\mathrm{CR}_{t\bar{t}+\mathrm{light}}^{5\mathrm{j}}$. Figure 5.7 presents the detailed definition of the signal and control regions in the resolved single lepton channel. The fraction of the different background components as well as the $t\bar{t}H$ signal purity for each of these categories is shown in Figures 5.8 and 5.9, respectively.

In the dilepton channel, the same approach as above is followed and 7 analysis categories are defined, four of which are signal regions.

5.2.3.2. Use of Multivariate techniques

To enhance the separation between the $t\bar{t}H(H \to b\bar{b})$ signal and the $t\bar{t}$+jets background, thus obtaining high signal purity bins, multivariate techniques (MVAs) are used. Firstly, three intermediate methods which exploit the event topology and the kinematic properties of the selected objects in order to build discriminating variables for the signal and $t\bar{t}$ + jets background, are used. The outputs of these MVAs are then fed as input to a classification BDT together with global event kinematic variables and the b-tagging weight of jets. The classification BDT is trained to separate the $t\bar{t}H(H \to b\bar{b})$ signal from the $t\bar{t}$ + jets background. The intermediate MVAs used are the following:

Reconstruction BDTs

The reconstruction BDTs are used in all single lepton resolved and dilepton categories. They are trained to find the correct matching between the reconstructed jets and the partons stemming from the top quarks and Higgs boson decays and reject any other combination based on the event topology

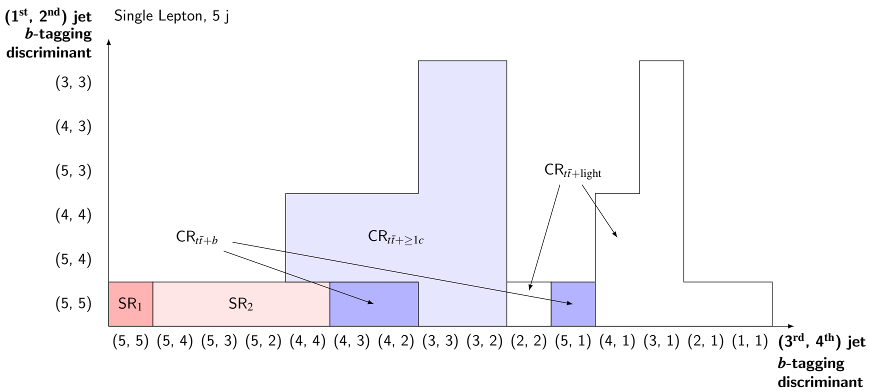

(a)

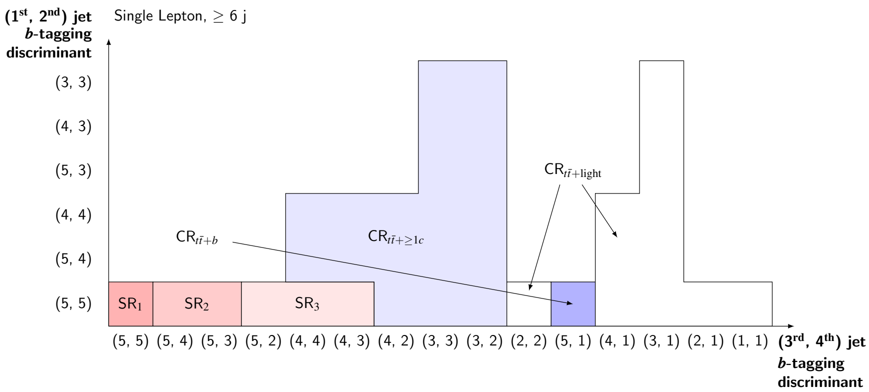

(b)

Figure 5.7.: Definition of the (a) five-jet and (b) six-jet signal and control regions in the single lepton resolved channel as a function of the *b*-tagging discriminant of the four leading jets in MV2c10 score [128]. The vertical axis shows the values of this discriminant for the first two jets while the horizontal axis shows these values for the third and fourth jets.

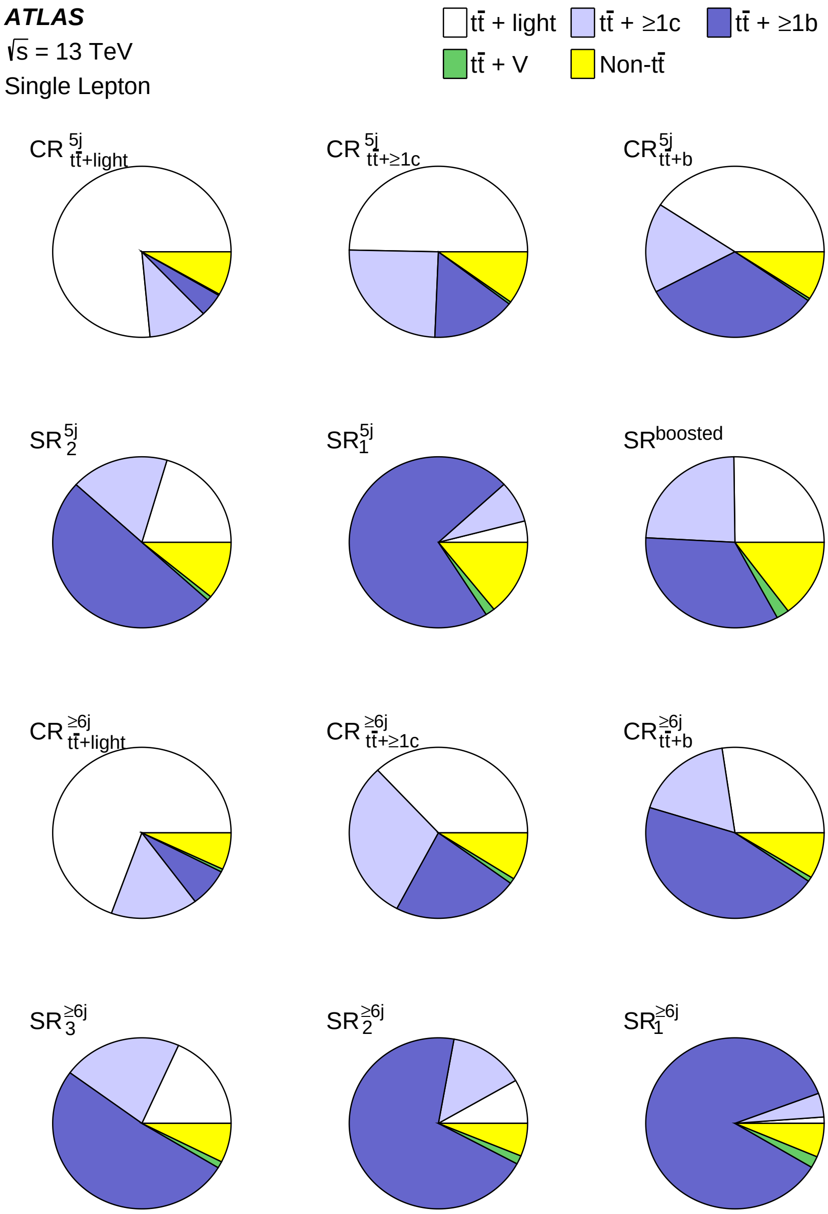

Figure 5.8.: The fraction of the different background components relative to the total background in each of the 12 categories of the $t\bar{t}H(H \rightarrow b\bar{b})$ single lepton channel [128].

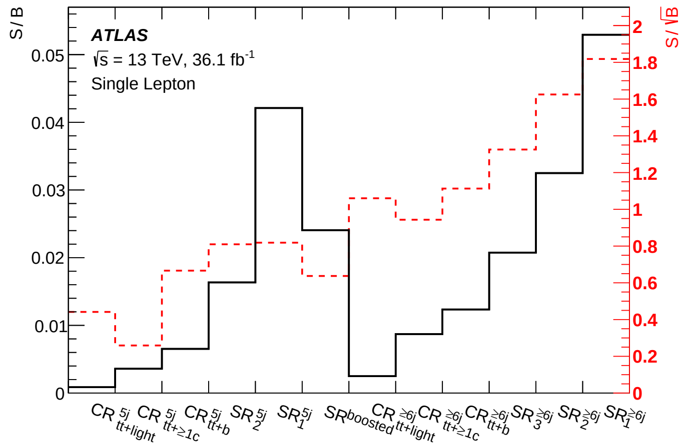

Figure 5.9.: The ratios S/B (black solid line, referring to the vertical axis on the left) and $S/\sqrt{B}$ (red dashed line, referring to the vertical axis on the right) for each of the 12 categories defined in the $t\bar{t}H(H \to b\bar{b})$ single lepton channel [128].

and the kinematics of the $t\bar{t}H$ decay products. To this end, W boson, top quark and Higgs boson candidates are built from combinations of jets and leptons.

In the single lepton categories with ≥ 6 jets, the $t\bar{t}$ system is reconstructed in a similar way to that described in Section 4.2.3.2 except for not allowing the leading four jets, instead of only the leading two, in MV2c10 b-tagging weight to be used as the light-jets from the hadronic W. The two leading additional jets in b-tagging weight that were not used to build the $t\bar{t}$ system, are used to reconstruct the Higgs boson. In the 5-jet categories, the hadronic W boson is not reconstructed since the missing jet in the events entering these categories mostly originates from the subleading quark from the W boson; a partial top is built in this case by pairing a b-tagged jet and a light-jet. In the dilepton channel, leptonically decaying W candidates are not built and top quark candidates are formed by one lepton and one jet.

Reconstruction BDTs are trained using all allowed combinations built in $t\bar{t}H$ events. In each event, the combination of jet-parton assignments corresponding to the highest BDT score is chosen to compute the kinematic and topological information of the top quark and Higgs boson candidates which are used as inputs to the classification BDT.

The above reconstruction techniques are not used in the single lepton boosted category as the Higgs boson and top quark candidates are directly obtained from the selected large R-jets as described in Section 5.2.1.

Likelihood discriminant (LHD)

The LHD is computed for each event combining its probability to satisfy the $t\bar{t}H(H \to b\bar{b})$ and $t\bar{t}$ + jets hypotheses. These probabilities are computed as the product of one dimensional probability density functions (pdfs) for the signal and background hypotheses. The pdfs are constructed for various kinematic distributions characterizing the selected jets and leptons, similar to those used for the reconstruction BDT. The LHD is used as input to the classification BDT in the single lepton resolved categories only. More details about this method can be found in [128] and the references therein.

Matrix Element Method (MEM)

The MEM discriminant is calculated for each event combining its likelihood for being consistent with the $t\bar{t}H(H \to b\bar{b})$ signal and the $t\bar{t} + b\bar{b}$ background hypotheses. These likelihoods are obtained based on the integration of the matrix element for each event assuming the signal or background Feynman diagrams at the LO accuracy. The MEM discriminant is used only in the most sensitive single lepton signal region, $\mathrm{SR}_1^{\geq 6\mathrm{j}}$. More details about this method can be found in [128] and the references therein.

The outputs of the above intermediate MVAs are ranked as the most powerful variables in the classification BDT.

5.2.4. Profile likelihood fit

The $t\bar{t}H(H \to b\bar{b})$ analysis relies on a complex fit model namely in terms of describing the $t\bar{t}+\geq 1b$ systematic uncertainties. The correction of the predicted distributions to be statistically compatible with data is performed through a template profile likelihood fit which utilizes nuisance parameters and normalization factors as degrees of freedom to achieve this matching.

The number of data events observed $N_{c,i}^{\mathrm{data}}$ in each bin i of each analysis category c for a given distribution, is compared through the fit procedure to its expected content given by:

$$N_{c,i}^{\mathrm{exp}}(\mu, \boldsymbol{k}, \boldsymbol{\theta}) = \mu \cdot N_{\mathrm{c,i,sig}}^{\mathrm{exp}}(\boldsymbol{\theta}_{\mathrm{sig}}) + \sum_{\mathrm{b} \in \mathrm{b}} k_b \cdot N_{\mathrm{c,i,b}}^{\mathrm{exp}}(\boldsymbol{\theta}_{\mathrm{b}}) \tag{5.1}$$

where $\boldsymbol{\theta}$ corresponds to the set of nuisance parameters affecting the signal ($\boldsymbol{\theta}_{\mathbf{sig}}$) as well as each of the backgrounds ($\boldsymbol{\theta}_{\mathbf{b}}$) samples considered in the analysis, $\mathbf{k}$ refers to the set of normalization factors where k_b acts on the background b normalization and $\mu = \sigma_{t\bar{t}H}/\sigma_{t\bar{t}H}^{\mathrm{SM}}$ is the signal strength. Each of the nuisance parameters modifies the shape and normalization of the templates according to the systematic uncertainty it encodes. The normalization factors and signal strength, however, act only on the normalization of the template distributions.

Data is expected to follow a Poisson probability in each bin. The main likelihood function is constructed as a product of Poisson probability terms over all bins in each considered distribution as follows:

$$L_{\mathrm{main}}(\mu, \boldsymbol{k}, \boldsymbol{\theta}) = \prod_{c \in \mathrm{cats}} \prod_{i \in \mathrm{bins}} \frac{\left(N_{c,i}^{\mathrm{exp}}(\mu, \boldsymbol{k}, \boldsymbol{\theta})\right)^{N_{c,i}^{\mathrm{data}}}}{N_{c,i}^{\mathrm{data}}!} \cdot e^{N_{c,i}^{\mathrm{exp}}(\mu, \boldsymbol{k}, \boldsymbol{\theta})} \tag{5.2}$$

Nuisance parameters are defined by a central value $\theta = 0$ corresponding to the best knowledge of a given parameter for which a systematic uncertainty is considered and a ± 1 shift reflecting the distribution variation resulting from its 1 σ uncertainty. The continuity of the nuisance parameters is implemented through the use of specific extrapolation ($|\theta| > 1$) and interpolation ($|\theta| < 1$) functions for both the normalization and shape components of the relevant systematic uncertainty [139]. The deviation of a nuisance parameter (and normalization factors including the signal strength) from their nominal value is referred to as a pull. Nuisance parameters are implemented in the likelihood function as Gaussian, log-normal or Poisson penalty terms to reflect prior knowledge from theory or auxiliary measurements. In contrast, no priors are considered for the normalization factors which are left to free float and are only constrained by the fit to the data. The best estimate for the parameter set (μ,$\boldsymbol{k}$,$\boldsymbol{\theta}$) is obtained by maximizing the likelihood function or alternatively minimizing the negative log likelihood which is numerically more stable.

As presented in section 5.2.3.1, the $t\bar{t}H(H \to b\bar{b})$ analysis counts 12 and 9 categories in the single lepton and dilepton channels, respectively. The predicted events yield in each of the single lepton channel categories before the fit compared to the number of observed data events is shown in Figure 5.10. The prediction is exceeded by data in several categories which have a large contribution of $t\bar{t}+\geq 1b$ and $t\bar{t}+\geq 1c$ backgrounds however these discrepancies are covered by the systematic uncertainties considered in the analysis (see Section 5.2.5) as well as the free floating $t\bar{t}+\geq 1b$ and $t\bar{t}+\geq 1c$ normalization factors. In each of the analysis signal regions, the classification BDT distribution with an optimized binning, is used as the final discriminant in the profile likelihood fit. In the control regions, the overall event yield is used as input except in those enriched with $t\bar{t}+\geq 1c$ in the single lepton channel where the scalar sum of the p_T of jets, H_T^{had}, distribution is used to further constrain this background.

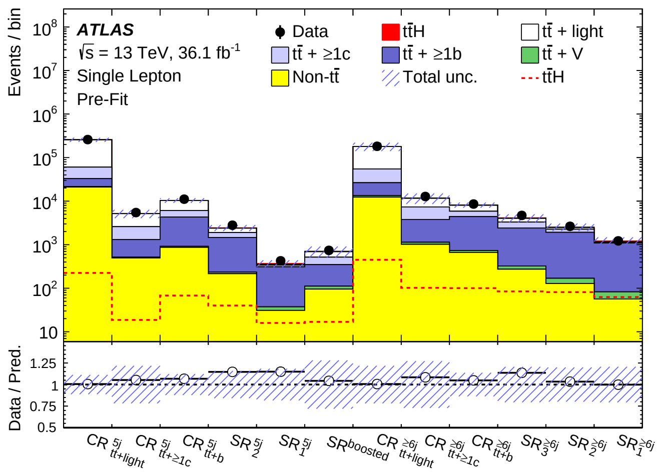

Figure 5.10.: Comparison of the predicted and observed events yield in each of the single lepton channel categories before applying the corrections from the fit to data [128]. The $t\bar{t}H$ signal contribution is shown both as a filled red area stacked on the backgrounds and separately as a dashed red line. The hatched area represents the total uncertainty on the prediction. Uncertainties on the $t\bar{t}+\geq 1b$ and $t\bar{t}+\geq 1c$ backgrounds normalization are not included as these are free floating parameters in the fit.

5.2.5. Systematic uncertainties

An overview of the various nuisance parameters incorporated in the analysis fit model is given in the following.

5.2.5.1. $t\bar{t}$ modeling uncertainties

A complex systematic model is devised for the $t\bar{t}$ + jets background with large theoretical uncertainties which follows from the fact that no stringent constraints from data measurements are available so far for this process, especially for the $t\bar{t}+\geq 1b$ and $t\bar{t}+\geq 1c$ components.

The set of systematic uncertainties affecting the modeling of this background are summarized in Table 5.2. An uncertainty of ±6% is assigned to the inclusive $t\bar{t}$ NLO+NNLL production cross-section [118]. The individual normalizations of both $t\bar{t}+\geq 1b$ and $t\bar{t}+\geq 1c$ components are left to float freely in the fit since they are underestimated in MC simulations.

Systematic source	Description	$t\bar{t}$ categories
$t\bar{t}$ cross-section	Up or down by 6%	All, correlated
$k(t\bar{t}+\geq 1c)$	Free-floating $t\bar{t}+\geq 1c$ normalization	$t\bar{t}+\geq 1c$
$k(t\bar{t}+\geq 1b)$	Free-floating $t\bar{t}+\geq 1b$ normalization	$t\bar{t}+\geq 1b$
SHERPA5F vs. nominal	Related to the choice of NLO event generator	All, uncorrelated
PS & hadronization	POWHEG+HERWIG 7 vs. POWHEG+PYTHIA 8	All, uncorrelated
ISR / FSR	Variations of μ_{R}, μ_{F}, h_{damp} and A14 Var3c parameters	All, uncorrelated
$t\bar{t}+\geq 1c$ ME vs. inclusive	MG5_aMC@NLO+HERWIG++: ME prediction (3F) vs. incl. (5F)	$t\bar{t}+\geq 1c$
$t\bar{t}+\geq 1b$ SHERPA4F vs. nominal	Comparison of $t\bar{t}+b\bar{b}$ NLO (4F) vs. POWHEG+PYTHIA 8 (5F)	$t\bar{t}+\geq 1b$
$t\bar{t}+\geq 1b$ renorm. scale	Up or down by a factor of two	$t\bar{t}+\geq 1b$
$t\bar{t}+\geq 1b$ resumm. scale	Vary μ_{Q} from $H_{\mathrm{T}}/2$ to μ_{CMMPS}	$t\bar{t}+\geq 1b$
$t\bar{t}+\geq 1b$ global scales	Set μ_{Q}, μ_{R}, and μ_{F} to μ_{CMMPS}	$t\bar{t}+\geq 1b$
$t\bar{t}+\geq 1b$ shower recoil scheme	Alternative model scheme	$t\bar{t}+\geq 1b$
$t\bar{t}+\geq 1b$ PDF (MSTW)	MSTW vs. CT10	$t\bar{t}+\geq 1b$
$t\bar{t}+\geq 1b$ PDF (NNPDF)	NNPDF vs. CT10	$t\bar{t}+\geq 1b$
$t\bar{t}+\geq 1b$ UE	Alternative set of tuned parameters for the underlying event	$t\bar{t}+\geq 1b$
$t\bar{t}+\geq 1b$ MPI	Up or down by 50%	$t\bar{t}+\geq 1b$
$t\bar{t}+\geq 3b$ normalization	Up or down by 50%	$t\bar{t}+\geq 1b$

Table 5.2.: Summary of the sources of systematic uncertainty considered for the $t\bar{t}$ + jets modeling [128].

Systematic uncertainties in the shapes are derived based on comparisons between the nominal PWG+PYT8 sample and various alternative $t\bar{t}$ samples. The latter are reweighted such that they have the same $t\bar{t}+\geq 1b$ and $t\bar{t}+\geq 1c$ fractions as the nominal sample in order to avoid double counting the uncertainties on the normalization of the $t\bar{t}$ + HF components which are free floating in the fit. Moreover, the relative fractions of the $t\bar{t}+\geq 1b$ subcomponents, except for the $t\bar{t}+b$ (MPI/FSR) subcategory, are scaled in the alternative samples similarly to the nominal prediction, in order to match the SHERPA4F predictions which are subjected to separate uncertainties as discussed later.

The uncertainty associated with the choice of the $t\bar{t}$ NLO event generator is defined as the relative difference between the PWG+PYT8 sample and the SHERPA prediction. The latter refers to a $t\bar{t}$ inclusive sample generated using Sherpa 2.2.1 with the five flavor NNPDF3.0NNLO PDF set. This sample should not be confused with the NLO $t\bar{t}b\bar{b}$ SHERPA4F sample described in section 5.2.2.2. Since the SHERPA sample is generated with a dedicated parton shower and hadronization model different from what is used for the nominal sample, the NLO generator uncertainty partially accounts for the uncertainty associated with the choice of the parton shower. The uncertainty on the parton shower is also taken into account through an independently assigned systematic uncertainty defined as the relative difference between the nominal prediction and the PWG+HW7 sample. This sample is produced with the same setup as that described in Section 4.1.2. The uncertainty in the modeling of the initial and final state radiation (ISR/FSR) is estimated based on two alternative PWG+PYT8 samples [140]. One sample corresponds to the up variation, produced with the nominal setup but with the renormalization and factorization scales decreased by a factor of two, the *hdamp* parameter doubled and uses the Var3cUp variation of the A14 parameters set. A second sample corresponding to the down variation is generated with the nominal setting except that the Var3cDown variation of the A14 tune is used along with doubled scales. Each of the above shape uncertainties are applied uncorrelated among $t\bar{t}+\geq 1b$, $t\bar{t}+\geq 1c$ and $t\bar{t}$ + light components.

As mentioned earlier, there are two classes of available descriptions for the modeling of the $t\bar{t}+\geq 1b$ process: the inclusive predictions with $t\bar{t}$ described at NLO in the ME with the 5FS PDF set (e.g the nominal PWG+PYT8 sample) and the dedicated predictions where $t\bar{t}b\bar{b}$ is described at NLO in the ME with the 4FS PDF set (e.g the SHERPA4F sample). In this regard, I have probed closely the modeling differences between these two sets of predictions in several kinematic distributions characterizing the $t\bar{t}+\geq 1b$ process. For instance, the modeling of the $\frac{p_T(\text{b-hadron})}{p_T(b-jet)}$ ratio obtained by these predictions for additional single b-jets was checked as shown in Figure 5.11(a). This distribution inherently describes the fragmentation of b-quarks into b-hadrons. A key feature is noticed at low p_T ratio values (~ 0.1):

an excess of jets with high p_T matched to low p_T b-hadrons from which they likely do not originate, is observed in the 5FS samples but not in the 4FS one. The effect from such jets is found to be negligible in the analysis given their low b-tagging efficiency as illustrated in Figures 5.11(b) and 5.11(c) in the case of the nominal $t\bar{t}$ sample; the excess in these jets is mitigated when selecting events with a high number of b-tagged jets or when requiring the additional b-jets to be b-tagged. Moreover, the modeling of properties related to the $t\bar{t}+B$ subcategory such as the ΔR separation between the leading and subleading b-hadrons inside B-jets, shown in Figure 5.12(a) was also checked. In the 4FS sample, b-hadrons tend to be closer than in the 5FS samples. This trait remains when further requiring the B-jets to be b-tagged as depicted in Figure 5.12(b). To account for such modeling differences, an additional source of shape uncertainty is considered where the nominal PWG+PYT8 prediction is compared to the SHERPA4F one. This uncertainty is not applied for the $t\bar{t}+b$ (MPI/FSR) subcategory as it is absent in the 4FS calculation.

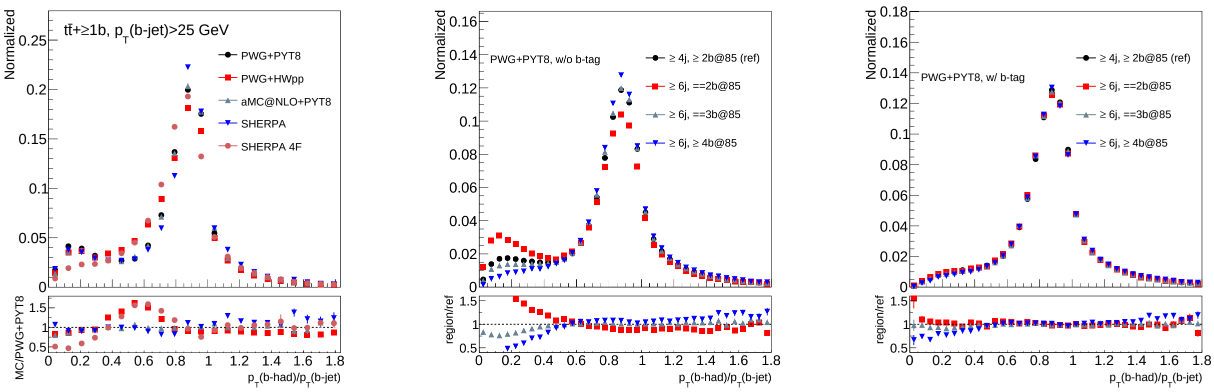

(a) (b) (c)

Figure 5.11.: p_T ratio of the b-hadrons to that of the corresponding single additional b-jets for (a) various 5FS inclusive $t\bar{t}$ samples compared to a dedicated $t\bar{t}b\bar{b}$ 4FS calculation, (b) in the nominal PWG+PYT8 sample for different event selection criteria and (c) in the latter sample when further requiring the single additional b-jets to be b-tagged.

The uncertainties in the $t\bar{t}+b$, $t\bar{t}+b\bar{b}$, $t\bar{t}+B$ and $t\bar{t}+\geq 3b$ fractions are derived separately based on the alternative Sherpa+OpenLoops samples as listed in Table 5.2. For each variation, the differences in the fractions compared to the nominal SHERPA4F predictions define the corresponding systematic uncertainty which is correlated across $t\bar{t}+\geq 1b$ subcategories. Furthermore, a 50% normalization uncertainty is applied to the $t\bar{t}+\geq 3b$ category to cover the large difference between the 4FS prediction and the various 5FS predictions for this process. The relative fraction of the $t\bar{t}+b$ (MPI/FSR) component is not fixed in the alternative $t\bar{t}$ samples used to derive the systematic uncertainties associated with the choice of the NLO generator, parton shower and hadronization model and with radiation. Hence, variations in the normalization and shape of the $t\bar{t}+b$ (MPI/FSR) subcategory are already accounted for by these sources of uncertainties. On top of these, an extra 50% normalization uncertainty is assigned to this component based on studies of different event sets of tuned parameters.

For the $t\bar{t}+\geq 1c$ background, there is also little guidance from theory or experimental measurements to conclude on whether the nominal prediction in which the c-jets primarily originate from the parton shower is more or less accurate compared to a prediction with $t\bar{t}+c\bar{c}$ computed at NLO in the matrix element. Therefore, an NLO prediction with $t\bar{t}+c\bar{c}$ in the matrix element using the 3F scheme for the PDF set is produced with Madgraph5_aMC@NLO interfaced to Herwig++. The difference between

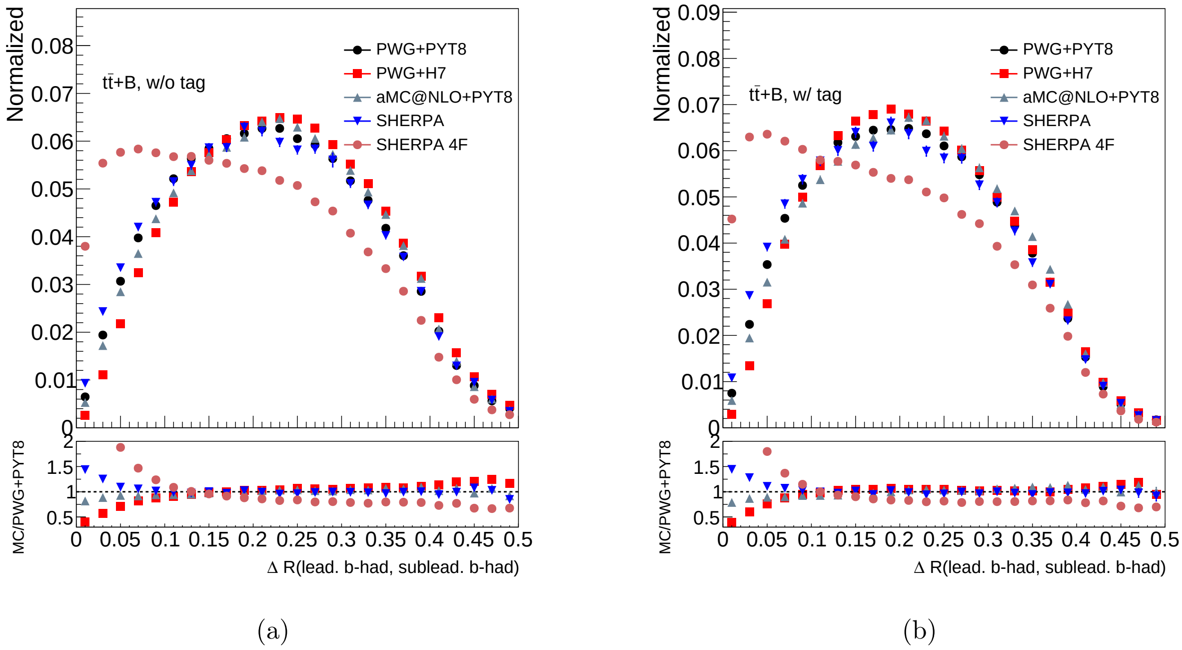

Figure 5.12.: ΔR separation between the leading and subleading b-hadrons inside double additional B-jets (a) when the B-jets are not required to be matched to reconstructed jets and (b) when they are required to be matched to reconstructed jets which are b-tagged at the 85% working point.

this sample and an inclusive $t\bar{t}$ sample produced with the same generator setup but using a 5FS PDF set such that the $t\bar{t}+\geq 1c$ process originates only from parton shower, is taken as an additional systematic on the $t\bar{t}+\geq 1c$ background prediction.

5.2.5.2. Non-$t\bar{t}$ modeling uncertainties

The modeling systematic uncertainties considered in the $t\bar{t}H(H \to b\bar{b})$ analysis for the signal as well as all backgrounds except for $t\bar{t}$ + jets are summarized in table 5.3. Most of these uncertainties are small and affect marginally the sensitivity to the signal apart from the signal uncertainties and in particular the parton shower systematic which contributes the most to it. Nevertheless, the impact of the latter is sub-dominant compared to the $t\bar{t}$ + jets systematics. More details about these uncertainties can be found in ref [128].

Additionally, the statistical uncertainty of the prediction which incorporates the statistical uncertainty of the MC events and that of data-driven fake and non prompt lepton estimate is included in the likelihood in the form of additional nuisance parameters referred to as γ's. These are treated as uncorrelated across all the analysis bins.

5.2.5.3. Experimental uncertainties

An uncertainty of 2.1% is applied to the normalization of all MC samples considered in the analysis. It accounts for the uncertainty on the measurement of the combined 2015+2016 integrated luminosity which is derived based on a method similar to that described in [141].

A total of twenty independent systematic uncertainties are attributed to the jet energy scale (JES) incorporating uncertainties from jet calibration techniques, jet flavor, pile-up mismodeling corrections,

Process	Type	Systematic uncertainties
$t\bar{t}H$	N	QCD scale and PDF cross-section uncertainties
	N	Branching fractions: uncorrelated across Higgs boson decay modes
	SN	Parton shower choice: nominal vs Madgraph5_aMC@NLO + Herwig++
W+jets	N	40% cross-section uncertainty
	N	30% W+2-heavy-flavored-jets normalization uncertainty
	N	30% W+ ≥3-heavy-flavored-jets normalization uncertainty
Z+jets	N	35% normalization uncertainty uncorrelated across jet bins.
Single top: W-channel	N	$^{+5\%}_{-4\%}$ cross-section uncertainty
	SN	Parton shower choice and radiation: similar to $t\bar{t}$ + jets
	SN	Uncertainty on the interference between Wt and $t\bar{t}$ at NLO: nominal "diagram removal" scheme vs "diagram subtraction" scheme
Single top: t-channel	N	$^{+5\%}_{-4\%}$ cross-section uncertainty
	SN	Parton shower choice and radiation: similar to $t\bar{t}$ + jets
Single top s-channel	N	$^{+5\%}_{-4\%}$ cross-section uncertainty
Di-boson	N	50% cross-section uncertainty
$t\bar{t}W/t\bar{t}Z$	N	15% cross-section uncertainty including PDF and QCD scale uncertainties
	SN	NLO generator and parton shower choice: nominal vs Sherpa
4-tops	N	50% cross-section uncertainty
tZ, $t\bar{t}WW$, tHjb and WtH	N	PDF and QCD scale uncertainties
tWZ	N	50% cross-section uncertainty
Fake and non prompt lepton	N	For single lepton channel: 50% normalization uncertainty → uncorrelated across e and μ channels → uncorrelated across jet bins and for boosted category Dilepton channel: 25% normalization uncertainty correlated across lepton flavors and all analysis categories

Table 5.3.: Systematic uncertainties on the signal and on the non-$t\bar{t}$ backgrounds. The second column specifies the type of the uncertainty such that N stands for normalization only, S for shape only and SN for both.

η interpolation and high jet p_T extrapolation [93]. Additional uncertainties accounting for the jet energy resolution (JER) and the efficiency to pass the JVT selection are considered. Even though these uncertainties are relatively small for individual jets, their effect is amplified by the large number of jets in the final state.

The efficiency to correctly tag a b-jet and the mis-tag rates for c-jets and light-jets obtained from simulation are corrected via scale factors to match those measured in data [104, 142]. The b-jet, c-jet and light-jet scale factors are first derived as a function of the jet kinematics for each of the four working points used in the analysis and later combined into a calibration of the b-tagging discriminant distribution, with the corresponding uncertainties taking into account the correlations across multiple working points. The uncertainties associated with the b-tagging efficiency are factorized into 30 independent sources while those corresponding to the mis-tag rates for c-jets (light-jets) are factorized into 15 (80) sources.

Lepton uncertainties originating from the corresponding trigger, reconstruction, identification and isolation efficiencies as well as energy and momentum scales are considered. These uncertainties have a very small effect in the analysis.

Uncertainties in lepton and jet energy scales or resolutions are propagated to the missing transverse momentum (E_T^{miss}). Additional uncertainties related to the resolution and scale of the E_T^{miss} soft term are considered. These uncertainties have a negligible impact on the analysis.

5.2.6. Fit results

Figure 5.13 shows the observed event yields in the different categories of the single lepton channel, compared to the corrected prediction based on the profile likelihood fit to data (postfit). The fit is performed combining simultaneously all signal and control regions in the single lepton and dilepton channels. Figures 5.14 and 5.15 show the H_T^{had} distribution in the $\geq$ 6j $t\bar{t}+\geq 1c$ enriched control region and the classification BDT distribution in the most sensitive signal region of the single lepton channel, respectively, both before and after the fit to data. All these distributions are reasonably well modeled prefit within the estimated uncertainties. The level of agreement is improved postfit as a result of the nuisance parameters being pulled with respect to their nominal values, by the fit. The best-fit values of $k(t\bar{t}+\geq 1b)$ and $k(t\bar{t}+\geq 1c)$ are 1.24 ± 0.10 and 1.63 ± 0.23, respectively. The uncertainty is reduced post-fit due to the fit introducing constraints and correlations.

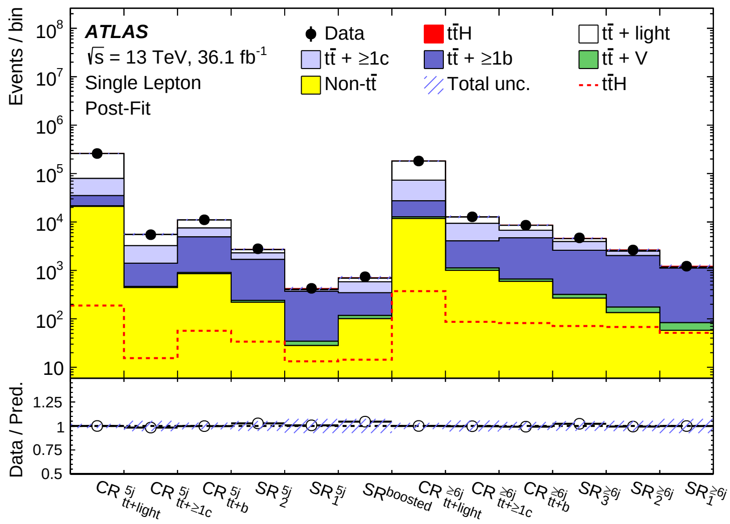

Figure 5.13.: Comparison of the predicted and observed event yields in each of the single lepton categories after applying the corrections obtained from the fit to data [128]. The $t\bar{t}H$ signal contribution is shown both as a filled red area stacked on the backgrounds and separately as a dashed red line, normalized to the corrected signal prediction.

The best-fit value for the signal strength is:

$$\mu = 0.84 \pm 0.29(\text{stat})^{+0.57}_{-0.54}(\text{syst}) = 0.84^{+0.64}_{-0.61}$$

This measurement is consistent with the expectation from the SM. A value higher than 2 is excluded at the 95% confidence level. An excess of events over the expected SM background is found with an

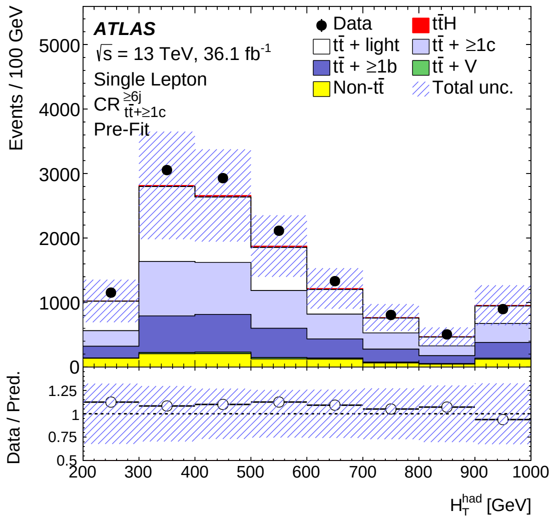

Figure 5.14.: Comparison between data and prediction for the H_T^{had} distribution in the $\geq 6j$ $t\bar{t}+\geq 1c$ enriched control region of the single lepton channel before (left) and after (right) the fit to the data [128]. The $t\bar{t}H$ signal contribution, albeit small in this regions, is shown stacked at the top of the background prediction, normalized to the SM cross-section before the fit and to the fitted μ after the fit. The prefit plots do not include an uncertainty for the $t\bar{t}+\geq 1b$ or $t\bar{t}+\geq 1c$ normalization.

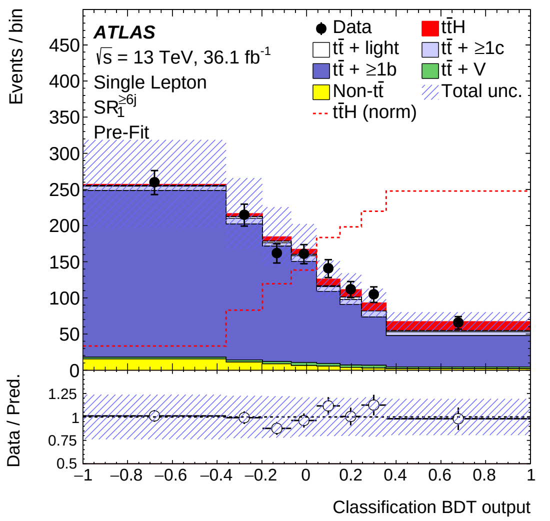

Figure 5.15.: Comparison between data and prediction for the classification BDT distribution in the most sensitive signal region ($\text{SR}_1^{\geq 6\text{j}}$) of the single lepton channel before (left) and after (right) the fit to the data [128]. The $t\bar{t}H$ signal yield (solid red) is normalized to the SM prediction before the fit and to the fitted μ after the fit. The dashed line shows the $t\bar{t}H$ signal distribution normalized to the total background prediction. The prefit plots do not include an uncertainty for the $t\bar{t}+\geq 1b$ or $t\bar{t}+\geq 1c$ normalization.

observed (expected) significance of 1.4 (1.6) σ. Alternatively, a combined fit where the single lepton and dilepton channels are assigned independent signal strengths is also performed. The corresponding results are summarized in Figure 5.16, compared to the combined μ case. The probability of the difference between the two independent signal strength parameters being equal or greater than the one obtained is 19% which points to the good compatibility between the signal strengths in the two channels.

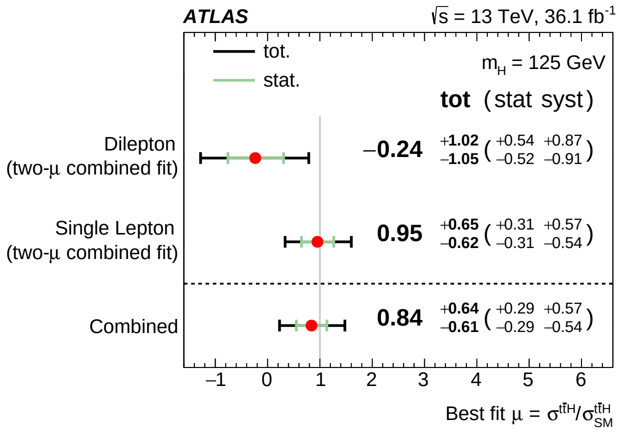

Figure 5.16.: Summary of the signal-strength measurements in the individual channels and for the combination [128].

The total uncertainty on the measurement of the signal strength is dominated by the systematic component. The 20 leading nuisance parameters for which the associated systematic uncertainties exhibit the largest contribution to the total uncertainty on the signal strength measurement are shown in Figure 5.17. For each of these, the best-fit value as well as the best-fit uncertainty are shown. The NLO event generator systematic affecting the $t\bar{t}+\geq 1b$ background has the largest impact on the signal strength. This large effect is due in great part to the limited size of the SHERPA MC sample used to derive this systematic as discussed in Section 5.2.7. The leading systematic is followed by three uncertainties related also to the modeling of the $t\bar{t}+\geq 1b$ background component. The theoretical predictions of this process suffer from large uncertainties as manifested in the size of the differences among the alternative MC samples used to model it. This in turn results in the large systematic uncertainties defined for this process which is a limiting factor to the sensitivity of the analysis.

Table 5.4 reports the contributions to the uncertainty on μ arising from the different categories of uncertainty sources. The theoretical uncertainties on the $t\bar{t}+\geq 1b$ modeling and the limited amount of events in the backgrounds MC samples, especially in the dominating $t\bar{t}$ + jets background (see Section 5.2.7), are the two leading sources of systematic uncertainties in the $t\bar{t}H(H \rightarrow b\bar{b})$ channel.

Thorough checks were made to ensure the robustness of the fit. The origin of the shifts in the nuisance parameters compared to their nominal values was traced back to correct mainly the prediction of the $t\bar{t}$ background to the observed data in multiple regions. The capability of the fit to constrain the systematic uncertainties which result in large deviations from data was validated on the Asimov data set [143] generated from the nominal prediction and on another pseudo-data sample where the nominal $t\bar{t}$ prediction is replaced by an alternative sample Powheg+Pythia6 [120], not used in the systematics definition.

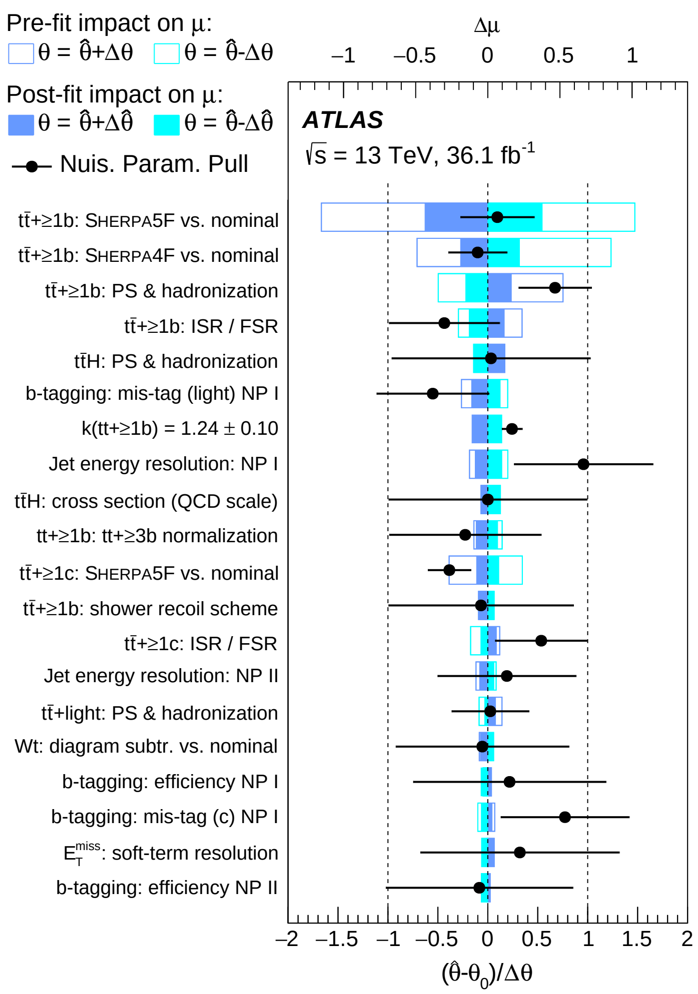

Figure 5.17.: Ranking of the nuisance parameters considered in the fit based on their impact on the measured signal strength; only the 20 leading parameters are shown [128]. The prefit (postfit) impact on μ is indicated by the empty (filled) blue rectangles which refer to the upper scale. The impact of each nuisance parameter, $\Delta\mu$, is obtained by comparing the nominal best-fit value of μ with the result of the fit when fixing the considered nuisance parameter to its best-fit value, $\hat{\theta}$, shifted by its prefit (post-fit) uncertainties $\pm\Delta\theta$ ($\pm\Delta\hat{\theta}$). The black points show the pulls of the nuisance parameters with respect to their nominal values, θ_0. These pulls and their relative postfit errors, $\Delta\hat{\theta}/\Delta\theta$, refer to the bottom scale.

Uncertainty source	$\Delta\mu$	
$t\bar{t}+\geq 1b$ modeling	$+0.46$	-0.46
Background-model stat. unc.	$+0.29$	-0.31
b-tagging efficiency and mis-tag rates	$+0.16$	-0.16
Jet energy scale and resolution	$+0.14$	-0.14
$t\bar{t}H$ modeling	$+0.22$	-0.05
$t\bar{t}+\geq 1c$ modeling	$+0.09$	-0.11
JVT, pileup modeling	$+0.03$	-0.05
Other background modeling	$+0.08$	-0.08
$t\bar{t}+$ light modeling	$+0.06$	-0.03
Luminosity	$+0.03$	-0.02
Light lepton (e,μ) id., isolation, trigger	$+0.03$	-0.04
Total systematic uncertainty	$+0.57$	-0.54
$t\bar{t}+\geq 1b$ normalization	$+0.09$	-0.10
$t\bar{t}+\geq 1c$ normalization	$+0.02$	-0.03
Intrinsic statistical uncertainty	$+0.21$	-0.20
Total statistical uncertainty	$+0.29$	-0.29
Total uncertainty	$+0.64$	-0.61

Table 5.4.: Summary of the effects of the nuisance parameters on the $t\bar{t}H(H\to b\bar{b})$ signal strength, grouped in categories corresponding to different sources [128].

5.2.7. Impact of the finite size of $t\bar{t}$ + heavy-flavor-jets MC samples on the analysis sensitivity

The finite number of simulated events in the MC samples used in the $t\bar{t}H(H \to b\bar{b})$ analysis limits the achievable sensitivity through two distinct effects. The first one is induced by the limited number of generated events in the nominal MC samples used to build the prediction. This effect is taken into account in the analysis using the γ nuisance parameters which encode the statistical uncertainty of the prediction as explained in Section 5.2.5.2. Table 5.4 shows that the statistical uncertainty associated with the background MC samples is the second leading source of systematic uncertainty in the analysis. On the other hand, the second effect arises from the statistical component of systematic uncertainties namely those defined using alternative MC samples which suffer from large statistical uncertainties. Contrary to the former effect, the impact of the finite size of the alternative MC samples is not accounted for in the likelihood fit. Hence, toys are used to assess the impact of this effect on the analysis sensitivity. Close investigations of the effects listed above are discussed in the following.

Detailed studies were carried out in the single lepton channel to quantify the impact of the limited amount of MC events in each of the nominal background samples independently. The statistical uncertainty on the $t\bar{t}$ + HF ($t\bar{t}$+$\geq$1b and $t\bar{t}$+$\geq$1c) templates obtained from the PWG+PYT8 sample has by far the largest impact on the analysis sensitivity compared to that from the rest of the backgrounds. In particular, the impact is more pronounced in the signal enriched regions namely the $\mathrm{SR}_1^{\geq 6j}$and $\mathrm{SR}_2^{\geq 6j}$(see Section 5.2.3.1). Figure 5.18 displays the classification BDT distribution for the different $t\bar{t}$ + jets components in the $\mathrm{SR}_1^{\geq 6j}$region as well as the per-bin statistical uncertainties in these distributions compared with the signal template in the same region: the statistical uncertainties on the $t\bar{t}$ + HF components are relatively large across the BDT bins including those most sensitive to the signal.

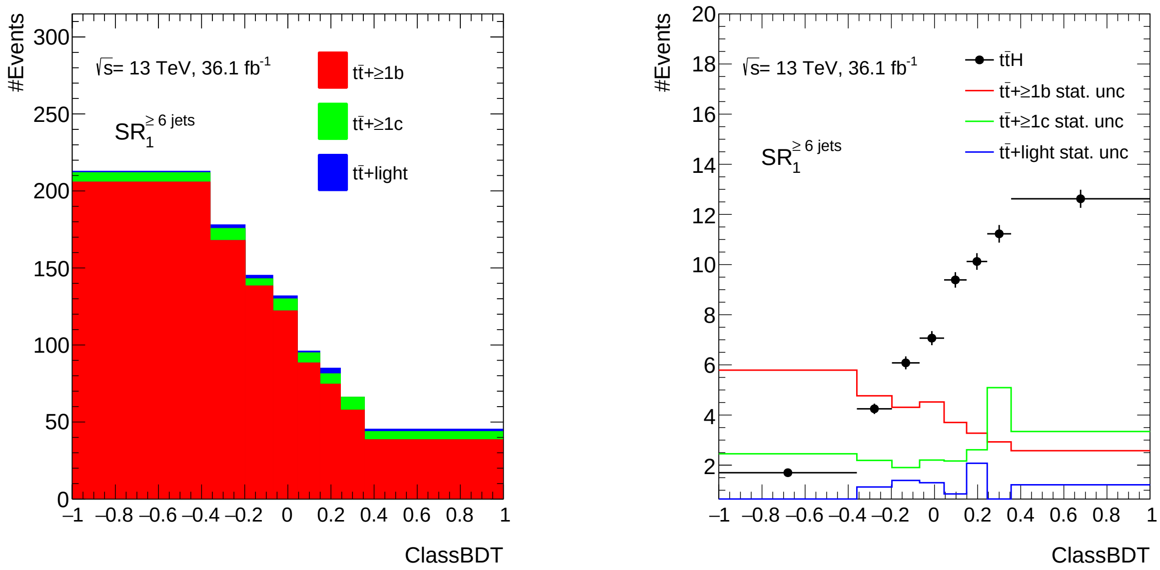

(a) (b)

Figure 5.18.: The distribution of (a) the classification BDT for the three $t\bar{t}$ + jets components in the $\mathrm{SR}_1^{\geq 6j}$region and (b) the corresponding per-bin statistical uncertainties (solide lines) compared to the $t\bar{t}H$ signal yields (black dots).

Furthermore, the impact on the analysis sensitivity resulting from the finite number of $t\bar{t}$ + HF MC events in the alternative $t\bar{t}$ samples was thoroughly checked in the particular case of the $t\bar{t}$+$\geq$1b generator uncertainty in the single lepton channel [120]. This systematic, found to have the largest impact on the analysis sensitivity (see Section 5.2.6), is defined using the SHERPA sample. In particular, 500 toys with each corresponding to a fluctuation of the Sherpa distribution within its statistical uncertainty were used to assess the impact of the statistical component of the $t\bar{t}+\geq 1b$ generator uncertainty. The distribution of the uncertainty on the signal strength obtained from the 500 fits to Asimov dataset such that each fit is performed after re-evaluating the $t\bar{t}+\geq 1b$ generator systematic, is shown in Figure 5.19(a). The baseline value of the uncertainty on μ was found to be 1 σ higher than the mean value obtained from the $t\bar{t}+\geq 1b$ NLO generator toys. The 1 σ variation of the uncertainty on the error on μ resulting from the limited size of the SHERPA MC sample was found to be 0.04 which amounts to 6% of the total error on μ and 10% of the contribution to the error on μ of the $t\bar{t}+\geq 1b$ generator systematic alone. Furthermore, a large spread of $\Delta\mu = 0.21$, at one standard variation, is observed in the distribution of the measured signal strength obtained from the 500 toy fits to data shown in Figure 5.19(b). This represents around half of the uncertainty on μ which comes from the impact of the $t\bar{t}+\geq 1b$ generator nuisance parameter and 30% of the total uncertainty on μ.

The significant impact on the analysis sensitivity stemming from the large statistical uncertainties on the $t\bar{t}$ + HF components in both the nominal and SHERPA predictions are present despite the devoted efforts to produce larger $t\bar{t}+\geq 1b$ samples using dedicated b-filters. This is why, new heavy flavor filters need to be developed to increase the number of simulated $t\bar{t}$ + HF MC events in the nominal and alternative $t\bar{t}$ samples in view of reducing the impact of their statistical uncertainties in the next round of the analysis (see Section 5.3.2).

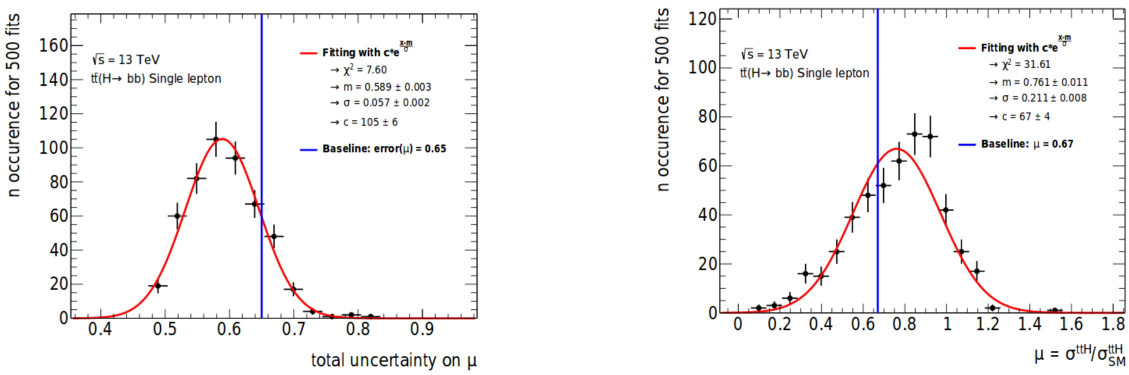

(a)

(b)

Figure 5.19.: Distribution of (a) the signal strength uncertainty from the fits to Asimov dataset and (b) the measured signal strength from the fits to data in the single lepton channel, with 500 toys of the $t\bar{t}+\geq 1b$ NLO generator systematic [120]. The distributions are fitted with a Gaussian function to derive the mean of the distributions and their 1 σ variation from the statistical uncertainty on the Sherpa sample.

5.2.8. $t\bar{t}H$ observation

The $t\bar{t}H(H \to b\bar{b})$ search results, obtained using 36.1 fb^{-1}of pp collision data, were combined with those obtained in the following $t\bar{t}H$ channels in which other Higgs boson decay modes are probed [144]: **$t\bar{t}H$ multilepton (ML)** [145] where final states with three or more leptons or two light leptons with the same sign of charge are targeted, $\boldsymbol{H \to \gamma\gamma}$ [146] and $\boldsymbol{H \to ZZ^{(*)} \to 4\ell}$ [147].

The last two searches were performed using pp collision data collected by the ATLAS detector from 2015 to 2017 which amounts to a total integrated luminosity of 79.8 fb^{-1}while the $t\bar{t}H$ ML search makes use of the same dataset as $t\bar{t}H(H \to b\bar{b})$. In these channels, the $t\bar{t}H$ production was modeled using the same MC generator setup where a Higgs boson mass corresponding to the measured value of 125.09 ± 0.24 GeV is assumed.

The best fit value for the $t\bar{t}H$ signal strength extracted from the combined likelihood fit of the four searches as well as those obtained in the individual channels are shown in Figure 5.20. The production cross-section of this process at 13 TeV is measured in the datasets listed above to be:

$$\sigma_{t\bar{t}H} = 670 \pm 90 \text{ (stat) } {}^{+110}_{-100} \text{ (syst) fb}$$

The corresponding observed significance relative to the background only hypothesis is 5.8 σ while the expected significance is 4.9 σ. A combination with the 7 and 8 TeV datasets corresponding to integrated luminosities of 4.5 fb^{-1}and 20.3 fb^{-1}respectively, was also performed yielding an observed (expected) significance of 6.3 (5.1) σ with respect to the background only hypothesis. These results represent a direct observation of the $t\bar{t}H$ production mode.

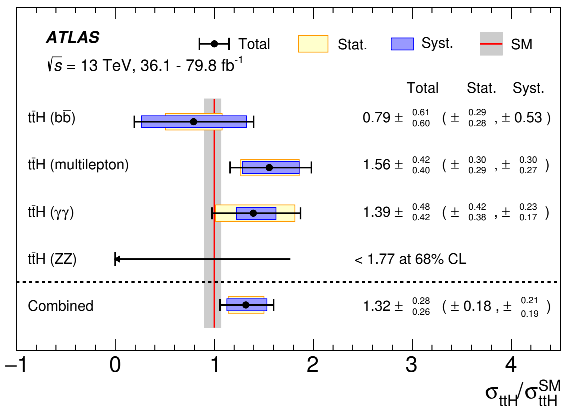

Figure 5.20.: Best-fit $t\bar{t}H$ signal strength values obtained in the individual analyses (see text) and their combination [144].

5.3. Towards a $t\bar{t}H(H \to b\bar{b})$ analysis with the full Run 2 data

The new round of the $t\bar{t}H(H \to b\bar{b})$ analysis aims to exploit the full Run 2 dataset (139 fb^{-1}) to enhance the sensitivity to the $t\bar{t}H(H \to b\bar{b})$ signal with respect to that achieved in the previous round of the analysis. While benefiting from a larger dataset would certainly improve the statistical precision, it is not enough to improve the overall sensitivity since the analysis is dominated by systematic uncertainties as discussed in Section 5.2.6. In particular, the two leading factors found to limit the sensitivity of the analysis are:

- The large theoretical uncertainties on the $t\bar{t}+\geq1b$ modeling.
- The background model statistical uncertainty where the dominant contribution results from the limited amount of simulated $t\bar{t}$ + HF MC events.

Tackling the above limiting factors is the main focus of the new round of the analysis as reflected in the adopted strategy presented in Section 5.3.1. In this context, I worked on mitigating the effect of the large statistical fluctuations associated with the size of the $t\bar{t}$ + HF MC samples by designing new heavy flavor filters as explained in Section 5.3.2. Moreover, I explored an alternative model to estimate the $t\bar{t}$ background based on a data-driven method as described in Section 5.3.3.

With the full Run 2 dataset becoming available, it is feasible at this stage to go beyond the measurements of the inclusive production and decay rates of the Higgs boson and start exploring its differential properties. These are sensitive to subtle effects in the SM and to new physics phenomena. In this respect, the $t\bar{t}H(H \to b\bar{b})$ channel is expected to play a key role as it benefits from a large production rate compared to the other $t\bar{t}H$ channels. To this end, I developed the analysis for the measurement of the Higgs boson p_T in the $t\bar{t}H(H \to b\bar{b})$ channel and assessed the expected sensitivity for this measurement, as presented in Section 5.3.4.

5.3.1. Overview of the full Run 2 $t\bar{t}H(H \to b\bar{b})$ analysis strategy

Since the last round of the $t\bar{t}H(H \to b\bar{b})$ analysis, presented in details in section 5.2, several studies and developments have been ongoing to improve the sensitivity of the search. These developments are incorporated in the ongoing round of the analysis which includes the pp collision data recorded by the ATLAS detector during 2017 and 2018 in addition to the 36.1 fb^{-1}of data analyzed in the previous round. This amounts to a total integrated luminosity of 139 fb^{-1}for the full Run 2 data. In the following, I will highlight what is changed and updated in the analysis with respect to what was described in Sections 5.2.2, 5.2.3.1 and 5.2.5.1.

The generators setups used to model the nominal and alternative $t\bar{t}$ + jets samples are the same as in the previous round of the analysis except that updated versions of the parton showers are used. In the case of the PWG+PYT8 sample, for instance, the newer version of Pythia 8 features the additional option that allows to include internal shower weights which can be used to estimate the ISR/FSR radiation systematics instead of producing separate samples. The $t\bar{t}$ + jets samples, except for SHERPA , have been generated using new optimized filters to mitigate the impact of the statistical fluctuations associated with the $t\bar{t}$ + HF components. The ATLAS fast simulation (ATLFAST-II) was employed to produce these samples as a result of requiring multiple filtered samples and increasing the total number of events generated compared to the last iteration of the analysis. Regarding the systematic model, the alternative $t\bar{t}$ sample used to estimate the uncertainty on the choice of the NLO matching scheme is changed from SHERPA to aMC@NLO+PYT8 for a better definition of this systematic since using the former was partially accounting for the uncertainty on the choice of the parton shower too.

The $t\bar{t}H$ signal sample is generated with the same setup as the nominal $t\bar{t}$ + jets sample. This differs from the one used in the previous round where the Madgraph5_aMC@NLO package was used for the ME computation. The uncertainty on the modeling of the signal is parameterized in a similar fashion to that affecting the $t\bar{t}$ + jets background in terms of the choice of the NLO matching scheme, the ISR/FSR radiation and the parton shower choice. The former two were not included in the previous round.

The approach adopted for categorizing events in the ongoing analysis round is fairly simplified in comparison to the last round where the b-tagging information was heavily used. Single lepton events are first split into two categories based on the jets multiplicity similarly to the previous round: one with exactly 5 jets and another with at least 6 jets. Each of these categories is then further divided into three regions depending on the number of b-tagged jets as follows: one category with exactly 3 jets tagged at the 70% working point (3b@70), one with at least 4 jets tagged at the 70% working point such that only three of them at most also pass the 60% working point (4b@70(not@60)) and a last category with at least 4 jets tagged at the 60% working point (4b@60). Regions with at least 4 jets tagged at the 70% WP are relatively rich in the $t\bar{t}H$ signal and dominated by the $t\bar{t}+\geq1b$ component and to a lesser extent by the $t\bar{t}+\geq1c$ background. These categories are referred to as "signal regions". The remaining ones are enhanced in $t\bar{t}$ + light and are labeled "control regions". The boosted category used in the last round of the analysis is dropped in the studies presented in the remainder of this chapter. Figure 5.21 shows the fraction of the different background components as well as the $t\bar{t}H$ signal purity in each of the 6 categories of the single lepton channel. The $t\bar{t}$ + light background contribution to both control and signal regions is significantly reduced compared to that obtained with the complex categorization of the previous round. This is achieved by exploiting only the tightest working points of 70% and 60% for the regions definition. This choice was intended to partially mitigate the relatively large pulls and constraints introduced by the likelihood fit to correct for the mismodeling of the $t\bar{t}$ + light background in the control regions. The signal purity achieved with the new categorization is slightly better with respect to the last round: the S/B and $S/\sqrt{B}$[b] in the most sensitive region ($\geq$ 6 jets and $\geq$ 4 b@60) are 7.1% and $\sim$ 2 respectively, compared to 5.4% and 1.8 in the $SR_1^{\geq 6j}$region of the last round. The new event categorization simplifies the analysis and facilitates the incorporation of an alternative data-driven model for the $t\bar{t}$ background estimation which will be otherwise complex with the last round categorization.

Taking the above updates into account, the $t\bar{t}H(H \to b\bar{b})$ cross-section can be measured with a precision of $\sim$ 30% using the full Run 2 data, which is two times better than that achieved in the previous round.

[b]Scaled to an integrated luminosity of 36.1 fb^{-1}

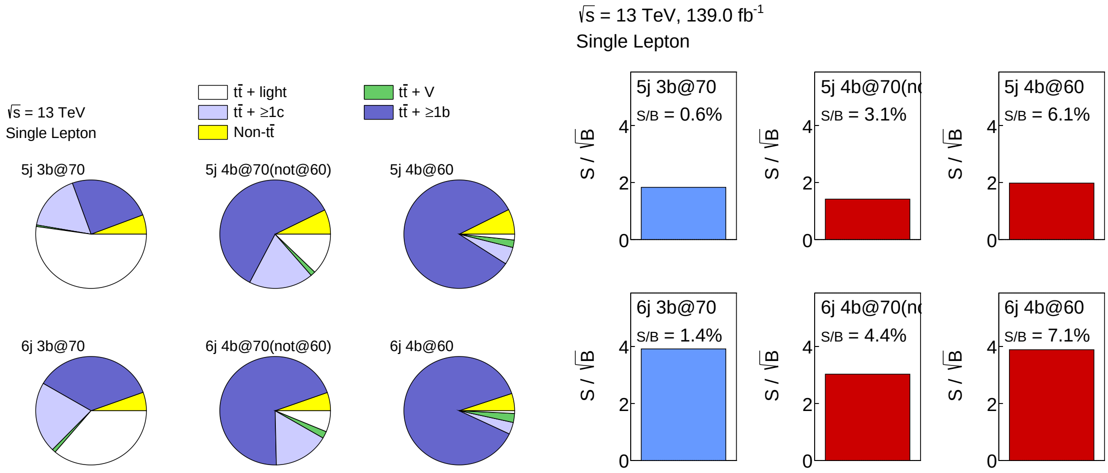

Figure 5.21.: The fraction of the different background components relative to the total background (left) and the S/B as well as $S/\sqrt{B}$ ratios in each of the 6 categories of the $t\bar{t}H(H \to b\bar{b})$ single lepton channel (right).

5.3.2. $t\bar{t}$ + heavy flavors filters optimization

As part of the MC event generation procedure (see Section 2.3.1), it is possible to use an event filter to select only a subset of the full MC sample output which features a given signature embedded in the filter selection criteria. This functionality is deployed prior to the event simulation step such that the available events quota per sample is only filled with simulated events falling in the targeted phase space where usually analyses suffer from large statistical uncertainties. Attempting to produce the same amount of events in this phase space without the use of filters would consume a lot of CPU power and is practically unfeasible. Filtered samples are combined properly with the inclusive samples (produced without the use of filters) to cover the full phase space for the process of interest with the advantage of reduced statistical uncertainties on the filtered component. In the previous round of the $t\bar{t}H(H \to b\bar{b})$ analysis, so called *b-filter* was used to increase the number of $t\bar{t}$ + HF events generated as explained in the following.

5.3.2.1. Filters optimization studies

A b-filter with loose cuts on the b-hadrons kinematics was used in the last round of the analysis to enlarge the size of the $t\bar{t}+\geq 1b$ component in the nominal and alternative $t\bar{t}$ + jets samples. More b-filtered events were generated for the nominal sample compared to the alternative $t\bar{t}$ samples. This filter required at least one additional b-hadron (not originating from top quarks) with $p_T > 5$ GeV and $|\eta| < 3$. The loose b-filter efficiency, i.e the fraction of $t\bar{t}$ events in the inclusive sample passing the filter cuts, in the case of the nominal PWG+PYT8 sample is 6%. However, out of these b-filtered events, only 46% are classified as $t\bar{t}+\geq 1b$ events in the analysis based on the adopted HF definition (see Section 5.2.2.2) whereas 48% are labeled as $t\bar{t}$ + light and 6% as $t\bar{t}+\geq 1c$. This large discrepancy between the filter decision and the analysis HF classification is due to the fact that the latter is much tighter than what is implemented at the filter level: additional truth jets with $p_T > 15$ GeV and $|\eta| < 2.5$ are used to label events instead of the hadrons with looser cuts. Moreover, a loose c-filter requiring at least one additional c-hadron with $p_T > 5$ GeV and $|\eta| < 3$ was also developed with a corresponding efficiency of 14%, but no $t\bar{t}$ c-filtered samples were produced in the previous round of the analysis.

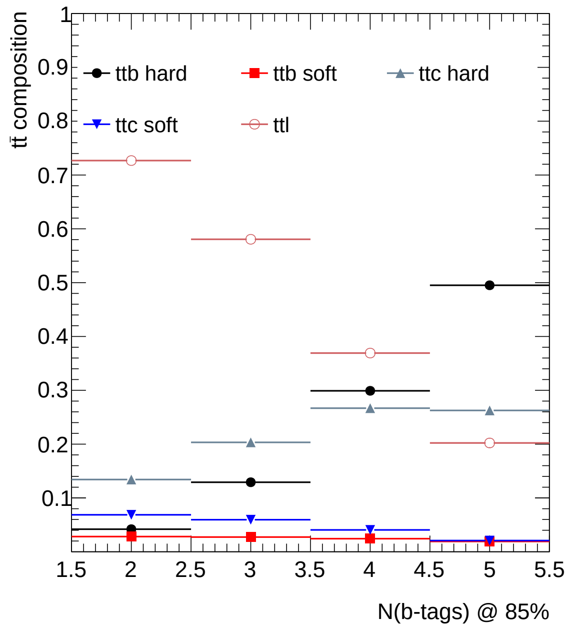

Figure 5.22.: $t\bar{t}$ events composition in the nominal PWG+PYT8 sample as a function of the number of b-tagged jets at the 85% working point. In each b-tag multiplicity bin, $t\bar{t}$ events are classified as follows: ttb (ttc) hard categories correspond to events which pass both the $b(c)$-filter and $t\bar{t}{+}{\geq}1b$ ($t\bar{t}{+}{\geq}1c$) classification criteria whereas events passing the $b(c)$-filter selection but not the $t\bar{t}{+}{\geq}1b$ ($t\bar{t}{+}{\geq}1c$) classification requirements enter the ttb (ttc) soft categories; the ttl category refers to events which are not selected by the filters and classified as $t\bar{t}$ + light in the analysis.

Figure 5.22 displays the composition of the $t\bar{t}$ events in the nominal PWG+PYT8 sample as a function of the number of b-tagged jets at the 85% working point; only single lepton events with at least 6 jets two of which at least are b-tagged at the 85% working point were considered. Events passing both the $b(c)$-filter and the $t\bar{t}+\geq 1b$ ($t\bar{t}+\geq 1c$) classification requirements enter the *ttb* (*ttc*) *hard* categories. In contrast, events which pass the $b(c)$-filter selection but do not satisfy the $t\bar{t}+\geq 1b$ ($t\bar{t}+\geq 1c$) definition criteria are labeled as *ttb* (*ttc*) *soft* e.g a b-filtered event classified as $t\bar{t}+\geq 1c$ or $t\bar{t}$ + light would enter the ttb soft category. The *ttl* category is made of events which fail to pass the filters cuts and are classified as $t\bar{t}$ + light in the analysis. The contribution of the soft categories decreases at high number of b-tags and becomes negligible (< 5%) in the 4 b-tags bin. Hence, if the $t\bar{t}+\geq 1b$ classification requirements were to be used as the b-filter selection criteria, the contribution of the ttb soft events can be suppressed in the b-filtered sample without compromising its phase space coverage and a gain of around 50% can be attained in the number of generated ttb hard events. However, for technical reasons, it is not straightforward to use the analysis HF definition for the filter. This is why I worked instead on designing tighter selection criteria on the kinematics and multiplicity of the additional hadrons as a mean to optimize the heavy flavor filters for the full Run 2 iteration of the analysis.

Several candidate filter selections were tested on the nominal PWG+PYT8 sample, where the cut on the transverse momentum of the additional heavy flavor hadrons was hardened going from the threshold of 5 GeV to 7, 10, 15 and 20 GeV . Moreover, the option of requiring at least two additional hadrons in addition to the default multiplicity requirement of at least 1, was explored. The absolute efficiencies of the tested b/c-filters and their relative efficiencies with respect to those of the default loose filters, are summarized in table 5.5.

Filter cuts		b-filter		c-filter	
lead. hadron p_T [GeV]	sublead. hadron p_T [GeV]	Absolute efficiency (%)	Relative efficiency (%)	Absolute efficiency (%)	Relative efficiency (%)
5	–	6.0	100	14.0	100
7	–	5.3	88	10.2	73
10	–	4.3	72	7.3	52
15	–	3.1	52	5.0	35
10	5	2.6	43	4.2	30
10	10	1.6	27	2.2	16
15	15	1.0	16	1.1	8
20	20	.6	10	.6	4

Table 5.5.: The efficiencies of the tested heavy flavor filters; the relative efficiencies are normalized to those of the default loose filters (third row). The filters selection cuts on the leading and subleading additional hadrons p_T are indicated in the first and second column respectively. Rows where both cuts are specified refer to filters where at least two additional hadrons are required whereas rows where only the leading hadron p_T cut is quoted correspond to filters requiring at least one additional hadron. All filters selections are tested on the nominal PWG+PYT8 sample.

Assuming the size of the new b-filtered samples is the same as that of the default one used in the last analysis iteration, a b-filter requiring at least one additional b-hadron with p_T > 15 GeV with a corresponding relative efficiency of 52% allows to double the number of simulated filtered events passing the analysis selection cuts compared to what is obtained with the default b-filtered sample.

Moreover, requiring both the leading and subleading additional b-hadrons to have $p_T > 15$ GeV allows to gain a factor 6 in the number of filtered events passing the analysis selection cuts. The latter case translates to a reduction by around a factor 2 in the relative statistical uncertainty associated with the corresponding filtered events.

For c-filtered samples, the use of the default c-filter requiring at least one additional c-hadron with $p_T > 5$ GeV will already bring a gain of factor 7 in the number of filtered events passing the analysis selection cuts, compared to what is available in the inclusive PWG+PYT8 sample. Additional gain of factor 3 can be achieved by requiring the leading additional c-hadron to pass $p_T > 15$ GeV .

As discussed above, tightening the kinematic and multiplicity cuts on the additional heavy flavor hadrons allows to increase significantly the number of simulated events satisfying the corresponding selection criteria. However, the impact of these tighter cuts on the coverage of the phase space of interest for the $t\bar{t}H(H \to b\bar{b})$ analysis namely in the signal regions, compared to the loose filters, had to be carefully checked. In this respect, the fraction of events which pass the analysis selection cuts but fail the tighter filters requirements was assessed. Figures 5.23 and 5.24 show the relative efficiencies of the tested tighter b/c-filters with respect to the corresponding loose filters, as a function of the number of b-tagged jets at the 70% and 60% working points, respectively. One can note that a significant fraction of events in the low number of b-tags analysis regions (i.e number of b-tags ≤ 2) are discarded by the tighter filters requiring additional hadrons with $p_T > 10$ GeV or at least two additional hadrons. For example, only 40% and 50% of the events having exactly one and two b-tags at the 60% working point, respectively, and selected by the loose b-filter are kept by the tighter filter which requires at least two additional b-hadrons with $p_T > 10$ GeV . However, this is not a source of major concern for the analysis as the limited number of simulated events in these regions had a negligibe impact on the search sensitivity in the last round. On the other hand, the fraction of events at higher b-tag multiplicity regions i.e ≥ 3 b-tags discarded by the tighter filters selections is not sizable. For instance, the filter requiring at least two additional b-hadrons with p_T>15 GeV preserves about 95% of the events having 4 b-tags at the 60% working point with respect to the loose b-filter selection. Similarly, the tighter c-filter requiring at least one additional c-hadron with p_T>15 GeV keeps around 75% of the events which have exactly 3 b-tags at the 60% working point and pass the loose c-filter selection. In order to avoid inflating the statistical uncertainty associated with the discarded loose b-filtered events with respect to the last round of the analysis, the decision of keeping the loose b-filter and combining it with a new tighter b-filter was made.

Taking into account the trade-off between the targeted statistical gain and the phase space coverage of the tested filter selections, the following new filters are adopted for the full Run 2 analysis iteration:

- **BBFilter**: requiring at least two additional b-hadrons with $p_T > 15$ GeV . This filter allows to gain a factor 6 in the number of simulated events passing its selection criteria with respect to what was available in the default b-filtered sample. Additionally, it does not compromise the coverage of the signal regions phase space.

- **BFilBBVeto**: this filter uses the default selection criteria used in the last analysis round i.e at least one additional b-hadron with $p_T > 5$ GeV . However, events passing the BBFilter selections are vetoed.

- **CFilBVeto**: requiring at least 1 additional c-hadron with $p_T > 15$ GeV . This filter allows to gain a factor 20 in the number of simulated events passing this selection compared to what was available in the nominal $t\bar{t}$ inclusive sample in the last round. Events passing the default b-filter selection cuts are vetoed.

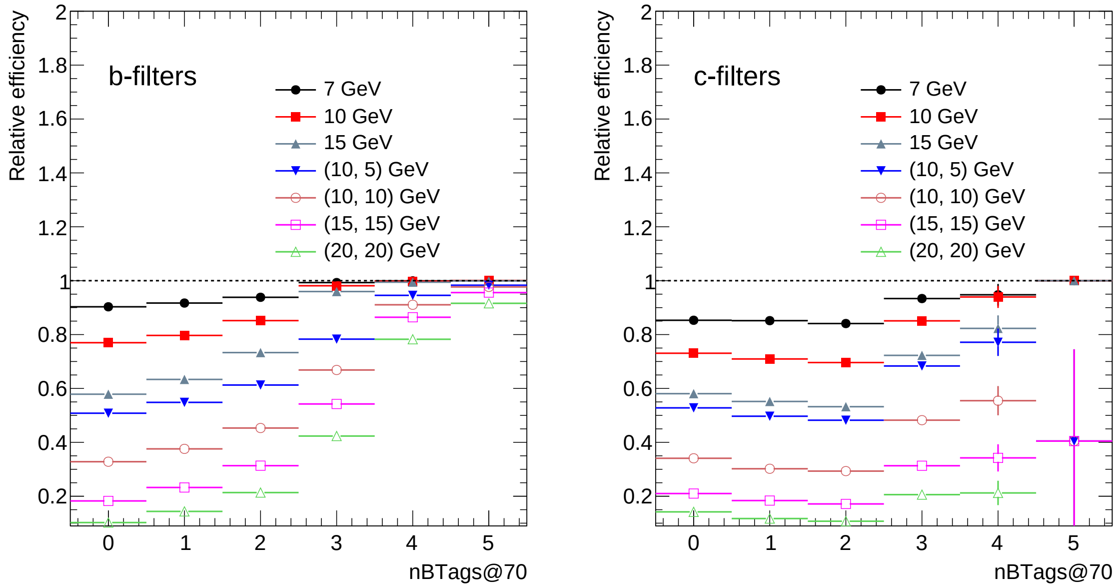

Figure 5.23.: The relative efficiencies of the tighter b-filters (left) and c-filters (right) tested, with respect to the corresponding loose filters, as a function of the number of b-tagged jets at the 70% working point. The values quoted in the legend correspond to the transverse momenta requirements on the leading and subleading additional $b(c)$-hadrons for the tested $b(c)$-filters (see Table 5.5). For filters requiring at least two additional hadrons, two p_T cuts are specified: the first value corresponds to the p_T cut on the leading hadron whereas the second refers to the p_T cut on the subleading hadron.

5.3.2.2. Impact of the new filters on the analysis

The proposed new heavy flavor filters were validated and adopted for the full Run 2 round of the $t\bar{t}H(H \to b\bar{b})$ analysis to produce the baseline MC samples for the $t\bar{t}$ background as mentioned in Section 5.3.1. HF-filtered samples were generated for the nominal PWG+PYT8 setup as well as the alternative PWG+HW7 and the aMC@NLO+PYT8 predictions. In contrast to the previous analysis round, the filtered samples produced with the alternative generators are of the same size as the nominal sample.

The relative statistical uncertainty as a function of the number of b-tagged jets at the 60% working point in the nominal $t\bar{t}$ sample generated with and without the new filters, is shown in Figure 5.25. The statistical uncertainty is significantly reduced namely in the analysis regions dominated by the $t\bar{t}$ + HF components i.e at high b-tag multiplicity regions. For instance, the relative statistical uncertainty associated with events in the analysis region with 4 b-tagged jets at the 60% working point is reduced by around 70% with respect to that achieved in the inclusive sample produced without the filters. Figure 5.26 depicts the shrinkage of the relative statistical uncertainty in bins of the classification BDT distribution, achieved with the filters in the nominal and alternative $t\bar{t}$ samples. One can see that the gain is more pronounced at high values of the BDT (up to 50%) where the $t\bar{t}$ + HF components are expected to contribute the most.

The new filtered samples were also adopted as baseline in other analyses where the $t\bar{t}$ background plays a major role and which are limited in their sensitivity by the large statistical uncertainties associ-

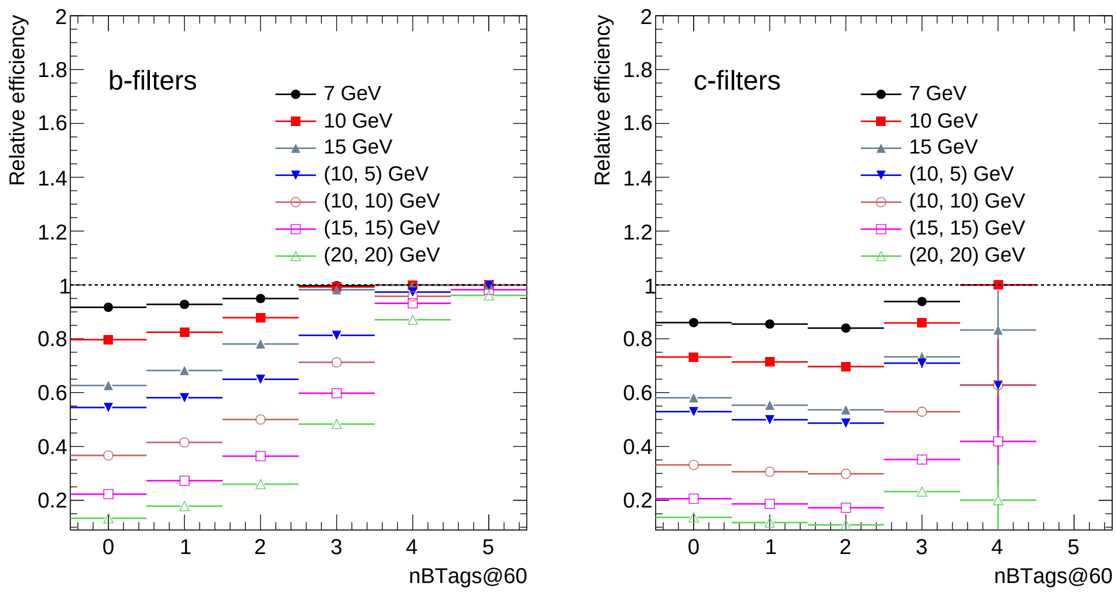

Figure 5.24.: The relative efficiencies of the tighter b-filters (left) and c-filters (right) tested, with respect to the corresponding loose filters, as a function of the number of b-tagged jets at the 60% working point. The values quoted in the legend correspond to the transverse momenta requirements on the leading and subleading additional $b(c)$-hadrons for the tested $b(c)$-filters (see Table 5.5). For filters requiring at least two additional hadrons, two p_T cuts are specified: the first value corresponds to the p_T cut on the leading hadron whereas the second refers to the p_T cut on the subleading hadron.

ated with the $t\bar{t}$ + HF components such as the analysis searching for the SM four-top production using the ATLAS Run 2 data.

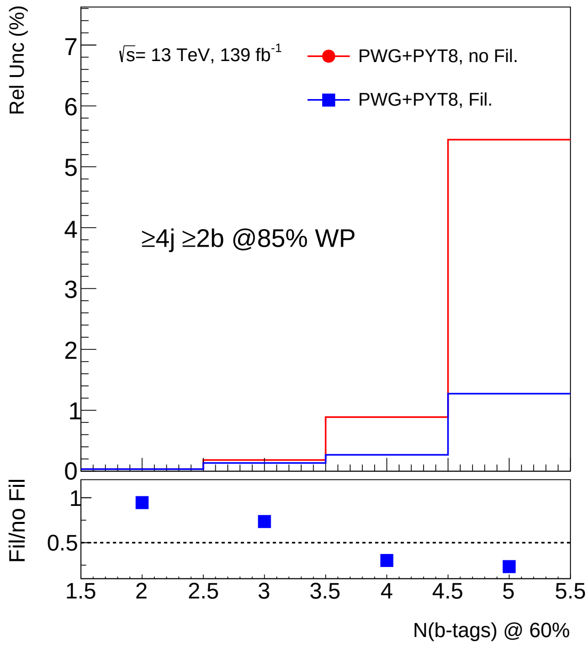

Figure 5.25.: The relative statistical uncertainty as a function of the number of b-tagged jets at the 60% working point in the nominal PWG+PYT8 sample produced without (red) and with (blue) the new heavy flavor filters. The lower pad shows the ratio of the relative statistical uncertainty in the filtered sample with respect to that in the inclusive sample.

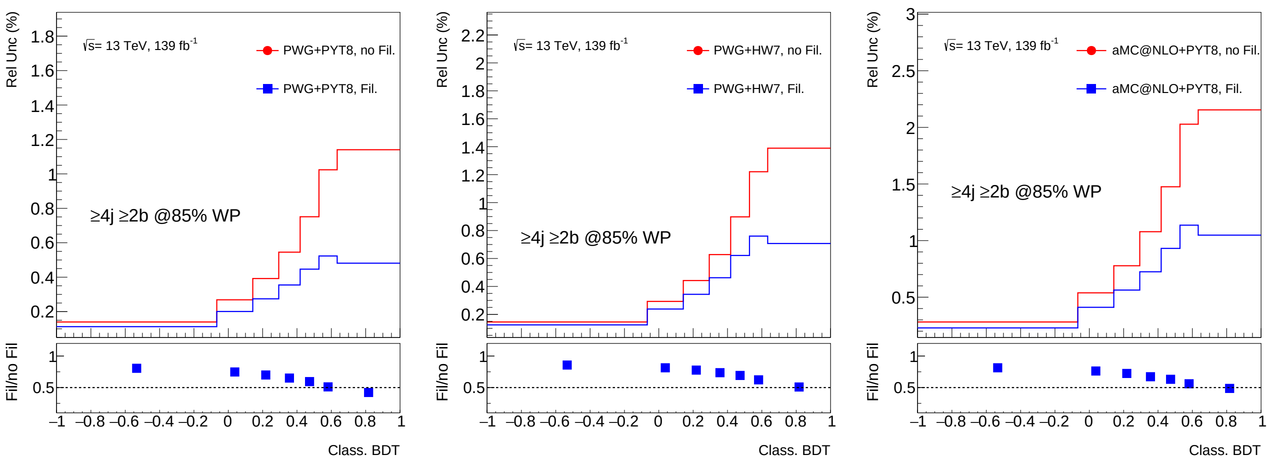

Figure 5.26.: Relative statistical uncertainty in bins of the classification BDT for the nominal (left), PWG+HW7 (middle) and aMC@NLO+PYT8 (right) $t\bar{t}$ samples: relative uncertainties achieved with the filtered samples (blue) are compared to those obtained when using the corresponding inclusive samples produced without the use of filters (red). The lower pads show the ratio of the relative statistical uncertainty in the filtered samples with respect to that in the inclusive samples.

5.3.3. Data-driven $t\bar{t}$ modeling

5.3.3.1. Motivation

The sensitivity of the $t\bar{t}H(H \to b\bar{b})$ analysis is primarily limited by the large theoretical uncertainties associated with the $t\bar{t}$ MC prediction and more importantly with the $t\bar{t}+\geq 1b$ component, as discussed in section 5.2.6. Moreover, some key kinematic variables in the analysis such as the number of jets, the H_T^{had} and jets p_T distributions are not well described with the MC-based $t\bar{t}$ model, as depicted in Figure 5.27. The correction of the shape mismodeling in these distributions relies heavily on the fit to data which requires several pulls of different uncertainties and it is not always evident if these corrections should be extrapolated to regions enriched in signal. In order to establish a more robust analysis and improve the modeling of data prior to the fitting step, I explored a new approach to model the $t\bar{t}$ process using data (data-driven) in addition to MC to provide an estimate for this background.

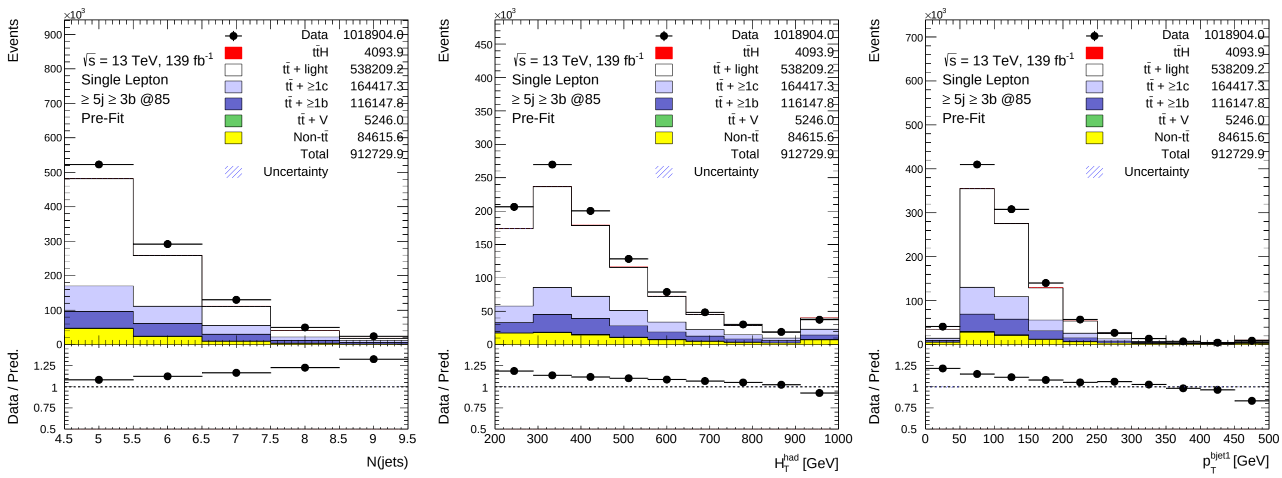

Figure 5.27.: Comparison of the predicted number of jets (left), H_T^{had} (middle) and leading b-jet p_T (right) distribution to that observed in data for events passing an inclusive selection requiring ≥ 5 jets and ≥ 3 b-tagged jets at the 85% working point. The predicted distributions are shown before the correction from the fit to data (prefit).

5.3.3.2. Overview of the data-driven $t\bar{t}$ method

The data-driven $t\bar{t}$ model consists in correcting the MC prediction based on comparison with data. This comparison takes place in a chosen Control Region (CR) where correction factors are extracted, allowing to match a given observable distribution obtained from the MC-based $t\bar{t}$ expectation to that from $t\bar{t}$ data. Unless stated otherwise, only the shapes of the MC distributions are corrected to that in $t\bar{t}$ data. The latter is built by subtracting the non-$t\bar{t}$ MC predictions including that of the $t\bar{t}H$ signal from the total observed data distribution. The obtained correction factors are then applied to the $t\bar{t}$ MC prediction in the signal enriched regions (SR) where the data-driven $t\bar{t}$ prediction is constructed.

Studies performed in the context of the previous round of the analysis have shown the kinematic variables and the b-tagging information to be relatively decorrelated. This property can be exploited to define the CR and SR based on the b-tagging score of jets which can be chosen such that a given $t\bar{t}$ flavor component is enhanced without biasing the kinematic distributions. The validity of the extrapolation of the correction factors from the CR to the SR based on this feature is tested in Section 5.3.3.3.

The definition of the CR must not allow for a large contribution of the signal otherwise the extracted correction factors will depend highly on the signal strength measurement which will compromise the analysis sensitivity.

The choice of the observable to consider for deriving global correction factors is one of the challenges of this method. The correction of one variable might lead to worse modeling in others. This is why, I investigated the option of building a single variable such that its correction brings an overall better agreement with data across various observables as described in Section 5.3.3.5.

In the baseline fit model adopted for the ongoing full Run 2 analysis, the theoretical and experimental systematic uncertainties affecting the MC-based $t\bar{t}$ prediction are estimated based on comparisons with alternative $t\bar{t}$ generators and variations of the nominal prediction. However, the extraction of the nominal $t\bar{t}$ prediction from data would require the fit model to be adjusted accordingly. Thus, all systematic variations about the nominal MC prediction would also have to be corrected to data using correction factors derived for each, following the same procedure applied to the nominal prediction. The residual differences between the nominal and systematic variations after the data-driven correction will account for systematic uncertainties associated with the extrapolation from the CR to the SR.

In the following, the data-driven method is tested in the single lepton channel only, considering events with at least 6 jets. The same procedure can be followed in regions with exactly 5 jets. The data-driven corrections are not provided separately for $t\bar{t}+\geq 1b$, $t\bar{t}+\geq 1c$ and $t\bar{t}$ + light since it was not feasible to separate these components in $t\bar{t}$ data, at the time of performing these studies.

To test the data-driven method, a CR built from events having exactly 3 b-tagged jets at the 70% working point, was chosen. This choice was made to minimize the statistical uncertainties on the derived correction factors as they are not taken into account in these studies. The defined data-driven CR is the same as the $\geq$ 6 jets control region from the baseline analysis categorization discussed in Section 5.3.1. The signal to background ratio in this region is around 1.4%. Events having at least 4 b-tagged jets at the 70% working point form the SR with the corresponding signal to background ratio being around 5.5%. Figure 5.28 shows the $t\bar{t}$ flavor composition in both the CR and SR. The $t\bar{t}+\geq 1b$ and $t\bar{t}$ + light components contribute equally in the chosen CR whereas the SR is dominated by the $t\bar{t}+\geq 1b$ fraction.

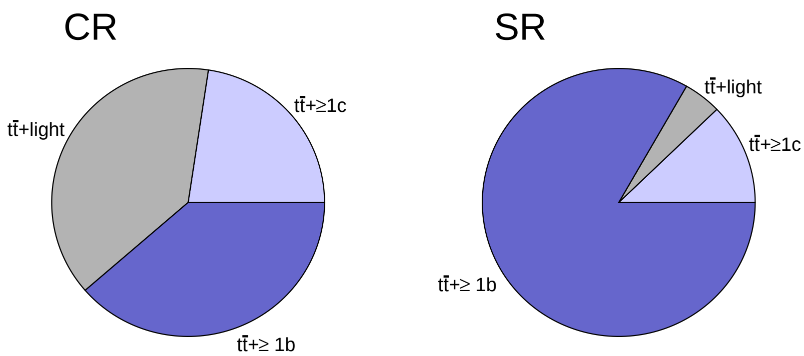

Figure 5.28.: Relative contribution of the $t\bar{t}$ background components in the data-driven CR (left) and SR (right) for the nominal $t\bar{t}$ MC prediction.

5.3.3.3. Data-driven correction extrapolation from control to signal regions

The validity of applying the data-driven correction factors in the SR which has a different background composition from the CR, is examined in the following using the PWG+HW7 $t\bar{t}$ sample as pseudo-data. In these tests, the correction factors are derived for the nominal and alternative $t\bar{t}$ predictions by matching them to that of the pseudo-data sample in the CR. The impact of two versions of these correction factors on the modeling of observables in the SR is checked. The first version of correction factors is extracted inclusively in $t\bar{t}$ while the second one is derived considering exclusively the $t\bar{t}+\geq 1b$ component.

Figure 5.29 shows the normalized H_T^{had} distribution in the $t\bar{t}$ pseudo-data sample and the considered MC predictions in the CR and in the SR before and after applying the inclusive correction factors derived for the H_T^{had} variable. The level of modeling discrepancies relative to the pseudo-data, e.g up to 10% in the case of the nominal PWG+PYT8 sample, is fairly similar between the CR and SR despite their different $t\bar{t}$ flavor composition. Hence, applying the inclusive correction factors derived from the CR in the SR allows to improve significantly the agreement of the corrected MC distributions with the pseudo-data in addition to reducing the differences among them. The impact of both the inclusive and $t\bar{t}+\geq 1b$ exclusive correction factors on the $t\bar{t}+\geq 1b$ subcomponent predictions in the CR and SR is shown in Figure 5.30. Although the inclusive correction factors yield a full closure in the CR for inclusive $t\bar{t}$ predictions by construction, this is not ensured for the $t\bar{t}+\geq 1b$ subcomponent, which hints at a slight dependence of the shape of the H_T^{had} distribution on the flavor of the additional jets. This explains why a full closure is not obtained in the SR for $t\bar{t}+\geq 1b$ and by extension for $t\bar{t}$ inclusive since this region is dominated by $t\bar{t}+\geq 1b$ events. Consequently, injecting the $t\bar{t}+\geq 1b$ exclusive correction factors in the SR for the $t\bar{t}+\geq 1b$ predictions leads to a full closure. Even though the H_T^{had} distribution is slightly biased by the heavy flavor composition in the CR, the performance of the data-driven method is marginally affected for this observable.

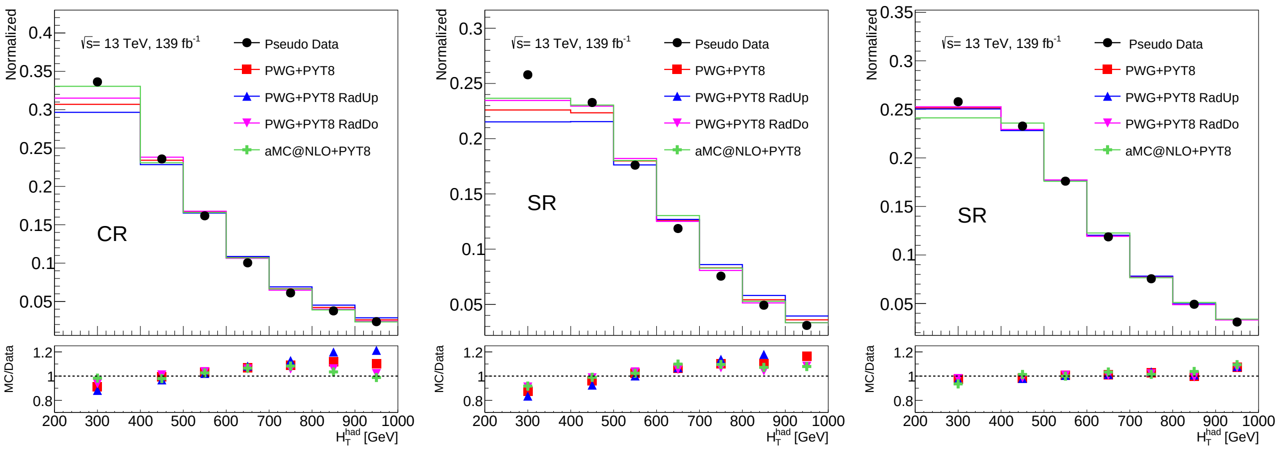

Figure 5.29.: Comparison of the normalized H_T^{had} distribution among different $t\bar{t}$ MC predictions in the CR (left), the SR (middle) and in the SR after applying the inclusive data-driven correction factors (right). The correction factors are derived for the H_T^{had} observable, considering the PWG+HW7 prediction as $t\bar{t}$ data.

Similar checks were carried out in the case of the ΔR(add jets) observable, defined as the angular

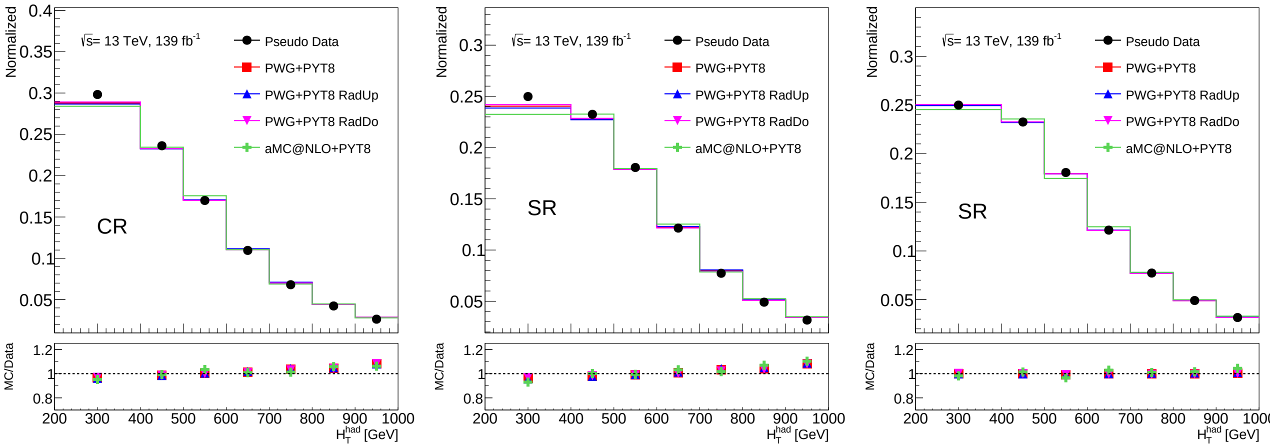

Figure 5.30.: Comparison of the normalized H_T^{had} distribution for the $t\bar{t}+\geq 1b$ component among different $t\bar{t}$ MC predictions in the CR after applying the inclusive data-driven correction factors (left), in the SR after applying these correction factors (middle) and in the SR after applying the $t\bar{t}+\geq 1b$ exclusive correction factors (right). The correction factors are derived for the H_T^{had} variable, considering the PWG+HW7 prediction as $t\bar{t}$ data.

separation between the two leading additional jets in b-tagging[c]. Figure 5.31 shows the normalized ΔR(add jets) distribution in the considered $t\bar{t}$ predictions in the CR and in the SR before and after applying the inclusive correction factors derived for this observable. In contrast to the H_T^{had} observable, a difference in the level of discrepancies exhibited by the predictions with respect to the pseudo-data is noticed between the CR and SR namely towards small ΔR. The modeling of this variable in the SR is already quite good as reflected in the agreement of the different predictions with the pseudo-data as well as the small differences among them. The modeling remains good in this region after the injection of the inclusive correction factors. The impact of the inclusive and $t\bar{t}+\geq 1b$ exclusive correction factors on the $t\bar{t}+\geq 1b$ predictions in the CR and SR is shown in Figure 5.32. The inclusive factors yield an almost full closure for the $t\bar{t}+\geq 1b$ component in the CR which indicates that the ΔR(add jets) distribution does not depend much on the $t\bar{t}$ flavor composition in the CR. Thus, the differences between the CR and SR observed in the modeling discrepancies for this variable are due to the different b-tagging selection cuts used to define these regions. The application of the inclusive correction factors of ΔR(add jets) to the $t\bar{t}+\geq 1b$ predictions in the SR results in a worse agreement compared to that achieved in the case of inclusive $t\bar{t}$ predictions. This effect is mitigated when injecting the exclusive $t\bar{t}+\geq 1b$ correction factors. Despite the biases introduced by the b-tagging selection cuts, the data-driven method performance is not significantly affected for the ΔR(add jets) variable.

Additional tests were performed in the same manner as above for alternative observables. These checks allowed to gain confidence in the validity of extrapolating the correction factors from the CR to the SR. The modeling of $t\bar{t}$ distributions is overall improved (with respect to the pseudo-data) despite the slight biases introduced in some of the kinematic distributions by the b-tagging selection cuts chosen to define the CR and SR and the heavy flavor composition which are different between the two regions.

[c] The additional jets are selected by a BDT trained to reconstruct the $t\bar{t}$ system in a region having at least 6 jets, 3 of which at least are tagged at the 85 % working point.

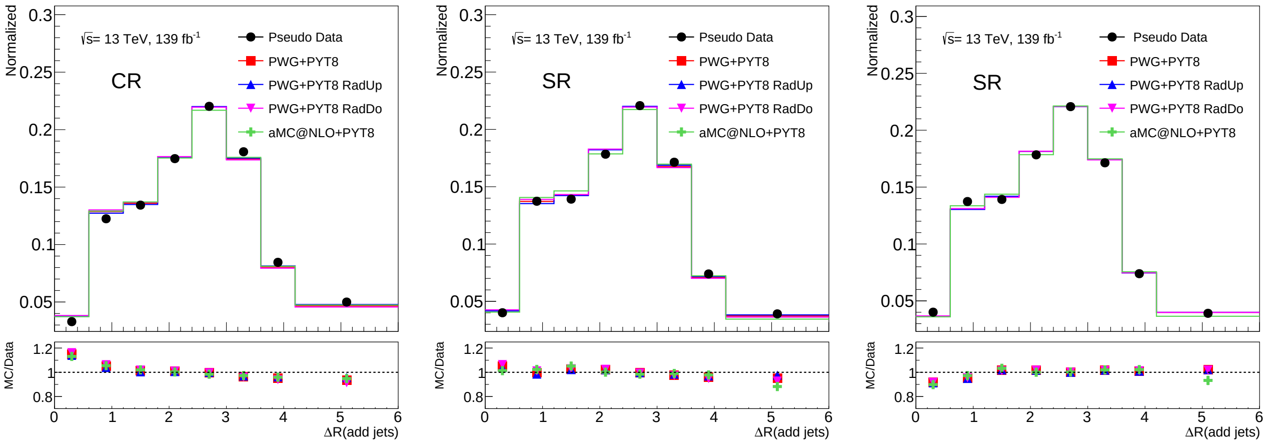

Figure 5.31.: Comparison of the normalized ΔR(add jets) distribution among different $t\bar{t}$ MC predictions in the CR (left), the SR (middle) and in the SR after applying the inclusive data-driven correction factors (right). The correction factors are derived for the ΔR(add jets), considering the PWG+HW7 prediction as $t\bar{t}$ data.

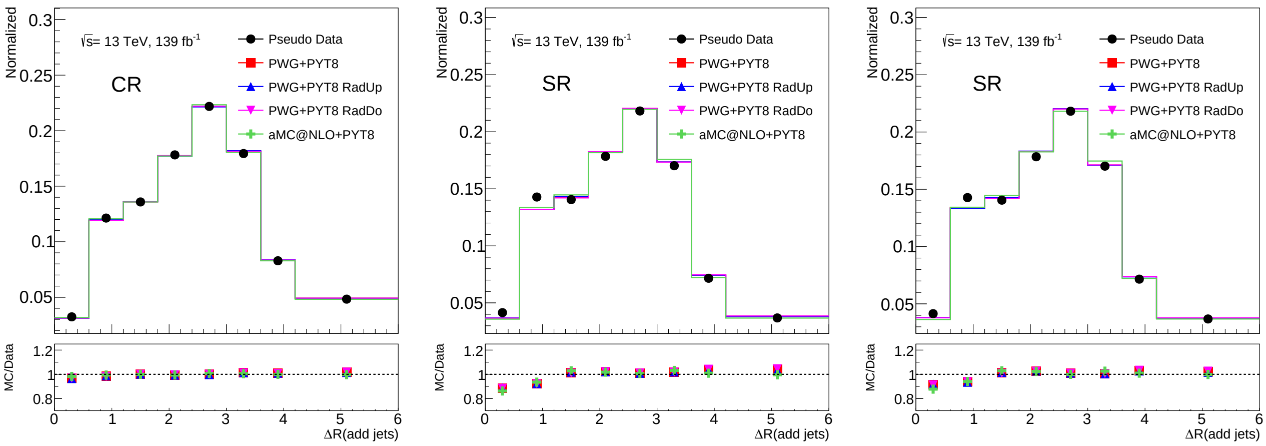

Figure 5.32.: Comparison of the normalized ΔR(add jets) distribution for the $t\bar{t}+\geq 1b$ component among different $t\bar{t}$ MC predictions in the CR after applying the inclusive data-driven correction factors (left), in the SR after applying these correction factors (middle) and in the SR after applying the $t\bar{t}+\geq 1b$ exclusive correction factors (right). The correction factors are derived for the ΔR(add jets) observable, considering the PWG+HW7 prediction as $t\bar{t}$ data.

5.3.3.4. Performance of the data-driven $t\bar{t}$ method

The performance of the data-driven $t\bar{t}$ method described in Section 5.3.3.2 is examined for different observables using real $t\bar{t}$ data in the following. For each of these variables, the MC-based and data-driven $t\bar{t}$ predictions are compared in the SR and confronted to $t\bar{t}$ data to gauge the goodness of modeling obtained by both predictions. Data-driven correction factors are derived exclusively for the variable under consideration. The performance of the method is checked for the nominal and alternative $t\bar{t}$ MC samples in addition to a subset of the instrumental variations of the nominal prediction.

Figures 5.33, 5.34, 5.35 and 5.36 display the normalized H_T^{had}, centrality, MET and ΔR(add jets) distributions, respectively, for the nominal and alternative $t\bar{t}$ predictions compared to $t\bar{t}$ data in the CR and in the SR before and after applying the data-driven corrections. The differences between the $t\bar{t}$ MC predictions are overall reduced in the SR when injecting the correction factors especially in the case of the H_T^{had} observable. Furthermore, the agreement with $t\bar{t}$ data is generally improved in the case of the corrected distributions compared to the MC-based ones except for the ΔR(add jets) distribution where the modeling becomes worse at small ΔR.

The impact of the data-driven corrections on a subset of the instrumental variations around the nominal $t\bar{t}$ prediction of the H_T^{had} observable is shown in Figure 5.37. The agreement with $t\bar{t}$ data in the SR is also improved for these variations after applying the corrections.

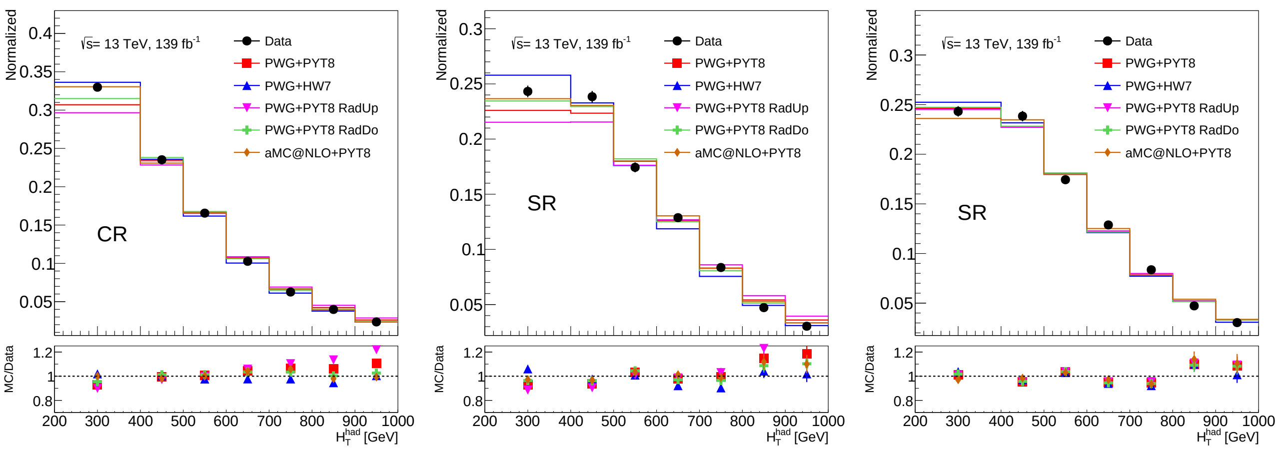

Figure 5.33.: Comparison of the normalized H_T^{had} distribution between the various $t\bar{t}$ MC predictions and $t\bar{t}$ data in the CR(left), SR before (middle) and after (right) applying the data-driven correction factors. The correction factors are extracted such that the H_T^{had} distribution in the $t\bar{t}$ MC samples is matched to that in $t\bar{t}$ data in the CR.

As previously mentioned, for each of the observables checked above, data-driven correction factors are derived to improve its modeling in the SR. However, correcting a single kinematic distribution in the $t\bar{t}$ MC sample to match that in data does not necessarily lead to better modeling for the remaining distributions characterizing the sample. Figure 5.38 illustrates the impact of different kinematic distributions corrections on the H_T^{had}, ΔR(add jets) and centrality distributions in the CR for the nominal $t\bar{t}$ prediction. Apart from the dedicated corrections that match the distributions to data, the other variables corrections leave these essentially unchanged with respect to the initial MC-based prediction i.e before applying any correction; in the case of the nominal centrality distribution, the modeling is already good in the CR and hence the differences between the various corrections are negligible.

In order to correct the full $t\bar{t}$ MC model and avoid deriving correction factors for each variable of

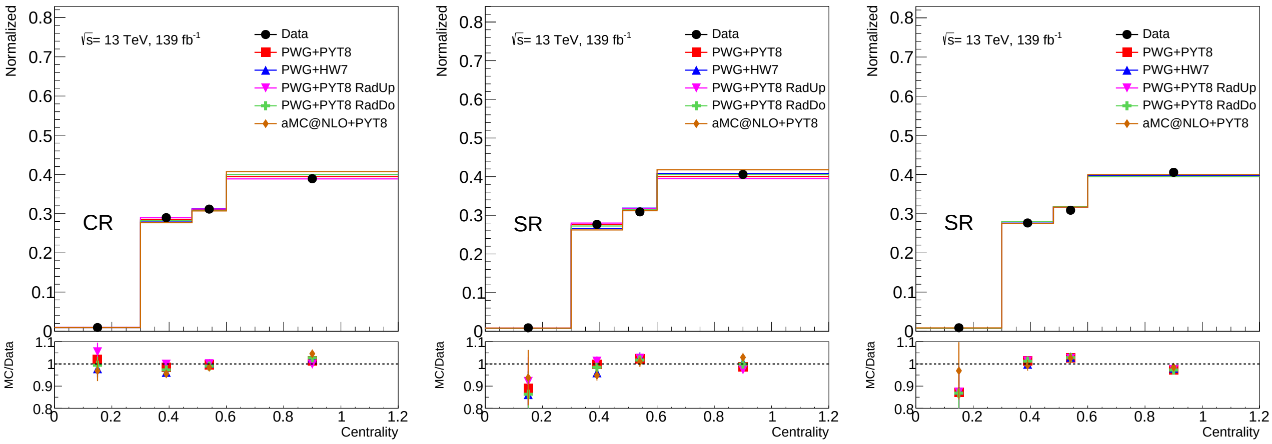

Figure 5.34.: Comparison of the normalized centrality distribution between the various $t\bar{t}$ MC predictions and $t\bar{t}$ data in the CR (left), SR before (middle) and after (right) applying the data-driven correction factors. The correction factors are extracted such that the centrality distribution in the $t\bar{t}$ MC samples is matched to that in $t\bar{t}$ data in the CR.

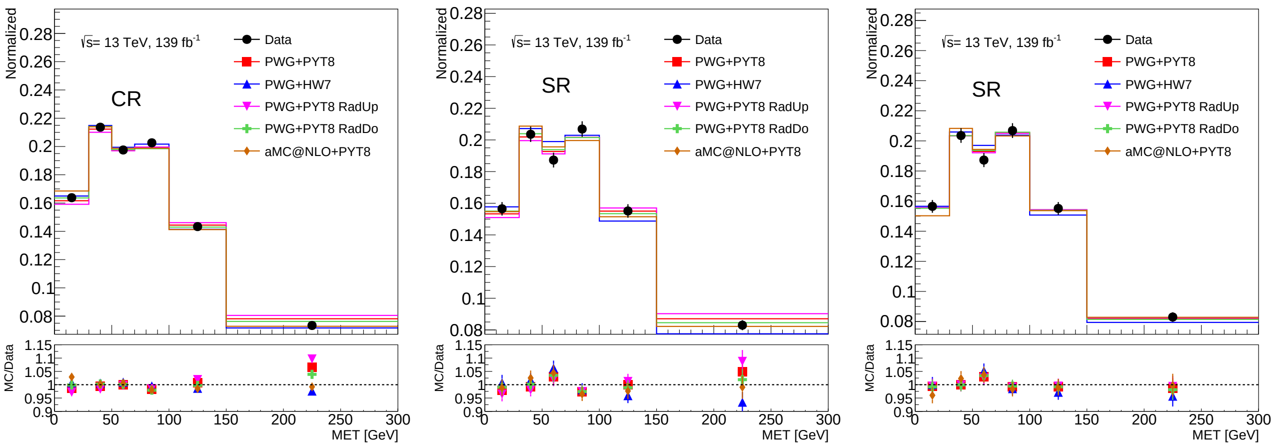

Figure 5.35.: Comparison of the normalized MET distribution between the various $t\bar{t}$ MC predictions and $t\bar{t}$ data in the CR (left), SR before (middle) and after (right) applying the data-driven correction factors. The correction factors are extracted such that the MET distribution in the $t\bar{t}$ MC samples is matched to that in $t\bar{t}$ data in the CR.

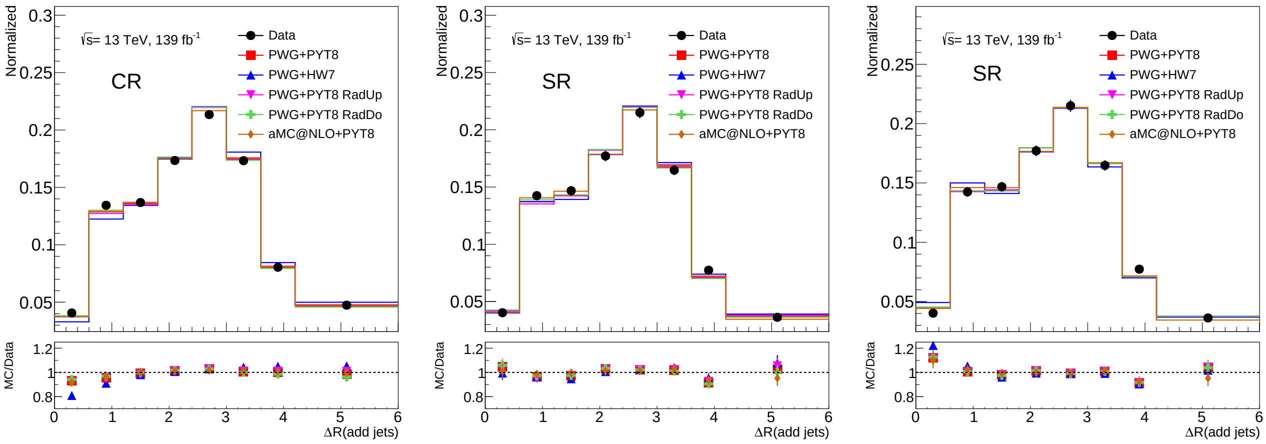

Figure 5.36.: Comparison of the normalized distributions of ΔR(add jets) between various $t\bar{t}$ MC predictions and $t\bar{t}$ data in the CR (left), SR before (middle) and after (right) applying the data-driven correction factors. The correction factors are extracted such that the ΔR(add jets) distribution in the $t\bar{t}$ MC samples is matched to that in $t\bar{t}$ data in the CR.

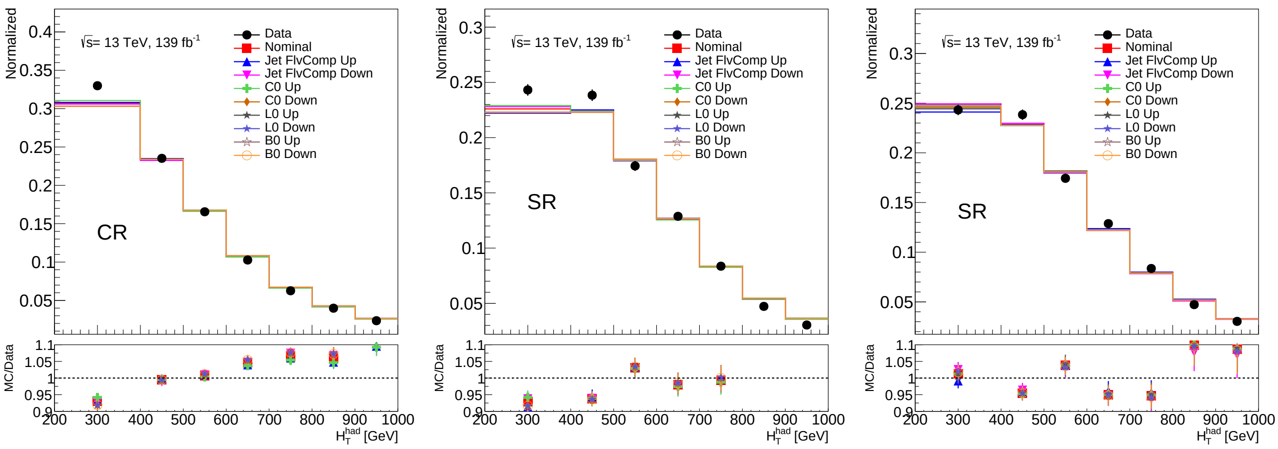

Figure 5.37.: Comparison of the normalized H_T^{had} distributions for various $t\bar{t}$ detector variations and $t\bar{t}$ data in the CR (left), SR before (middle) and after (right) applying the data-driven correction factors. The correction factors are extracted such that the H_T^{had} distribution in the $t\bar{t}$ instrumental variations is matched to that in $t\bar{t}$ data in the CR. The nominal $t\bar{t}$ prediction is also shown.

interest in the analysis, it is important to determine a single variable such that its correction brings an overall improvement in the modeling across several kinematic distributions in the $t\bar{t}$ sample.

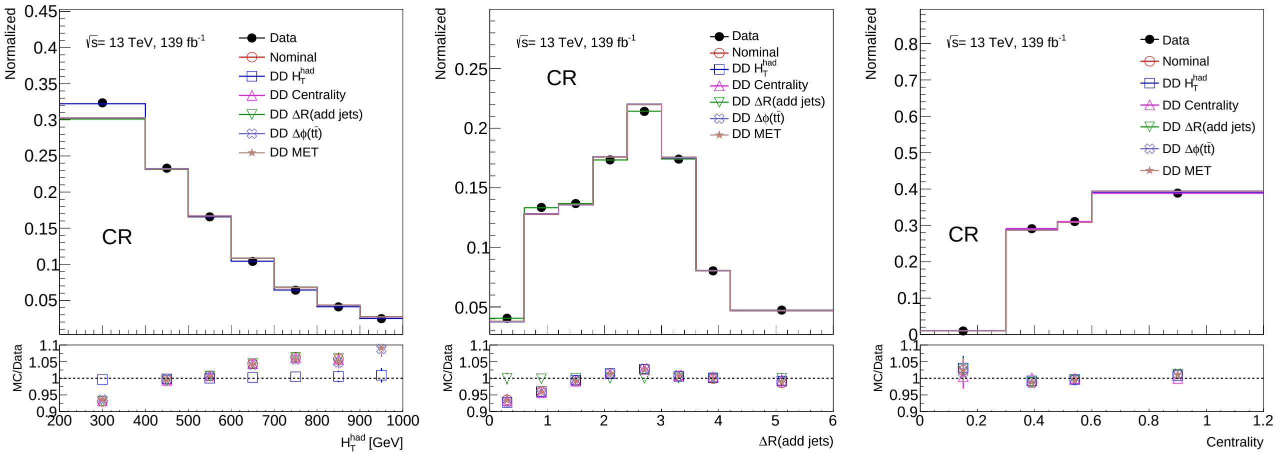

Figure 5.38.: Impact of data-driven corrections derived in various variables on the H_T^{had} (left), ΔR(add jets) (middle) and centrality (right) distributions in the nominal $t\bar{t}$ sample compared to $t\bar{t}$ data in the CR.

5.3.3.5. Reweighting BDT correction

In view of finding a single variable based on which global correction factors can be derived to improve the modeling of $t\bar{t}$, I tested the option of using the output of a BDT referred to in the following as the *reweighting BDT*. The latter is trained in the CR to discriminate between data (or $t\bar{t}$ pseudo-data for checks) and the $t\bar{t}$ MC prediction (nominal or alternative) for which data-driven correction factors need to be extracted. To train this BDT, simple event-level kinematic variables such as H_T^{had}, MET and centrality were used in addition to $t\bar{t}$ related variables such as the $\Delta\phi$ and ΔR separation between the top quarks as well as ΔR(add jets). The $t\bar{t}$ related variables are retrieved based on the $t\bar{t}$ reconstruction BDT developed in the context of the $t\bar{t}$ + HF studies presented in Section 4.2.3. The set of variables used in the BDT training was chosen to combine those for which the corresponding correction only improves the modeling of the variable in question and leaves the other observables distributions in the sample unchanged with respect to the MC prediction or with a worse modeling.

Figure 5.39 shows the impact of the reweighting BDT correction compared with that of other variables corrections, on the modeling of the H_T^{had} distribution in the CR and SR for the nominal $t\bar{t}$ prediction. The data-driven corrections are derived using the $t\bar{t}$ PWG+HW7 sample as pseudo-data. The correction associated with the reweighting BDT yields a full closure in the CR in accordance with the dedicated correction of the H_T^{had} observable as opposed to the other variables corrections leaving the distribution the same as in the MC-based prediction. Furthermore, the modeling of the H_T^{had} observable in the SR with respect to the pseudo-data is improved under the effect of the reweighting BDT correction similarly to that of the dedicated correction. The impact of the reweighting BDT correction on the modeling of the ΔR(add jets) and the centrality distributions in the CR is shown in Figure 5.40 and, like in the H_T^{had} distribution case, it yields a similar effect to that from the dedicated variables corrections; for the centrality distribution, the different variables corrections, including the reweighting BDT, are compatible as the distribution is already well modeled by the MC prediction. The reweighting BDT correction factors seem to be able to act globally on the $t\bar{t}$ MC sample allowing to improve the modeling across multiple kinematic distributions.

The effect of the reweighting BDT correction was also tested using real $t\bar{t}$ data. Figure 5.41 shows the impact of the different variables corrections, derived to match real $t\bar{t}$ data, on the H_T^{had} distribution in the CR and SR for the nominal $t\bar{t}$ prediction. The impact of the reweighting BDT correction is less pronounced compared to the case of $t\bar{t}$ pseudo-data. However, the differences between the various corrections are smaller for real $t\bar{t}$ data. More tests are needed to understand the smaller effect of the reweighting BDT in the case of real $t\bar{t}$ data such as optimizing the list of input variables used to train the BDT against real data.

The tests peformed above show that the reweighting BDT varibale could be a good candidate to derive global correction factors. However, to make a decision on the global correction variable, the performance of the data-driven $t\bar{t}$ method must be tested within the analysis fit machinery for different candidate variables and check in each case the impact of the method on the robustness of the fit and the analysis sensitivity.

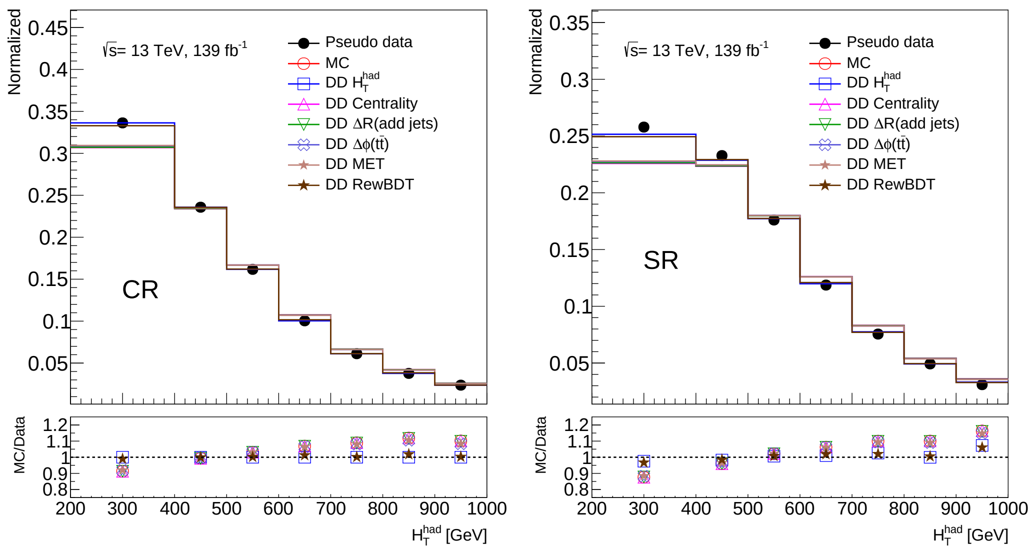

Figure 5.39.: Impact of the reweighting BDT correction on the modeling of the H_T distribution in the nominal prediction compared to that from other variables corrections, in the CR (left) and SR (right). The correction factors are derived using the PWG+HW7 $t\bar{t}$ as pseudo-data.

5.3.3.6. Implementation of the data-driven $t\bar{t}$ method in the fit model

The baseline $t\bar{t}H(H \to b\bar{b})$ fit model adopted in the ongoing full Run 2 analysis is fairly similar to that used in the previous iteration described in details in Section 5.2.4. This model can be adjusted to implement the data-driven $t\bar{t}$ method as described in the following.

To build the data-driven $t\bar{t}$ prediction, the correction factors extracted from the ≥ 6 jets CR for a chosen observable are applied, in the ≥ 6 jets signal regions, to the $t\bar{t}$ nominal and alternative predictions as well as the detector systematic variations affecting this background. In what follows, only a subset of the instrumental variations namely those which are pulled with respect to their nominal values in the baseline fit model are corrected such as the JES flavor composition and response as well as the flavor tagging eigen vectors for b, c and light-jets; the remaining instrumental systematics have a negligible impact on the analysis sensitivity and therefore were not corrected. Even though the correction factors are derived inclusively in $t\bar{t}$, the residual systematic uncertainties associated with the

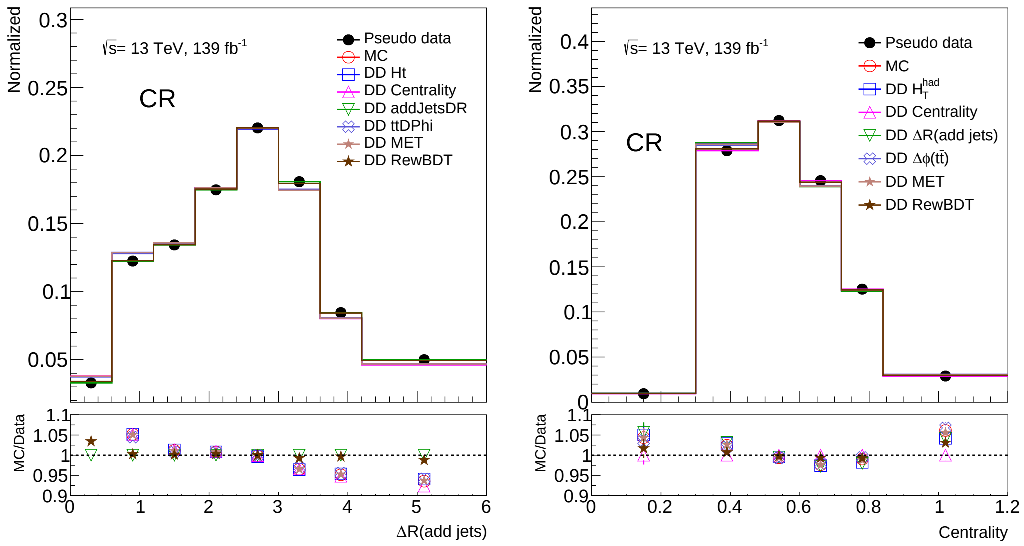

Figure 5.40.: Impact of the reweighting BDT correction on the modeling of the ΔR(add jets) (left) and centrality (right) distributions in the nominal prediction compared to that from other variables corrections, in the CR. The data-driven corrections are derived using the PWG+HW7 $t\bar{t}$ sample as pseudo-data.

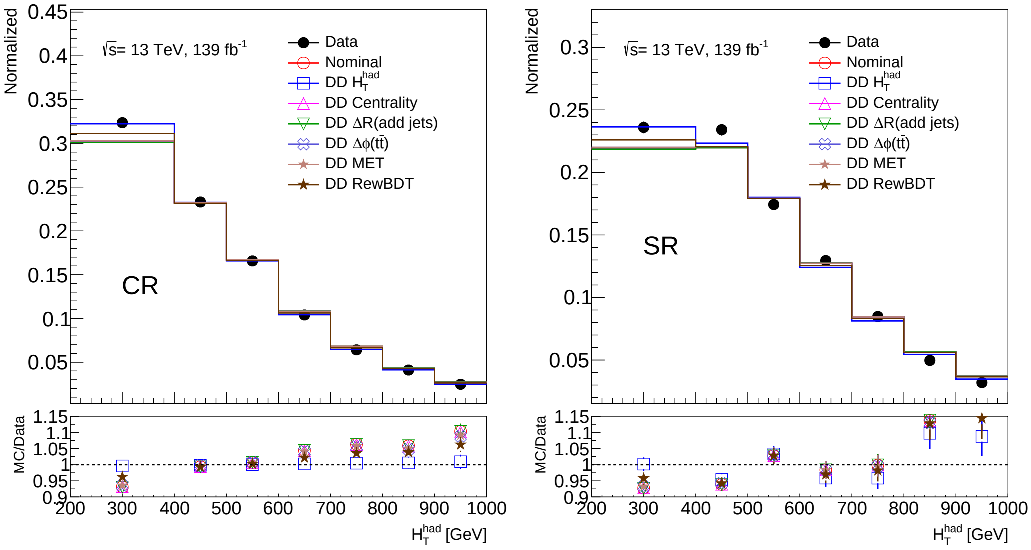

Figure 5.41.: Impact of the reweighting BDT correction on the modeling of the H_T distribution in the nominal prediction compared to that from other variables corrections, in the CR (left) and SR (right). The correction factors are derived using real $t\bar{t}$ data.

extrapolation of the data-driven correction from the CR to the SR are decorrelated among the $t\bar{t}+\geq 1b$, $t\bar{t}+\geq 1c$ and $t\bar{t}$ + light components. In order not to duplicate the use of events which were utilized to extract the correction factors, the ≥ 6 jets CR is dropped when these are applied prior to the fit.

To gauge the impact of adopting the data-driven $t\bar{t}$ estimate on the pulls introduced by the likelihood fit to correct for the $t\bar{t}$ modeling, two Background-only (B-only) fit models are compared: "MC" and "DD". The configuration setup of these models in terms of the $t\bar{t}$ prediction considered, analysis regions and fit inputs are summarized in Table 5.6. The data-driven $t\bar{t}$ prediction used in the "DD" fit setup is obtained by applying the correction factors derived for the H_T^{had} variable; these correction factors correct both the normalization and shape of the H_T^{had} distribution to match that in $t\bar{t}$ data in the CR.

Configuration \ Label	MC	DD
$t\bar{t}$ prediction	MC	data-driven, H_T^{had} correction
Regions	All regions	All regions,except ≥ 6 jets CR
Data B-only fit input	H_T^{had} everywhere	

Table 5.6.: The configuration setup of the two fit models compared to assess the impact of the data-driven $t\bar{t}$ method (see text). The data-driven $t\bar{t}$ prediction used in the "DD" fit is obtained by correcting the H_T^{had} observable.

Figures 5.42 and 5.43 show the best fit values of the modeling and instrumental nuisance parameters, respectively, obtained after the B-only fits to data for the two setups mentioned above; the associated uncertainties relative to their nominal values, are also displayed. Some of the nuisance parameters associated with the corrected systematic variations, namely the instrumental ones, have their pulls reduced in the case of the "DD" fit model compared to the MC model e.g. the $t\bar{t}$ + light and $t\bar{t}+\geq 1c$ NLO generator and radiation systematics, the b-jets Eigen Vector 0 and the JES flavor composition systematics. Larger pulls are observed, however, for the $t\bar{t}+\geq 1b$ NLO generator and parton shower as well as the light-jet EV 0 systematics, in the case of the "DD" fit. Although some systematics exhibit larger pulls, a general reduction of pulls for many systematics is observed. Further investigation of the fit results and tuning of the data-driven method is needed to achieve a wider reduction of the pulls.

The preliminary tests performed above to probe the impact of the data-driven $t\bar{t}$ method on the analysis robustness yield promising results. However, this method is still in its early stages and extensive studies are required to establish it as baseline in the $t\bar{t}H(H \to b\bar{b})$ analysis. In particular, the effect of multiple correction variables including the reweighting BDT need to be checked in the fit machinery and compared to assess the dependence of the analysis robustness on the chosen correction variable. The impact of the data-driven $t\bar{t}$ method on the sensitivity to the signal needs to be quantified as well. Moreover, the CR definition should be optimized taking into account the trade-off between the statistical uncertainties on the derived correction factors and the bias introduced by the chosen b-tagging selection cuts.

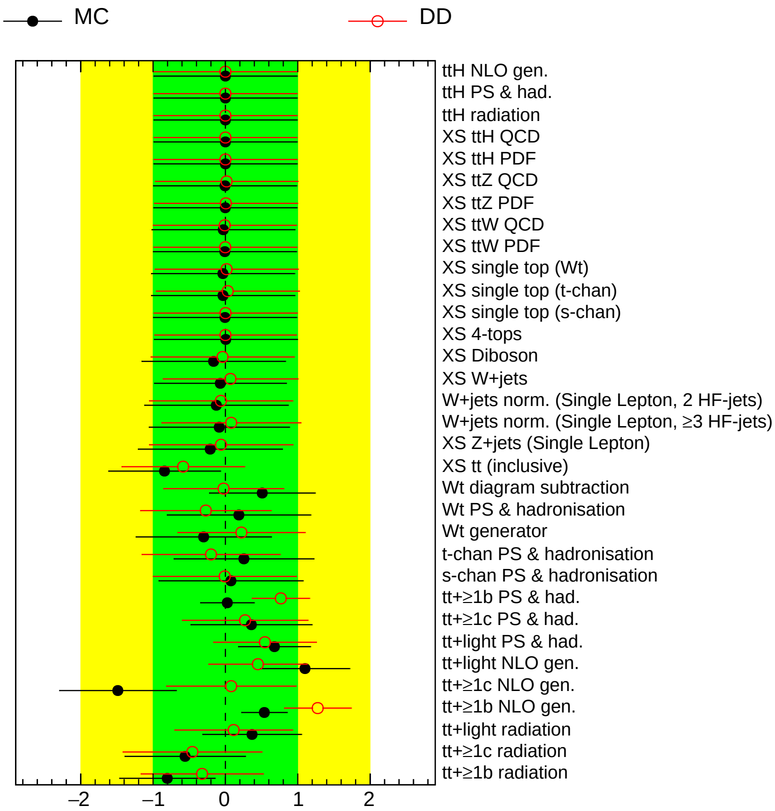

Figure 5.42.: Post-fit theoretical systematic uncertainties obtained from B-only fits to data comparing two models: the MC-based $t\bar{t}$ prediction is used in the "MC" model whereas the data-driven $t\bar{t}$ estimate is used in the "DD" model. The green (yellow) area represents the $\pm 1(2)$ band on the pre-fit systematic uncertainty. The position of the points and the size of the associated horizontal bars give the pulls and constraints in units of standard deviation, respectively.

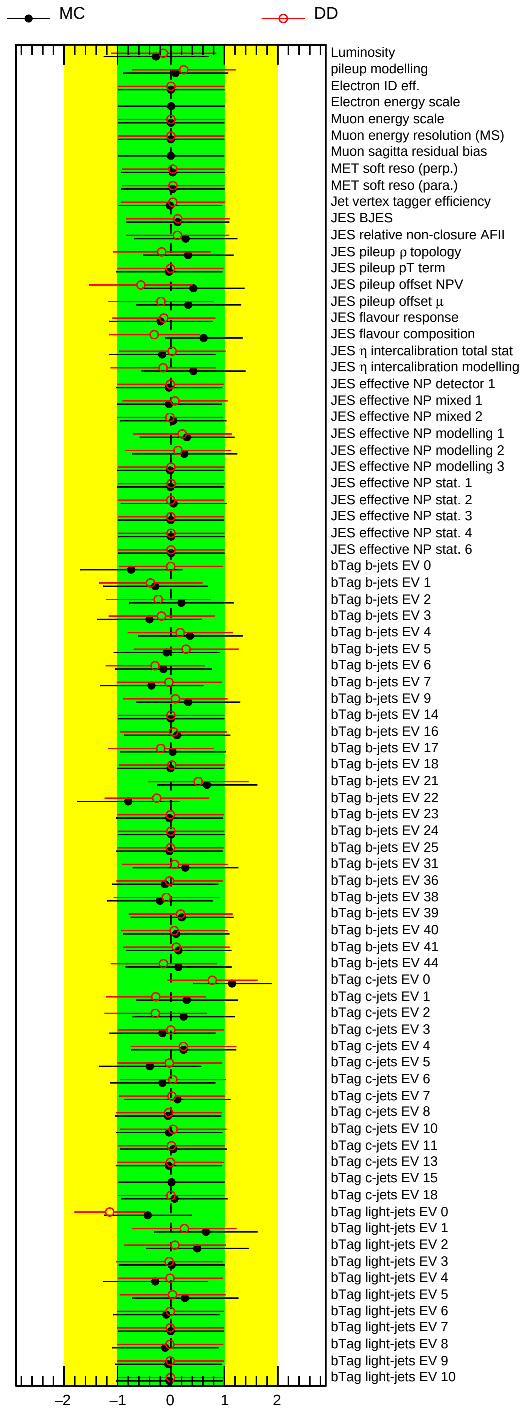

Figure 5.43.: Post-fit instrumental systematic uncertainties obtained from fits to data comparing two models: the MC-based $t\bar{t}$ prediction is used in the "MC" model whereas the data-driven $t\bar{t}$ estimate is used in the "DD" model. The green (yellow) area represents the ±1(2) band on the pre-fit systematic uncertainty. The position of the points and the size of the associated horizontal bars give the pulls and constraints in units of standard deviation, respectively.

5.3.4. Feasibility of measuring the Higgs boson p_T in the $t\bar{t}H(H \to b\bar{b})$ channel

5.3.4.1. Motivation

The measurement of the Higgs boson p_T in the $t\bar{t}H$ production mode is of great interest as it allows to probe the CP structure of the Higgs boson coupling to the top quark [148]. Figure 5.44, shows the Higgs boson p_T distributions normalized to unity and to the total cross-section for three scenarios of the $t\bar{t}H$ system interaction: the CP even case which corresponds to the SM expectation ($a_t = 1$, $b_t = 0$)[d], the CP odd or pseudo-scalar case ($a_t = 0$, $b_t = 1$) and the CP-violating ($a_t = 1$, $b_t = 1$) case; the two latter scenarios are allowed in many extensions of the SM. Some distinct features can be discerned in these distributions. The p_T spectrum in the CP odd case is harder with respect to the SM scenario while for the same coupling magnitude the cross-section of the former is suppressed compared to the scalar case. Hence, the Higgs boson p_T spectrum is a useful observable to measure as it has the potential to discriminate among these different scenarios and can be exploited for instance to reveal CP-violating effects in the Higgs-top coupling and constrain BSM models. In addition to exploring the CP nature of the Higgs boson, this observable can also serve to put limits on the Higgs self-coupling [149].

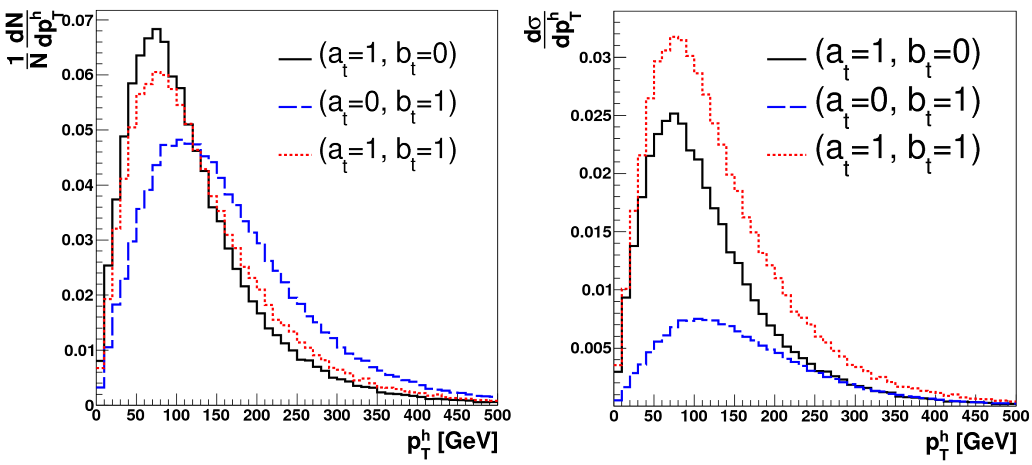

Figure 5.44.: The Higgs boson transverse momentum distribution normalized to unity (left) and to the total cross-section (right). Three scenarios are compared: SM case ($a_t = 1$, $b_t = 0$), pseudo-scalar ($a_t = 0$, $b_t = 1$) , and CP-violating case ($a_t = 1$, $b_t = 1$) [148].

The contribution of the $t\bar{t}H(H \to b\bar{b})$ channel to the differential measurements of the Higgs boson properties is of key importance. Firstly, it benefits from a large enough production rate to tackle even the high p_T regime compared e.g to the $t\bar{t}H$ ($H \to \gamma\gamma$) channel [146]. Secondly, it can profit from a good reconstruction of the Higgs boson thanks to the development and optimization of a dedicated reconstruction BDT (see section 5.2.3.2), as opposed to the $t\bar{t}H$ multilepton channel [145] in which the Higgs boson reconstruction is challenging due to the abundance of neutrinos in the final states probed in this channel.

[d] a_t, b_t are coefficients parameterizing the relative contributions of the CP even and CP odd components of the Higgs-top coupling, respectively.

5.3.4.2. Simplified template cross-sections framework (STXS)

Simplified template cross-sections (STXS) [150] have been adopted by the LHC experiments as a common framework to evolve the Higgs boson signal strength measurements performed during Run 1 of the LHC. On one hand, they provide more finely-granular measurements for specific Higgs boson production modes in exclusive kinematic regions referred to as "bins". This allows to reduce the theoretical uncertainties which are directly folded into the measurements. On the other hand, STXS grants a common framework for the combination of measurements in different decay channels and ultimately between experiments. STXS measurements can then be used as inputs for subsequent interpretations both in and beyond the SM.

STXS measurements were already carried out successfully in individual and in combinations of several Higgs boson decay channels. They were performed with the so called "stage 1.0" kinematic bins definitions designed for Run 1 measurements. However, these definitions needed to be revised for the different Higgs boson production modes in view of the Run 2 measurements as reported in ref [150], in which they are referred to as "stage 1.1" bins. For the $t\bar{t}H$ production mode, a split in the Higgs boson p_T is considered, but at the time of writing, "stage 1.1" bins for this mode have not been determined yet as dedicated studies are required to define the optimal binning boundaries. In this regard I tested several binning scenarios in the $t\bar{t}H(H \to b\bar{b})$ channel checking in each case the expected sensitivity, as discussed in Section 5.3.4.4, in order to find an optimal binning.

5.3.4.3. Higgs boson p_T-based event categorization

To assess the feasibility of measuring the Higgs boson p_T in the $t\bar{t}H(H \to b\bar{b})$ channel, I adapted the regions definition of the baseline single lepton analysis presented in Section 5.3.1, to test various binning scenarios with two and three bins in p_T. For these setups, the $t\bar{t}H$ signal sample is split based on the value of the truth Higgs boson p_T resulting in either two or three components in accordance with the probed STXS binning scenario. Each of these components has a signal strength parameter associated with it. To reach a good sensitivity on the measured signal strength per p_T bin, it is essential to disentangle the contributions of the different $t\bar{t}H$ components into separate analysis regions. This is achieved by redistributing events in the ≥ 6 jets signal regions i.e in the 4b@70(not@60) and 4b@60 regions into kinematic bins defined by the reconstructed Higgs boson p_T. The boundaries of these p_T bins are chosen to match those used to split the $t\bar{t}H$ signal sample. The remaining event categories are kept the same as in the baseline analysis. A good separation between the different $t\bar{t}H$ p_T components can be attained with this categorization thanks to the high correlation ($\sim 70\%$) between the truth and reconstructed Higgs boson p_T as illustrated in Figure 5.45.

5.3.4.4. Sensitivity for the Higgs boson p_T measurement

The expected uncertainty on the signal strength measurement in the exclusive Higgs boson p_T bins is assessed via Asimov fits. In these likelihood fits, the classification BDT distribution is used as discriminant in the signal regions whereas the H_T^{had} distribution is employed in the control regions. Figures 5.46 and 5.47 show the classification BDT distributions in the ≥ 6 jets signal regions for scenarios with two and three p_T bins, respectively; the signal regions are defined following the categorization approach described in Section 5.3.4.3. As expected, a good separation between the $t\bar{t}H$ signal components is achieved: low Higgs p_T regions are more populated by the low p_T $t\bar{t}H$ slice compared to the other p_T components whereas high Higgs p_T regions are dominated by the high p_T $t\bar{t}H$ component.

A fairly good level of sensitivity is achieved for the measurement of the Higgs boson p_T in the $t\bar{t}H(H \to b\bar{b})$ channel. In particular, for a scenario with three bins in the p_T defined as follows [0-150,150-250,250-∞[, the uncertainty is expected to be around 50% on the low p_T, 70% on the

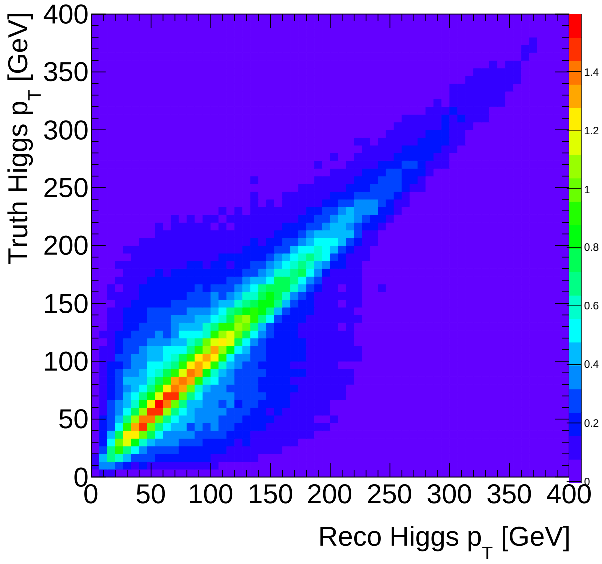

Figure 5.45.: Truth versus reconstructed Higgs boson p_T in the nominal $t\bar{t}H$ signal sample. Only single lepton events with $\geq$ 6 jets and $\geq$4 b-tagged jets at the 70% working point are considered.

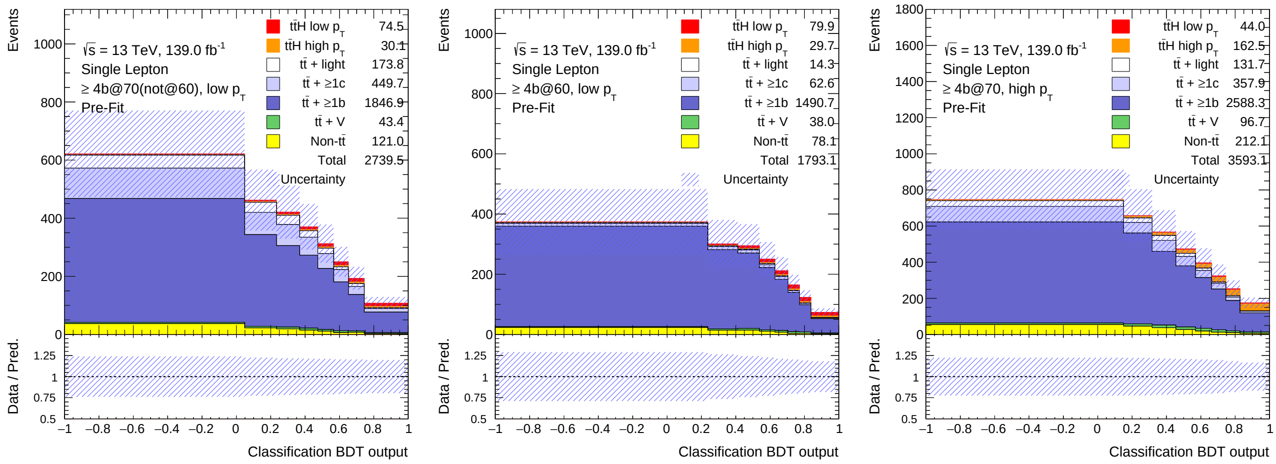

Figure 5.46.: Classification BDT distributions in the low Higgs p_T (left and middle) and high Higgs p_T (right) regions used as input to the Asimov fit for the following binning scenario: [0-120,120-∞[; the bin boundary is quoted in GeV .

medium p_T and 60% on the high p_T signal strengths. The anti-correlation among the signal strengths is quite small (up to 13% in the nearsest bins) which points to the small bin to bin migrations of the signal p_T components. This is due to the good purity of the Higgs boson reconstruction method in the $t\bar{t}H(H \to b\bar{b})$ analysis resulting in the good sensitivity achieved across the p_T bins. These results demonstrate that the attained degree of precision in the signal strength measurement remains quite good when evolving the baseline analysis with one bin in p_T, where the precision is around ~ 30%, towards the STXS version probed above. Furthermore, the level of constraints on the theory and instrumental nuisance parameters was found to be compatible between the baseline analysis and the STXS variant.

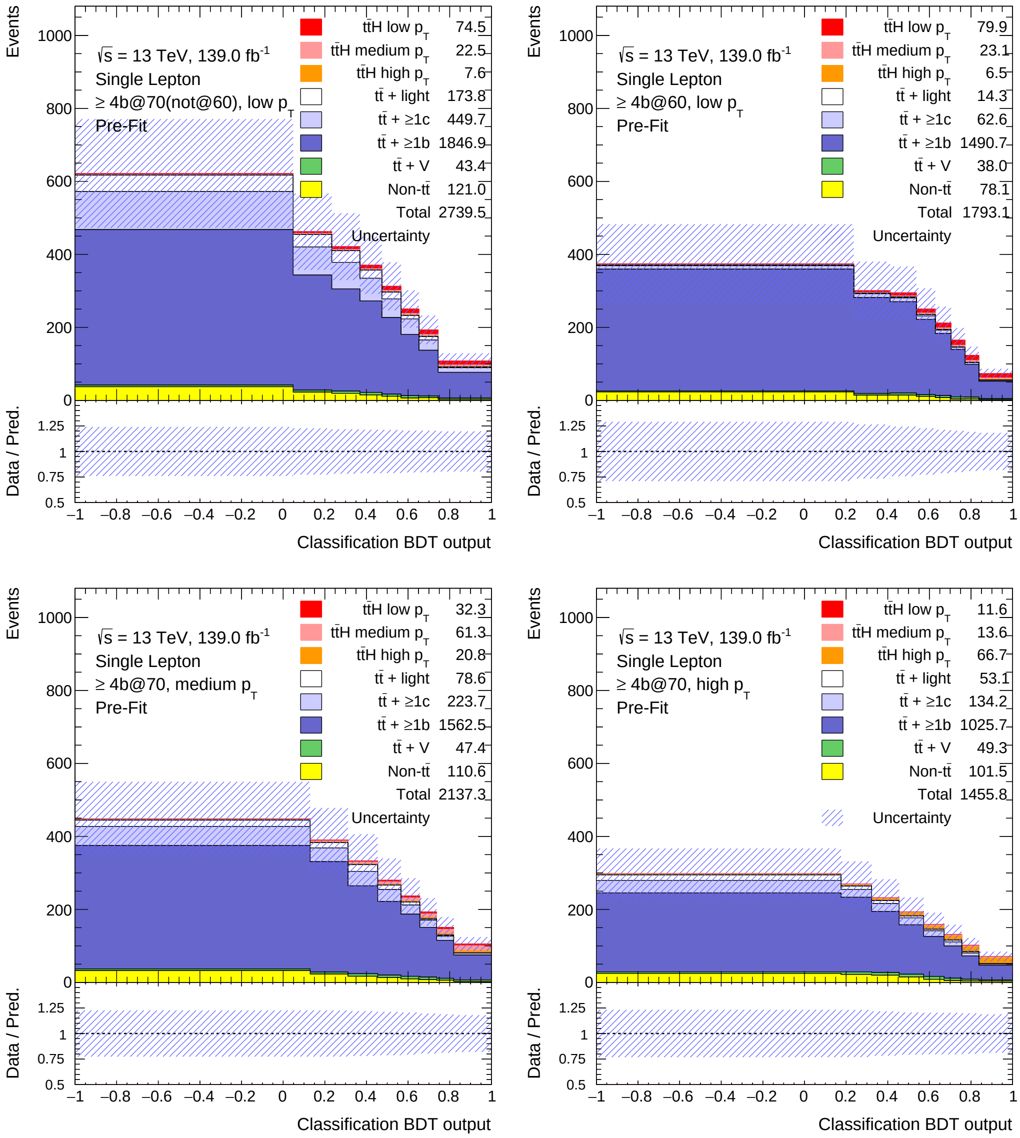

Figure 5.47.: Classification BDT distributions in the low Higgs p_T (upper row) and medium and high Higgs p_T (bottom row) regions used as input to the Asimov fit for the following binning scenario: [0-120,120-200,200-∞[; the bins boundaries are quoted in GeV .

Several scenarios with two and three bins in the Higgs boson p_T were tested. Tables 5.7 and 5.8 summarize the expected errors on the signal strengths corresponding to the exclusive Higgs boson p_T bins and the correlations among these signal strengths, respectively, for each of the tested scenarios. The p_T binning discussed above was found to yield the most uniform sensitivity distribution across the p_T bins among the tested three bins scenarios.

p_T boundaries [GeV]	low p_T bin	medium p_T bin	high p_T bin
120	+0.64,-0.58	–	+0.42,-0.38
150	+0.57,-0.52	–	+0.43,-0.39
100,200	+0.79,-0.72	+0.68,-0.63	+0.52,-0.48
120,200	+0.62,-0.58	+0.86,-0.79	+0.52, -0.48
150,250	+0.55,-0.50	+0.69,-0.63	+0.62,-0.56
150,300	+0.56,-0.51	+0.56,-0.50	+0.78,-0.70

Table 5.7.: Expected upper (positive) and lower (negative) errors on the signal strengths associated with the exclusive Higgs boson p_T bins for the tested binning scenarios. For scenarios with two bins in the Higgs boson p_T only one boundary value x separating the low and high p_T bins is quoted such that the corresponding binning is $[0\text{-}x, x\text{-}\infty[$. Two boundary values ($x_1$, x_2) are quoted for scenarios with three bins in the Higgs boson p_T i.e $[0\text{-}x_1, x_1\text{-}x_2, x_2\text{-}\infty[$.

p_T boundaries [GeV]	120	150	100,200	120,200	150,250	150,300
(low,medium) μ correl.	–	–	-11.2	-7.4	-0.8	5.2
(low,high) μ correl.	0.1	-4.7	-0.5	1.9	0.3	-9.1
(medium,high) μ correl	–	–	-18.6	-20.7	-12.4	-12.5

Table 5.8.: Linear correlation coefficients among the signal strengths associated with the exclusive Higgs boson p_T bins as assessed by the Asimov fits. For scenarios with two bins in the Higgs boson p_T only one boundary value x separating the low and high p_T bins is quoted such that the corresponding binning is $[0\text{-}x, x\text{-}\infty[$. Two boundary values ($x_1$, x_2) are quoted for scenarios with three bins in the Higgs boson p_T i.e $[0\text{-}x_1, x_1\text{-}x_2, x_2\text{-}\infty[$. The quoted values are in percentage.

5.4. Summary

The $t\bar{t}H(H \to b\bar{b})$ channel grants direct access to the top quark Yukawa coupling which is the strongest in the SM. The search for $t\bar{t}H(H \to b\bar{b})$ production using 36.1 fb^{-1}of 13 TeV data recorded by the ATLAS detector in 2015 and 2016 is presented. The major challenge of this analysis is the overwhelming background of $t\bar{t}$ + jets production, and more importantly the $t\bar{t}+\geq 1b$ component. Hence, controlling this background is an important aspect of the $t\bar{t}H(H \to b\bar{b})$ analysis. A plethora of MC predictions are available for the $t\bar{t}+\geq 1b$ background with sizable differences among them especially in the phase space probed by the analysis. This in turn leads to large modeling uncertainties attributed to this background. In this respect, I performed extensive modeling studies comparing the various $t\bar{t}+\geq 1b$ predictions, namely the 5FS and 4FS computations, in order to assess the differences among them and gain more confidence in the complex systematic model built for this background. The results of the $t\bar{t}H(H \to b\bar{b})$ search yielded a combined signal strength of $\mu = 0.84^{+0.64}_{-0.61}$ for the single lepton and dilepton channels with an observed (expected) significance of 1.4 (1.6) σ. The two leading sources of systematic uncertainties limiting the sensitivity of the search were found to be the large $t\bar{t}+\geq 1b$ modeling uncertainties and the sizable statistical fluctuations induced by the limited amount of the generated $t\bar{t}$ + HF events. Reducing the impact of these systematics is the main focus of the ongoing round of the $t\bar{t}H(H \to b\bar{b})$ analysis aiming to reach an evidence using the full Run 2 data.

To mitigate the impact of the limited size of the $t\bar{t}$ + HF MC samples, I developed new Heavy Flavor filters with optimized selection criteria to increase the number of simulated $t\bar{t}+\geq 1b$ and $t\bar{t}+\geq 1c$ events especially in the signal phase space region. These filters were adopted to produce the $t\bar{t}$ + jets MC samples used in the current round of the analysis. Making use of the filtered samples allows to reduce the relative statistical uncertainty by more than 70%, for instance, in the signal regions with 4 b-tagged jets at the 60% working point.

The $t\bar{t}$ + jets background is poorly described by the available MC predictions in the phase of interest for the analysis. Improving its modeling prior to the likelihood fit is essential to increase the robustness of the analysis. In this line, I put in place an alternative method to estimate this background based on data with less dependence on the MC prediction. This method consists in deriving correction factors in a chosen control region where $t\bar{t}$ data and MC predictions are compared and applying these corrections to the predictions in the signal regions. Preliminary tests yielded promising results for this method in terms of reducing the size of the differences between the available predictions of the $t\bar{t}$ + jets background and improving its modeling. However more studies are needed to validate this method and establish it as a baseline in the analysis. In particular, the challenges of the data-driven method reside in the appropriate definition of the control region as well as the choice of the variable in which global correction factors are extracted. For the latter, I developed a variable referred to as the *reweighting BDT* which has the potential to correct the MC predictions in many kinematic distributions as opposed to simple variables which only correct the corresponding distribution and can lead to worse agreement in others.

With the full Run 2 data becoming available, it is possible to measure the differential production cross-section of the Higgs boson as a function of the Higgs boson kinematics. These measurements can be used, for instance, to probe the CP structure of the Higgs boson coupling to the top quark and constrain BSM models that predict CP violating effects. The $t\bar{t}H(H \to b\bar{b})$ channel is expected to play a key role in these measurements as it benefits from a larger production rate compared to the other $t\bar{t}H$ channels. In this respect, I developed the analysis with an adapted event categorization for the measurement of the Higgs boson p_T in the $t\bar{t}H(H \to b\bar{b})$ channel. I assessed the expected sensitivity of this measurement for various binning scenarios of the Higgs boson p_T. The level of sensitivity reached was found to be quite promising. In particular, the expected precision ranges between 50% and 70% for a binning scenario of [0-150,150-250,250-∞[GeV while it amounts to 30% in the baseline analysis with one bin in p_T. The encouraging level of sensitivity achieved is mainly due to the good purity of the Higgs boson reconstruction method in the $t\bar{t}H(H \to b\bar{b})$ analysis.

Conclusion

The Higgs boson discovery in July 2012 by the ATLAS and CMS collaborations at the Large Hadron Collider (LHC) was an exceptional triumph for the Standard Model (SM). Since the discovery, the main goal of the LHC shifted towards the measurement of the properties of the newly found particle, such as its couplings to fermions, in order to establish its compatibility with the SM predictions. In particular, the top quark Yukawa coupling is of special interest as it is the largest in the SM and has a key role in the SM stability at high energies: a significant deviation in this coupling from its SM expectation would indicate the existence of new physics lying beyond the SM. The associated production of the Higgs boson with a pair of top quarks ($t\bar{t}H$) grants direct access to the top quark Yukawa coupling and allows to measure it in a model independent way. This production mode, however, was not established with the LHC Run 1 data and its observation became one of the main targets of the LHC Run 2 program.

This thesis presented the search for $t\bar{t}H$ events where the Higgs boson subsequently decays into a pair of bottom quarks ($t\bar{t}H(H \rightarrow b\bar{b})$). The search was performed using 36.1 fb^{-1}of proton-proton collision data at a center-of-mass energy of 13 TeV recorded by the ATLAS detector in 2015 and 2016. The major challenge of this analysis is the dominating background of $t\bar{t}$ production with additional jets ($t\bar{t}$ + jets), especially when these are b-jets ($t\bar{t}+\geq 1b$). Several Monte Carlo (MC) predictions are available for this background, however, they exhibit sizable differences especially in the phase space targeted by the analysis. In this regard, I conducted detailed studies comparing the modeling of $t\bar{t}$+jets among the various predictions available to assess these differences and gain more confidence in the systematic model designed for this background. The results of the search yielded a signal strength of $\mu = 0.84^{+0.64}_{-0.61}$ corresponding to a 1.4 σ excess of signal events over the background only hypothesis in data while 1.6 σ were expected. Although the $t\bar{t}H(H \rightarrow b\bar{b})$ production mode is not established at this stage, the combination of these results with those from other $t\bar{t}H$ channels using up to 80 fb^{-1}of collision data led to the observation of the $t\bar{t}H$ production for the first time. The $t\bar{t}H(H \rightarrow b\bar{b})$ analysis sensitivity is primarily limited by the systematic component of the total uncertainty on the reconstructed signal. The leading sources of this component are identified to be the large modeling uncertainties on the $t\bar{t}+\geq 1b$ background followed by the sizable statistical uncertainties associated with the simulated $t\bar{t}+\geq 1b$ and $t\bar{t}+\geq 1c$ events ($t\bar{t}$ + HF). Tackling these systematics is the main focus of the ongoing round of the $t\bar{t}H(H \rightarrow b\bar{b})$ analysis aiming to reach an evidence using the full Run 2 data.

My contribution to the ongoing round of the $t\bar{t}H(H \rightarrow b\bar{b})$ analysis addresses the aforementioned systematic uncertainties. To reduce the impact of the statistical fluctuations induced by the limited amount of $t\bar{t}$+HF events generated, I developed new Heavy Flavor filters and optimized their selection criteria to increase the number of simulated $t\bar{t}+\geq 1b$ and $t\bar{t}+\geq 1c$ events especially in the signal phase space. These filters were used to produce the $t\bar{t}$ + jets MC samples used in the current round of the analysis and allowed to reduce the relative statistical uncertainty by more than 70% in the signal regions with 4 b-tagged jets at the 60% b-tagging efficiency working point. On the other hand, to improve the modeling of the $t\bar{t}$ + jets background which is poorly described by the MC predictions available, and to increase the robustness of the analysis, I explored an alternative method to estimate this background based on data with less dependence on MC. The data-driven method consists in extracting correction factors for a given observable in a chosen control region where $t\bar{t}$ data and MC predictions are compared and subsequently applying these corrections to the predictions in the signal regions. Tests of this method yield encouraging preliminary results as it is able to improve the modeling of $t\bar{t}$ + jets prior to the likelihood fit and reduce the differences between the various predictions. However, more studies are needed to validate this method before adopting it as the baseline in the analysis. In particular, special care should be given to the control region definition and the choice of the variable to use for deriving the correction factors. Regarding the observable choice, I developed a variable referred to as the *reweighting BDT* which would be a good candidate to derive global correction factors allowing to improve the modeling of many kinematic distributions in the MC predictions at once.

The large dataset collected by the ATLAS detector during Run 2, amounting to an integrated luminosity of 139 fb^{-1}, allows to measure the $t\bar{t}H(H \to b\bar{b})$ production cross-section with a precision of 30%. Furthermore, the full Run 2 data opens the possibility for measuring the differential properties of the Higgs boson. These measurements would allow, for instance, to probe the CP structure of the Higgs-top interaction and constrain new physics models. The $t\bar{t}H(H \to b\bar{b})$ channel is expected to play a key role in these measurements as it benefits from a larger production rate compared to the remaining $t\bar{t}H$ channels. In this regard, I developed the analysis for measuring the Higgs boson transverse momentum (p_T) in the $t\bar{t}H(H \to b\bar{b})$ channel. Furthermore, I assessed the sensitivity of this measurement as a function of the Higgs boson p_T. The expected precision ranges between 50% and 80% for $p_T < 150$ GeV and $p_T > 200$ GeV ; this encouraging level of sensitivity is achieved thanks to the good purity of the Higgs boson reconstruction method developed for the $t\bar{t}H(H \to b\bar{b})$ analysis. These studies give access for the first time to information about the Higgs boson p_T in the $t\bar{t}H$ channel.

While adopting a data-driven method to estimate the challenging $t\bar{t}b\bar{b}$ background is a promising approach to enhance the $t\bar{t}H(H \to b\bar{b})$ analysis sensitivity in the short term, it is crucial to improve the MC modeling of this process for the longer term prospects of the analysis. To this end, measurements of the $t\bar{t}b\bar{b}$ production cross-section are highly awaited as they provide valuable inputs to better understand the modeling of this process and identify which of the predictions are best at describing data. The analysis performed to measure the inclusive and differential production cross-section of $t\bar{t}b\bar{b}$ in both the single lepton and dilepton channels, using the 36.1 fb^{-1}dataset was also presented in this thesis. The measured differential cross-sections are unfolded to the particle level in a well defined fiducial volume. I carried out detailed simulation studies to assess the purity of the selected $t\bar{t}b\bar{b}$ sample prior to the unfolding procedure in the single lepton channel. The predicted cross-sections were found to be all in agreement with data within uncertainties. Furthermore, the considered differential distributions do not yield enough differences for the data to favor a particular set of MC predictions. This is why, I proposed a method to improve the sensitivity of these measurements for future iterations of the analysis. The method consists in explicitly identifying the b-jets origin based on the reconstruction of the $t\bar{t}$ system using a Boosted Decision Tree. This approach allows to highlight the differences between the predictions in the distributions corresponding to the b-jets as opposed to assuming the origin based on their kinematics.

The identification of jets originating from b-quarks, referred to as b-tagging, plays a crucial role in many physics analyses at the LHC and by extension also at the foreseen High Luminosity LHC (HL-LHC). The b-tagging algorithms widely used in ATLAS rely heavily on the tracking information provided by the Inner Detector and were optimized based on its design. However, the Inner Detector will be entirely replaced by the Inner Tracker (ITk) for operation under the extreme conditions of HL-LHC with up to 200 pile-up collisions per bunch-crossing. The studies that I performed to optimize the b-tagging algorithms to be in line with the new tracker geometry were also presented. Namely, a new optimal track categorization was put in place for the impact-parameter (IP) based algorithms (IP3D) to reflect the ITk geometry. The reference histograms used as input for the computation of the IP b-tagging discriminants for ITk were updated based on the new categorization. Making use of this classification enhances significantly the background rejection compared to the Run 2 categorization for the IP3D tagger: the light-jet rejection is doubled at the 70% b-tagging efficiency working point. The MV2c10 tagger was retrained taking into account the categorization optimization and its performance was also improved compared to the Run 2 setup. The b-tagging performance of the ITk was characterized based on these optimizations and was shown to surpass that of the Inner Detector despite the harsher pile-up conditions. Additionally, to characterize the ITk layout, the robustness of the optimized taggers response was gauged against various HL-LHC pile-up configurations and ITk dead pixel modules scenarios. A degradation in the performance of the *b*-tagging algorithms is observed at lower pile-up e.g a drop of around 30% in the IP3D light-jet rejection at the 70% working point is noticed for the 0 pile-up interaction case with respect to the nominal case of 200 interactions. This artificial loss of performance was found to be mitigated if the pile-up conditions are taken into account when extracting the IP reference histograms and training the MV2c10 BDT. Similarly, the degradation in performance induced by potential failures in the ITk pixel detector modules is partially reduced when the detector conditions are accounted for in deriving the IP reference histograms and training the MV2c10 BDT; for instance, the 40 % drop in the IP3D light-jet rejection at the 70% working point is lessened to 20% in the scenario where 10% of the modules are not operational.

Bibliography

[1] S. L. Glashow, *Partial-symmetries of weak interactions*, Nuclear Physics **22** (1961) p. 579 (cit. on p. 33).

[2] A. Salam and J. Ward, *Electromagnetic and weak interactions*, Physics Letters **13** (1964) p. 168 (cit. on p. 33).

[3] S. Weinberg, *A Model of Leptons*, Phys. Rev. Lett. **19** (21 1967) p. 1264 (cit. on p. 33).

[4] Patrignani, C. *et al.* (Particle Data Group), *Review of Particle Physics*, Chin. Phys. **C40** (2016) p. 100001 (cit. on pp. 33, 34).

[5] M. E. Peskin and D. V. Schroeder, *An introduction to quantum field theory*, Westview, 1995, URL: `https://cds.cern.ch/record/257493` (cit. on p. 34).

[6] F. Englert and R. Brout, *Broken Symmetry and the Mass of Gauge Vector Mesons*, Phys. Rev. Lett. **13** (9 1964) p. 321 (cit. on pp. 35, 36).

[7] P. Higgs, *Broken symmetries, massless particles and gauge fields*, Physics Letters **12** (1964) p. 132 (cit. on pp. 35, 36).

[8] P. W. Higgs, *Broken Symmetries and the Masses of Gauge Bosons*, Phys. Rev. Lett. **13** (16 1964) p. 508 (cit. on pp. 35, 36).

[9] G. Rajasekaran, *Fermi and the Theory of Weak Interactions*, arXiv e-prints (2014), arXiv: `1403.3309 [physics.hist-ph]` (cit. on p. 35).

[10] P. A. M. Dirac, *The Quantum Theory of the Emission and Absorption of Radiation*, Proceedings of the Royal Society of London A: Mathematical, Physical and Engineering Sciences **114** (1927) p. 243 (cit. on p. 35).

[11] E. Fermi, *Quantum Theory of Radiation*, Rev. Mod. Phys. **4** (1 1932) p. 87 (cit. on p. 35).

[12] F. J. Dyson, *The Radiation Theories of Tomonaga, Schwinger, and Feynman*, Phys. Rev. **75** (3 1949) p. 486 (cit. on p. 35).

[13] F. J. Dyson, *The S Matrix in Quantum Electrodynamics*, Phys. Rev. **75** (11 1949) p. 1736 (cit. on p. 35).

[14] R. P. Feynman, *Space-Time Approach to Non-Relativistic Quantum Mechanics*, Rev. Mod. Phys. **20** (2 1948) p. 367 (cit. on p. 35).

[15] R. P. Feynman, *Relativistic Cut-Off for Quantum Electrodynamics*, Phys. Rev. **74** (10 1948) p. 1430 (cit. on p. 35).

[16] J. A. Wheeler and R. P. Feynman, *Interaction with the Absorber as the Mechanism of Radiation*, Rev. Mod. Phys. **17** (2-3 1945) p. 157 (cit. on p. 35).

[17] J. Schwinger, *On Quantum-Electrodynamics and the Magnetic Moment of the Electron*, Phys. Rev. **73** (4 1948) p. 416 (cit. on p. 35).

[18] J. Schwinger, *Quantum Electrodynamics. I. A Covariant Formulation*, Phys. Rev. **74** (10 1948) p. 1439 (cit. on p. 35).

[19] F. L. Wilson, *Fermi's Theory of Beta Decay*, American Journal of Physics **36** (1968) p. 1150 (cit. on p. 35).

[20] T. D. Lee and C. N. Yang, *Question of Parity Conservation in Weak Interactions*, Phys. Rev. **104** (1 1956) p. 254 (cit. on p. 35).

[21] J. Goldstone, A. Salam, and S. Weinberg, *Broken Symmetries*, Phys. Rev. **127** (3 1962) p. 965 (cit. on p. 38).

[22] D. J. Griffiths, *Introduction to elementary particles; 2nd rev. version*, Physics textbook, Wiley, 2008, URL: https://cds.cern.ch/record/111880 (cit. on p. 38).

[23] The TEVNPH Working Group, f. t. CDF, and D0 Collaborations, *Combined CDF and D0 Search for Standard Model Higgs Boson Production with up to 10.0 fb-1 of Data*, arXiv e-prints (2012), arXiv: 1203.3774 [hep-ex] (cit. on p. 39).

[24] ALEPH Collaboration, DELPHI Collaboration, L3 Collaboration, OPAL Collaboration, The LEP Working Group for Higgs Boson Searches, *Search for the Standard Model Higgs boson at LEP*, Physics Letters B **565** (2003) p. 61 (cit. on p. 39).

[25] ATLAS Collaboration, *Observation of a new particle in the search for the Standard Model Higgs boson with the ATLAS detector at the LHC*, Physics Letters B **716** (2012) p. 1 (cit. on pp. 39, 43).

[26] CMS Collaboration, *Observation of a new boson at a mass of 125 GeV with the CMS experiment at the LHC*, Physics Letters B **716** (2012) p. 30 (cit. on pp. 39, 43).

[27] ATLAS Collaboration, *Measurements of the Higgs boson production and decay rates and coupling strengths using pp collision data at* $\sqrt{s} = 7$ *and* 8 *TeV in the ATLAS experiment*, The European Physical Journal C **76** (2016) p. 6 (cit. on p. 41).

[28] D. de Florian et al., *Handbook of LHC Higgs Cross Sections: 4. Deciphering the Nature of the Higgs Sector*, (2016), arXiv: 1610.07922 [hep-ph] (cit. on pp. 42, 45, 127).

[29] S. Heinemeyer, C. Mariotti, G. Passarino, et al., *Handbook of LHC Higgs Cross Sections: 3. Higgs Properties*, (CERN, Geneva, 2013), arXiv: 1307.1347 [hep-ph] (cit. on pp. 42, 127, 162).

[30] ATLAS and CMS Collaborations, *Measurements of the Higgs boson production and decay rates and constraints on its couplings from a combined ATLAS and CMS analysis of the LHC pp collision data at* $\sqrt{s} = 7$ *and* 8 *TeV*, Journal of High Energy Physics **2016** (2016) p. 45 (cit. on pp. 43, 44, 159).

[31] ATLAS Collaboration, *Observation of* $H \to b\bar{b}$ *decays and VH production with the ATLAS detector*, Physics Letters B **786** (2018) p. 59 (cit. on p. 43).

[32] CMS Collaboration, *Observation of Higgs Boson Decay to Bottom Quarks*, Phys. Rev. Lett. **121** (12 2018) p. 121801 (cit. on p. 43).

[33] CMS Collaboration, *Observation of* $t\bar{t}H$ *Production*, Phys. Rev. Lett. **120** (23 2018) p. 231801 (cit. on p. 44).

[34] ATLAS Collaboration, *Measurement of the Higgs boson mass in the* $H \to ZZ^* \to 4\ell$ *and* $H \to \gamma\gamma$ *channels with* $\sqrt{s}$*=13TeV pp collisions using the ATLAS detector*, Physics Letters B **784** (2018) p. 345, ISSN: 0370-2693 (cit. on p. 44).

[35] ATLAS and CMS Collaborations, *Combined Measurement of the Higgs Boson Mass in pp Collisions at* $\sqrt{s} = 7$ *and 8 TeV with the ATLAS and CMS Experiments*, Phys. Rev. Lett. **114** (19 2015) p. 191803 (cit. on p. 44).

[36] ATLAS Collaboration, "Combined measurements of Higgs boson production and decay using up to 80 fb^{-1} of proton–proton collision data at $\sqrt{s} = 13$ TeV collected with the ATLAS experiment," tech. rep. ATLAS-CONF-2019-005, CERN, 2019, URL: http://cds.cern.ch/record/2668375 (cit. on pp. 44, 45).

[37] ATLAS Collaboration,
Study of the spin and parity of the Higgs boson in diboson decays with the ATLAS detector,
The European Physical Journal C **75** (2015) p. 476, ISSN: 1434-6052 (cit. on p. 45).

[38] The ATLAS collaboration, *Measurement of the Higgs boson coupling properties in the $H \to ZZ^* \to 4\ell$ decay channel at $\sqrt{s}$=13TeV with the ATLAS detector*,
Journal of High Energy Physics **2018** (2018) p. 95, ISSN: 1029-8479 (cit. on p. 45).

[39] ATLAS Collaboration, *Constraints on off-shell Higgs boson production and the Higgs boson total width in $ZZ \to 4\ell$ and $ZZ \to 2\ell 2\nu$ final states with the ATLAS detector*,
Physics Letters B **786** (2018) p. 223 (cit. on p. 45).

[40] L. R. Evans and P. Bryant, *LHC Machine*, J. Instrum. **3** (2008) S08001. 164 p, This report is an abridged version of the LHC Design Report (CERN-2004-003),
URL: https://cds.cern.ch/record/1129806 (cit. on p. 46).

[41] O. S. Brüning, P. Collier, P. Lebrun, et al., *LHC Design Report*, CERN, 2004,
URL: https://cds.cern.ch/record/782076 (cit. on p. 46).

[42] p. c. W.J. Stirling, *Parton Luminosity and Cross-section plots*, (),
URL: http://www.hep.ph.ic.ac.uk/~wstirlin/plots/plots.html (cit. on p. 47).

[43] F. Marcastel, *CERN's Accelerator Complex. La chaîne des accélérateurs du CERN*,
(2013), General Photo, URL: https://cds.cern.ch/record/1621583 (cit. on p. 48).

[44] J.-L. Caron, "Cross section of LHC dipole.. Dipole LHC: coupe transversale.,"
AC Collection. Legacy of AC. Pictures from 1992 to 2002., 1998,
URL: https://cds.cern.ch/record/841539 (cit. on p. 49).

[45] R. Alemany-Fernandez, E. Bravin, L. Drosdal, et al.,
Operation and Configuration of the LHC in Run 1, (2013),
URL: https://cds.cern.ch/record/1631030 (cit. on p. 50).

[46] R. Bruce, G. Arduini, H. Bartosik, et al., "LHC Run 2: Results and Challenges,"
tech. rep. CERN-ACC-2016-0103, CERN, 2016, URL: https://cds.cern.ch/record/2201447
(cit. on p. 50).

[47] by Le groupe Opérations et Stéphane Fartoukh (BE-ABP) and C. Pralavorio,
Dernières nouvelles du LHC : luminosité record en 2017, (2017),
URL: http://cds.cern.ch/record/2295013 (cit. on p. 50).

[48] by Rende Steerenberg and A. Schaeffer, *LHC Report: Protons: mission accomplished*, (2018),
URL: http://cds.cern.ch/record/2645638 (cit. on p. 50).

[49] ATLAS, *Luminosity Public Results Run 2*, (), URL:
https://twiki.cern.ch/twiki/bin/view/AtlasPublic/LuminosityPublicResultsRun2
(cit. on p. 50).

[50] The ATLAS Collaboration, *The ATLAS Experiment at the CERN Large Hadron Collider*,
Journal of Instrumentation **3** (2008) S08003 (cit. on pp. 50, 53–60, 62).

[51] The CMS Collaboration, *The CMS experiment at the CERN LHC*,
Journal of Instrumentation **3** (2008) S08004 (cit. on p. 50).

[52] The LHCb Collaboration, *The LHCb Detector at the LHC*,
Journal of Instrumentation **3** (2008) S08005 (cit. on p. 50).

[53] The ALICE Collaboration, *The ALICE experiment at the CERN LHC*,
Journal of Instrumentation **3** (2008) S08002 (cit. on p. 51).

[54] LHCf Collaboration, *The LHCf detector at the CERN Large Hadron Collider*, Journal of Instrumentation **3** (2008) S08006 (cit. on p. 51).

[55] The TOTEM Collaboration, *The TOTEM Experiment at the CERN Large Hadron Collider*, Journal of Instrumentation **3** (2008) S08007 (cit. on p. 51).

[56] B. Acharya, J. Alexandre, J. Bernabeu, et al., *The Physics Programme Of The MoEDAL Experiment At The LHC*, Int. J. Mod. Phys. A **29** (2014) 1430050. mult. p, URL: `https://cds.cern.ch/record/1705285` (cit. on p. 51).

[57] ATLAS Collaboration, "Studies of the ATLAS Inner Detector material using $\sqrt{s}$ =13 TeV *pp* collision data," tech. rep. ATL-PHYS-PUB-2015-050, CERN, 2015, URL: `https://cds.cern.ch/record/2109010` (cit. on p. 54).

[58] G. Aad, M. Ackers, F. A. Alberti, et al., *ATLAS pixel detector electronics and sensors*, JINST **3** (2008) P07007 (cit. on p. 55).

[59] A. L. Rosa, *The ATLAS Insertable B-Layer: from construction to operation*, Journal of Instrumentation **11** (2016) p. C12036 (cit. on pp. 55, 56).

[60] University of Pennsylvania, *Transition Radiation Tracker - TRT*, (), URL: `http://www.hep.upenn.edu/atlas/trt/` (cit. on p. 57).

[61] The ATLAS Collaboration, *Drift Time Measurement in the ATLAS Liquid Argon Electromagnetic Calorimeter using Cosmic Muons*, The European Physical Journal C **70** (2010) p. 755 (cit. on p. 59).

[62] ATLAS Collaboration, *ATLAS experiment -Public results*, (), URL: `https://twiki.cern.ch/twiki/bin/view/AtlasPublic/ApprovedPlotsDAQ` (cit. on p. 63).

[63] J. C. Collins, D. E. Soper, and G. F. Sterman, *Factorization of Hard Processes in QCD*, Adv. Ser. Direct. High Energy Phys. **5** (1989) p. 1, arXiv: `hep-ph/0409313 [hep-ph]` (cit. on p. 64).

[64] M. Dobbs and J. B. Hansen, *The HepMC C++ Monte Carlo event record for High Energy Physics*, Comput. Phys. Commun. **134** (2001) p. 41 (cit. on p. 64).

[65] S. Frixione and B. R. Webber, *Matching NLO QCD computations and parton shower simulations*, JHEP **0206** (2002) p. 029 (cit. on pp. 64, 162).

[66] P. Nason, *A New method for combining NLO QCD with shower Monte Carlo algorithms*, JHEP **0411** (2004) p. 040 (cit. on pp. 64, 87, 127).

[67] S. Frixione, P. Nason, and C. Oleari, *Matching NLO QCD computations with Parton Shower simulations: the POWHEG method*, JHEP **0711** (2007) p. 070 (cit. on pp. 64, 87, 127).

[68] S. Alioli, P. Nason, C. Oleari, et al., *A general framework for implementing NLO calculations in shower Monte Carlo programs: the POWHEG BOX*, JHEP **1006** (2010) p. 043 (cit. on pp. 64, 87, 127).

[69] S. Höche, F. Krauss, M. Schönherr, et al., *QCD matrix elements + parton showers: The NLO case*, JHEP **04** (2013) p. 027 (cit. on pp. 64, 127).

[70] S. Catani, F. Krauss, B. R. Webber, et al., *QCD Matrix Elements + Parton Showers*, Journal of High Energy Physics **2001** (2001) p. 063 (cit. on p. 65).

[71] M. L. Mangano, M. Moretti, F. Piccinini, et al., *Matching matrix elements and shower evolution for top-pair production in hadronic collisions*, Journal of High Energy Physics **2007** (2007) p. 013 (cit. on p. 65).

[72] T. Sjöstrand, S. Mrenna, and P. Z. Skands, *PYTHIA 6.4 Physics and Manual*, JHEP **0605** (2006) p. 026 (cit. on p. 65).

[73] T. Sjöstrand, S. Mrenna, and P. Z. Skands, *A Brief Introduction to PYTHIA 8.1*, Comput. Phys. Commun. **178** (2008) p. 852 (cit. on p. 65).

[74] M. Bähr, S. Gieseke, M. A. Gigg, et al., *Herwig++ physics and manual*, The European Physical Journal C **58** (2008) p. 639 (cit. on pp. 65, 142, 166).

[75] J. Bellm, S. Gieseke, D. Grellscheid, et al., *Herwig 7.0/Herwig++ 3.0 release note*, The European Physical Journal C **76** (2016) p. 196 (cit. on pp. 65, 127).

[76] S. Agostinelli et al., *GEANT4: A Simulation toolkit*, Nucl. Instrum. Meth. **A506** (2003) p. 250 (cit. on pp. 65, 87).

[77] W. Lukas, "Fast Simulation for ATLAS: Atlfast-II and ISF," tech. rep. ATL-SOFT-PROC-2012-065, CERN, 2012, URL: https://cds.cern.ch/record/1458503 (cit. on p. 65).

[78] J. Pequenao, "Event Cross Section in a computer generated image of the ATLAS detector.," 2008, URL: http://cds.cern.ch/record/1096081 (cit. on p. 66).

[79] T. Cornelissen, M. Elsing, S. Fleischmann, et al., "Concepts, Design and Implementation of the ATLAS New Tracking (NEWT)," tech. rep. ATL-SOFT-PUB-2007-007. ATL-COM-SOFT-2007-002, CERN, 2007, URL: https://cds.cern.ch/record/1020106 (cit. on p. 66).

[80] ATLAS Collaboration, "The Optimization of ATLAS Track Reconstruction in Dense Environments," tech. rep. ATL-PHYS-PUB-2015-006, CERN, 2015, URL: https://cds.cern.ch/record/2002609 (cit. on p. 66).

[81] ATLAS Collaboration, "Reconstruction of primary vertices at the ATLAS experiment in Run 1 proton–proton collisions at the LHC," tech. rep. arXiv:1611.10235. CERN-EP-2016-150, CERN, 2016, URL: https://cds.cern.ch/record/2235651 (cit. on p. 66).

[82] T. G. Cornelissen, N. Van Eldik, M. Elsing, et al., "Updates of the ATLAS Tracking Event Data Model (Release 13)," tech. rep. ATL-SOFT-PUB-2007-003. ATL-COM-SOFT-2007-008, CERN, 2007, URL: https://cds.cern.ch/record/1038095 (cit. on p. 67).

[83] R. Fruhwirth, *Application of Kalman filtering to track and vertex fitting*, Nucl. Instrum. Meth. **A262** (1987) p. 444 (cit. on p. 67).

[84] ATLAS collaboration, *A neural network clustering algorithm for the ATLAS silicon pixel detector*, Journal of Instrumentation **9** (2014) P09009 (cit. on p. 68).

[85] ATLAS Collaboration, *Comparison of the impact parameter resolution in Run 1 and Run 2*, (), URL: https://atlas.web.cern.ch/Atlas/GROUPS/PHYSICS/PLOTS/IDTR-2015-007/ (cit. on p. 68).

[86] "Vertex Reconstruction Performance of the ATLAS Detector at $\sqrt{s}$ = 13 TeV," tech. rep. ATL-PHYS-PUB-2015-026, CERN, 2015, URL: http://cds.cern.ch/record/2037717 (cit. on p. 69).

[87] ATLAS collaboration, *Muon reconstruction performance of the ATLAS detector in proton–proton collision data at $\sqrt{s}$ = 13 TeV*, The European Physical Journal C **76** (2016) p. 292 (cit. on pp. 69, 70).

[88] ATLAS Collaboration, "Electron and photon reconstruction and identification in ATLAS: expected performance at high energy and results at 900 GeV," tech. rep. ATLAS-CONF-2010-005, CERN, 2010, URL: https://cds.cern.ch/record/1273197 (cit. on p. 71).

[89] "Electron efficiency measurements with the ATLAS detector using the 2015 LHC proton-proton collision data," tech. rep. ATLAS-CONF-2016-024, CERN, 2016, URL: https://cds.cern.ch/record/2157687 (cit. on pp. 71, 72).

[90] W. Lampl, S. Laplace, D. Lelas, et al., "Calorimeter Clustering Algorithms: Description and Performance," tech. rep. ATL-LARG-PUB-2008-002. ATL-COM-LARG-2008-003, CERN, 2008, URL: https://cds.cern.ch/record/1099735 (cit. on pp. 71, 73).

[91] ATLAS Collaboration, "Photon identification in 2015 ATLAS data," tech. rep. ATL-PHYS-PUB-2016-014, CERN, 2016, URL: https://cds.cern.ch/record/2203125 (cit. on p. 72).

[92] M. Cacciari, G. P. Salam, and G. Soyez, *The anti- k t jet clustering algorithm*, Journal of High Energy Physics **2008** (2008) p. 063 (cit. on pp. 73, 88).

[93] ATLAS Collaboration, *Jet energy scale measurements and their systematic uncertainties in proton-proton collisions at $\sqrt{s}$ = 13 TeV with the ATLAS detector*, Phys. Rev. D **96** (7 2017) p. 072002 (cit. on pp. 74, 176).

[94] ATLAS Collaboration, "Tagging and suppression of pileup jets with the ATLAS detector," tech. rep. ATLAS-CONF-2014-018, CERN, 2014, URL: https://cds.cern.ch/record/1700870 (cit. on pp. 74, 75).

[95] ATLAS Collaboration, "Tau Reconstruction and Identification Performance in ATLAS," tech. rep. ATLAS-CONF-2010-086, CERN, 2010, URL: https://cds.cern.ch/record/1298857 (cit. on p. 75).

[96] "Performance of missing transverse momentum reconstruction for the ATLAS detector in the first proton-proton collisions at at $\sqrt{s}$= 13 TeV," tech. rep. ATL-PHYS-PUB-2015-027, CERN, 2015, URL: https://cds.cern.ch/record/2037904 (cit. on pp. 75, 76).

[97] "Expected performance of missing transverse momentum reconstruction for the ATLAS detector at $\sqrt{s}$ = 13 TeV," tech. rep. ATL-PHYS-PUB-2015-023, CERN, 2015, URL: https://cds.cern.ch/record/2037700 (cit. on p. 76).

[98] G. Apollinari, I. Béjar Alonso, O. Brüning, et al., *High-Luminosity Large Hadron Collider (HL-LHC): Preliminary Design Report*, CERN Yellow Reports: Monographs, CERN, 2015, URL: https://cds.cern.ch/record/2116337 (cit. on p. 77).

[99] A. Collaboration, "Technical Proposal: A High-Granularity Timing Detector for the ATLAS Phase-II Upgrade," tech. rep. CERN-LHCC-2018-023. LHCC-P-012, CERN, 2018, URL: https://cds.cern.ch/record/2623663 (cit. on p. 77).

[100] G. Piacquadio and K. Jakobs, "Identification of b-jets and investigation of the discovery potential of a Higgs boson in the $WH \to l\nu b\bar{b}$ channel with the ATLAS experiment," Presented on 11 Jan 2010, 2010, URL: https://cds.cern.ch/record/1243771 (cit. on p. 80).

[101] ATLAS Collaboration, "Optimisation of the ATLAS *b*-tagging performance for the 2016 LHC Run," tech. rep. ATL-PHYS-PUB-2016-012, CERN, 2016, URL: http://cds.cern.ch/record/2160731 (cit. on pp. 81–83, 93).

[102] ATLAS Collaboration,
"Secondary vertex finding for jet flavour identification with the ATLAS detector,"
tech. rep. ATL-PHYS-PUB-2017-011, CERN, 2017, URL: http://cds.cern.ch/record/2270366
(cit. on p. 82).

[103] G Piacquadio and C Weiser, *A new inclusive secondary vertex algorithm for b-jet tagging in ATLAS*, Journal of Physics: Conference Series **119** (2008) p. 032032 (cit. on p. 82).

[104] ATLAS Collaboration, *Performance of b-jet identification in the ATLAS experiment*,
Journal of Instrumentation **11** (2016) P04008 (cit. on pp. 83, 176).

[105] ATLAS Collaboration, "Technical Design Report for the ATLAS ITk Pixel Detector,"
tech. rep. ATLAS-TDR-30, CERN, 2017, URL: https://cds.cern.ch/record/2285585
(cit. on pp. 84–88, 100, 107, 115).

[106] ATLAS Collaboration, "Technical Design Report for the ATLAS Inner Tracker Strip Detector,"
tech. rep. ATLAS-TDR-025, CERN, 2017, URL: https://cds.cern.ch/record/2257755
(cit. on pp. 84–87, 92).

[107] T. Sjostrand, S. Mrenna, and P. Z. Skands, *PYTHIA 6.4 Physics and Manual*, JHEP **05** (2006) p. 026,
arXiv: hep-ph/0603175 [hep-ph] (cit. on pp. 87, 142).

[108] E. Bouhova-Thacker, T. Koffas, V. Kostyukhin, et al.,
"Vertex reconstruction in the ATLAS experiment at the LHC,"
2008 IEEE Nuclear Science Symposium Conference Record, 2008 p. 1720 (cit. on p. 87).

[109] ATLAS Collaboration, "ATLAS Insertable B-Layer Technical Design Report,"
tech. rep. ATLAS-TDR-19, CERN, 2010, URL: https://cds.cern.ch/record/1291633
(cit. on p. 87).

[110] ATLAS Collaboration,
"Optimisation and performance studies of the ATLAS *b*-tagging algorithms for the 2017-18 LHC run,"
tech. rep. ATL-PHYS-PUB-2017-013, CERN, 2017, URL: http://cds.cern.ch/record/2273281
(cit. on pp. 114, 116).

[111] The ATLAS collaboration,
Measurements of inclusive and differential fiducial cross-sections of $t\bar{t}$ production with additional heavy-flavour jets in proton-proton collisions at $\sqrt{s} = 13$ TeV with the ATLAS detector,
Journal of High Energy Physics **2019** (2019) p. 46 (cit. on pp. 126, 128, 130, 132, 138–141).

[112] R. D. Ball, V. Bertone, S. Carrazza, et al., *Parton distributions for the LHC run II*,
Journal of High Energy Physics **2015** (2015) p. 40 (cit. on pp. 127, 162).

[113] ATLAS Collaboration, "ATLAS Run 1 Pythia8 tunes," tech. rep. ATL-PHYS-PUB-2014-021, 2014,
URL: https://cds.cern.ch/record/1966419 (cit. on pp. 127, 162).

[114] ATLAS Collaboration, "Studies on top-quark Monte Carlo modelling for Top2016,"
tech. rep. ATL-PHYS-PUB-2016-020, CERN, 2016,
URL: https://cds.cern.ch/record/2216168 (cit. on p. 127).

[115] J. Alwall, R. Frederix, S. Frixione, et al., *The automated computation of tree-level and next-to-leading order differential cross sections, and their matching to parton shower simulations*,
Journal of High Energy Physics **2014** (2014) p. 79, ISSN: 1029-8479 (cit. on p. 127).

[116] The ATLAS collaboration,
"Modelling of the $t\bar{t}H$ and $t\bar{t}V$ $(V = W, Z)$ processes for $\sqrt{s} = 13$ TeV ATLAS analyses,"
tech. rep. ATL-PHYS-PUB-2016-005, CERN, 2016,
URL: https://cds.cern.ch/record/2120826 (cit. on p. 127).

[117] T. Gleisberg, S. Höche, F. Krauss, et al., *Event generation with SHERPA 1.1*, Journal of High Energy Physics **2009** (2009) p. 007 (cit. on pp. 127, 163).

[118] M. Czakon and A. Mitov, *Top++: A program for the calculation of the top-pair cross-section at hadron colliders*, Computer Physics Communications **185** (2014) p. 2930 (cit. on pp. 128, 172).

[119] M. Cacciari, G. P. Salam, and G. Soyez, *The catchment area of jets*, Journal of High Energy Physics **2008** (2008) p. 005 (cit. on p. 128).

[120] T. P. Calvet, A. Duperrin, and G. Aad, "Search for the production of a Higgs boson in association with top quarks and decaying into a b-quark pair and b-jet identification with the ATLAS experiment at LHC," Presented 08 Nov 2017, 2017, URL: `https://cds.cern.ch/record/2296985` (cit. on pp. 129, 179, 183).

[121] Atlas Collaboration, *Corrigendum to: "Measurement of the $t\bar{t}$ production cross-section using $e\mu$ events with b-tagged jets in pp collisions at $\sqrt{s} = 13$ TeV with the ATLAS detector; [Phys. Lett. B 761 (2016) 136-157]*, Physics Letters B **772** (2017) p. 879 (cit. on p. 130).

[122] The ATLAS collaboration, "Estimation of non-prompt and fake lepton backgrounds in final states with top quarks produced in proton-proton collisions at $\sqrt{s} = 8\,TeV$ with the ATLAS detector," tech. rep. ATLAS-CONF-2014-058, CERN, 2014, URL: `https://cds.cern.ch/record/1951336` (cit. on pp. 130, 166).

[123] G. D'Agostini, *A multidimensional unfolding method based on Bayes' theorem*, Nuclear Instruments and Methods in Physics Research Section A: Accelerators, Spectrometers, Detectors and Associated Equipment **362** (1995) p. 487 (cit. on p. 137).

[124] T. Adye, *Unfolding algorithms and tests using RooUnfold*, arXiv e-prints (2011), arXiv: `1105.1160 [physics.data-an]` (cit. on p. 137).

[125] A. Hoecker, P. Speckmayer, J. Stelzer, et al., *TMVA - Toolkit for Multivariate Data Analysis*, arXiv e-prints (2007), arXiv: `physics/0703039 [physics.data-an]` (cit. on p. 151).

[126] ATLAS Collaboration, *Search for the Standard Model Higgs boson produced in association with top quarks and decaying into $b\bar{b}$ in pp collisions at $\sqrt{s} = 8$ TeV with the ATLAS detector*, The European Physical Journal C **75** (2015) p. 349 (cit. on p. 159).

[127] The CMS collaboration, *Search for the associated production of the Higgs boson with a top-quark pair*, Journal of High Energy Physics **2014** (2014) p. 87 (cit. on p. 159).

[128] ATLAS Collaboration, *Search for the standard model Higgs boson produced in association with top quarks and decaying into a $b\bar{b}$ pair in pp collisions at $\sqrt{s} = 13$ TeV with the ATLAS detector*, Phys. Rev. D **97** (7 2018) p. 072016 (cit. on pp. 159, 163, 166, 168–173, 175, 177–181).

[129] B. Nachman, P. Nef, A. Schwartzman, et al., *Jets from jets: re-clustering as a tool for large radius jet reconstruction and grooming at the LHC*, Journal of High Energy Physics **2015** (2015) p. 75 (cit. on p. 161).

[130] D. J. Lange, *The EvtGen particle decay simulation package*, Nuclear Instruments and Methods in Physics Research Section A: Accelerators, Spectrometers, Detectors and Associated Equipment **462** (2001) p. 152, BEAUTY2000, Proceedings of the 7th Int. Conf. on B-Physics at Hadron Machines (cit. on p. 162).

[131] F. Cascioli, P. Maierhöfer, and S. Pozzorini, *Scattering Amplitudes with Open Loops*, Phys. Rev. Lett. **108** (11 2012) p. 111601 (cit. on p. 163).

[132] M. Guzzi, P. Nadolsky, E. Berger, et al., *CT10 parton distributions and other developments in the global QCD analysis*, arXiv e-prints (2011), arXiv: 1101.0561 [hep-ph] (cit. on p. 163).

[133] J. Gao, M. Guzzi, J. Huston, et al., *CT10 next-to-next-to-leading order global analysis of QCD*, Phys. Rev. D **89** (3 2014) p. 033009 (cit. on p. 163).

[134] T. Gleisberg and S. Höche, *Comix, a new matrix element generator*, Journal of High Energy Physics **2008** (2008) p. 039 (cit. on p. 165).

[135] S. Schumann and F. Krauss, *A parton shower algorithm based on Catani-Seymour dipole factorisation*, Journal of High Energy Physics **2008** (2008) p. 038 (cit. on p. 165).

[136] ATLAS Collaboration, "Measurement of W and Z Boson Production Cross Sections in pp Collisions at $\sqrt{s}$ = 13 TeV in the ATLAS Detector," tech. rep. ATLAS-CONF-2015-039, CERN, 2015, URL: http://cds.cern.ch/record/2045487 (cit. on p. 165).

[137] P. Z. Skands, *Tuning Monte Carlo generators: The Perugia tunes*, Phys. Rev. D **82** (7 2010) p. 074018 (cit. on p. 166).

[138] J. Pumplin, D. R. Stump, J. Huston, et al., *New Generation of Parton Distributions with Uncertainties from Global QCD Analysis*, Journal of High Energy Physics **2002** (2002) p. 012 (cit. on p. 166).

[139] K. Cranmer, G. Lewis, L. Moneta, et al., "HistFactory: A tool for creating statistical models for use with RooFit and RooStats," tech. rep. CERN-OPEN-2012-016, New York U., 2012, URL: https://cds.cern.ch/record/1456844 (cit. on p. 171).

[140] ATLAS Collaboration, *Studies on top-quark Monte Carlo modelling with Sherpa and MG5_aMC@NLO*, ATL-PHYS-PUB-2017-007, 2017, URL: https://cds.cern.ch/record/2261938 (cit. on p. 173).

[141] ATLAS Collaboration, *Luminosity determination in pp collisions at $\sqrt{s}$ = 8 TeV using the ATLAS detector at the LHC*, The European Physical Journal C **76** (2016) p. 653 (cit. on p. 175).

[142] ATLAS Collaboration, "Measurement of b-tagging Efficiency of c-jets in $t\bar{t}$ Events Using a Likelihood Approach with the ATLAS Detector," tech. rep. ATLAS-CONF-2018-001, CERN, 2018, URL: https://cds.cern.ch/record/2306649 (cit. on p. 176).

[143] G. Cowan, K. Cranmer, E. Gross, et al., *Asymptotic formulae for likelihood-based tests of new physics*, Eur. Phys. J. **C71** (2011) p. 1554, [Erratum: Eur. Phys. J.C73,2501(2013)] (cit. on p. 179).

[144] ATLAS Collaboration, *Observation of Higgs boson production in association with a top quark pair at the LHC with the ATLAS detector*, Phys. Lett. B **784** (2018) p. 173 (cit. on pp. 183, 184).

[145] ATLAS Collaboration, *Evidence for the associated production of the Higgs boson and a top quark pair with the ATLAS detector*, Phys. Rev. D **97** (7 2018) p. 072003 (cit. on pp. 183, 208).

[146] ATLAS Collaboration, *Measurements of Higgs boson properties in the diphoton decay channel with 36 fb^{-1} of pp collision data at $\sqrt{s}$ = 13 TeV with the ATLAS detector.*, Phys. Rev. D **98** (2018) 052005. 136 p (cit. on pp. 183, 208).

[147] ATLAS Collaboration, *Measurement of the Higgs boson coupling properties in the $H \to ZZ^* \to 4\ell$ decay channel at $\sqrt{s}$ = 13 TeV with the ATLAS detector.*, JHEP **1803** (2017) 095. 59 p (cit. on p. 183).

[148] F. Boudjema, D. Guadagnoli, R. M. Godbole, et al.,
Laboratory-frame observables for probing the top-Higgs boson interaction,
Phys. Rev. D **92** (1 2015) p. 015019 (cit. on p. 208).

[149] F. Maltoni, D. Pagani, A. Shivaji, et al.,
Trilinear Higgs coupling determination via single-Higgs differential measurements at the LHC,
European Physical Journal C **77** (2017) p. 887 (cit. on p. 208).

[150] M. Delmastro, N. Berger, C. Bertella, et al., "Simplified Template Cross Sections – Stage 1.1,"
tech. rep. arXiv:1906.02754, CERN, 2019, URL: https://cds.cern.ch/record/2669925
(cit. on p. 209).

Auxiliary materials

A. Impact of the new ITk track categories on the IP2D performance

Figure .48 shows the b-tagging performance in terms of light-jet and charm-jet rejections for the IP2D tagger, comparing the performance obtained with the Run 2 categories (out-of-the-box PDFs) to that with the ITk optimal configuration categories, with the reference histograms derived based on simulations of Step 2.2 layout

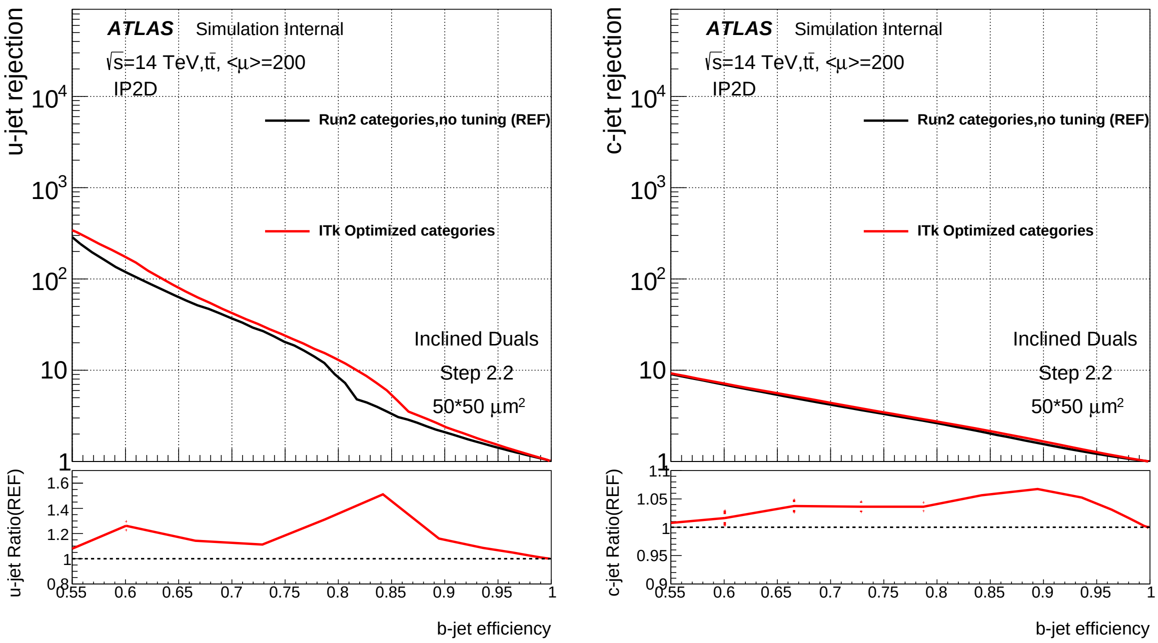

Figure .48.: Light-jet (left) and charm-jet (right) rejection *vs* b-tagging efficiency for the IP2D algorithm, evaluated in $t\bar{t}$ events with 200 pile-up events for the ITk layout. The results obtained with the out-of-the-box Run 2 categories (black) and the new ITk ones (red) are compared and their ratio is shown on the bottom pad.

Figures .49 and .50 depict the b-tagging performance of IP2D in exclusive p_T and η regions respectively, comparing the performance obtained with the optimal ITk categories with respect to the one obtained with the Run 2 categories.

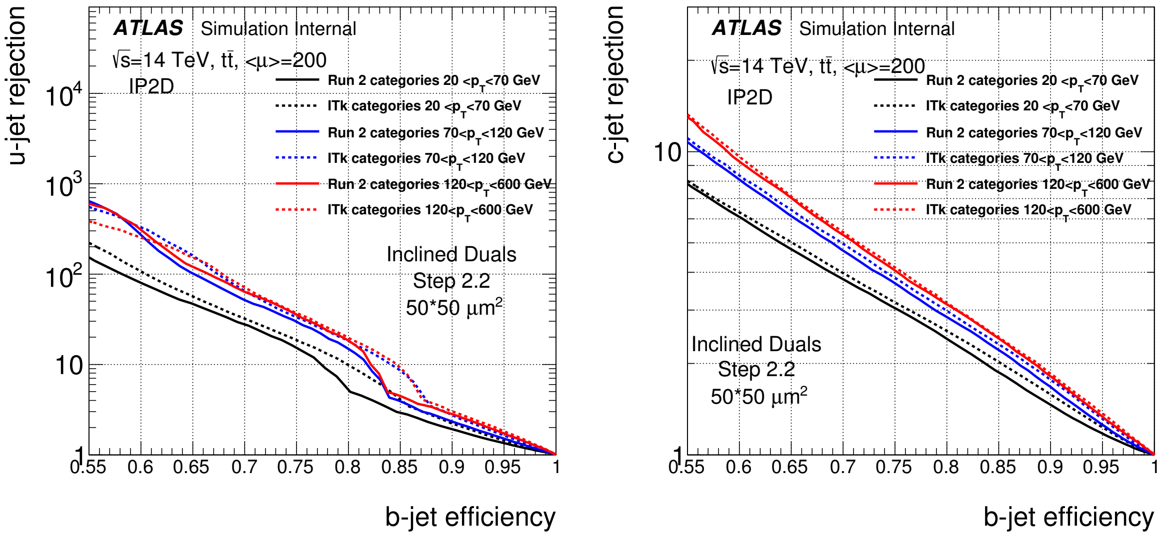

Figure .49.: Light-jet (left) and charm-jet (right) rejection *vs* b-tagging efficiency for the IP2D tagging algorithm, evaluated in $t\bar{t}$ events with 200 pile-up events for the ITk layout. The results obtained with the out-of-the-box Run 2 categories (solid line) and the new ITk ones (dashed line) are compared in different p_T regions: $20 < p_T < 70$ GeV (black), $70 < p_T < 120$ GeV (blue) and $120 < p_T < 600$ GeV (red).

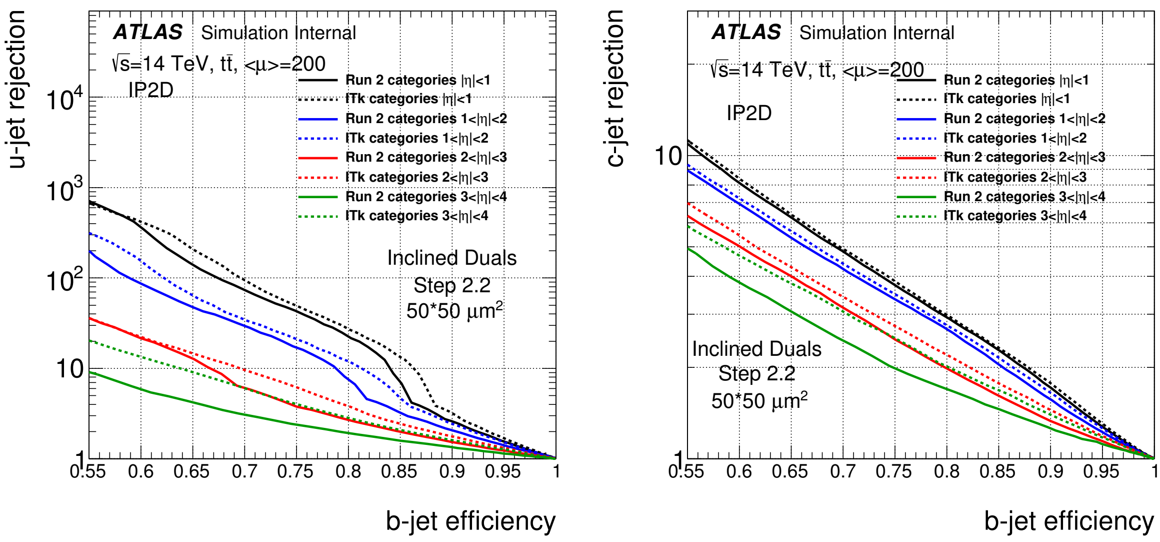

Figure .50.: Light-jet (left) and charm-jet (right) rejection *vs* b-tagging efficiency for the IP2D tagging algorithm, evaluated in $t\bar{t}$ events with 200 pile-up events for the ITk layout. The performances obtained with the out-of-the-box Run 2 (solid lines) and the new ITk (dashed lines) PDFs are compared in different η regions: $|\eta| < 1$ (black), $1 < |\eta| < 2$ (blue), $2 < |\eta| < 3$ (red) and $3 < |\eta| < 4$ (green).